TECHNISCHE UNIVERSITÄT MÜNCHEN

Ingenieurfakultät Bau Geo Umwelt

Lehrstuhl und Prüfamt für

Grundbau, Bodenmechanik, Felsmechanik und Tunnelbau

Experimental evaluation of the suction-induced effective stress and the shear strength of as-compacted silty sands

Ludwig Angerer

Vollständiger Abdruck der von der Ingenieurfakultät Bau Geo Umwelt der Technischen Universität München zur Erlangung des akademischen Grades eines

Doktor-Ingenieurs

genehmigten Dissertation.

Vorsitzender: Prof. Dr.-Ing. Kai-Uwe Bletzinger

Prüfer der Dissertation:

1. Prof. Dr.-Ing. Roberto Cudmani
2. Prof. Dr.-Ing. Ivo Herle
3. Prof. Dr.-Ing. Jürgen Grabe

Die Dissertation wurde am 08.03.2019 bei der Technischen Universität München eingereicht und durch die Ingenieurfakultät Bau Geo Umwelt am 19.11.2019 angenommen.

Preface of the Editor

Despite of the considerable effort made in the basic research in the last decades, the shear behaviour of partially saturated soils has not been comprehensively understood. In this context, Ludwig's innovative concepts and approaches are an important contribution to clarify and describe the complex shear behaviour, especially the shear strength of partially saturated coarse granular materials containing non-plastic fines.

Against the opinion of many researchers and practitioners, Ludwig shows that due to the dual effect of the suction the (Bishop's) effective stress and the density are not sufficient to describe the shear behaviour of compacted partially saturated granular soils. Moreover, he demonstrates that for practical purposes the contribution of the suction-induced effective stress (first effect of suction) to the shear strength can be neglected in coarse granular soil containing non-plastic fines. This is an important result from the practical point of view as the measurement of suction is time consuming and costly. The shear strength is actually enhanced by a fabric-induced dilatancy, which depends on the compaction water content and, through the SWRC, on the suction (second effect of suction).

The experimental contribution of Ludwig is outstanding. The uniaxial tension, uniaxial compression and the triaxial compression testing devices for partially saturated soils were developed by him and constructed under his guidance. From them, the uniaxial tension device, which can determine tensile strengths as low as 0.1 kPa, is so far unique. Meticulously, he investigated the error sources of each of these devices and proposed corrections factors to account for them. In addition, he successfully met several challenges associated with the soil sample preparation, suction measurement and reproducibility of the initial density and homogeneity of the soil samples. For the interpretation of the test results, several assumptions were necessary. Herein, it is worth special mention the novel method proposed for the interpretation of the uniaxial tension test and the combination with uniaxial compression test to estimate the shear strength at very low stresses. To my knowledge, this approach is new in partially saturated soil mechanics.

Ludwig's research topic was motivated by the verification of the stability of existing railway embankments consisting of partially saturated silty sands, which were designed and constructed between the end of the 19th and the beginning of the 20th century based mostly on empirical rules. Although the embankments have been performing satisfactorily for more than 100 years, their stability cannot be verified based on the classical Limit Equilibrium Theory if the effect of fabric is disregarded. To facilitate the application of the results to this practical case, Ludwig proposes an evaluation of the shear resistance in analogy to the Mohr-Coulomb yield criterion, in which the peak friction angle depends nonlinearly on the effective stress and the fabric. The proposed yield criterion provides a transition between the shear strength for low stresses, controlled by the fabric, and high stresses, by which the influence on fabric can be disregarded. In a very simple case study, Ludwig also closes the gap between the basic research and the practical application by showing how the proposed yield criterion can contribute to improve the "computational" safety of the old railway embankments.

Roberto Cudmani

Abstract

When evaluating shear tests on as-compacted soils in peak condition, the shear strength is increased compared to the saturated condition due to the dual effect of suction on effective stress and dilatancy. Especially at low stress levels, the dependency of the non-linearity of the failure criterion on microstructure and suction makes it difficult to distinguish clearly between these two effects. In this paper, a concept for the experimental determination of the effect of suction on effective stress and the effect of suction on dilatancy for as-compacted silty sand with aggregated fines is presented. To assess the shear strength at low stresses experimentally, uniaxial shear tests were carried out, whereas triaxial compression tests were carried out to assess higher stresses. Within the presented concept, the evaluation of test results indicates that suction has a minor effect on the effective stress. The increase in shear strength is mainly caused by a stronger dilatancy, which depends on the interaction between suction and microstructure. This interaction is shown by performing mercury intrusion porosimetries and measuring soil-water retention curves. The dilatancy is strongest for samples with solid-like aggregated fines exhibiting high suction-induced intra-aggregate stress. Finally, a case study shows how this shear behavior can be included in a standard-compliant calculation of slope stability using the Mohr-Coulomb failure criterion.

Zusammenfassung

Bei der Auswertung von Scherversuchen an verdichteten Böden im Peak ist die Scherfestigkeit im Vergleich zum gesättigten Zustand aufgrund des Effekts der Saugspannung sowohl auf die effektive Spannung als auch auf die Dilatanz erhöht. Die Abhängigkeit der Nichtlinearität der Bruchbedingung von Mikrostruktur und Saugspannung macht es besonders im niedirgen Spannungsbereich schwierig, diese beiden Effekte klar zu unterscheiden. In dieser Arbeit wird ein Konzept zur experimentellen Bestimmung des Effekts der Saugspannung sowohl auf die effektive Spannung als auch auf die Dilatanz für einen verdichteten, schluffigen Sand mit aggregiertem Feinkorn vorgestellt. Zur experimentellen Ermittlung der Scherfestigkeit bei niedrigen Spannungen wurden einaxiale Scherversuche durchgeführt, während zur Beurteilung der Scherfestigkeit bei höheren Spannungen triaxiale Kompressionsversuche durchgeführt wurden. Die Versuchsauswertung mit dem vorgeschlagenen Konzept ergibt, dass die Saugspannung einen geringen Einfluss auf die effektive Spannung hat. Die Erhöhung der Scherfestigkeit wird hauptsächlich durch eine stärkere Dilatanz verursacht, die von der Wechselwirkung zwischen Saugspannung und Mikrostruktur abhängt. Diese Wechselwirkung wird mit Hilfe von Quecksilber-Porosimetrien und Saugspannungs-Wassergehalts-Beziehungen aufgezeigt. Die Ergebnisse zeigen, dass die Dilatanz bei Proben mit feststoffähnlichen aggregierten Feinanteilen, die hohe saugspannungsinduzierte Intra-Aggregat-Spannungen aufweisen, am stärksten ist. Anhand eines Fallbeispiels wird abschließend gezeigt, wie dieses Scherverhalten mit Hilfe des Mohr-Coulomb-Bruchkriteriums in eine normgerechte Berechnung der Böschungsstandsicherheit einbezogen werden kann.

Table of contents

1 Introduction

1.1 Background

Guaranteeing the slope stability of traffic embankments is an indispensable task of geotechnical engineering. Synthetic earthwork embankments must be able to resist loads due to the weight of the soil and loads due to structures like railways and roads. In addition, embankments must be able to cope with temporary and exceptional loads caused by natural events like floods or earthquakes. The ability of the soil to withstand these loads depends on various factors (i.e., on the soil type and on its *in situ* conditions, such as density, stress state within the embankment and water content). In this context, traffic embankments are characterized by the fact that they lie above the groundwater level. In general, they can therefore be regarded as being predominantly unsaturated.

Slope stability is currently most often addressed using the limit equilibrium theory (LET). The LET considers the equilibrium of acting and resisting forces along the interfaces between rigid bodies, assuming that the shear strength is fully mobilized. Therefore, a major prerequisite of the application of LET is the realistic description of shear strength.

In slope stability analysis using LET, the shear strength τ is commonly described by the Mohr–Coulomb failure criterion:

$$\tau = \sigma' \cdot \tan\varphi' + c' \tag{1.1}$$

with σ' Effective stress

φ' Effective friction angle

c' Effective cohesion

Mohr–Coulomb failure criteria are therefore typified by two parameters: the effective friction angle φ' and the effective cohesion c'. For constant friction angles φ', the above approach is linear with respect to the effective stress state. In general, the higher the normal stress, the higher the shear strength available.

At the beginning of the 20th century, traffic embankments were built without adequate quality assurance, since the construction methods of the time contained “rules of thumb.” This construction procedure often led to traffic embankments with steep slopes (when compared to modern traffic embankments) made of poorly compacted soils. This work investigates traffic embankments from Eastern Germany. In these embankments, the material is predominantly silty sands showing low water content while exhibiting aggregated fines (Angerer, Birle, and Vogt 2013, Angerer, Birle, and Cudmani 2016).

To date, the standard-compliant slope stability of many of these traffic embankments cannot be verified using LET (Angerer, Birle, and Vogt 2013). Consequently, costly remediation measures on the embankments may become necessary, although these embankments have

been performing satisfactorily for more than 100 years. In reality, discrepancy between the calculated slope stability and the observed behavior of embankments arises when the Mohr–Coulomb failure criterion is used to describe the shear strength, in particular when the required shear strength parameters (c' and φ') are determined through conventional laboratory tests.

In particular, two important mechanisms are neglected in conventional stability analysis:

i. Non-linear dependency of the shear strength on the effective stress state: It is well-known that the dependency of shear strength on effective stress is non-linear. In addition, the shear strength of granular soils - such as sands - is affected by the density (Taylor 1948, Lambe and Whitman 1969). For granular soils, the denser the material and the lower the stress state, the stronger the dilatancy, i.e., the higher the shear strength. Especially in medium-dense to dense granular soils at low to moderately high effective stresses, the shear strength is likely to show a distinct non-linear dependency on the effective stress (Ponce and Bell 1971, Fukushima and Tatsuoka 1984).

   When the Mohr–Coulomb's failure criterion (1.1) is used to analyze slope stability, high stresses are usually selected for the experimental determination of the shear strength parameters (Figure 1.1). From the results of these shear tests, a constant friction angle φ'_{M-C} and a constant cohesion c'_{M-C} is determined. This procedure therefore results in a linearization of the non-linear shear strength in the tested stress range. As indicated in Figure 1.1, in particular at low to moderate stresses, the non-linearity of the failure criterion cannot be described with this approach. Low to moderate stresses, however, predominate within traffic embankments. With the application of the shear strength parameters derived from conventional laboratory tests, the actual shear strength may thus significantly exceed the linear shear strength described by the Mohr–Coulomb failure criterion.

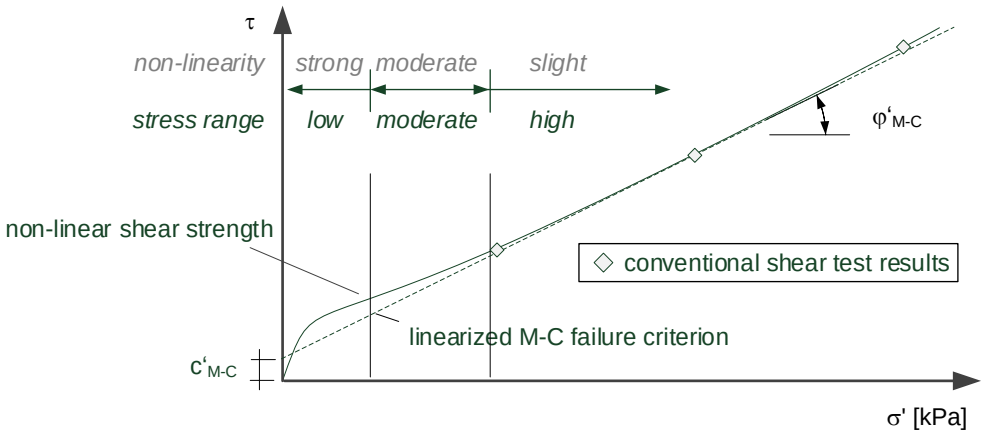

Figure 1.1: Definition of the stress range (low, moderate, high) and idealized deviation of the linearized Mohr–Coulomb failure criterion

ii. Dual effect of suction on shear strength: Under unsaturated conditions, the pore-water pressure is less than the atmospheric pressure. The pressure difference between the pore-air pressure and the pore-water pressure $s = u_a - u_w$ is referred to as suction or matric suction (Lu and Likos 2004), which mainly depends on the water content and the microstructure of the soil. On the one hand, suction increases grain-to-grain contact forces, which increase inter-particle friction and thus shear strength. On the other hand, dilatancy increases with increasing suction, which leads to an additional non-linear increase in shear strength (e.g., Gan & Fredlund 1996). For compacted soils, such as those found in traffic embankments, the stronger dilatancy may be related to a bimodal microstructure caused by the formation of aggregated fines (Toll 2000). Suction is thus considered as having a dual, enhancing effect on the shear strength (Nuth and Laloui 2007).

Therefore, to assess slope stability, a stress-dependent failure criterion rather than a linearized Mohr–Coulomb type of failure criterion should be used. For unsaturated conditions, the failure criterion should also depend on the enhancing effect of suction on dilatancy. The non-linearity of the failure criterion may therefore be more pronounced than in saturated conditions. In addition, the enhancing effect of suction on the effective stress state should be considered.

Since traffic embankments are exposed to climate and weather, however, the embankment material can exist in various hydraulic (unsaturated) states. As a consequence, for the experimental evaluation of shear strength, it is essential to assess the present *in situ* state of the soil, but also to predict the *in situ* state that will determine the shear strength in the long-term. Therefore, in addition to the soil type, the density and the microstructure, one must assess the local and the temporal distribution of both the water content and the suction in the respective embankment cross-section.

Note that in the experimental determination of the effect of suction on the effective stress, shear strength data from critical states are usually evaluated (e.g. Khalili & Khabbaz 1998). This evaluation is done because in this state the initial microstructure is assumed to be fully degraded and the measured shear strength is no longer affected by dilatancy. Thus, it is assumed that at critical state, any increase in the measured shear strength due to suction must be induced by an increase in effective stress and not by a stronger dilatancy. However, the increase in effective stress may also depend on the microstructure of the soil. Since the microstructure evolves with (shear) deformation (Romero and Simms 2009), the microstructure at the critical state may differ from the microstructure at peak conditions. Therefore, *a priori*, the increase in effective stress due to suction derived from the shear strength at the critical state may differ from the increase in effective stress due to suction at peak shear strength.

In view of the above, it appears preferable to derive both the effective stress and the failure criterion from peak shear strength data. This will be done within the scope of this work.

Although considerable progress has been made in recent years in experimental investigation of soil behavior for unsaturated silty sands, the following issues remain:

- An experimental method to clearly distinguish the dual effect of suction on peak shear strength (i.e., the proportion of the increase in effective stress or dilatancy due to suction on the increase in shear strength) has not yet been developed.
- Regarding the prediction of suction-induced effective stress from the soil-water retention curve (SWRC), in particular at low water contents—which are relevant for the regarded traffic embankments—the predictions of the models available in the literature diverge significantly from one another (Angerer 2016).
- The shear behavior of unsaturated silty sands at very low effective stresses has rarely been investigated. From the findings on saturated silty sands, it appears that at low effective stresses, a pronounced influence of the soil's microstructure on the shear behavior may be expected (Lade 2016). It can be expected that the above influence is even more pronounced under unsaturated conditions (Alonso, Pinyol, and Gens 2013).

1.2 Scope of the work

The goal of this research is to find a procedure to assess the slope stability of existing traffic embankments realistically. In this context, the study focuses on the experimental determination of unsaturated shear strength under monotonic shearing. The experimental investigation is carried out on silty sand, which captures the average properties and *in situ* states of soils encountered within existing traffic embankments. In particular, this study concentrates on the effect of suction on the shear strength at a constant density and within a narrow range of water content representative of the *in situ* conditions encountered within the embankments. Emphasis is put on the low to moderate stress range prevailing in traffic embankments. The assessment of the effect of density on the unsaturated shear strength is not the subject of this study.

Note that additional strength-enhancing effects such as aging mechanisms or cementation are likely to occur in old existing embankments. Such effects, however, are not the subject of this study. They can therefore be regarded as potential additional shear strength reserves.

1.3 Methods

Within the above constraints, the following issues must be clarified to determine the shear strength and the effective stress of silty sands under unsaturated conditions:

1. What are the properties and the momentary *in situ* states of the soils that exist in the traffic embankments under investigation? In particular, what density, suction, water content and microstructure can be expected?

2. How does the climate affect the temporal and local distribution of water content and suction (hydraulic condition) in the traffic embankment? In particular, are there areas with constant hydraulic properties in the long-term?
3. In the range of the *in situ* state of the embankment material, how does the shear strength of the saturated soil under drained conditions vary with stress level, and how can this dependency be described?
4. How large an increase in effective stress and dilatancy due to the unsaturated conditions be expected in existing traffic embankments? Additionally, how does the microstructure, in particular aggregated fines, affect the shear strength?

The first issue is assessed by performing exploratory drilling on a characteristic old traffic embankment. To characterize the soils and to evaluate densitiy, suction, water content and microstructure, laboratory tests are carried out on disturbed and undisturbed soil samples.

The second issue is a complex boundary value problem. Since the exploratory drilling only gives a momentary picture of the hydraulic properties within the embankment, long-term *in situ* measurements of the distribution of suction and water content with the simultaneous recording of climatic conditions are required. Based on these measurements, a numerical model must be calibrated and applied to predict the hydraulic performance of the embankment over a period extending beyond the measuring time. Since *in situ* measurements over a long period were not possible in this study, the long-term hydraulic performance of the embankments considered is estimated based on data on similar structures available in the literature.

The third and fourth issues are approached experimentally, so they are dealt with together. In order to determine the effect of suction on both the effective stress and dilatancy, shear tests are carried out on samples of saturated and unsaturated silty sand. To assess low effective stress levels, uniaxial tensile tests (UTTs) and unconfined compression tests (UCTs) are conducted on unsaturated samples. The shear strength at moderate stress levels is evaluated by means of triaxial compression tests on saturated and unsaturated samples. Emphasis is put on the influence of the microstructure on the dilatancy and on the effective stress. Based on the test results, a function is proposed to describe the failure criterion of saturated and unsaturated silty sands covering the range from low to high stresses.

Finally, the proposed failure criterion is used in a modified LET analysis to evaluate the stability of a case-study embankment.

1.4 Thesis organization

Chapter 2 reviews the current understanding of the shear strength of saturated and unsaturated soils, the concept of effective stress for unsaturated soils, and the microstructure and the hydraulic performance of embankments of silty sands.

In order to generally assess the effective stress state of unsaturated granular soils, Chapter 3 re-evaluates data from shear tests on unsaturated silty sands and silts published in the literature, drawing upon the framework of Bishop's effective stress.

In Chapter 4, a typical old traffic embankment from Eastern Germany consisting of silty sand is investigated to determine the *in situ* state of the soils to be examined (suction, water content, density, stress state, microstructure). The investigation program and the results of the field and laboratory tests are also presented.

Based on the findings from Chapter 4, a representative silty sand is selected which will be used for the experimental investigations in this work. In Chapter 5, the index properties, the water-retention behavior and the microstructure of the silty sand are determined.

In Chapter 6, a new experimental method is proposed to determine the effective stress as a function of suction and the shear strength at low stress states by using UCTs and UTTs.

In Chapter 7, triaxial compression tests are carried out on saturated and unsaturated samples to investigate the shear strength of the silty sand at higher stresses. With regard to the findings from Chapter 6, a simple expression is proposed to describe the observed failure criterion for saturated and unsaturated conditions mathematically.

In Chapter 8, a procedure is proposed to apply the findings from the previous chapters to the conventional analysis of slope stability using LET.

A summary of the findings is presented in Chapter 9.

Chapter 10 presents an outlook, considering the issues that could not be examined in the context of this work or that have emerged from this study.

2 Literature review

2.1 Basic concepts of unsaturated soil mechanics

2.1.1 Suction

While classical soil mechanics considers the soil as a two-phase system comprising soil particles and either air or water, unsaturated soil mechanics treats the soil as a three-phase system in which the space between the soil particles is filled with both liquid (usually water) and gas (usually air) (Fredlund, Rahardjo, and Fredlund 2012).

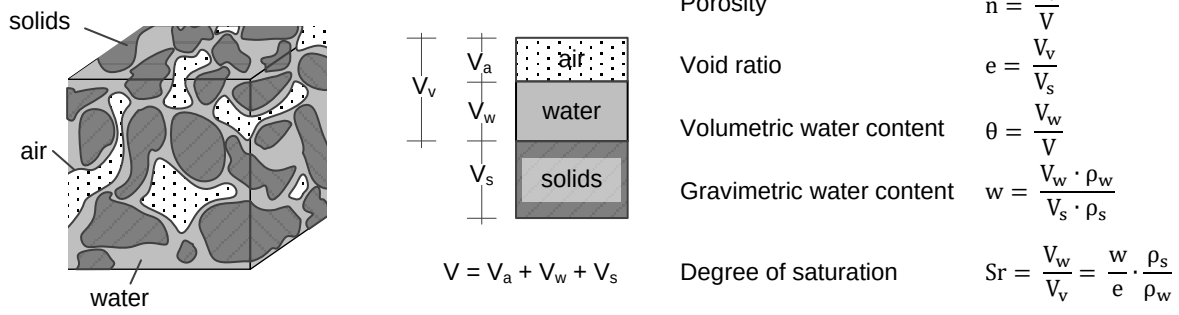

Figure 2.1: Soil element and its three-phase representation (adapted from Fredlund et al. 2012)

The interaction of the three phases and interfaces separating them leads to a complex energy state in the soil-water mass, commonly described by means of the concept of pore water potential (Nitao and Bear 1996). In a small soil element (for which potential gradients due to gravity or external pressures can be neglected), the energy state is often simply expressed as pore-water pressure u_w. The pressure u_w may fall well below the atmospheric air pressure u_a and achieves theoretical tensile stresses of several hundred megapascals. Note that such high tensile stresses can be mobilized only if no impurities (such as water bubbles or other materials) prevail in the water or on the interface between the confining material and the water, which give rise to the nucleation of cavities (Ridley and Burland 1993, Toker 2007, Marinho, Take, and Tarantino 2009).

Taking the atmospheric air pressure u_a as reference pressure, the potential of the pore water can be expressed through a positive value called *suction*:

$$s = u_a - u_w \tag{2.1}$$

From thermodynamic considerations, a relationship for the pore water potential relating the total suction to the relative humidity (RH) can be derived as follows (Murray and Sivakumar 2010):

$$s = u_a - u_w = -\frac{R_{gas} T \cdot \rho_w}{\omega_\upsilon} \cdot \ln RH \quad [Pa] \tag{2.2}$$

with R_{Gas} Universal gas constant $\left(8{,}314\ \frac{J}{mol \cdot K}\right)$

T Absolute temperature (K)

ω_υ Molar mass of water vapor $\left(18{,}016 \cdot 10^{-3}\ \frac{kg}{mol}\right)$

ρ_w Water density $\left(\frac{kg}{m^3}\right)$

RH Relative humidity (-).

Equation (2.1) is also termed *Kelvin's equation*.

Total suction is generally composed of matric suction (related to both capillary and adsorptive effects), osmotic suction (related to chemical imbalance of salt or contaminant concentrations as, e.g., occasionally present during seepage processes) and—to a lesser extent—thermal effects (Nitao and Bear 1996, Salager, El Youssoufi, and Saix 2007). In the absence of any significant temperature gradients and imbalances of salt or contaminants (as is the case in this work), contributions of osmosis and thermal effects are negligible (Fredlund, Rahardjo, and Fredlund 2012). Hence, total suction corresponds only to matric suction. It may thus be expected that only capillary and adsorbed water exists in the soil matrix, as illustrated in Figure 2.2. Therefore, instead of matric suction, the term *suction* is hereafter used to describe the pore water energy state caused by capillary and adsorption effects.

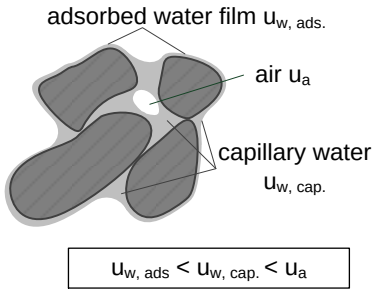

Figure 2.2: Components of pore-water pressure

Baker and Frydman (2009) compared the basic concepts of classical soil mechanics to modern concepts of soil physics. They noted that—strictly speaking—the adsorption component of the soil-water was a potential rather than a physical stress. The common allocation of a water pressure u_w to any adsorbed water, as indicated in Figure 2.2, would be questionable. Combining the water pressure u_w for adsorbed water with the capillary-induced water pressure into a single stress variable (matric suction or suction) would appear confusing. Baker and Frydman (2009) conclude that the term $s = u_a - u_w$ may be identified with the matrix potential only if one ignores adsorption. Thus, the term *suction* should solely account for mechanical tension of water.

However, the concept of suction may be seen as a desirably simplified approach to address unsaturated states constitutively, especially for mainly granular soils. The concept will thus be used within the scope of this work.

2.1.2 Conceptual model of capillary tubes

The capillary tube analogy (Figure 2.3) offers a useful tool to enhance the understanding of the concept of suction. In this conceptual model, a soil-pore of a certain size is equated with a capillary tube of a certain diameter.

Through equating the vertical forces acting along the water-air interphase (Figure 2.3a), this conceptual model results in a pressure deficiency of the water phase compared to the air phase (suction).:

$$s = \Delta u = u_a - u_w = \frac{2 \cdot T_w}{r} \cdot \cos \alpha_w \tag{2.3}$$

From the derivation, it follows that the water pressure is a function of the surface tension of the water–air interface T_w, the contact angle α_w and the capillary tube radius r.

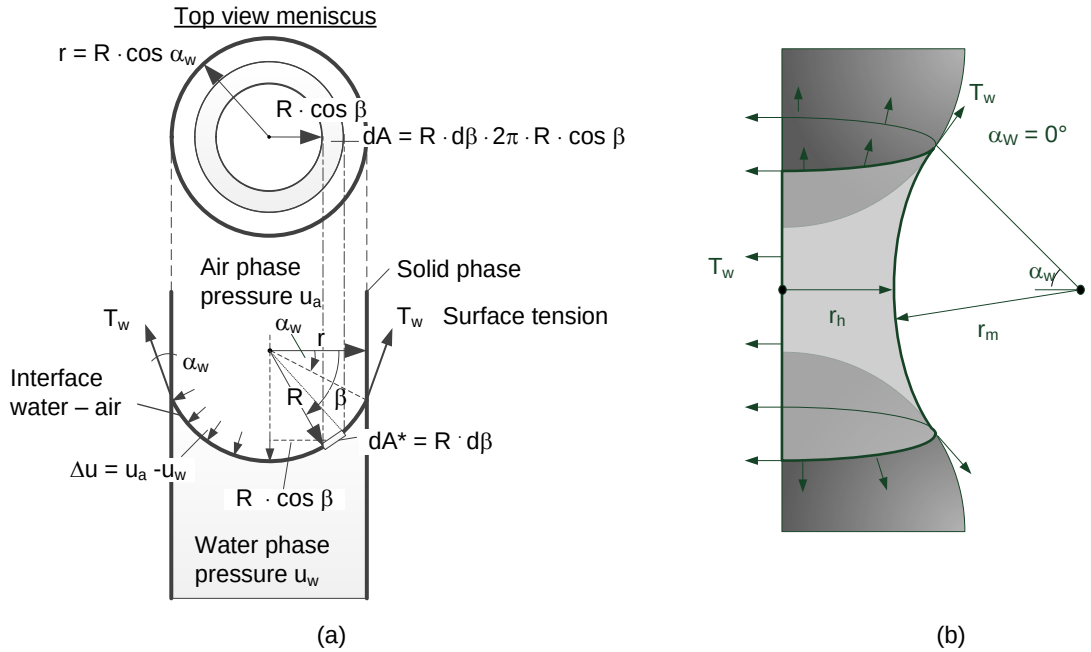

Figure 2.3: (a) Capillary tube and (b) double curved meniscus between adjacent soil particles

From the above equation it follows that the smaller the pore size, the higher the suction. Notwithstanding the reference to meniscus formation in capillary water, this analogy may also be applied to the adsorptive component of soil-water. Adsorptive water is naturally attached through hygroscopic effects to the mineral surfaces as a thin water film (Tarantino, Romero, and Cui 2009) and not through a physical stress (Baker and Frydman 2009). However, the binding potential of the adsorption water may be simplified by depicting it with the analogy of very thin capillary tubes, resulting in high values for suction.

Note that equation (2.3) describes a special case of the more general Young-Laplace equation for double curved air-water interfaces as shown in Figure 2.3b (Lu and Likos 2004):

$$s = u_a - u_w = T_w \left(\frac{1}{r_m} - \frac{1}{r_h}\right), \tag{2.4}$$

where r_m is the external radius and r_h is the internal radius of the capillary bridge (Figure 2.3b.). Note that to derive the above equation, the contact angle α_w was set to zero.

One advantage of the conceptual model of capillary tubes is that it helps to explain the dependency of suction on soil-water content. For example, equation (2.3) represents the local equilibrium along the curved interface between the water and air phase. In order to reach a global equilibrium, however, the water column in the pipe must rise to a certain height h at which the weight of the water column suspended at the water-solid interface is carried only by surface tension:

$$h \cdot \pi \cdot r^2 \cdot \gamma_w = T_w \cdot \cos \alpha_w \cdot 2\pi \cdot r$$

$$h = \frac{2 \cdot T_w}{r \cdot \gamma_w} \cdot \cos \alpha_w \tag{2.5}$$

with γ_w Unit weight of water [kN/m³].

This weight is transferred back into the wall of the capillary tube via adhesion. Equation (2.5) therefore indicates the capillary rise in soils.

The capillary forces from opposite menisci may balance each other in a closed pore system (Figure 2.2) or may not even be present in adsorption water, which may render the idea of a capillary rise less meaningful. Nevertheless, such a model remains suitable to depict the relationship between pore water and suction, as done by Scheuermann (2005). Since a soil mass comprises of a large number of different pore sizes and related volumes, the above-mentioned analogy leads to a bundle of capillary tubes of various diameters showing that the pore water is not evenly bonded in the soil matrix (Figure 2.4).

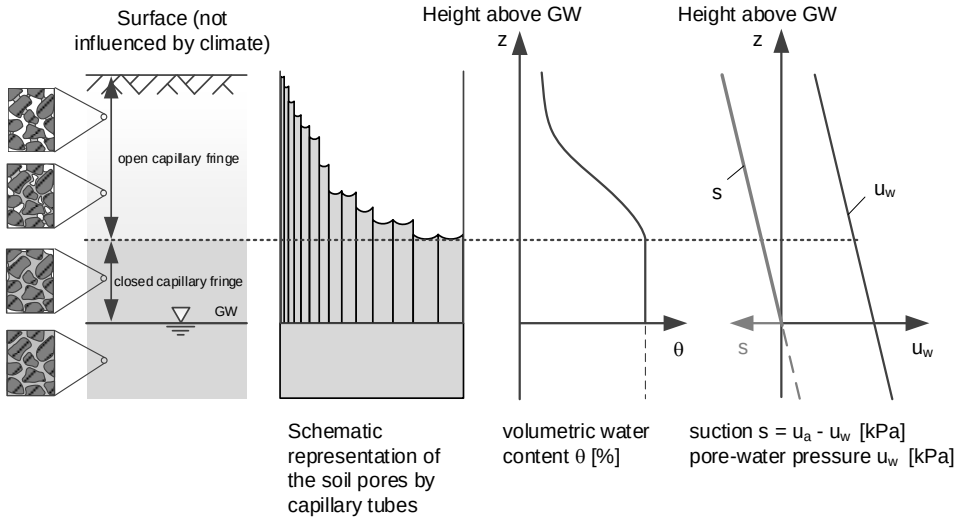

Figure 2.4: Capillary tube analogy, suction profile and profile of water content above groundwater table GW, adapted from Scheuermann (2005)

Thus, applying a certain level of suction to the soil will lead to a certain corresponding water content. In turn, the amount of water in a porous medium depends on the level of suction, as illustrated in Figure 2.4.

2.1.3 Measuring suction

A wide spectrum of techniques has been developed for the experimental determination of suction. Most techniques have in common that they achieve reliable results only within a limited range of suction. Since the magnitude of suction can vary between 0 kPa and approximately $1 \cdot 10^6$ kPa (Fredlund, Rahardjo, and Fredlund 2012), several experimental techniques have to be used to capture the full range of suction reliably. Some techniques record total suction, while others are used to measure matric or osmotic suction (Lu and Likos 2004). Furthermore, the various techniques differ in how suction is determined—either directly or indirectly. As described by Murray and Sivakumar (2010), direct methods measure the pore-water pressure at equilibrium of a soil-water system without involving any external medium, while indirect methods use an external medium that achieves equilibrium (e.g., moisture content of the air) with the soil.

A summary of commonly used techniques is shown in Table 2.1.

Method	**Suction component**	**Suction range [kPa]**	**Equilibrium time** (adapted from Ridley & Burland 1993)	**Remarks**
Conventional tensiometer	Matric	0–90	Hours	Direct measurement of pore-water pressure referred to atmospheric air pressure
High capacity tensiometer	Matric	0–1500	Hours	Direct measurement of pore-water pressure referred to atmospheric air pressure
Axis translation technique	Matric	0–1500	Days / weeks	Direct measurement of pore-water pressure referred to elevated controlled air pressure
Electrical and thermal conductivity sensor	Matric	0–400	Days	Indirect measurement via detection of electrical or thermal resistance
Filter paper	Matric	Entire range	Weeks	Indirect measurement via detection of absorbed water mass, filter paper in contact with specimen
	Total	1–50000	Weeks	Indirect measurement via detection of absorbed water mass, filter paper not in contact with specimen
Thermocouple psychrometer	Total	100–8000	Weeks / months	Indirect measurement via detection of relative humidity (RH) based on Kelvin's equation
Chilled mirror hygrometer	Total	$1000–1 \cdot 10^6$	Hours	Indirect measurement via detection of RH of suction based on Kelvin's equation

Table 2.1: Suction measurement techniques (adapted from Birle 2011)

This chapter considers only those techniques used within the scope of this work: conventional tensiometer measurements in the low suction range and measurements with the chilled mirror hygrometer in the high suction range. Further information regarding the different experimental techniques can be found, for example, in Scanlon et al. (2002), Lu and Likos (2004), Tarantino et al. (2009), Murray and Sivakumar (2010) or Fredlund et al. (2012).

2.1.3.1 Tensiometer

A tensiometer essentially consists of a differential pressure sensor to which the atmospheric air pressure and pore-water pressure are applied. It is therefore able to determine suction directly as the difference of both pressures. The pore-water pressure is applied through a saturated water compartment, usually an acrylic shaft that is connected to the unsaturated soil via a fully saturated porous ceramic tip. The working principle of a tensiometer is depicted in Figure 2.5. The capillary properties of the ceramic tip prevent air from penetrating into the measuring system unless the air entry value of the ceramic is exceeded. Thus, when a tensiometer is inserted into unsaturated soil, the menisci between soil and porous tip suck on the water column in the acrylic shaft. Equilibrium is normally reached within minutes or hours. A conventional tensiometer is able to capture suctions up to approximately 90 kPa beyond, which the cavitation of the water in the acrylic shaft usually begins. The measuring range may be higher if the whole measuring system is thoroughly saturated in such way that cavitation—starting with small, entrapped air bubbles—is minimized.

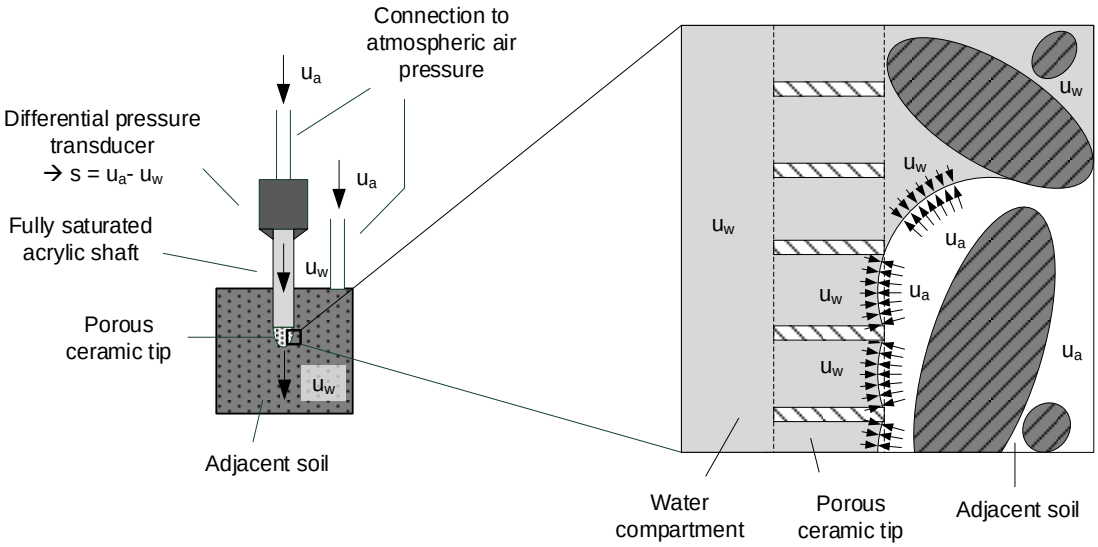

Figure 2.5: Working principle of a tensiometer

Note that in the case where impurities are not present in the measuring system (tensiometer and water), the measurable pore-water pressure may fall well below the atmospheric air pressure u_a. Theoretically, it may even achieve negative values of several hundred megapascals. Thus, with the reduction of the probability of occurrence of nucleation sites in the measuring system, it is possible to reach much higher suction values up to 1,500 kPa with tensiometers (Marinho, Take, and Tarantino 2009). Note that the limitation to suction

less than 1,500 kPa is due only to the highest achievable air entry values for the ceramic tips of the tensiometers. Such tensiometers, initially introduced by Ridley and Burland (1993), are called high capacity tensiometers. However, since high capacity tensiometers were not used in this study, they are not further discussed.

In general, tensiometers measure only matric suction, as the porosity of ceramic material seems to be high enough to permit the passage of dissolved ions from the soil-water to the water compartment. Thus, no osmotic effects can be measured (Marinho, Take, and Tarantino 2009).

2.1.3.2 Chilled mirror hygrometer

According to Kelvin's equation (2.1), a measurement of the suction with the chilled mirror hygrometer is based on the correlation between relative humidity (RH) and total suction s. Therefore, the partial vapor pressure of the soil $p_{T_{soil}}$ can be determined indirectly by measuring the RH in the test chamber. The RH is measured using the so-called dew point method. The temperature of a mirror T_{mirror} attached to the test chamber is decreased until a photo-optical sensor registers condensed water on it. At condensation, the RH directly at the mirror surface is 100%. At equilibrium, the partial vapor pressure in the sample chamber $p_{0,T_{mirror}}$ corresponds to the partial vapor pressure directly above the soil-water surface $p_{T_{soil}}$. The pore water potential, interpreted as suction, can be determined by additionally controlling the soil temperature T_{soil}. The exact procedure is described in more detail in Fredlund et al. (2012), and it can be summarized as follows:

$RH = 1 \rightarrow T_{mirror}$

Partial vapor pressure

$$p_{T_{soil}} = p_{0,T_{mirror}} = 0.611 \cdot e^{17.27 \cdot \frac{T_{mirror} - 273.2}{T_{mirror} - 36}} \quad [kPa]$$

Saturated vapor pressure

$$p_{0,T_{soil}} = 0.611 \cdot e^{17.27 \cdot \frac{T_{soil} - 273.2}{T_{soil} - 36}} \quad [kPa]$$

Kelvin's equation (2.1)

$$s = -\frac{R_{gas} T_{soil} \rho_{w,T_{soil}}}{\omega_{\upsilon}} \cdot \ln \frac{p_{T_{soil}}}{p_{0,T_{soil}}} \quad [Pa]$$

In comparison to the afore-mentioned tensiometer measurements, total suction is measured with the chilled mirror hygrometer.

2.1.4 Soil-water retention curve

The soil-water retention curve (SWRC) describes the relationship between suction and a volumetric or gravimetric measure of the amount of water, such as the degree of saturation Sr, the volumetric water content θ or the gravimetric water content w (see Figure 2.1 definitions of these terms).

An example of a SWRC is shown in Figure 2.6. Note that other terms are sometimes used to describe this relationship, such as *soil-water characteristic curve* (SWCC) or *water retention curve* (WRC).

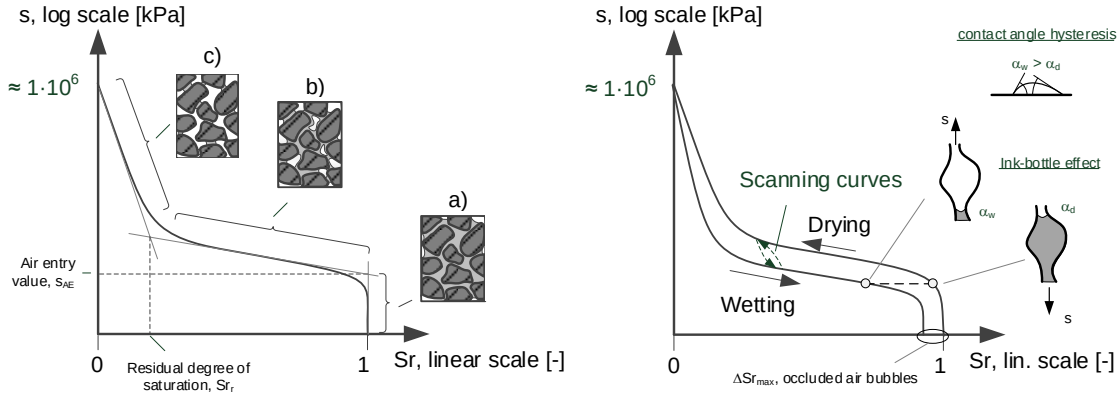

Figure 2.6: Soil-water retention curve (SWRC)

Following a drainage process that starts from the fully saturated condition (Sr = 1) of a small soil element with negligible gravimetric influence, the SWRC may generally be characterized by three domains (Figure 2.6, left):

a) *Capillary (saturated) zone:* At zero suction (s = 0), the soil element is fully saturated, since there are no menisci-inducing pore water deficiencies. When suction increases, the first menisci are formed along the boundaries of the element. Due to the very small volume of water that has to be extracted, the soil remains almost completely saturated. When suction is further increased, the so-called air entry value of suction ($s = s_{AE}$) is reached, from which the first menisci at the element boundaries are disrupted, and water is extracted from the element's inside, causing air to enter into the element.

b) *Transition or funicular zone (continuous water phase):* In this zone, the soil is no longer fully saturated, but it still exhibits a continuous water phase. With increasing suction, menisci are progressively overcome—from the largest to the smallest pore entrance sizes—and assemblages of saturated voids are emptied (Figure 2.7). In this zone, the slope of the SWRC is rather flat. This flatness is due to the presence of water clusters, which may cause several saturated voids to be emptied at a high enough specific suction. Thus, the water content decreases rapidly. This process continues to a point at which only isolated capillary bridges between soil particles or adsorbed water films on the particle surfaces remain. The corresponding degree of saturation is called *residual degree of saturation*, Sr_r as defined by Vanapalli et al. (1998).

c) *Residual or pendular zone (continuous air phase):* From the residual water content (or residual degree of saturation Sr_r) onwards, soil-water is mostly hygroscopically adsorbed or is only present in isolated capillary bridges between adjacent soil particles. Since the continuous water phase does not exist here, little hydraulic flow happens in this zone, aside from some water vapor movement. In the residual zone, it becomes more energy-

intensive to extract further water from the element. This stronger bonding of the soil water is indicated by a sharp increase in the slope of the SWRC (Figure 2.6, left). For convenience, zero saturation (Sr = 0) is usually defined as terminated at oven-dry conditions, with a theoretical limiting suction of approximately $1 \cdot 10^6$ kPa (Fredlund, Rahardjo, and Fredlund 2012).

The SWRC shows hysteretic behavior for drying and wetting processes (Figure 2.6, right). At constant suction, the water content on the drying branch is higher than that on the wetting branch. For granular soils, the cause for this behavior may be primarily attributed to the pore shape irregularities causing the ink-bottle effect or contact angle hysteresis (Schubert 1982), as illustrated in Figure 2.6. When the direction of hydraulic loading changes (e.g., from drying to wetting), so-called scanning paths arise, which approach the boundary curves for wetting or vice versa (Figure 2.6, right).

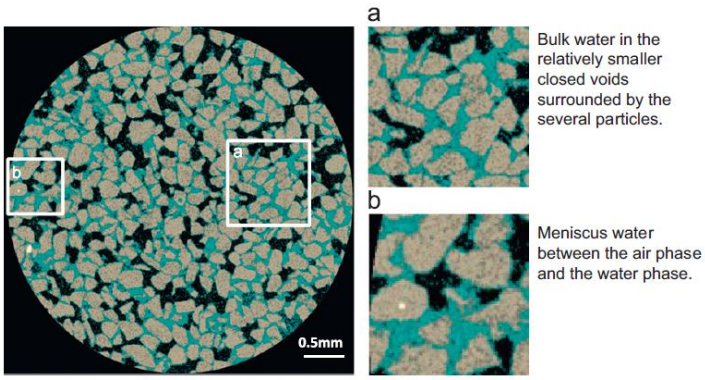

Figure 2.7: Distribution of soil-water in the transition zone of a sand sample (Sr = 60.4%, s ≈ 2 kPa), CT-images from Higo et al. (2013)

Figure 2.8 shows the distribution of the pore water in an unsaturated sand at a suction of 1.6 kPa after drying (left) and after wetting (right), detected by X-Ray CT, confirming the hysteretic behavior of the SWRC (Khaddour 2015).

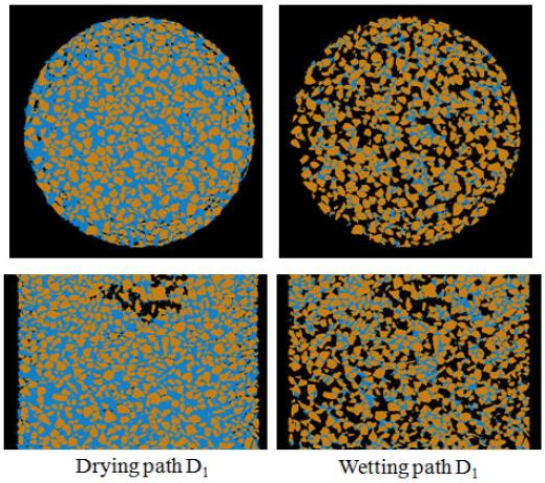

Figure 2.8: Hysteretic effects on the amount of soil-water for sand at s = 1.6 kPa, drying path (left) and wetting path (right), CT image from Khaddour (2015)

Due to the lower proportion of adsorbed water on the mineral surfaces and the larger pores in which capillary water is bounded, the SWRC has a flatter slope for granular soils than for fine-grained soils (Hartge and Horn 1991).

Furthermore, the SWRC depends on soil density, which in turn affects the pore sizes and their distribution (Gallipoli, Wheeler, and Karstunen 2003). In essence, unsaturated soils exhibit a hydro-mechanically coupled behavior in which changes in suction cause changes in density and vice versa (Figure 2.9). In order to better account for changes in density with mechanical and hydraulic loading, a volumetric measure of the amount of water (such as the degree of saturation Sr) is therefore preferred (Fredlund, Rahardjo, and Fredlund 2012).

Various models have been proposed to describe the relationship between suction and the degree of saturation for different hydraulic paths and densities (van Genuchten 1980, Fredlund and Xing 1994, Pham, Fredlund, and Barbour 2005, Gallipoli 2012, Salager, El Youssoufi, and Saix 2010).

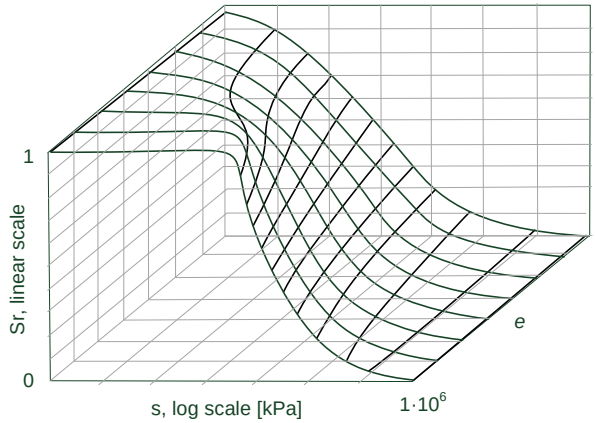

Figure 2.9: Dependency of soil-water retention curve (SWRC) on void ratio e or microstructure by the example of drying paths (adapted from Salager et al. 2010)

A deeper understanding of the SWRC is obtained when one considers that density is merely a macroscopic value. It represents an averaged, global measure of the actual microstructure of the soil at the micro-level, which may comprise complex local geometries as detailed in the following section. In essence, the SWRC depends not only on the soil type or its density, but also on other factors affecting microstructure, such as the sample preparation method or hydraulic or mechanical loading history.

2.2 Microstructure of silty sands

2.2.1 Definition of microstructure

The microstructure of soil is initially formed in nature by its field deposition and loading history, or—in the laboratory—by the method of sample preparation and consolidation process. Microstructure is not constant in soils, but may evolve by hydraulic or mechanical loading (Hall et al. 2012, Higo et al. 2013). According to Romero (2015), microstructure may be defined as the arrangement and inter-particle contacts of soil particles, such as aggregates, grains or pore networks into a specific configuration. Specifically, microstructure accounts for

- size, morphology, assemblages, orientation and stability of aggregates and particles,
- type, orientation and distribution of pore space, and
- orientation and stability of inter-particle contacts and contact forces.

Furthermore, the term *microstructure* encompasses both fabric and soil structure (as defined, e.g., by Lambe & Whitman 1969). For this reason, for simplicity, the terms *microstructure*, *fabric* and *structure* are used synonymously in this study.

2.2.2 Experimental assessment of microstructure

The distribution of the number and sizes of the pores can be regarded as a valuable measure of the microstructure of the soil. Considering the capillary tube analogy, the determination of the SWRC is an indirect method for identifying the pore-size distribution (PSD) of a soil (Lu and Likos 2004). Rearranging equation (2.3) leads to a suction-dependent equivalent pore radius r:

$$r = \frac{2 \cdot T_w}{s} \cdot \cos \alpha_w. \tag{2.6}$$

The volumetric portion of water-filled pores n_w can be expressed as follows:

$$n_w = Sr \cdot n \tag{2.7}$$

with Sr Degree of saturation

n Porosity.

Hence, the PSD can be incrementally calculated from the SWRC. For this purpose, the finite difference approximation of the derivative of the SWRC is calculated, expressing the volumetric water content as n_w and the suction as the equivalent pore radius r:

$$\omega = -\frac{n_w^i - n_w^{i-1}}{\log 2r^i - \log 2r^{i-1}} \qquad i = 2 \dots m \tag{2.8}$$

Equation (2.8) is also called the *pore-size density function*.

The PSD is commonly depicted as a function of the associated mean entrance diameter (Juang 1981):

$$\log D^i = \frac{1}{2}\left(\log 2r^{i-1} + \log 2r^i\right) \qquad i = 2 \dots m.$$
$$\rightarrow\ D^i = \sqrt{2r^{i-1} \cdot 2r^i} \qquad i = 2 \dots m. \tag{2.9}$$

In general, with regard to adsorbed water, the thickness of water films should also be accounted for, as mentioned in Lu and Likos (2004). Nevertheless, for granular materials, the distribution and geometry of adsorbed water films may be neglected without compromising the accuracy of the resulting PSD.

Another and more commonly used method, which utilizes the capillary analogy to determine the PSD, is mercury intrusion porosimetry (MIP). A non-wetting fluid, such as mercury, is used to penetrate the pore space of an initially fully dehydrated (Sr = 0) specimen under an externally applied positive pressure u_{MIP} (Lu and Likos 2004). The dehydration of the samples can be achieved by, for instance, freeze-drying heat- and dry-sensitive soils such as clays or oven-drying non-sensitive granular soils (Romero, Musso, and Jommi 2012). For mercury, the entrance pore radius is calculated from the applied pressure u_{MIP}, assuming a constant surface tension T_{Hg} (0.484 N/m at 25°C) and constant contact angle α_{Hg} (147° for quartz minerals at 25°C) as described in Juang (1981):

$$r = -\frac{2 \cdot T_{Hg}}{u_{MIP}} \cdot \cos \alpha_{Hg}. \tag{2.10}$$

The volume of the mercury that has penetrated into the sample's voids V_{Hg} is recorded for each applied pressure stage. At equilibrium, the recorded volume corresponds directly to the pore space intruded by the fluid. In this way, the volume occupied by mercury n_{Hg} may be calculated from the total intruded volume at the end of the test $V_{Hg,total}$ and the known porosity n:

$$n_{Hg} = \frac{V_{Hg}}{V_{Hg,total}} \cdot n. \tag{2.11}$$

Note that the intruded mercury volume exhibits a hysteretic behavior for intrusion and extrusion processes similar to the ink-bottle effects causing the hysteresis of the SWRC.

Similar to the PSD derived from the SWRC, (2.10) assumes cylindrical pores, which is sufficiently accurate for granular soils.

Analogous to the method for deriving the PSD from the SWRC, the pore-size density function ω is calculated from the intrusive curve using (2.8). For this purpose, n_w is replaced by n_{Hg}, while equivalent radius r is expressed through (2.10).

Besides the assumption of cylindrical pores, the MIP exhibits some further limitations, as described by Juang (1981), among others:

- Completely isolated pores cannot be intruded, as solids enclose them.
- The assumption of a constant contact angle and surface tension may not be true for the intrusion process.
- Large pores that are accessible only through smaller ones (i.e., with the ink-bottle effect) are not detected until the smaller pores have been penetrated. Thus, the measured pore sizes are called *limiting* or *entrance* pore sizes.
- Pores are detected only if they have an apparent diameter corresponding to the pressure within the range of the testing instrument. Thus, the maximum and minimum applicable pressure of the apparatus restricts the minimum and maximum detectable pore sizes.
- Microstructure may change during the penetration process due to the isotropic loading when pressure is applied to the mercury surrounding the sample.

While for the MIP test a rigid porous medium is assumed, the SWRC directly reflects changes in microstructure due to changes in suction and water content (Delage 2002). Both methods for deriving the PSD may therefore be seen as qualitative approaches to assessing microstructure. Note that the two methods may yield equivalent results only if a non-evolving microstructure is assumed during hydraulic paths. This assumption may yield erroneous results for deformable soils (Li and Zhang 2007). However, for non-deformable soils the hypothesis may be valid. For such soils, equating the capillary tube radii of both methods leads to an expression for the suction depending on the pressure applied during the MIP test:

$$s = -\frac{T_w \cos \alpha_w}{T_{Hg} \cos \alpha_{Hg}} \cdot u_{MIP}. \tag{2.12}$$

Note that in order to calculate the corresponding water content of the sample at any given pressure correctly, the intruded mercury volume must be corrected for non-penetrated voids (Birle 2011).

In summary, the MIP can be used to evaluate the PSD at a certain (*frozen*) state of microstructure. The SWRC, on the other hand, may not be capable of representing the entire PSD at a certain (*frozen*) state of microstructure, but directly reflects its changes with the hydraulic path. Especially regarding deformable soils, the conversion from one method into the other allows a rather qualitative, although valuable, insight into the microstructure, as it provides indirect information about the size and quantity of the pores (Simms and Yanful 2002, Romero and Simms 2009).

Note that direct observation methods such as scanning electron microscopy (SEM) or X-ray computed tomography (CT) are used to obtain visual information on the local distribution of soil particles, pore space and pore water (Desrues et al. 1996, Delage et al. 1996, Yamamuro, Wood, and Lade 2008, Khaddour 2015, Desrues et al. 2018). Although X-ray CT

can track the evolution of microstructure during mechanical and hydraulic loading, it is a complex technique, costly and time consuming. Therefore, X-ray CT is usually carried out only as a supplement to other tests in order to better interpret soil behavior. Nevertheless, it is a reliable and non-destructive method that gives valuable insight into the microstructure of soils (Willson, Lu, and Likos 2012).

2.2.3 Microstructural aspects of silty sands

With respect to laboratory tests, the initial microstructure of silty sands is mainly influenced by the sample preparation technique. For sands and silty sands, various sample preparation methods have been developed which can be roughly categorized into three types (Yamamuro and Wood 2004, Lade 2016):

- *dry deposition:* tapped, dry, or fast funnel deposition; air pluviation; mixed dry deposition;
- *wet deposition:* water sedimentation and slurry deposition; and
- *compaction of moist soils:* moist tamping, rodding and static compaction.

Yamamuro et al. (2008) performed SEM analyses to evaluate the particle arrangement in silty sand samples produced by different sample preparation methods. They found that—for dry deposition methods—the silt particles are likely to deposit between the sand particles and push them apart, producing unstable microstructures. In wet deposition methods, however, the silt particles tend to deposit inside of the voids of a coarse grain skeleton, leading to comparably stable microstructures.

By conducting bender element tests, Salgado et al. (2000) and Lee et al. (2004) measured the small strain shear stiffness of silty sands prepared by slurry deposition described in Kuerbis and Vaid (1988). The small strain shear stiffness decreased with increasing silt content. The authors concluded that the microstructure initially got weaker with increasing fines content. With ongoing shear deformations, the samples contracted and sand particles got closer, while fines predominantly existed in the pores between touching sand particles. The influence of the initial microstructure on the stiffness at small strains seemed to be less pronounced at higher stress states.

For compaction processes—as pointed out by Delage et al. (1996) for a well-graded low plasticity silt (Jossigny silt)—the distribution of fines may be already predefined to a certain extent due to the mixing procedure of the soil mass with various amounts of water prior to compaction. Delage et al. (1996) have noted that mixing the soil with low water content resulted in the formation of granular aggregates of silt particles, which introduced a double-porosity (Figure 2.10 left). Clay particles typically coated the silt grains or formed grain joint infills. At higher water content, the fines tended to settle on the surface of the silt grains or fill the intergranular voids. Thus, a less pronounced double-porosity was formed due to less aggregated fines (Figure 2.10 right). Depending on both the applied compaction energy and the strength of the aggregates, the pre-defined components of the pore structure were destroyed or retained during the compaction process itself. Note that with respect to

saturated testing, a final change in microstructure may be expected during saturation. In particular, this may be the case when the capillary effects on aggregate strength and compressibility have ceased, as this process may cause some additional breakdown of unstable contacts (collapse) or swelling of a clay fraction (Li and Zhang 2007).

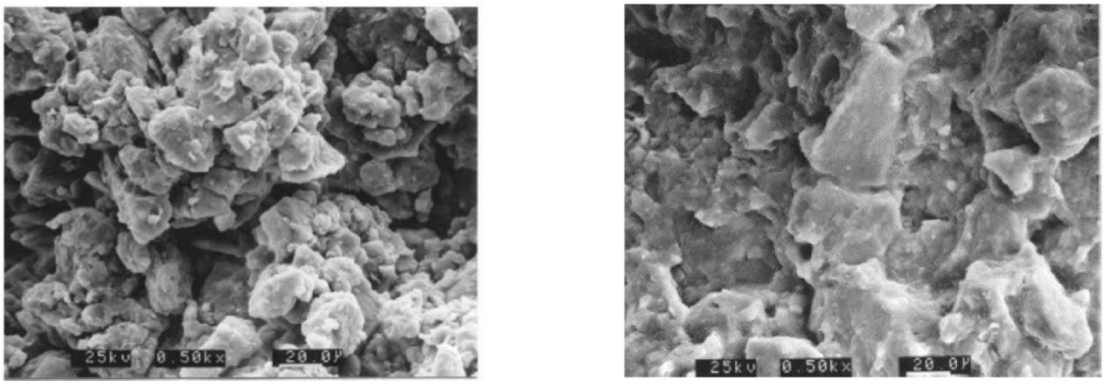

Compacted at dry side *Compacted at wet side*

Figure 2.10: Scanning electron microscopy (SEM) micrograph of a compacted Jossigny silt, from Delage (2007)

The general behavior described above may also be transferred to the behavior of compacted silty sands with just small amounts of silt, even though the characteristics may not be as evident. For example, Watabe et al. (2000) noted a pronounced effect of compaction conditions on the SWRC and the saturated hydraulic conductivity of a non-plastic silty sand. They attributed these conditions to the development of double porosity when the samples were compacted dry of Proctor optimum.

Juang (1981) performed MIP tests on clean sands and clayey sands. He solved the problem of sampling pure Ottawa sand for the MIP tests without destroying the microstructure by adding a small amount of powdered phenolic resin (0.5% by dry weight) to the soil before pluvial deposition. During subsequent oven-drying, the resin acted like a glue, with no associated chemical reactions occurring. This procedure led to reproducible results of MIP tests for pure sands. Clayey sands were dynamically compacted, and permeability tests were carried out. Subsequently, the samples were freeze-dried and prepared for MIP testing, whereby a small amount of shrinkage due to freeze-drying was observed. The measured PSDs are shown in Figure 2.11a for clean sand and in Figure 2.11b for a clayey sand with a clay fraction of 10% compacted at different water contents.

The clean sand showed only macropores, as no aggregated structure could develop, due to the lack of fine particles and the selected dry deposition method (Figure 2.11a). By adding some fines to the sand and mixing it with water prior to compaction, aggregates could develop. This addition resulted in a structure with double porosity (Figure 2.11b). Even though microporosity was not very pronounced for the sand with a fines content of 10%, its presence was obvious. The dryer the soil was compacted, the more pronounced was the double porosity. This observation accords with the microstructure observed for compacted fine grained soils, as described in Lambe and Whitman (1969).

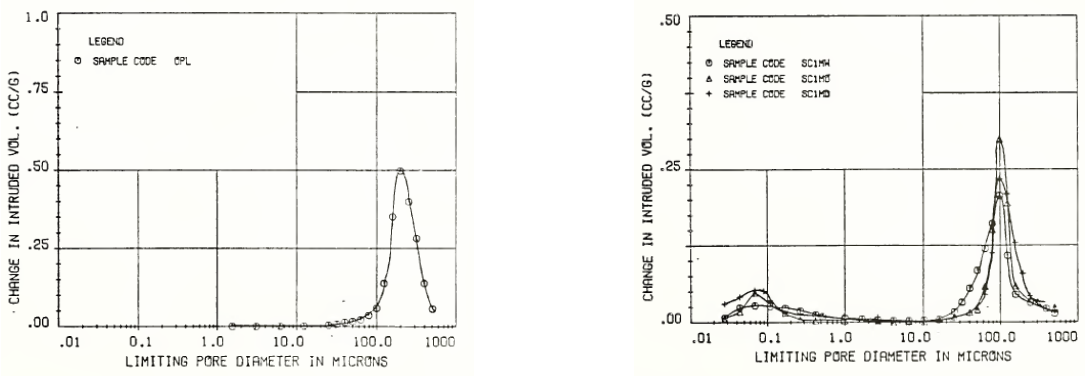

(a) (b)

Figure 2.11: Pore size distribution (PSD) of (a) clean sand and (b) sand with 10% clay compacted at different water content (SC1MW: wet side, SC1MO: Proctor optimum, SC1MD: dry side), from Juang (1981)

Zhao et al. (2013) performed MIP tests on a well-graded sand with silt and gravel. After compacting the soil by moist tamping, they observed a bimodal PSD (Figure 2.12). Although the results indicated some changes in the microstructure due to the swelling or shrinking of the clay fraction, the double porous microstructure was widely preserved upon drying or saturation of the compacted sample.

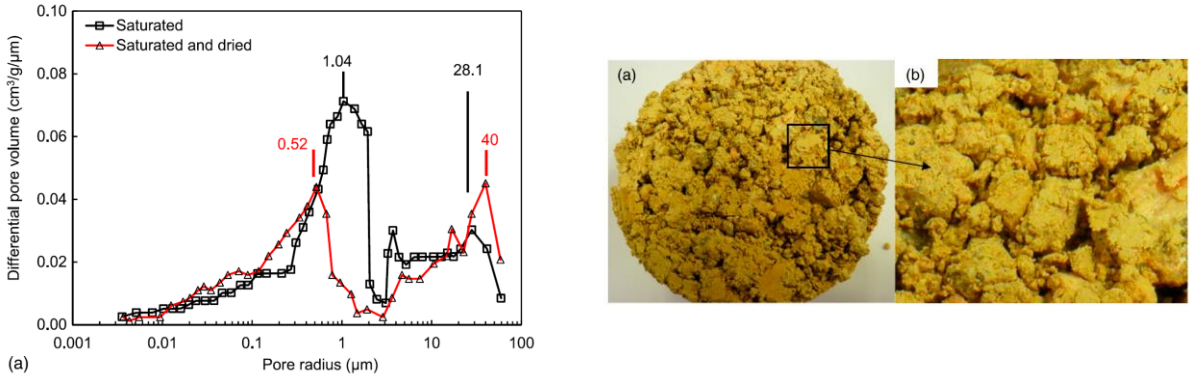

Figure 2.12: Pore size distribution (PSD) and photographs of the microstructure of a compacted well-graded sand, from Zhao et al. (2013)

Under the provision that their fines content is mainly non-plastic and its fraction of the total soil does not exceed certain limits (Lade, Liggio, and Yamamuro 1998, Thevanayagam et al. 2002)—and based on the results of Juang (1981), Delage et al. (1996), Watabe et al. (2000), Yamamuro et al. (2008) and Zhao et al. (2013)—the microstructure of the reconstituted silty sands may roughly be summarized as shown in Figure 2.13.

In general, since the PSD and SWRC qualitatively correspond to each other, a bimodal porosity (double porosity) leads to a bimodal SWRC, and vice versa (Zhao, Zhang, and Fredlund 2013, Burger and Shackelford 2001, Ciervo et al. 2015). Starting from fully saturated conditions, the retention behavior of, for example, a double porous silty sand is at first governed only by the drainage of the macropores (Figure 2.13 right), leading to a flat

evolution of increasing suction with decreasing water content, similar to clean sands. Once the macropores are almost fully drained, the suction has to increase at almost constant water content until the air entry value of the micropores within the aggregates $s_{AE,micro}$ is reached. The micropores begin to drain once the air entry value $s_{AE,micro}$ is exceeded. A bimodal SWRC may thus be approximated by two superimposed unimodal SWRCs, corresponding to macro- or microporosity, respectively (Figure 2.13 right).

Note that the particle size distribution, the sample's density, the sample preparation technique and the loading history influence the height and location of the peaks of the PSD.

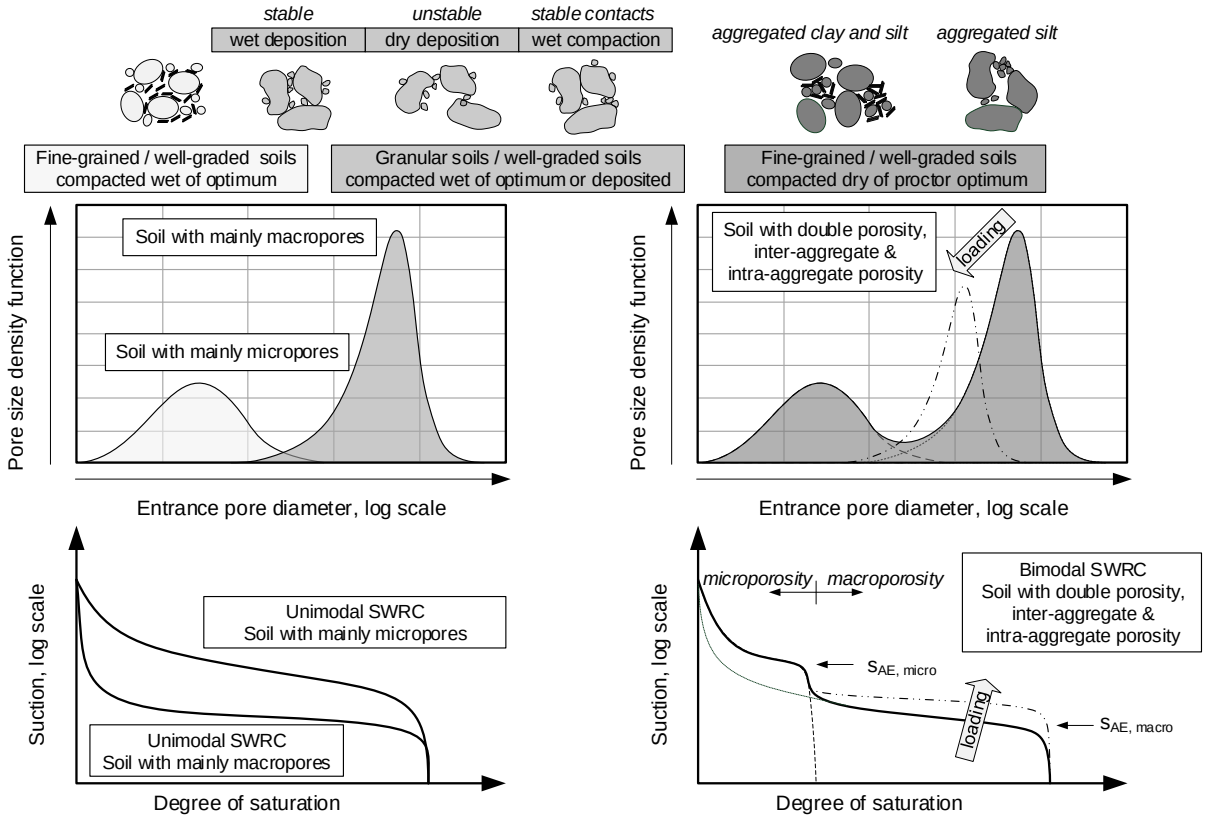

Figure 2.13: Pore size distributions (PSDs), particle arrangements and soil-water retention curves (SWRCs) of fine-grained and mixed graded soils formed by different specimen preparation methods (schematic)

2.3 Shear strength of saturated silty sands

2.3.1 General remarks

The shear strength of granular soils results from inter-particle friction induced by grain-to-grain forces and from the granulometric properties (grain size, grain shape, grain mineralogy, soil structure) of the grain skeleton (Santamarina and Cho 2004). The transfer of the shearing behavior at the particle level to a continuum mechanical equivalent system (i.e., the *smearing* of these effects on a macroscopic level), remains the main task of classical soil mechanics. Shear strength is then no longer described on a microscopic level, but depends on average quantities such as density, strain and stress (see e.g., Figure 2.14).

The following is a summary of the main findings available in the literature on the non-linear shear strength of saturated granular soils.

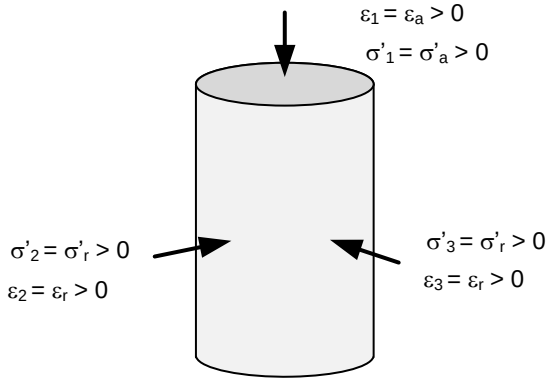

Deviatoric stress	$q = \sigma'_1 - \sigma'_3$
Effective mean stress	$p' = \frac{1}{3}(\sigma'_1 + 2\sigma'_3)$
Deviatoric strain	$\varepsilon_q = \frac{2}{3}(\varepsilon_1 - \varepsilon_3)$
Volumetric strain	$\varepsilon_v = \varepsilon_1 + 2\varepsilon_3$

Figure 2.14: Stress state and straining of a cylindrical triaxial specimen in drained triaxial compression with sign convention

2.3.2 The behavior of granular soils under drained triaxial compression

An idealized behavior of clean sand under drained triaxial compression is shown in Figure 2.15.

As Verdugo (1992) pointed out, the tendency of sheared soils to change their volume is a major difference with many other engineering materials. At the same stress level, loose samples of a soil tend to reduce their volume (contraction), while dense samples tend to increase their volume (dilatancy). Santamarina and Cho (2004) have noted that dilatancy is related to interlocking effects, as schematically shown in Figure 2.15 and Figure 2.16. At large shear strains, the void ratios of the dilative and the contractive samples converge to a unique void ratio e_{CS}, which does not change with further shearing. At this state, the changes in volumetric strains are zero ($\delta\varepsilon_v \approx 0$). Santamarina and Cho (2004) have described the state of constant volume shearing on a micro-level as being a statistical equilibrium between volume reduction due to chain collapse and volume dilatancy required to reduce interlocking

effects. On a macro level, this flow-like condition is referred to as critical state (Schofield and Wroth 1968, Lambe and Whitman 1969).

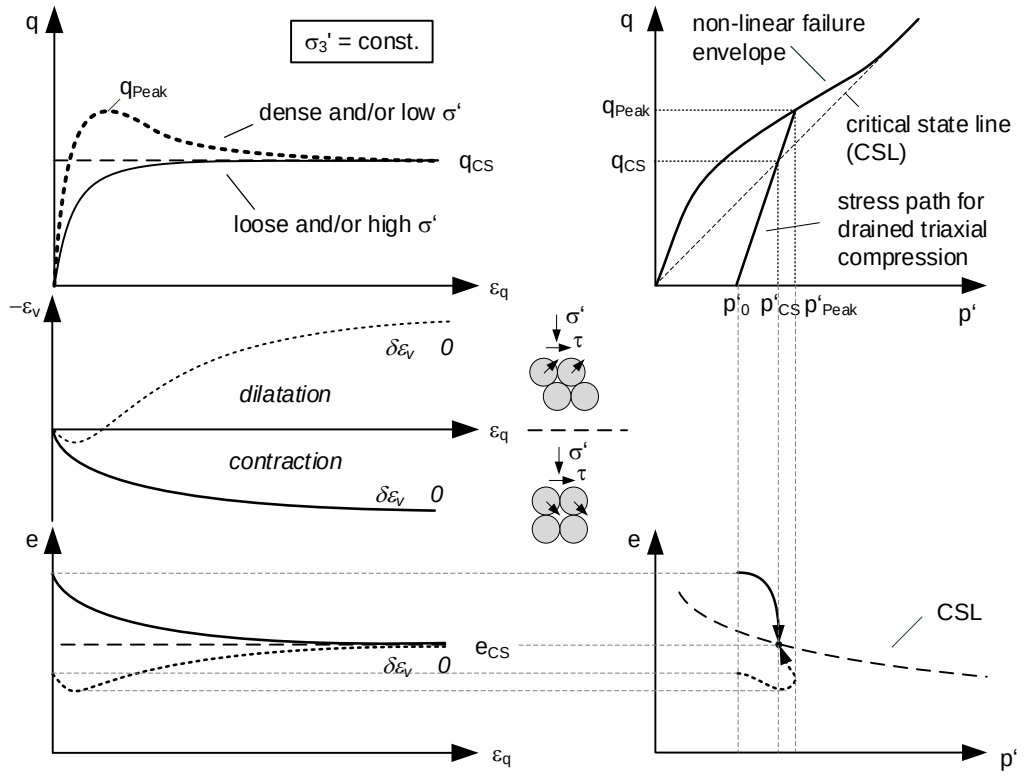

Figure 2.15: Schematic illustration of an ideal behavior of sand under drained triaxial compression

For drained conditions, at the same stress level, the maximum shear strength of a dilative sample q_{Peak} is higher than that of a contractive sample. In the q - ε_1 diagram, dilative samples usually show a peak, which is related to interlocking effects (Bolton 1986, Chakraborty and Salgado 2010).

At the critical state, the mobilized shear strength of both the dilative and the contractive samples converge toward a common value of $q = q_{CS}$, which does not change with further shearing. In the case of contractive samples, which do not show a peak, the maximum mobilized shear strength corresponds to the shear strength at critical state q_{CS}.

For different stress states, the stress pairs at a critical state (q_{CS} and p'_{CS}) result in a linear line in the q - p’ plane called critical state line (CSL). The CSL is independent of the initial void ratio and passes through the origin of the stress axes (Figure 2.15). In the e - log p’ plane (e_{CS} vs. p'_{CS}), the CSL has been demonstrated as being a non-linear curve (Been, Jefferies, and Hachey 1991, Verdugo 1992, Bauer 1995, Klotz and Coop 2002, Yu 2017).

The shift from dilative to contractive behavior takes place for initial void ratios close to the critical state void ratio e_{CS}. Since e_{CS} is stress-dependent (e.g., Bauer 1995), the state of a specimen cannot be described solely by its density, but by the position of its current state in the e - p’ plane, relative to the CSL (Been, Jefferies, and Hachey 1991). To illustrate this interrelation, the results of drained triaxial compression tests at increasing confining

pressures on two sets of samples, each with the same initial void ratio, are mapped in Figure 2.16.

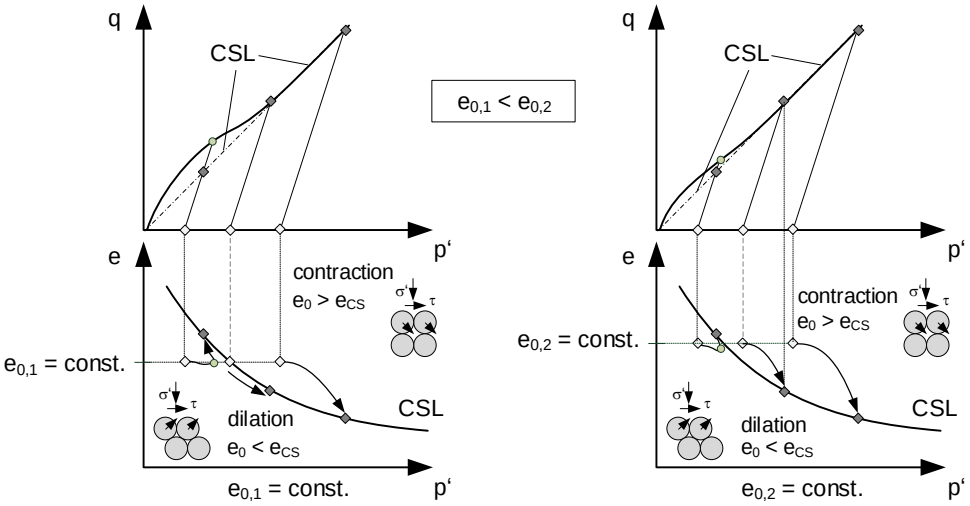

Figure 2.16: Schematic stress-strain behavior of specimens with the same initial void ratio e_0 under drained triaxial compression at increasing confining pressures

When depicting the stress pairs at peak (q_{Peak} and p'_{Peak}) for different confining pressures but same initial void ratio, it can be observed that the resulting shear strength depends non-linearly on the stress state and the value of the initial void ratio (Figure 2.16). Under pressures at which the initial void ratio first approaches and subsequently exceeds e_{CS}, the specimens show a decreasing dilative behavior, and the peak shear strength eventually merges the shear strength at critical state. Due to the lack of cohesion between the grains, the shear strength at zero effective stress is also zero (e.g., Lancelot et al. 2006).

In terms of the secant peak friction angle,

$$\varphi'_{\mathrm{Peak}} = \arcsin\left(\frac{\sigma_1' - \sigma_3'}{\sigma_1' + \sigma_3'}\right)_{\mathrm{Peak}}, \tag{2.13}$$

the non-linearity of the peak shear strength results—at low stress states corresponding to the initial position in the e - p' plane (Figure 2.16)—in friction angles higher than the critical state friction angle (Figure 2.17). With increasing stress levels, the friction angles approach the critical friction angle and finally merge. The increase in peak friction angle compared to the critical state friction angle can therefore be traced back to dilatancy (Bolton 1986).

Note that in the q - p' plane the peak state is represented by the stress obliquity at peak:

$$\mathrm{M_{Peak}} = \left(\frac{q}{p'}\right)_{\mathrm{Peak}} = \left(\frac{\sigma_1' - \sigma_3'}{\frac{1}{3}(\sigma_1' + 2\sigma_3')}\right)_{\mathrm{Peak}} = \frac{6 \cdot \sin\varphi'_{\mathrm{Peak}}}{3 - \sin\varphi'_{\mathrm{Peak}}}. \tag{2.14}$$

At critical state, the secant friction angle is

$$\varphi'_{\mathrm{CS}} = \arcsin\frac{3 \cdot \mathrm{M_{CS}}}{6 + \mathrm{M_{CS}}} = \arcsin\left(\frac{\sigma_1' - \sigma_3'}{\sigma_1' + \sigma_3'}\right)_{\mathrm{CS}}. \tag{2.15}$$

The stress obliquity at the critical state is

$$M_{CS} = \left(\frac{q}{p'}\right)_{CS} = \left(\frac{\sigma_1' - \sigma_3'}{\frac{1}{3}(\sigma_1' + 2\sigma_3')}\right)_{CS} = \frac{6 \cdot \sin \varphi'_{CS}}{3 - \sin \varphi'_{CS}}. \quad (2.16)$$

For triaxial extension ($\sigma_a < \sigma_r$ = const.), the relationship between friction angle and stress obliquity is

$$M_{Peak/CS} = \frac{6 \cdot \sin \varphi'_{Peak/CS}}{3 + \sin \varphi'_{Peak/CS}}. \quad (2.17)$$

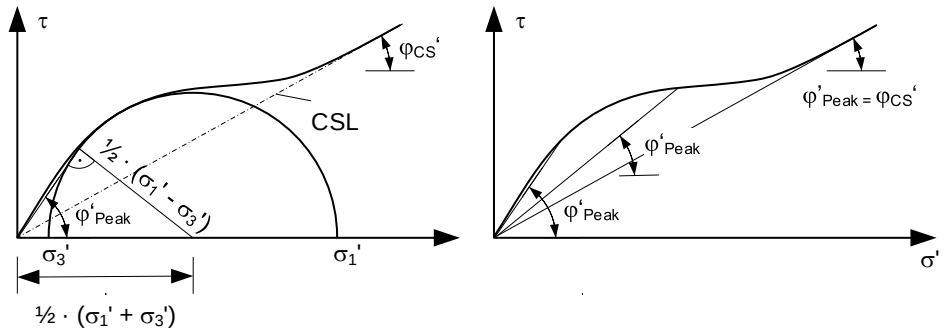

Figure 2.17: Definition of secant peak friction angle

2.3.3 Strain localization

As is well-known, strain localization in shear bands or bulging of the soil sample may occur during shearing (Oda 1972).

Among others, Oda and Kazama (1998), Watanabe et al. (2012) and Bhandari and Powrie (2013) were able to visualize the onset of strain localization. For dilative sand samples, strain localization was observed to take place near the peak of the stress-strain curves.

Other researches performed local and global strain measurements, suggesting corrections to the test results in order to accommodate, for example, barrel-shaped sample deformation at large shear strains, thus improving data analysis (e.g., Klotz & Coop 2002).

Measures taken to counteract strain localization, such as lubricated end platens, may cause the globally visible sample geometry to appear homogeneous, but can ultimately not prevent local strain concentrations (Desrues et al. 1996). Strictly understood, as soon as strain localization or bulging occurs, the test can no longer be considered an element test with a homogeneous stress-strain distribution. A homogeneous stress-strain field, in turn, is a common assumption for the development of constitutive models for the analytical or numerical solution of boundary-value problems in geotechnical engineering.

Recently, Desrues et al. (2018) published new findings regarding the occurrence of strain localization in sand samples under triaxial compression. They performed X-ray CT tests on samples of loose and dense Hostun sand. They observed for both dense and loose

specimens early strain localizations, which were distributed over the specimens and began to develop almost immediately after the start of the tests (Figure 2.18). Since a real onset could not be identified, the authors concluded that the emergence of a major shear band is essentially a smooth rather than an abrupt process. Based on these results, Desrues et al. (2018) noted that even in apparently homogeneously deformed samples, strain localization occurs almost from the beginning of the test.

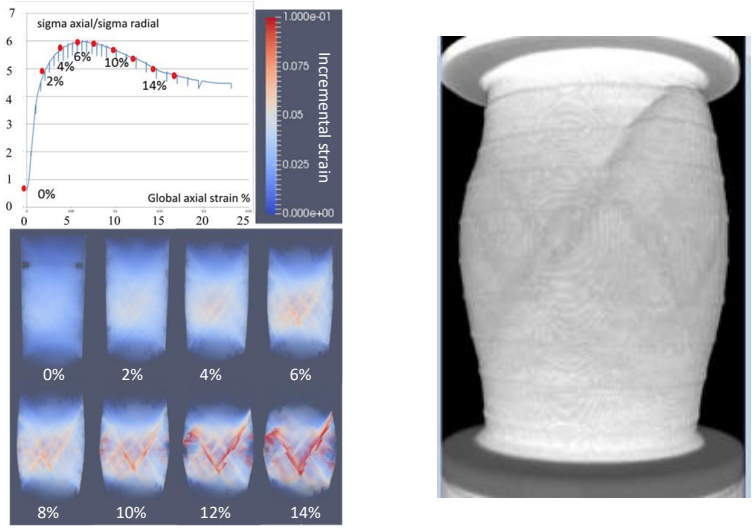

(a) (b)

Figure 2.18: Stress strain response of dense (e = 0.62) Hostun Sand with non-lubricated end platens, H/D = 2, (a) incremental strain field, (b) final state, from Desrues et al. (2018)

Nevertheless, the possible effect of strain localization on the shear strength is not explicitly considered in this study. It is therefore assumed that the stress-strain field is homogeneously distributed in sheared samples. From the practical point of view, this assumption is acceptable as long as the strain localizations are homogeneously distributed. In Figure 2.18, for practical purposes, this homogenous distribution might be assumed for global axial strains of up to approximately ε_a = 6% to ε_a = 10%, which are actually close to the peak.

2.3.4 Critical state

As pointed out by Santamarina and Cho (2001), a major experimental challenge arises from the fact that in order to reach the critical state, very large shear strains are required. With such strain, the authors noted, the initially existing fabric—which may have still affected the peak behavior with less strain—will be completely degraded.

In order to investigate critical states, usually drained and undrained triaxial compression tests are carried out. However, as already discussed in Section 2.3.3, both types of experiments are prone to inhomogeneous deformation and strain localization. With large strains, the findings of Desrues et al. (2018) raise further doubts about the correct interpretation of test results (Figure 2.18). Particularly near the critical state, the external measurement of the

deformations does not seem to be meaningful even if various corrections are considered. It also seems that when local strains are recorded with external displacement transducers, the truly occurring strain patterns (shown in Figure 2.18) cannot be correctly detected. Local strain measurements may even become physically meaningless due simply to discrete processes within shear bands at the particle level taking place at this stage (Higo et al. 2013). For practical purposes, the assessment of strains at a critical state may be significantly improved by accounting for non-homogeneous specimen deformations (Mooney, Finno, and Viggiani 1998, Klotz and Coop 2002, Castro et al. 1982, Lade 2016).

From the above considerations, it follows that a unique critical state is difficult to achieve experimentally. However, the determination of CSL in the q - p' plane has proven relatively unaffected by the effects described above. The corresponding critical state friction angle φ'_{cs} is well established, since it represents an intrinsic soil parameter correlating to other intrinsic parameters such as particle size distribution, shape and surface roughness (Santamarina and Cho 2004, Li 2017). Typical values for critical state friction angles of clean sands lie in the range of φ'_{cs} = 32° to 37° (Salgado, Bandini, and Karim 2000). In case of a mixture of sands and fines, critical state friction angles depend on the amount and mineralogy of the fines. On the one hand, for sands with plastic fines, such as clays, both the critical state friction angle and the peak friction angle decrease with increasing fines content, liquid limit or plasticity index (Lambe and Whitman 1969, Li 2017). On the other hand, for sands with non-plastic silts, the critical state friction angle increases with increasing fines content as long as a certain limiting fines content is not exceeded (Salgado, Bandini, and Karim 2000, Polito and Martin 2003). The focus of the present work is on the behavior of low-plasticity silty sands. Therefore, the behavior of sands with plastic fines is discussed no further.

2.3.5 Shear strength at peak

2.3.5.1 General remarks

In drained triaxial compression tests on dilative soil samples, the peak occurs at lower shear strains (a few percent) compared to the shear strains required to reach the critical state, usually higher than 20%. At peak, the initial fabric is therefore much less degraded, and the initial microstructure is expected to affect the shear strength. Even though occasional strain localizations may already be present at peak (Section 2.3.3), they are less pronounced than at the large deformations in the critical state.

Therefore, it is expected that shear strength at peak is less affected by strain localization than the shear strength at critical states. In particular when accounting for microstructure, the analysis of peak shear strength on the basis of experimental data may thus be more reliable.

2.3.5.2 Experimental data

Taylor (1948) was one of the first to present results on the dependency of shear strength on the effective stress state and density. Taylor noted that the peak friction angle increases with both the decreasing void ratio and decreasing cell pressure. Since then, many studies have

been performed on the peak behavior of sands at moderate to high stress states. Bolton (1986) summarized the results of shear tests conducted by different laboratories on 17 different clean sands. Based on this summary, the author developed a relationship for estimating the peak friction angle as a function of the critical state friction angle and the rate of dilatancy at peak, which in turn depends on the relative density and the stress level.

Among others, Ponce and Bell (1971), Fukushima and Tatsuoka (1984), and Sture et al. (1998) have carried out drained triaxial compression tests on sands at low stress levels. The resulting secant peak friction angles are summarized in Figure 2.19 as a function of the confining pressure.

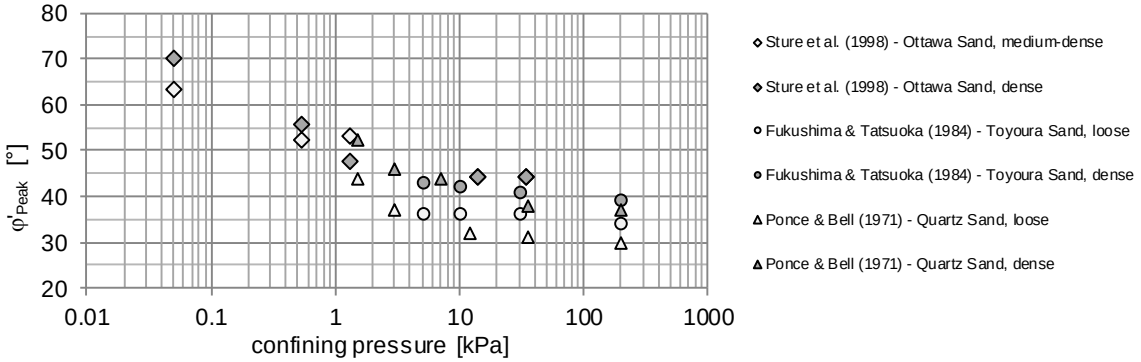

Figure 2.19: Peak friction angles of clean sands at very low to moderate confining pressures (adapted from the literature)

Ponce and Bell (1971) investigated the shear behavior of saturated quartz sand. Triaxial tests were carried out on loose and dense saturated samples at confining pressures from 1.4 kPa to 241 kPa. Samples were prepared by dry funnel deposition. The test evaluation accounted for factors affecting the experimental results at low stress levels, such as strength contribution due to stretched membrane, the self-weight of the specimen or friction in the plunger bearing.

Fukushima and Tatsuoka (1984) noted that peak friction angles at low stress levels may vary widely among different kinds of sands and should therefore always be evaluated. The authors expanded the database of peak friction angles by carrying out drained triaxial tests on saturated Toyoura Sand in loose and dense states at confining pressures ranging from 2 kPa to 392 kPa. Similar to Ponce and Bell (1971), samples were prepared by dry funnel deposition. In addition to the corrections of test results applied by Ponce and Bell (1971), lubricated end platens were used to minimize end restraint effects.

Sture et al. (1998) used two space shuttle missions to conduct drained triaxial compression tests in space, eliminating the influence of gravity at terrestrial conditions on the test results. Thus, experiments could be performed on dry Ottawa sand at medium-dense to dense relative densities (approx. 65% or 87%) at extremely low confining pressures of 0.05 kPa, 0.52 kPa, and 1.30 kPa. Samples were prepared in a terrestrial laboratory by air pluviation. Although oversized end platens were used, they did not prevent the sample from showing

strain localizations. The associated deformations were detected by three cameras, which provided 360° coverage of the specimen.

The volume changes of the samples used in Ponce and Bell (1971) and in Fukushima and Tatsuoka (1984) were measured externally. For the samples used in Sture et al. (1998), local optical strain measurements were applied. Note that most samples showed a dilative behavior, especially at low confining pressures and medium-dense to dense packings. Figure 2.19 shows that peak friction angles of up to 70° were observed for the various tested sands and densities. With increasing confining pressures, the peak friction angles asymptotically approach the friction angles characterizing the critical state of the respective soils. Even sands prepared in a loose state tended to exhibit dilative behavior at confining pressures less than 10 kPa.

Chakraborty and Salgado (2010) tried to merge the results for low stress states reported in Fukushima and Tatsuoka (1984) with Bolton's relationship by extending it to account for the small stress range. However, the shear strength data of Toyoura sand for only one preparation method was included. Therefore, the proposed relationship cannot be generalized, the authors affirm.

Based on the test results on silty sand reported by Salgado et al. (2000) and Lee et al. (2004), Xiao et al. (2014) proposed an equation for the relationship between peak friction angle and dilatancy. The authors thereby incorporate the observed influence of fines content and account for low stress levels. Because of its derivation from only one soil type and only one sample preparation method, the proposed relationship, however, has the same limitations as that of clean Toyoura Sand proposed by Chakraborty and Salgado (2010).

2.3.6 Influence of fines content and sample preparation method

2.3.6.1 Fines content

It is well known that microstructure influences both the mechanical and the hydraulic behavior of granular soils or mixed soils (Lambe and Whitman 1969, Kuerbis, Negussey, and Vaid 1988, Lade, Liggio, and Yamamuro 1998, Hoeg, Dyvik, and Sandbaekken 2000, Yamamuro and Wood 2004, Romero and Simms 2009, Birle 2011, Alonso, Pinyol, and Gens 2013).

Salgado et al. (2000) and Lee et al. (2004) performed a large number of drained triaxial compression tests on Ottawa sand, with varying amounts of non-plastic fines. At the tested stress levels, they observed increasing peak friction angles with increasing silt contents up to 20%, which they attributed to an increase in both dilatancy and critical state friction angle.

To assess how the fines content influences shear behavior of gap-graded sands, Kuerbis et al. (1988) and Thevanayagam et al. (2002) conducted undrained tests on sand mixed with various amounts of silt. They conclude that below a limiting fines content, the mechanical behavior of the specimens is governed mainly by inter-coarse-grain friction. In order to capture the observed mechanical behavior, they suggested various methods of calculating

equivalent void ratios depending on fines content or microstructure. However, they failed to find a unique index suitable to characterize the behavior of the entire spectrum (Thevanayagam et al. 2002). Furthermore, apparently contradictory results were obtained. For a maximum fines content of 20%, Kuerbis et al. (1988) observed increasing dilative behavior with an increasing amount of silt, whereas Thevanayagam et al. (2002) observed increasing contractive behavior with an increasing silt content.

2.3.6.2 Sample preparation method

The different findings concerning the influence of non-plastic fines on the shear behavior described above may be related to the different sample preparation techniques used to form the specimens. Kuerbis et al. (1988), Salgado et al. (2000) and Lee et al. (2004) used wet deposition methods yielding a stable microstructure with fines supporting the coarse-grained skeleton. On the other hand, Thevanayagam et al. (2002) used air deposition and moist tamping technique (presumably at the dry side) forming rather unstable particle contacts (Figure 2.13).

In general, the influence of the preparation method on shear behavior was initially investigated in the field of liquefaction on mainly wet or dry deposited sands and silty sands. As such, many of the tests carried out in these studies were undrained triaxial tests (e.g., Kuerbis et al. 1988; Polito & Martin 2003; Yamamuro & Wood 2004; Yamamuro et al. 2008). The results revealed a response to undrained shear loading depending on the tendency of the soil to dilate or contract. Samples prepared by wet deposition showed rather dilative behavior, the result of a more stable fabric (as described in Section 2.2.3). Samples prepared by dry deposition, on the other hand, suggested rather unstable microstructures tending to be more contractive (Figure 2.13). For undrained shear tests, Sivathayalan (2000) observed that different microstructures affected the development of effective stress, but did not influence the mobilized friction angle.

Sadrekarimi and Olson (2012) performed drained ring shear tests on specimens of two clean sands and one silty sand, all three sand types being prepared at a wide range of low relative densities. They found that for all sands moist tamped samples contracted throughout shearing regardless of their densities. Air-pluviation was found to cause different dilative or contractive behavior for the two clean sands. The silty sand did not seem to behave differently for the chosen specimen preparation techniques.

Santucci de Magistris and Tatsuoka (2004) showed for statically compacted silty sands that, after saturation, only the drained shear behavior at small strains was influenced by the different initial microstructures, which were achieved by compacting the samples at various water content. For moderate strains necessary to reach the peak, the behavior of compacted silty sands seemed to be controlled solely by initial density. In this context, note that the microstructure may have a more pronounced influence on the shear strength if soils, particularly compacted soils, are tested under unsaturated conditions (Toll 1988).

In view of the above findings, since different sample preparation methods produce different microstructures that may influence shear behavior to some extent (e.g., Lauer and Engel 2005), as has been concluded in the literature, the specimen preparation method should closely replicate the field depositional method. For example, moist tamping should be used to replicate samples of moist dumped sand and air pluviation to replicate samples of natural alluvial (Sadrekarimi and Olson 2012). Note that each sample preparation method incorporates various advantages and disadvantages in terms of homogeneity, reproducibility, attainable densities and segregation of fines (Lade 2016). These attributes are taken into account in the discussion of the present study's methods (Chapter 4 through 7).

2.4 Shear strength of unsaturated silty sands

2.4.1 Testing techniques

2.4.1.1 Suction control

To test unsaturated soils in shearing devices (e.g., triaxial or direct shear test), the testing equipment must be modified such that the pore-air pressure can be controlled or measured in addition to the pore-water pressure.

Various testing methods may be applied to unsaturated specimens. These methods differ with regard to the consolidation procedure and the drainage conditions. The latter define the parameters that must be measured or controlled during the tests (Table 2.2).

Test method	Consolidation	Drainage		Shearing		
		Pore-air	Pore-water	u_a	u_w	$\Delta V_{specimen}$
Consolidated drained (CD)	Yes	Yes	Yes	C	C	M
Constant water content (CW)	Yes	Yes	No	C	M	M
Consolidated undrained (CU)	Yes	No/yes	No	M	M	M
Unconsolidated undrained (UU)	No	No	No	M	M	M
Unconfined compression (UC)	No	No	No	--	--	--

Note: C = controlled, M = measured

Table 2.2: Triaxial testing methods for unsaturated soil samples, modified from Fredlund and Vanapalli (2002)

During shear tests, techniques such as the vacuum method (e.g., Milatz 2016), osmotic control (e.g., Cui & Delage 1996) or RH control (e.g., Blatz et al. 2009) were successfully used to control suction. The axis-translation technique (e.g., Vanapalli et al. 2009) is the most common method to control or determine suction, although some criticism exists concerning the prevention of cavitation this method involves, which is not likely to happen under natural conditions (Baker and Frydman 2009). Nevertheless, the axis-translation technique is discussed in detail here since it will be used in this study to perform triaxial tests on silty sands at suctions less than s = 100 kPa.

In general, the axis-translation technique translates the origin of the reference pore-air pressure u_a from standard atmospheric pressure to a controlled, elevated air pressure (Vanapalli, Nicotera, and Sharma 2009). Thus, suctions can be applied or measured at positive pore-water pressures. This procedure increases the range of the applicable suction while decreasing the threat of cavitation of water in the measuring system (Hoyos, Laloui, and Vassallo 2009). To control the air pressure and the pore-water pressure separately, a saturated high air entry (HAE) ceramic disk is placed underneath the sample. With this arrangement of the disk, the pore-water pressure is applied (or measured) at the bottom of

the sample, and the air pressure is applied at the top. The pressure difference $u_a - u_w$ corresponds to the suction in the specimen.

The working principle of the axis translation technique is illustrated in Figure 2.20.

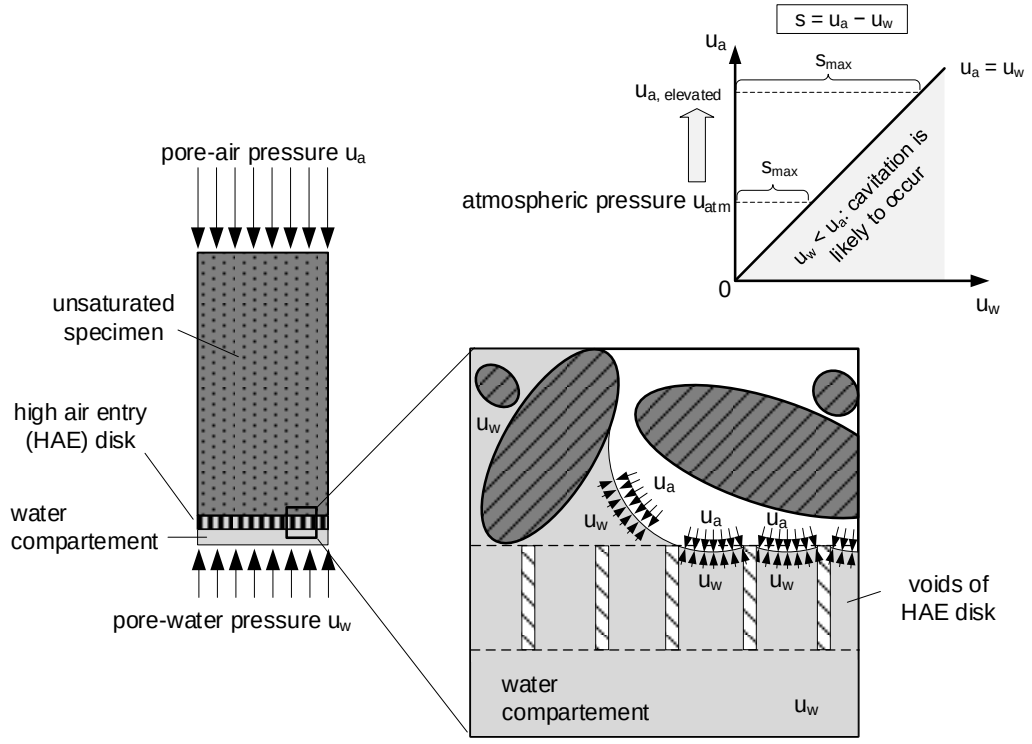

Figure 2.20: Working principle of the axis translation technique

When adjusting suction by changing either u_a or u_w, the water in the sample has to redistribute in order to get into equilibrium. Some water may be expelled from the sample or sucked into the sample. Due to the low permeability of both the unsaturated soils and the HAE disk, these processes can significant time (Rampino, Mancuso, and Vinale 1999, Thu, Rahardjo, and Leong 2006). Similarly, with an evolving microstructure during testing, the amount or distribution of water has to change continuously to stay in equilibrium with the applied suction. For this reason, the shearing rate has to be sufficiently low to ensure homogeneous conditions in the sample throughout the test (Ho and Fredlund 1982, Patil, Puppala, and Hoyos 2014). As a result of the generally long test durations, however, diffusion of pore air through the ceramic into the water compartment below the specimen may occur. This can lead to an accumulation of air bubbles underneath the HAE disk. The diffused air volume increases with increasing suction and should be accounted for by regularly flushing the water supply lines and the water compartment (Fredlund, Rahardjo, and Fredlund 2012).

Note that the controllable suction is limited by the air entry value of available ceramic disks, up to approximately 1,500 kPa (Lu and Likos 2004).

2.4.1.2 Volume change measurement

In unsaturated soils, a change in pore volume is composed of a change in pore-air volume and pore-water volume (drained testing). Even if the pore-water volume is kept constant in the experiment (constant water content testing), the volume of the air phase can still change.

In contrast to saturated soils, a volume change in unsaturated soils can therefore not be determined by simply monitoring the changes in the pore-water volume. Keeping the specimen volume constant during the experiment is not as easy as with saturated soils, where the drainage line of the pore water is simply closed before shearing. For this reason, several techniques to measure volume change have been developed. These techniques can be classified into three categories (Hoyos, Laloui, and Vassallo 2009):

- indirect measurement via displaced cell liquid,
- direct measurement of air- and water-volume changes, and
- local measurements: local displacements, laser techniques, image processing.

A comparison of the most commonly used methods in the three categories is given in Table 2.3.

Type of device	Advantages	Limitations
Indirect method via displaced cell liquid		
Inner cell or double-wall triaxial cell	Relatively simple	– Plexiglas creep under constant stress or water adsorption – Water leakage, entrapped air bubbles – Influence of temperature
Air-water volume measurement		
Air filled controller or mixed air-water filled controller	Direct measurement	– Undetectable air-leakage – Influence of temperature and atmospheric pressure
Direct measurement on the specimen		
Local displacement with radial strain measurement	Direct measurement on specimen	– Several measurement devices preferable to capture inhomogeneous deformation – Mounting of transducer requires rigid specimen
Laser technique	Direct, non-contacting measurement of entire profile	– High costs – Long calibration process
Image processing		– Not valid for asymmetric specimen when using only one camera

Table 2.3: Methods of volume change measurements, adapted from Lade (2016)

Details of the various measuring techniques can be found, for example, in Patil (2014). Note that less common methods such as X-ray CT were also successfully applied to mechanical testing of unsaturated granular soils (Khaddour 2015).

In the present study, a double-wall triaxial cell was used to detect the volumetric deformation of unsaturated silty sand specimens in triaxial testing. This method is based on the measurement of the displaced water volume of the inner cell. The outer cell is pressurized to

the same level as the inner cell, preventing the inner cell from pressure-dependent deformations. The method of volume change measurement may be associated with the indirect method via displaced cell liquid, as mentioned in Table 2.3 (see Chapter 7 for the details of the method).

2.4.1.3 Shearing rate

As mentioned above, the suction-controlled testing of unsaturated soils must be slow enough to allow the pore water to redistribute continuously within the specimen. The slow shearing rate is necessary to maintain hydraulic equilibrium during the test. The tendency of the sample to change the soil-water potential (suction) locally must be compensated by appropriate water movement from regions with higher water potentials to regions with lower water potentials. Since the permeability of unsaturated samples is much lower than that of unsaturated samples, the water movement within the soil is slow. In drained tests, an additional exchange in water mass between specimen and water compartment has to take place, which is necessary to maintain suction during the test. Regarding the axis-translation technique, this exchange is done through the HAE disk, whose permeability is generally lower than that of the tested unsaturated soil. Thus, shearing rates should be low enough to ensure the equalization of pore-water pressure during shearing and additionally ensure fully drained conditions in consolidated drained (CD) tests.

With respect to the desired test conditions, numerous studies have been carried out demonstrating the influence of the strain rate on the results of suction-controlled shear tests (Delage 2002, Fredlund, Rahardjo, and Fredlund 2012). If the axis-translation technique is used, a change in shearing rate usually results in a change in shear strength and volumetric behavior during shearing. Delage (2002) noted that the shearing rate depends on the volumetric behavior, the drainage length and the permeability of the sample, as well as on the permeability of the HAE disk. There are theoretical approaches to estimate the shearing rate for experiments with the axis translation technique (Ho and Fredlund 1982). However, these estimates tend to indicate the strain rate too cautiously (Patil 2014). Thus, either suitable shearing rates are determined by laboratory tests (which encompass some trial and error) or they are based on experiences from the literature.

For example, Patil (2014) has demonstrated the influence of the shearing rate on the shear strength of a compacted sandy silt with 45% fines in CD tests, in which suction was controlled through the axis-translation technique. The author noted that the faster the shearing rate, the more dilative the specimen responded and the higher the peak shear strength (Figure 2.21). The critical state was apparently not noticeably influenced.

Fredlund et al. (2012) noted that, in general, below a certain shearing rate, the shear strengths measured for various shearing rates eventually merge into an approximately constant behavior. This shearing rate indicates a suitable value for suction-controlled triaxial testing.

For suction-controlled CD tests on silts and silty sands, Table 2.4 summarizes shearing rates from the literature, expressed as axial strain rates. For most tested soils, shearing rates in the range of 10^{-5}% sec^{-1} were found to be appropriate.

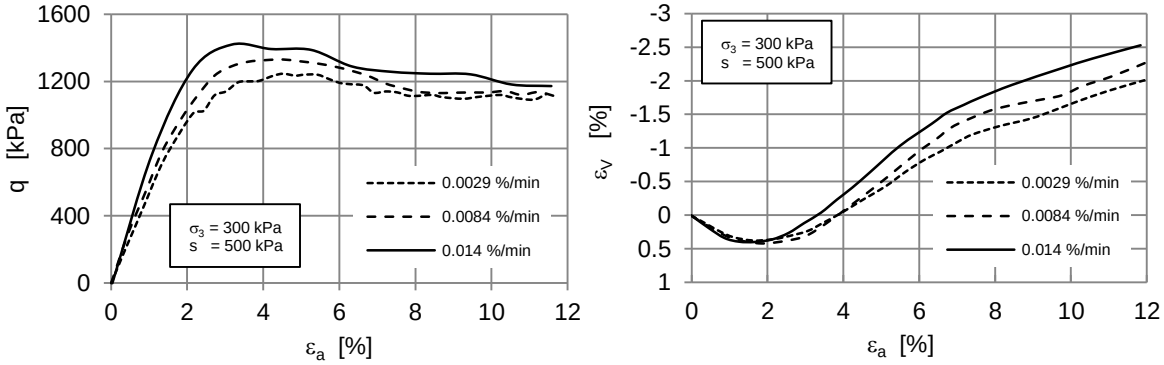

Figure 2.21: Shear strength and volumetric strain of unsaturated sandy silt as a function of the axial strain for different shearing rates, data from Patil (2014)

Note that suction-controlled constant water content (CW) tests can be run, on average, about half a power of 10 times faster than suction-controlled CD tests, since no water exchange has to take place through the HAE disk (Fredlund, Rahardjo, and Fredlund 2012).

Author	Soil	Drainage length	Strain rate [% sec^{-1}]
Bishop and Donald (1961)	Brahead Silt	Height of specimen H	$3.55 \cdot 10^{-5}$
Ho & Fredlund (1982)	Silty Sand, sandy silt	H	$2.38 \cdot 10^{-5}$
Delage et al. (1987)	Jossigny LP silt, I_p = 19	H/2	$1.67 \cdot 10^{-5}$
Romero et al. (1997)	Barcelona LP silt, I_p=16	H/2	$1.67 \cdot 10^{-5}$
Rampino et al. (1999)	Silty sand, I_p = 13	H	$2.10 \cdot 10^{-5}$
Laloui et al. (1997), Geiser (1999)	Sion sandy silt, I_p = 8	H	$2.50 \cdot 10^{-5}$
Houston et al. (2008)	Non-plastic sands	H	$33.3 \cdot 10^{-5}$
Patil (2014)	Silty sand	H	$14 \cdot 10^{-5}$

Table 2.4: Strain rates for suction-controlled consolidated drain (CD) tests, modified from Delage (2002)

2.4.1.4 Conventional shear testing at constant water content

As discussed above, performing suction-controlled shear tests is time-consuming and cost-intensive. It also requires a high level of expertise from the laboratory (Oloo and Fredlund 1996). The assessment of shear behavior of unsaturated soils may therefore seem simpler when using conventional shear testing methods applied to unsaturated specimens. However, if such conventional methods are used to test unsaturated soils, one can no longer control suction. Hence, assumptions have to be made about the initial suction and its evolution during tests.

Oloo and Fredlund (1996) compared the shear behavior of a statically compacted silt in a conventional direct shear apparatus without suction control and in a modified direct shear

apparatus with suction control. The authors found that both testing methods led to similar relationships between shear strength and suction. Based on this finding, they assumed that, at a relatively fast shearing rate, only small changes in suction occurred during the conventional direct shear tests. At peak, suction would be essentially equal to the initial suction at the beginning of the test.

For various compacted soils, Tarantino and El Mountassir (2013) note that conventional constant water content tests, such as direct shear or triaxial tests, may represent a method of making a rather conservative estimate of shear strength. They suppose that the effective stress remains fairly constant or decreases slightly during suction-controlled constant water content tests, but never increases. They conclude that the initial suction and degree of saturation might be used to approximate the hydraulic properties during shearing.

Heitor et al. (2013) and Heitor et al. (2017) have determined the compaction curves of a low-plasticity silty sand for several compaction energies. They found that for constant water content below the optimal water content, the measured suction did not change with changing density (Figure 2.22).

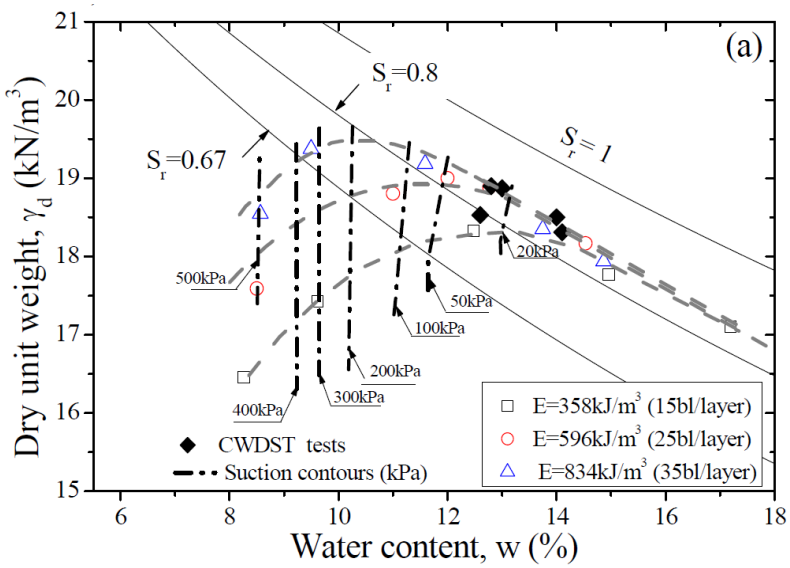

Figure 2.22: Compaction curves of a silty sand and lines of constant suction, from Heitor et al. (2017)

From suction-controlled constant water content tests on an agricultural soil, Wulfsohn et al. (1998) have concluded that—during shearing at low degrees of saturation—suction will remain fairly constant. Similar results were obtained from suction-controlled constant water content tests on a silty sand by Maleki and Bayat (2012).

Fern et al. (2014) conducted conventional and suction-controlled triaxial constant water content tests on compacted poorly graded sand. They found that the shear strength derived from the two test types compared well to each other.

Heitor et al. (2013) performed conventional direct shear tests on a silty sand at constant water content. They assumed that due to the narrow shear zone and the adjacent rather

large soil mass, suction would not change considerably during shear. They also noted that in comparison to suction-controlled shear tests, conventional tests make higher shearing rates possible.

From the above findings, an important conclusion already noted by Delage (2002) can be drawn. When considering conventional shear tests on samples at low degrees of saturation, a constant water content test is approximately equivalent to a constant suction test. Under these conditions, conventional testing methods may thus be suitable to approach unsaturated shear strength experimentally in a fast but controlled manner.

2.4.1.5 Uniaxial tests at constant water content

Apart from suction-controlled shear tests and conventional constant water content tests, an increase in soil strength due to suction can also be determined by means of uniaxial tensile tests (UTTs) and unconfined compression tests (UCTs). These tests are carried out at constant water content. They differ from the conventional tests in that volumetric deformations are typically not measured. With regard to unsaturated soil testing, assumptions as to the degree of saturation and suction must therefore be made.

Unconfined compression tests

The UCT is well established in soil testing in order to determine the shear strength of specimens under zero confining pressure. It is also increasingly used as a simple method to estimate the shear strength of unsaturated soils (Cunningham et al. 2003, Milatz 2016, Zhou, Xu, and Garg 2016, Taylor et al. 2018). The test interpretation is based on the assumption that no significant water content changes occur and that a uniform and fairly constant suction equal to the initial suction exists during the tests.

Colmenares and Ridley (2002) performed UCTs on unsaturated clayey silt while using a miniature tensiometer to measure the evolution of suction during shearing. For high suctions, they observed just a slight decrease in suction with decreasing axial strain. For low suctions, they observed a pronounced increase in suction with axial strain. It may therefore be concluded that at low degrees of saturation, suction does not decrease significantly if the peak is reached with small strains. Nevertheless, at high degrees of saturation, considerable changes in suction during shearing may occur.

Uniaxial tensile tests

The tensile strength of granular soils can essentially be regarded as caused by capillary effects, as long as there are no chemical bonds in the form of cementation, for example. Based on the methods for determining the tensile strength of concrete or of fine-grained soils (e.g., Heibrock et al. 2005; Che et al. 2015), a number of UTT devices were developed to measure the tensile strength of unsaturated granular soils (e.g., Mikulitsch & Gudehus 1995; Nahlawi et al. 2004; Lu et al. 2005). In essence, all UTT devices consist of two containers that can be moved against each other (e.g., Goulding 2006). The specimens are commonly directly installed into the connected containers. Subsequently, the containers are torn apart

by force or displacement control. The maximum measured tensile force, divided by the transmitting cross-sectional area, is then interpreted as being the tensile strength. Uniaxial tensile tests are also referred to as direct tensile tests.

The examination of the tensile strength is based on the assumption that the initial suction does not change significantly during testing. Junge et al. (2000) performed direct tensile tests on two as-compacted, well-graded fine-grained soils while measuring the suction with the help of two tensiometers. One was installed in the assumed failure zone, and the other a few centimeters away from the failure zone. The authors observed a considerable decrease in suction in the failure zone when the maximal tensile strength was reached. The decrease in suction some distance away from the failure zone was not very significant. A considerable displacement was necessary to bring the samples to failure, indicating rather ductile behavior. However, the samples seem to have been compacted wet of Proctor optimum, as relatively small suctions ($s < 40$ kPa) were measured. In fine-grained soils, these suctions correspond to high degrees of saturation near the air entry value. Thus, for such tests, the assumption of constant suction at constant water content is no longer valid.

In view of the above, it can be concluded that UTTs and UCTs apply only to relative dry samples. Only at these conditions may an approximately constant suction be assumed during the test. These findings confirm the conclusion in Section 2.4.1.4 that at low water content, a constant water content test is also a constant suction test.

2.4.2 Evolution of shear strength with suction

Likos et al. (2010) performed suction-controlled direct shear tests on a poorly graded clean sand at low net normal stresses and low suction. Sample preparation was done by shaking a known dry mass to a desired, approximately medium-dense packing. Suction was controlled with a hanging column assembly. The results of the suction-controlled tests show an increase in the peak shear strength:

$$\Delta\tau_{Peak} = \tau_{Peak,unsat} - \tau_{Peak,sat} \quad (2.18)$$

with $\tau_{Peak,unsat}$ Shear strength of the unsaturated samples

$\tau_{Peak,sat}$ Shear strength of the saturated samples,

exhibiting a maximum value at s = 2.5 kPa (Figure 2.23a).

From the corresponding SWRC it can be seen that the effect of suction on the measured shear strength decreased from degrees of saturation Sr < 30% corresponding to the beginning of the residual zone of the SWRC (Figure 2.23b).

The additional shear strength due to suction $\Delta\tau_{peak}$ seemed to be independent of the net normal stress with one exception at s ≈ 2.5 kPa (Figure 2.23a).

Note that the net normal stress is defined as follows (see also Section 2.5.1):

$$\sigma_{N,net} = \sigma_N - u_a \quad (2.19)$$

with σ_N Total normal stress

u_a Pore-air pressure.

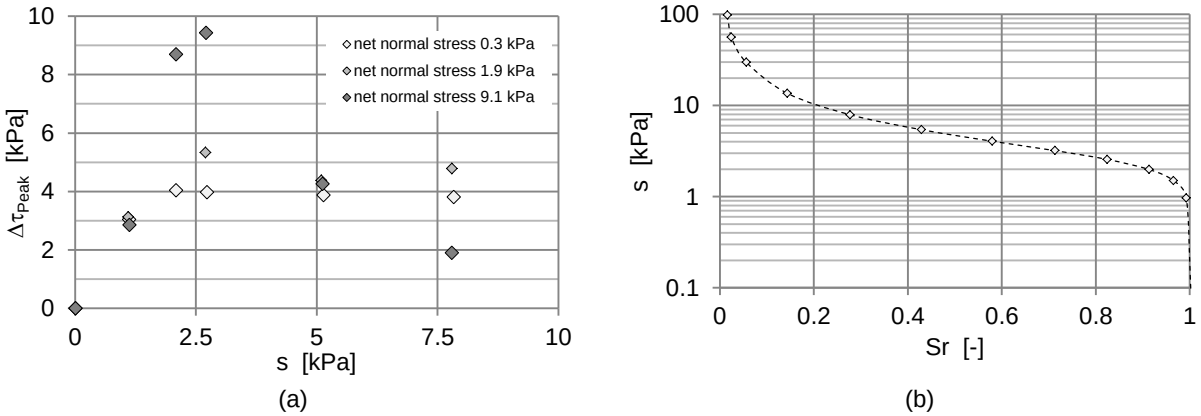

Figure 2.23: (a) Increase in shear strength $\Delta\tau_{peak}$ of clean sand vs. suction s and (b) SWRC of the clean sand, data from Likos et al. (2010)

Also, note that from the shear strength data for saturated conditions presented in Likos et al. (2010), peak friction angles up to $\varphi'_{peak} = 70°$ can be derived (Figure 2.24). These friction angles are in good agreement with those presented in Section 2.3.5.

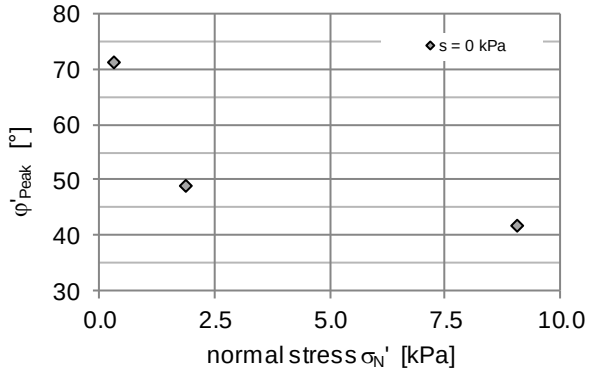

Figure 2.24: Peak friction angle φ'_{peak} of clean saturated sand vs. effective normal stress σ'_N, derived from direct shear test data presented in Likos et al. (2010)

Donald (1956) carried out suction-controlled direct shear tests on four silty soils, which were prepared in a loose state by slurry deposition. The tested soils ranged from silt (soil named FF) to sandy silts (named GF and MF) to silty sand (named BS). During the tests, suction was controlled with the hanging water-column technique. For each soil, the increase in peak shear strength $\Delta\tau_{peak} = \tau_{unsat} - \tau_{sat}$ is shown in Figure 2.25a as a function of suction. The SWRCs of the four soils are shown in Figure 2.25b.

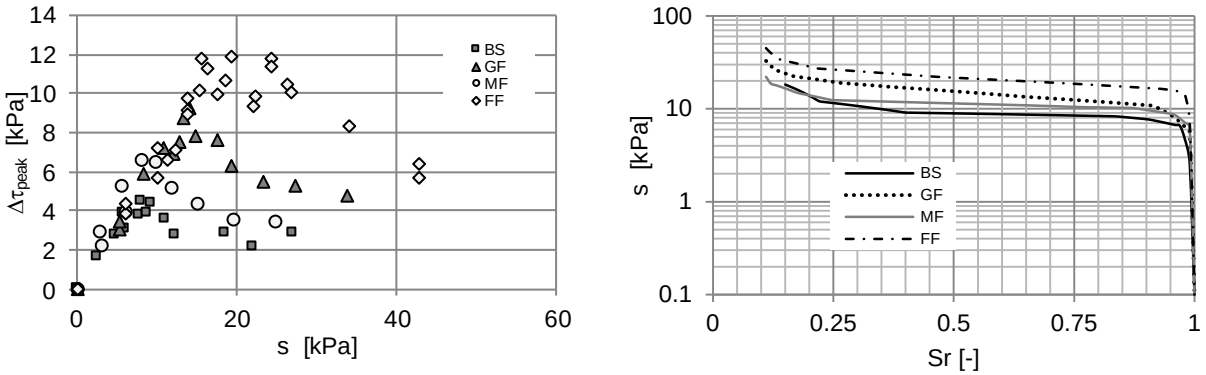

(a) (b)

Figure 2.25: (a) Increase in shear strength $\Delta\tau_{peak}$ of four silty soils vs. suction s, data from Donald (1956). (b) Soil-water retention curves (SWRCs) of the silty soils, data from Aitchison and Donald (1956)

Figure 2.25 shows that the higher the air entry value of the SWRC, the higher $\Delta\tau_{peak}$. For suctions below the air entry value, the $\Delta\tau_{peak}$ increased approximately linearly with increasing suction according to $\Delta\tau_{peak} \approx \tan\varphi' \cdot s$. As the suction was further increased, $\Delta\tau_{peak}$ decreased as a result. The maximum $\Delta\tau_{peak}$ was reached at suctions between $s = 10$ kPa and $s = 20$ kPa. After the maximum, $\Delta\tau_{peak}$ dropped toward zero or slightly above. This drop

apparently happened at suctions corresponding to degrees of saturation Sr < 10%, indicating the beginning of the residual zone of the respective SWRCs (Figure 2.25b).

Nishimura et al. (2008) performed direct shear tests on a compacted non-plastic silt at constant water content (presumably without suction-control). Samples were compacted wet of Proctor optimum to approximately 92% of the maximum dry density. From Figure 2.26a, a decrease in the additional shear strength $\Delta\tau_{peak} = \tau_{unsat} - \tau_{sat}$ could be observed at initial suctions corresponding to degrees of saturation Sr < 20%, indicating the beginning of the residual zone of the SWRC (Figure 2.26b). For lower degrees of saturation, the contribution of suction to shear strength was approximately constant. However, the saturated shear strength was not recovered even for almost fully dry conditions ($\Delta\tau_{peak} > 0$). Nishimura et al. (2008) further observed that the influence of the hysteresis of the SWRC on the shear strength was negligible in the residual zone of the.

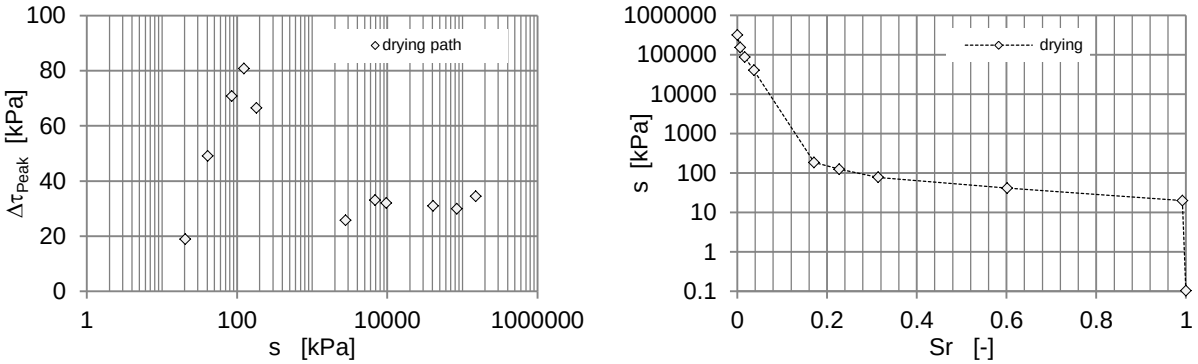

Figure 2.26: (a) Increase in shear strength $\Delta\tau_{peak}$ of a non-plastic silt vs. suction s. (b) Soil-water retention curve (SWRC) of the silt, data from Nishimura et al. (2008)

Schnellmann et al. (2013) performed suction-controlled direct shear tests on a silty sand with 10.5% fines. The specimens were compacted at the dry side of Proctor optimum, while suction was controlled with the axis-translation technique. Figure 2.27a exemplifies the stress-displacement curves for a net normal stress of $\sigma_{N,net} = 50$ kPa and for different suctions. Figure 2.27b shows the corresponding evolution of the vertical displacement with the horizontal displacement. From Figure 2.27a, one can see that the higher the suction, the higher the peak shear strength and the more pronounced the peak. Figure 2.27b reveals that the more pronounced the peak, the more dilative the samples (a negative vertical displacement indicates an increase in volume).

In general, for each applied net normal stress, the additional peak shear strength $\Delta\tau_{peak}$ increased non-linearly with suction (Figure 2.28a). A plateau or a maximum was reached at suctions corresponding to the residual zone of the SWRC (Figure 2.29).

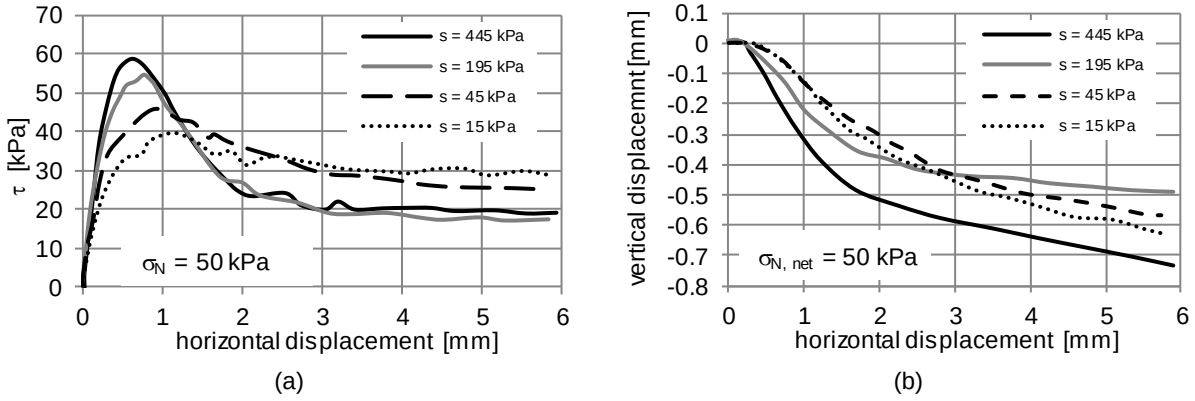

Figure 2.27: (a) Shear stress and (b) vertical displacement of silty sand for $\sigma_{N,net}$ = 50 kPa vs. horizontal displacement, data from Schnellmann et al. (2013)

Figure 2.28b shows the angle of dilatancy derived from the relationship between the measured vertical displacement (v) and the horizontal displacement (x) at peak for each tested suction and net normal stress. The rate of dilatancy increases with increasing suction, while it exhibits a trend similar to the increase in shear strength $\Delta\tau_{peak}$ with increasing suction (Figure 2.28a).

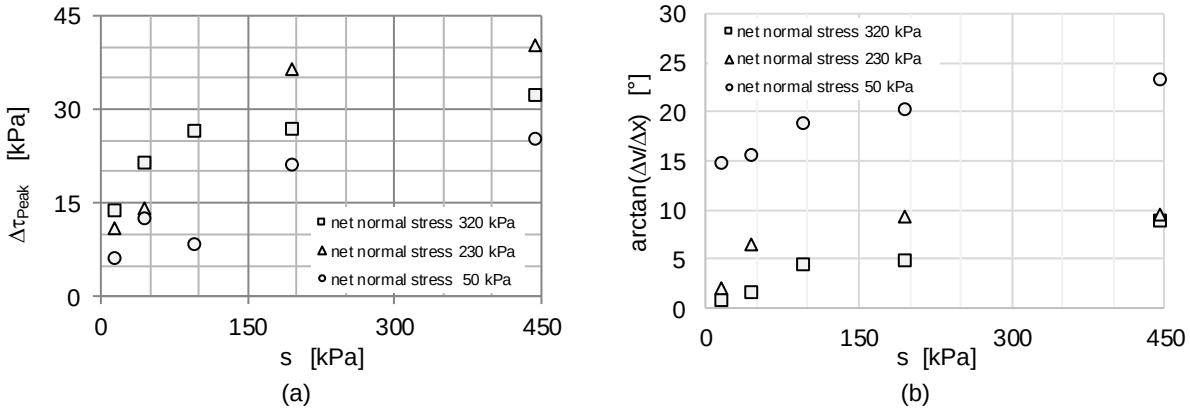

Figure 2.28: (a) Increase in shear strength of silty sand vs. suction and (b) maximum rate of dilatancy, data from Schnellmann et al. (2013)

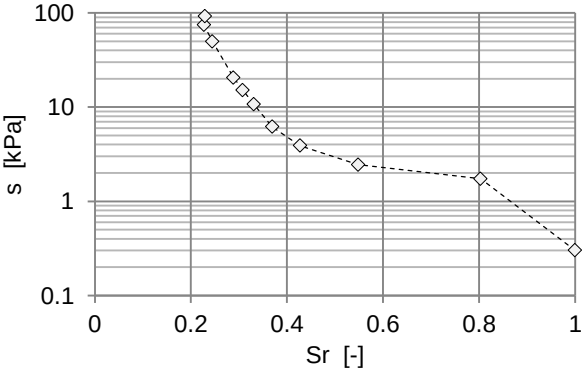

Figure 2.29: Soil-water retention curve (SWRC) of silty sand, data from Schnellmann et al. (2013)

Toll (1988) conducted triaxial compression tests on saturated and unsaturated compacted samples of gravel with aggregated fines. The axis-translation technique was used to measure the suction during constant water content tests. He observed that the unsaturated soil samples exhibited a stronger dilatancy than the saturated samples. The rate of dilatancy depended on the initial density, total stress and suction. Under the same unsaturated conditions, dense samples dilated more than loose samples. Samples with high suctions dilated more than samples with low suctions. Dilatancy was suppressed with increased confining pressure. Toll (1988) further observed increased shear strength as a result of increased dilative behavior for low water content at which the pore water had already withdrawn into the aggregates where no inter-particle forces between the solid grains remained.

Fern et al. (2014) carried out constant water content tests and suction-controlled triaxial tests on Chiba sand with 6% fines compacted at various densities. For the suction-controlled tests, the axis-translation technique was used. The authors noted that the shear strength at the critical state increased with increasing suction. The observed additional strength was attributed to an increase in effective stress. They also observed an increase in the ratio of deviatoric stress at peak to the deviatoric stress at critical state q_{peak}/q_{crit} with increasing suction. They attributed this phenomenon to an increase in the rate of dilatancy with increasing suction.

Houston et al. (2008) performed suction-controlled triaxial CD tests on a silty sand with 27% fines. The soil samples were compacted wet of Proctor optimum to 90% of the maximum dry density. Suction was controlled with the axis-translation technique. The silty sand shows a gradual increase in peak shear strength $\Delta q_{peak} = q_{peak,unsat} - q_{peak,sat}$ with increasing suction, which tends toward a maximum or a plateau at the highest applied suction, for all tested confining pressures (Figure 2.30a). The maximum angle of dilatancy, for simplicity defined as $\arctan(\Delta\varepsilon_v/\Delta\varepsilon_a)_{max}$, showed a behavior qualitatively similar to that of Δq_{peak} (Figure 2.30b).

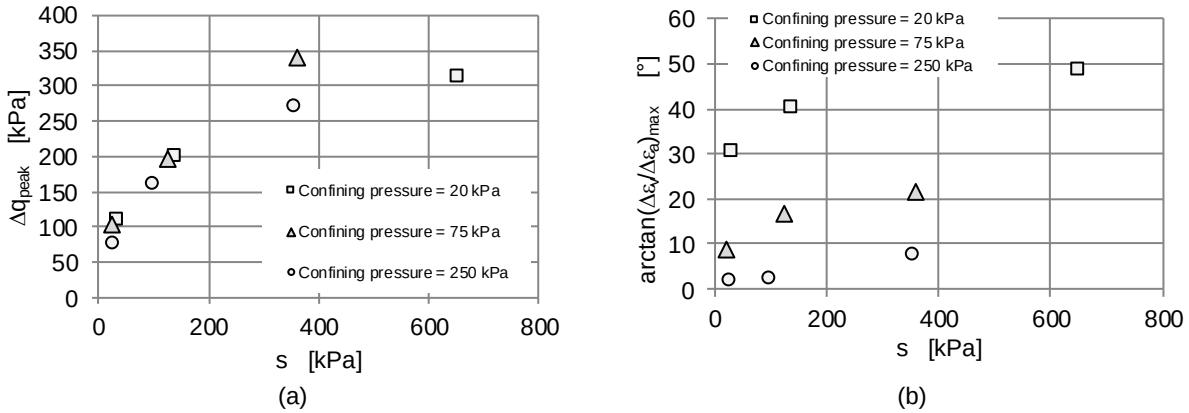

Figure 2.30: (a) Increase in shear strength Δq_{peak} of a silty sand vs. suction s and (b) angle of dilatancy $\arctan(\Delta\varepsilon_v/\Delta\varepsilon_a)_{max}$ vs. suction s, data from Houston et al. (2008)

Note that when taking the SWRC of the soil into account, the highest applied suction of s ≈ 625 kPa was still in the transitional zone of the SWRC (see Figure 2.31).

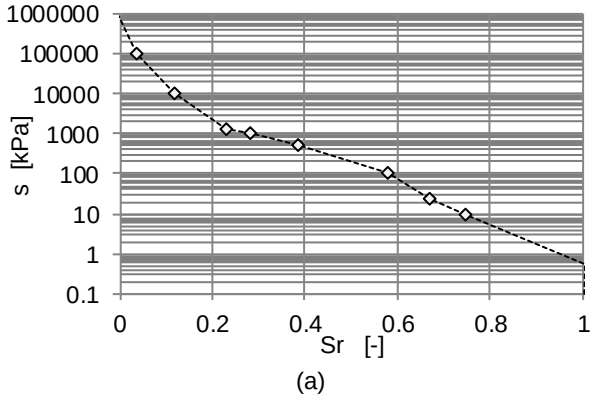

Figure 2.31: Soil-water retention curve (SWRC) of silty sand (27% fines), from Houston et al. (2008)

Based on the above findings, the dependency of the unsaturated shear strength of granular soils with fines on suction can be described as schematically shown in Figure 2.32.

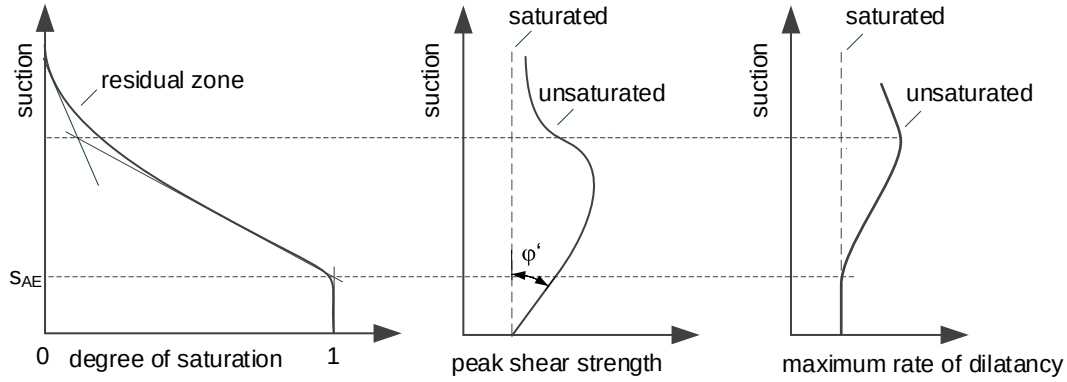

Figure 2.32: Schematic of the shear strength of unsaturated granular soils with fines

Starting from the fully saturated state, the shear strength initially increases with increasing suction in the ratio of the effective friction angle for saturated conditions ($\Delta\tau \approx \tan \varphi' \cdot s$). As soon as the air entry value s_{AE} is exceeded, the rate of the increase in shear strength gradually decreases with increasing suction until a maximum shear strength is reached. Subsequently, the shear strength decreases with increasing suction until it becomes nearly independent of suction in the residual zone of the SWRC. This shear strength corresponds to the saturated shear strength or may be slightly higher. Qualitatively, in the transition zone of the SWRC, the maximum rate of dilatancy may have a similar dependency on suction as does shear strength. Less is known about the evolution of dilatancy in the residual zone of the SWRC. For granular soils having aggregates, however, it can be expected that the dilatancy in this zone remains enhanced compared to saturated conditions (Toll 1988).

2.4.3 Dual effect of suction on shear behavior

On a micro-level, capillary-induced water menisci either enclose water clusters or exist as separated water bridges between adjacent particles (Section 2.1.4). Related inter-particle forces are caused by the mutual effects of the different pressures in each phase of the soil mass and the surface tension of the air-water interfaces.

On a macro-level, a change in suction has a dual effect on soil behavior (Khalili and Khabbaz 1996):

i. Change of inter-particle forces and thus effective stress state.

ii. Hardening or softening of the soil skeleton due to the evolution or devolution of air-water interfaces (Nuth and Laloui 2008).

Figure 2.33 simply illustrates the dual effect of suction through the behavior of both saturated and unsaturated samples of a granular soil with aggregated fines under drained (suction-controlled) triaxial compression.

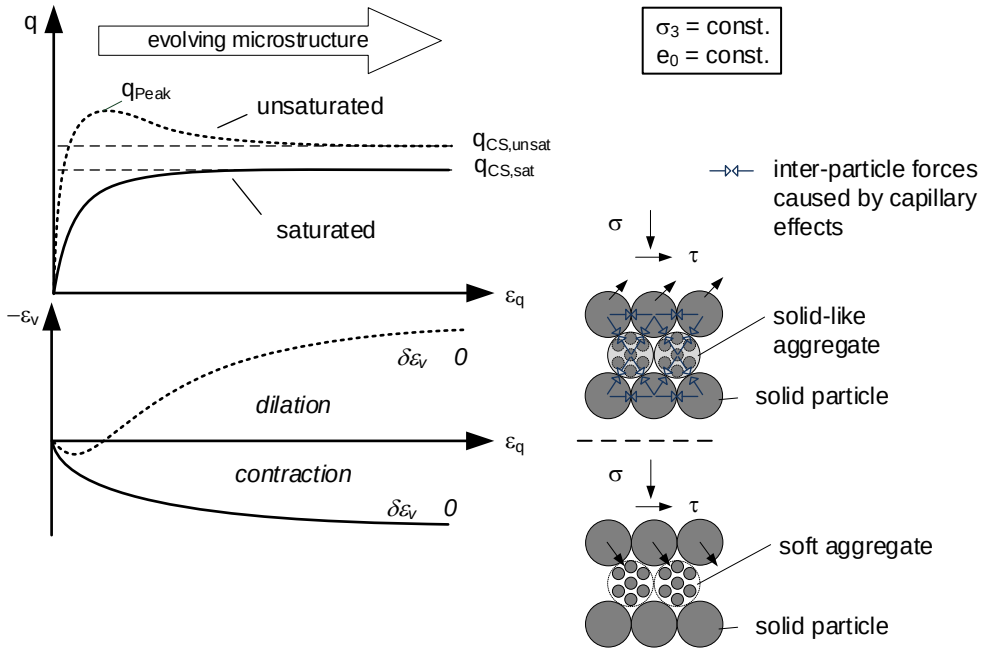

Figure 2.33: Drained shear behavior of a granular soil with aggregated fines under saturated and unsaturated conditions (schematic)

At the same confining pressure σ_3 and initial void ratio e_0, the soil behaves more dilative (effect ii) and has a higher effective stress state (effect i) under unsaturated conditions than under saturated conditions. The increased dilatancy is due to the suction-induced inter-particle forces within the aggregates, which gives strength to them and causes the aggregates to behave like large solid-like particles (Toll 2000, Munkholm and Kay 2002, Toll and Ong 2003, Houston, Perez-Garcia, and Houston 2008). The soil therefore behaves in a more granular way than would be justified by its grading (Toll 1988). Note that the effect of suction on dilatancy increases with increasing suction and decreasing stress level, as

mentioned in Section 2.4.2. The higher effective stress is due to the suction-induced inter-particle forces between the solid particles and solid-like particles.

From the dual effect of suction, one can draw the following conclusions regarding the shear strength of unsaturated and saturated samples of a granular soil with aggregated fines under drained triaxial compression:

- At peak, the shear strength of the unsaturated samples is increased not only by the increase in effective stress (effect i), but also by the increase in dilatancy (effect ii).
- At the critical state, the effect of suction on the dilatancy disappears, as the initial microstructure of the unsaturated sample is largely destroyed. The shear strength at critical state, however, will still be higher under unsaturated conditions than under saturated conditions due to the suction-induced increase in effective stress (effect i).
- Saturation of the soil causes a breakdown of all inter-particle menisci, which eliminates the suction-induced effective stress as well as the suction-induced strength of the aggregates. The latter leads to a reduction of the rate of dilatancy. Both effects cause the saturated sample to have less shear strength than the unsaturated sample.

Note that the assumption of the vanishing effect of suction on the dilatancy at critical state was shown to be an appropriate approach in a comprehensive study on the critical shear strength of sandy to clayey soils carried out by Tarantino and El Mountassir (2013).

Also, note that in aggregated granular soils with low water content, the pore water is present only within the aggregates (Section 2.2.3). Therefore, no suction-induced forces between the solid particles and the solid-like particles are generated in the soil, causing the suction-induced effective stress to vanish. However, an enhancing effect of suction on the strength of the aggregates and thus on dilatancy may persist at such low water content (Toll 1988). Hence, the peak shear strength of unsaturated soils can remain increased even though the suction-induced effective stress has already dissipated.

2.5 Effective stress in unsaturated soils

2.5.1 Bishop's concept of effective stress

Terzaghi's formulation of effective stress for saturated soils is as follows:

$$\sigma'_{ij} = \sigma_{ij} - u \cdot \delta_{ij} \tag{2.20}$$

with σ_{ij} Total stress tensor

δ_{ij} Kronecker-Delta

u Fluid pressure: corresponds to water pressure u_w, if saturated with water or to air pressure u_a, if saturated with air.

Terzaghi's equation has been empirically proven correct even though it converts a two-phase system of grain-to-grain contact forces—governed by pore-water pressures at the micro-level—into a single-phase system at the macro-level.

The definition of effective stress in unsaturated soils has to satisfy the inherent conflict between describing the soil behavior at the micro-level and the search for an average variable to describe the soil behavior at the macro-level.

An unsaturated soil consists of three phases (usually air, water and solids) and is therefore a rather heterogeneous mixture. The mechanisms that distinguish its behavior from that of a saturated soil are complex and on a micro-level. A change in suction or in degree of saturation causes a change in the magnitude, amount and distribution of inter-particle forces that (on average) may be isotropic. These changes in micro-level forces cause globally measurable effects such as straining, change in stiffness or change in shear resistance.

In this context, the individual forces on the micro-level may be combined and averaged over a representative volume to form an equivalent effective stress in the sense of Terzaghi's formula. Applied to an equivalent single-phase continuum, the equivalent effective stress must then reproduce the impact of the combination of all micro-level processes on the mechanical soil behavior at the macro-level, as shown in Figure 2.34 (Khalili, Geiser, and Blight 2004, Nuth and Laloui 2008).

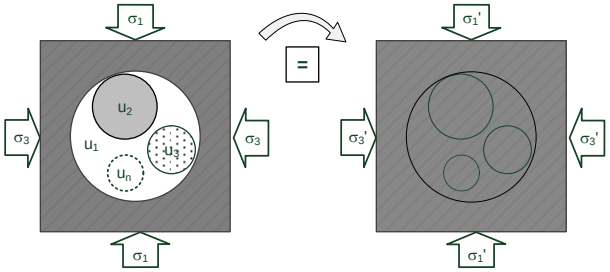

Figure 2.34: Conversion of a loaded multi-phase (I = 1...n) and multi-stress (σ, u_i) medium into a mechanically equivalent single-phase and single-stress continuum (σ'), adapted from Nuth and Laloui (2008)

With this purpose, Bishop (1959) extended Terzaghi's effective stress approach to unsaturated conditions (Nuth and Laloui 2008):

$$\sigma'_{ij} = \sigma_{ij} - u_a\delta_{ij} + \chi \cdot (u_a - u_w)\,\delta_{ij} = \sigma_{ij} - u_a\delta_{ij} + \chi \cdot s\,\delta_{ij} \tag{2.21}$$

with χ Bishop's state variable ($0 \leq \chi \leq 1$)

The state variable χ in the equation above is a scaling factor that considers the portion of suction that affects the effective stress. For granular materials, χ may best be illustrated as being the averaged portion of pore space occupied by the water phase in which suction or surface tension can act. At high degrees of saturation, in the capillary zone of the SWRC (Section 2.1.4), the pore space is almost fully occupied by soil water, while the soil behaves similarly to its behavior under saturated conditions with χ = 1 (Aitchison and Donald 1956). With decreasing water content, suction increases, whereas the pore-space occupied by water decreases. Since suction and surface tension can only act within the water phase, the effect of both on mechanical behavior depends on this limited pore space. As a consequence, Bishop's variable χ decreases to values smaller than 1. When the soil is further dried and all menisci between the solid particles and the solid-like particles have vanished (Section 2.4.3), the effect of suction on the effective stress vanishes (χ = 0).

For χ = 0 and χ = 1, Bishop's term for effective stress takes the form of Terzaghi's effective stress equation (2.20).

Note that different terms are used in the literature to describe the contribution of suction to the effective stress $\Delta\sigma' = \chi \cdot s$, for example suction stress (Lu and Likos 2006, Oh et al. 2013), averaged skeleton stress (Pagano et al. 2016) or isotropic capillary pressure (Mikulitsch and Gudehus 1995). In this thesis, this contribution is referred to as suction-induced effective stress or effective stress due to suction.

Some attempts have been made to derive a function for the state variable χ from contact forces on the micro-level, assuming spherical particles (e.g., Kim & Sture 2008; Lu et al. 2010). Although these models give valuable insight into the governing mechanisms in unsaturated granular soils, as already applied to the description of χ in this chapter, they cannot describe the dependency of the effective stress on suction unambiguously (Khalili and Khabbaz 1996).

The non-compliance of the dual effect of suction on soil behavior is considered the main reason for the misinterpretation of effective stress (Khalili and Khabbaz 1996). In fact, if the dual effect of suction is neglected, Bishop's effective stress apparently fails to cover some of the essential features of unsaturated soil behavior, such as collapse upon wetting (Burland and Jennings 1962) or the increase in the rate of dilatancy with increasing suction:

- If particle contacts at a certain stress level and degree of saturation are rather unstable, the wetting process can cause a collapse of the soil structure because suction decreases and the stabilizing menisci disappear (Lawton, Fragaszy, and Hardcastle 1989, Abbeche, Hammoud, and Ayadat 2007, Rabbi, Cameron, and Rahman 2014). Following (2.21),

decreasing the suction would lead to a decrease in effective stress, indicating swelling of the soil rather than a collapse. Moreover, if not wetted, an additional external loading would be necessary to achieve a similar volumetric deformation (Figure 2.35).

- Regarding the increasingly dilative behavior of soils with increasing suctions, from (2.21) it follows that dilatancy would increase with increasing effective stress. This conclusion contradicts the well-known feature of granular soils that dilatancy decreases with increasing effective stress.

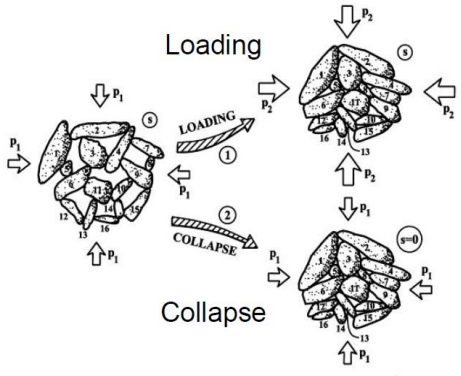

Figure 2.35: Volumetric contraction due to collapse upon wetting or loading, from Gens (2014)

For these reasons, early attempts to determine Bishop's state variable χ experimentally failed. This failure led to the assumption that a single stress variable may not be sufficient to describe unsaturated soil behavior (e.g., Jommi 2000; note that criticism of the effective stress formulation is detailed in Khalili et al. 2004).

Eventually, the discussion led to the development of the concept of two independent stress variables (Fredlund & Morgenstern 1977), in which any two of the three variables

$$\left(\sigma_{ij} - u_w\delta_{ij}\right), \qquad \left(\sigma_{ij} - u_a\delta_{ij}\right), \qquad (u_a - u_w)\delta_{ij}$$

are seen to fully represent the stress state. The common choice of the stress variables is these:

$$\left(\sigma_{ij} - u_a\delta_{ij}\right), \qquad (u_a - u_w)\delta_{ij}\,.$$

The first stress variable above is also called net stress, $\sigma_{ij,net} = \sigma_{ij} - u_a\delta_{ij}$.

However, it was not until appropriate constitutive frameworks accounting for the dual effect of suction were developed that researchers could describe the collapse due to wetting or interlocking effects in a unique manner (e.g., Alonso et al. 1990). Within the framework of elasto-plasticity, authors typically describe the dual effect of suction with the help of the suction-dependent widening of a yield surface (i.e., pre-consolidation pressure or suction hardening). Among others, Khalili and Khabbaz (1999) have noted that Bishop's effective stress formulation can be used in combination with constitutive models for saturated soils to model unsaturated soil behavior by properly considering the influence of suction on the state

variable χ and on the model parameters and by including the SWRC accounting for its dependency on the porosity and on the hydraulic path.

2.5.2 Determination of χ from shear strength

As explained above, effective stress and shear strength depend on degree of saturation and therefore on suction. Thus, they are linked to the soil's microstructure.

Most commonly, the state variable χ is evaluated from suction-controlled shear tests or conventional constant water content tests by introducing Bishop's effective stress equation (2.21) into Mohr–Coulomb's failure criterion or into the equivalent, Roscoe's failure criterion:

$$\begin{aligned} \tau &= [\sigma - u_a + \chi \cdot s] \cdot \tan\varphi' + c' \\ q &= [p - u_a + \chi \cdot s] \cdot M + c^* \end{aligned} \tag{2.22}$$

with $\sigma - u_a$ net stress σ_{net}

$p - u_a$ net mean stress p_{net}

φ' effective friction angle

$M = \frac{6 \sin\varphi'}{3 - \sin\varphi'}$

c' intersection of Mohr–Coulomb's failure criterion with the τ-axis (effective cohesion)

c^* Intersection of Roscoe's failure criterion with the q-axis.

The change in shear strength with suction is then attributed to the change in effective stress (Fredlund and Vanapalli 2002). As pointed out by Delage (2002), however, (2.22) is implicitly based on the hypothesis that the effective friction angle φ' is independent of suction. Given the dual effect of suction, this assumption can apply only to shear strength data from critical states where there is no increase in dilatancy due to suction.

Figure 2.36 schematically shows the dual effect of suction on the determination of χ from peak shear strength using the example of a direct shear test. According to Bolton (1986), at the same effective stress, a stronger dilatancy results in a higher secant peak friction angle ($\varphi'_{unsat} \geq \varphi'_{sat}$). However, since neither $\Delta\sigma'$ nor φ'_{unsat} are known during the test, the position of the failure point on the $\tau - \sigma'$ plane is not unique.

Therefore, the simultaneous increase in the effective stress and the friction angle makes it difficult to derive the stress variable χ from peak shear strength. For this reason, researchers usually focus on the determination of χ from the shear strength at the critical state. However, as discussed in Section 2.3.3, it is not always possible to reach the critical state unambiguously. In particular, regarding triaxial testing, end restraint effects may cause both strain localization and local pore-water pressure changes within shear bands. In addition,

since the microstructure may be considered fully decomposed, it is questionable whether χ derived from the critical state also applies to the peak state, where the initial microstructure, particularly aggregated fines, still significantly influences the shear behavior (Toll 1988).

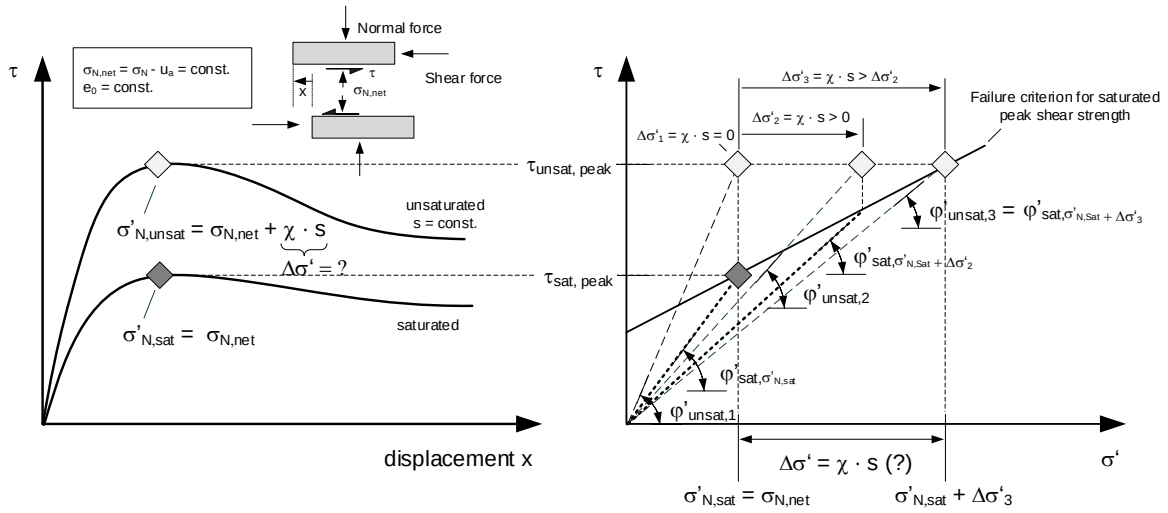

Figure 2.36: Dual effect of suction on the derivation of the state variable χ from peak shear strength (schematic)

2.5.3 Relationships between χ and the soil-water retention curve

Mainly based on the evaluation of shear strength data, different relationships for the state variable χ as a function of the degree of saturation has been proposed in the literature (Vanapalli et al. 1996, Öberg and Sällfors 1997, Lu, Godt, and Wu 2010). In other relationships, χ is directly linked to suction (Khalili and Khabbaz 1998, Bao, Gong, and Zhan 1998). Few researchers have explicitly considered microstructural aspects (Khalili et al. 2005, Alonso et al. 2010, Konrad and Lebeau 2015, Ciervo et al. 2015). What the approaches have in common is that they relate effective stress to the soil-water retention curve (SWRC). A summary of the proposed relationships is given in Table 2.5. Additional expressions for χ methods can be found in Sheng et al. (2011) or Schnellmann et al. (2013).

Table 2.5 reveals that most of the proposed equations based on the degree of saturation are similar, as they use the effective degree of saturation in the following form:

$$S^e = \langle \frac{Sr - Sr_0}{1 - Sr_0} \rangle \tag{2.23}$$

with Sr_0 Degree of saturation at which the contribution of suction to effective stress vanishes

$\langle x \rangle$ Macauly brackets $\langle x \rangle = \begin{cases} 0, & \text{for } x < 0 \\ x, & \text{for } x > 0 \end{cases}$.

Therefore, most of the approaches differ in their interpretation of the degree of saturation at which the contribution of suction to the effective stress vanishes (Sr_0) or in the constitutive equation that models the corresponding SWRC. An example of the effect of Sr_0 on the effective stresses predicted with (2.23) may be taken from Figure 2.37.

Reference	χ (for $s > s_{AE}$)	Parameters	
Vanapalli et al. (1996)	Sr^{κ} , or $\langle\frac{Sr - Sr_r}{1 - Sr_r}\rangle$	Sr_r	Residual degree of saturation
		κ	Fitting parameter
Öberg & Sällfors (1997)	Sr	-	
Bao et al. (1998)	$\langle\frac{\log s_r - \log s}{\log s_r - \log s_{AE}}\rangle$	s_r	Suction at residual degree of saturation
		s_{AE}	Suction at air entry value
Khalili & Khabbaz (1998)	$\left(\frac{s}{s_{AE}}\right)^m$	m	Fitting parameter
		s_{AE}	Air entry value of suction
Alonso et al. (2010)	Sr^{α} , or $\langle\frac{Sr - Sr_m}{1 - Sr_m}\rangle$	α	Fitting parameter
		Sr_m	Degree of saturation separating microstructure from macrostructure
Lu et al. (2010)	$(1 + [\alpha \cdot s]^n)^{-\frac{(n-1)}{n}}$	α, n	Parameters to fit the Soil-water retention curve (SWRC) expressed via the effective degree of saturation according to van Genuchten (1980)
	$= \langle\frac{Sr - Sr_r}{1 - Sr_r}\rangle$	Sr_r	Residual degree of saturation
Tarantino & Tombolato (2005)	$\langle\frac{e_w - e_{wm}}{e - e_{wm}}\rangle$	e_{wm}	Microstructural water ratio separating intra-aggregate pores from inter-aggregate pores
	$= \langle\frac{Sr - Sr_m}{1 - Sr_m}\rangle$	Sr_m	Degree of saturation separating intra-aggregate pores from inter-aggregate pores
Konrad & Lebeau (2015)	$1 - \left(1 - e^{-\Lambda \cdot s}\right)^{\alpha}$	α	Fitting parameter
		Λ	Fitting parameter
		e	Euler's number
	$= \langle\frac{Sr - Sr_a}{1 - Sr_a}\rangle$	Sr_a	Degree of saturation mostly ascribed to adsorptive forces

Table 2.5: Published equations for Bishop's state variable χ

In Figure 2.37, the drying branch of the SWRC of a silty sand (28% fines) is shown (Angerer and Birle 2016). For this SWRC, the performance of various approaches for $\chi = S^e$ from Table 2.5 were investigated by comparing the predicted increase in effective stress due to suction $\Delta\sigma' = S^e \cdot s$. Especially for degrees of saturation below the residual state of the SWRC, the predicted values of $\Delta\sigma'$ differ considerably. In the residual zone of the SWRC, $\Delta\sigma'$ may either drop to zero or take very high values. This peculiarity depends on the shape of the SWRC, the mathematical model used to describe S^e and the definition of Sr_0, the latter

indicated in the figure. In the funicular zone, the predicted effective stress is less influenced by the choice of χ or Sr_0. Therefore, considerable uncertainty is involved in the prediction of $\Delta\sigma'$ in the range of the residual zone.

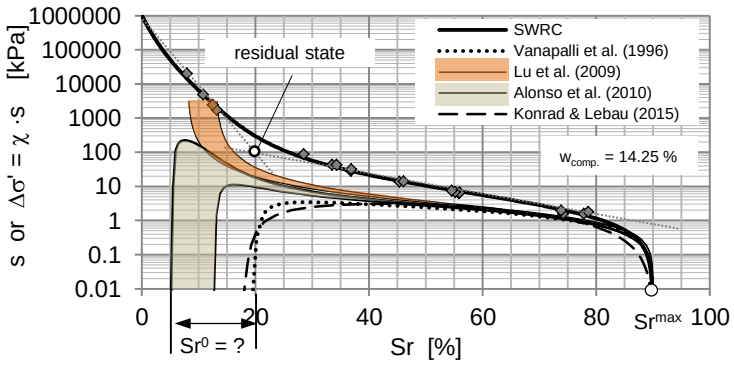

Figure 2.37: Effect of Sr_0 on the product $\Delta\sigma' = S^e \cdot s$ by the example of a statically compacted silty sand, soil-water retention curve (SWRC) from Angerer and Birle (2016)

Based on thermodynamic considerations, Jiang et al. (2017) recently derived a closed-form solution for the state variable χ. In contrast to other thermodynamic contributions, they avoided describing the complex shapes and distribution of menisci by directly introducing measured suction into the thermodynamic description. For the general case where the suction depends on both the degree of saturation and porosity, Jiang et al. (2017) assume a porosity-dependent SWRC of the following form:

$$s = A(1-n)^{\beta}\left[\frac{1-Sr}{Sr^{\alpha}}\right] \tag{2.24}$$

with A, α, β Fitting parameter

n Porosity

Sr Degree of saturation.

From (2.24), they derived an expression for χ as a function of the porosity and degree of saturation:

$$\chi = Sr - \beta \cdot n \cdot S_r \cdot \left[\frac{1-\alpha+\alpha Sr - Sr^{\alpha}}{\alpha(1-\alpha)(1-Sr)}\right]. \tag{2.25}$$

Figure 2.38 shows the influence of the parameters α, β and n of (2.24) on the SWRC and on the state variable χ, according to (2.25). The state variable χ is plotted in the figure against the suction ratio s/s_{AE}. A constant value of A = 15 was chosen since it did not influence the description of χ, as can be seen in (2.25).

The results in Figure 2.38 show that Bishop's state variable χ can be described as a linear relationship in a double-logarithmic scale. The porosity n and the parameter β do not

influence the evolution of χ as much as the parameter α. Therefore, the shape of the SWRC, especially its inclination in the transition zone, exerts the greatest influence on χ. The flatter the course in the transition zone of the SWRC, the steeper χ decreases with increasing suction ratio s/s_{AE}.

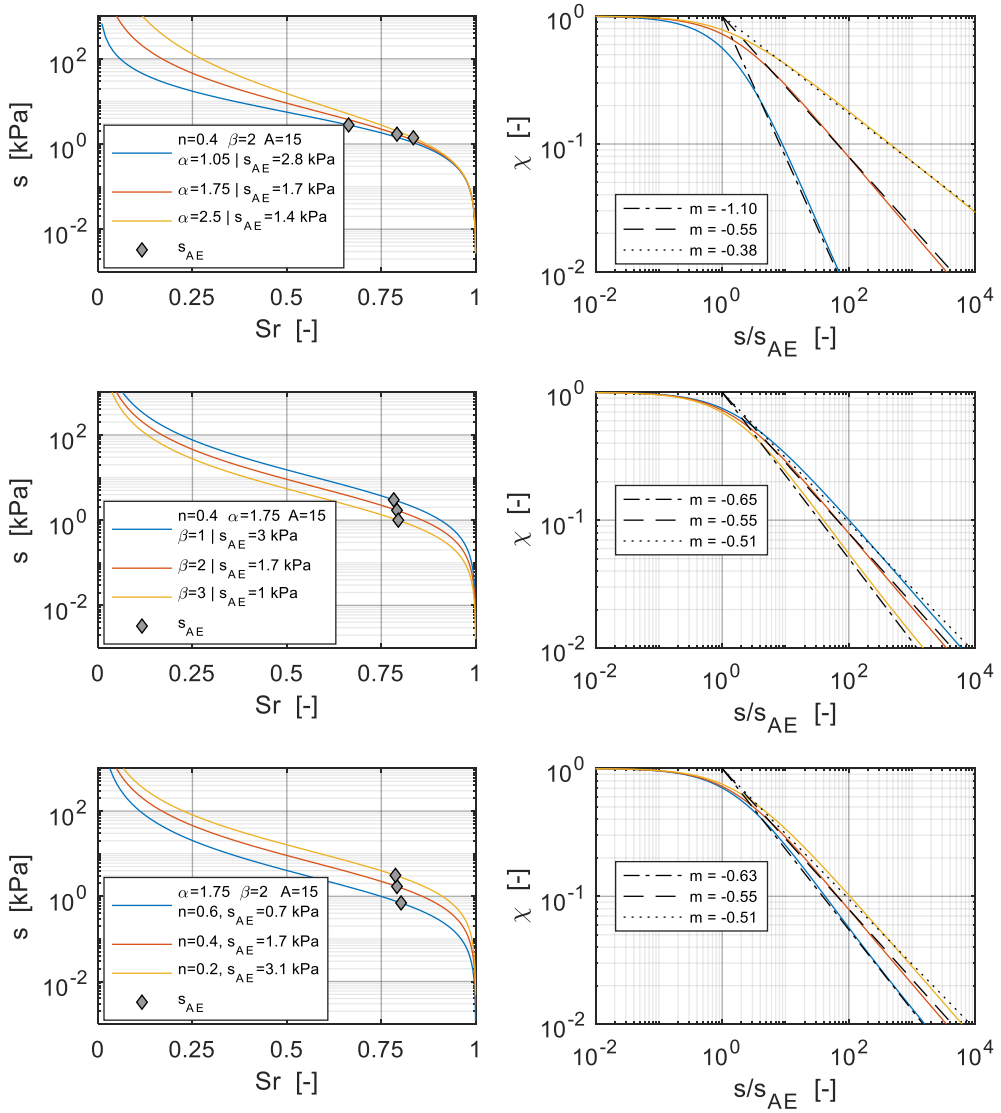

Figure 2.38: The effect of α, β and n on the soil-water retention curve (SWRC) and on χ (colored lines) and (2.26) for χ, fitted to the results of (2.25) for χ (black lines)

Note that in a double-logarithmic scale, the equation proposed by Khalili and Khabbaz (1998),

$$\chi = \begin{cases} 1 & \text{for } s \leq s_{AE} \\ \left(\frac{s}{s_{AE}}\right)^{m} & \text{for } s > s_{AE} \end{cases}, \tag{2.26}$$

can also approximate the evolution of χ with $s/s_{AE,} > 1$ as given by (2.25). Equation (2.26) was therefore fitted to these curves by choosing a proper value for the exponent m while using the air entry values of the respective SWRCs shown in Figure 2.38. The resulting evolutions of the state variable χ are depicted in Figure 2.38 as black lines. It can be seen that the constants $\alpha = 1.75$, $\beta = 2$ and $n = 0.4$ are appropriate to approximate the exponent $m = -0.55$ proposed by Khalili and Khabbaz (1998). However, higher or lower values of m are required for other shapes of the SWRCs, also shown in the figure. For suctions below the air entry value s_{AE} ($s/s_{AE} \leq 1$), Khalili and Khabbaz (1998) assume saturated conditions with $\chi = 1$. Therefore, in the range of small suction ratios ($\chi < 1$ for $s/s_{AE} \leq 1$), the results from (2.25) deviate slightly from those of (2.26).

Note that the air entry values s_{AE} may be estimated from the SWRCs by drawing two tangents to them (cf. Figure 2.6). This procedure naturally involved some uncertainties in the determination of s_{AE}. To calculate the suction ratios s/s_{AE}, the air entry values were therefore selected such that the asymptotes of the resulting curves from (2.25) went approximately through $\chi = 1$ at $s/s_{AE} = 1$. The values obtained for s_{AE} were considered appropriate (cf. Figure 2.38).

Because of the associated simple definition of the SWRC, (2.25) cannot account for all possible shapes of SWRCs (e.g., those including double porosity). Thus, this equation may be regarded as a simplified illustrative approach to the effective stress concept. In view of the above, although simple, Khalili's expression (2.26) appears to be appropriate to describe the evolution of χ with suction. For this purpose, the exponent m has to be regarded as a variable that mainly depends on the shape of the SWRC.

Note that the values of the exponent m for granular soils with fines are examined in more detail in Chapter 3.

2.6 Hydraulic performance of traffic embankments

As presented in the previous chapters the shear strength of unsaturated soils depends on the water content and suction. Within traffic embankments, the distribution of the water content and suction depends on the temporally fluctuating environmental influences, such as weather and climate. During precipitation, the rainwater infiltrates the embankment or runs off the surface of the embankment slopes. In addition, depending on the climatic conditions and vegetation, water is extracted from the embankment by evaporation and transpiration of the plants (Birle 2011).

In the embankment material, water is moved in both liquid and gaseous phases. Hydraulic and temperature gradients are the main causes of water movement in the liquid phase, while water movement in the gaseous phase results from humidity and temperature gradients. However, from studies on the hydraulic performance of embankments, it appeared that the climatically influenced layer has limited thickness. The underlying zone exhibits an approximately constant distribution of the water content and suction and is independent of the climatic conditions (Lu and Likos 2004).

For example, Bilz and Vieweg (1993) report the results of an investigation on the hydraulic performance of two embankments in Berlin, Germany. For both embankments, the influence of the groundwater and vegetation on the water content variation was negligible. The test embankments consisted mainly of sands with various amounts of fines, the grain size distributions of which are shown in Figure 2.39 (shaded area).

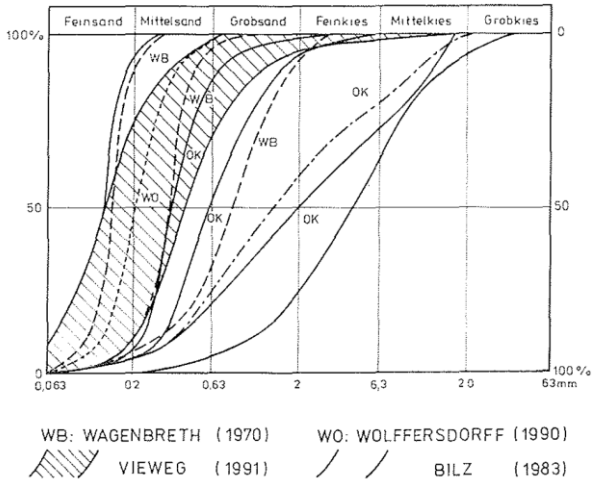

Figure 2.39: Grain size distributions of the sands in the tested embankments (shaded area), from Bilz and Vieweg (1993)

The measured variations in water content corresponded to precipitation, whereby a phase shift could be detected, increasing with depth. Pronounced changes in water content were observed only up to depths of about 40 cm to 60 cm. Absolute dehydration was not detected. Based on their results, Bilz and Vieweg (1993) divided the near-surface soil of the embankments into three zones (Figure 2.40).

In the variable saturation zone of up to approx. 40 cm, there were pronounced fluctuations in the degree of saturation of a maximum of about ΔSr = 14%. In the quasi-constant saturation range from approximately 80 cm downwards, the degree of saturation fluctuated by only about ΔSr = 7% to ΔSr = 9%. Between the variable saturation range and the quasi-constant saturation zone a 40 cm thick transition zone was formed.

Similar results for the hydraulic performance of embankments were found for various soils and climate conditions (e.g.: Delage et al. 2008; Cui & Delage 2009; Yao et al. 2016). In all cases, the layer that was climatically significantly influenced did not exceed approximately 1 m.

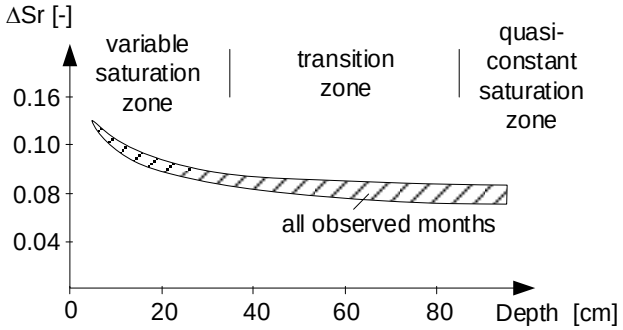

Figure 2.40: Depth-dependent changes in degree of saturation, from Bilz and Vieweg (1993)

The investigation of Bilz and Vieweg (1993), among others, reveals the potential of unsaturated soil mechanics in analyzing the slope stability of traffic embankments of silty sands. Once the distribution of the degree of saturation and suction within an embankment is known, invariable additional shear strengths may be applied to the embankment core, according to the hydraulic state. In the near-surface zone, where significant changes in water content are expected, the shear strength of the soils in saturated conditions should be applied.

3 Suction-induced effective stress in unsaturated silty sands from the literature

3.1 General remarks

To assess the magnitude of the suction-induced effective stress in silty sands, the results from shear tests on various soils published in the literature are re-evaluated within the framework of Bishop's effective stress concept in this chapter. Due to its simplicity and adaptability to the experimental results, Kahlili's expression (2.26) is used to describe the state variable χ (Section 2.5.3).

Based on a comprehensive study of shear strength data of 14 soils from the literature, ranging from clays to clayey sands, Khalili and Khabbaz (1998) proposed a value for m in (2.26). To derive χ, they used (3.1) by assuming constant saturated-drained shear strength parameters φ' and c' = 0 kPa.

$$\chi = \frac{\tau_{unsat} - \tau_{sat}}{s \cdot \tan \varphi'} \tag{3.1}$$

Figure 3.1 shows χ for some of the soils as a function of the suction ratio s/s_{AE}. Khalili and Khabbaz (1998) found that up to the limiting suction ratio $s/s_{AE} < 25$, a mean value of m = −0.55 fitted all test results sufficiently well (Figure 3.1).

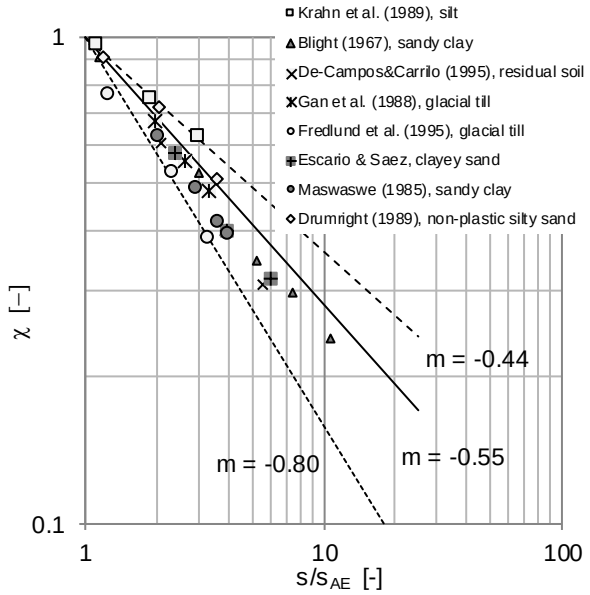

Figure 3.1: Measured and predicted state variable χ using different values of exponent m in (2.26) vs. suction ratio s/s_{AE}, data from Khalili and Khabbaz (1998)

The derivation of exponent m = −0.55 was based on the assumption of a constant air entry value s_{AE} of the samples corresponding to their initial state. Changes in the air entry value due to microstructural or density changes during the test were not accounted for. Khalili and Khabbaz (1998) further noted that they could not always use data from the critical state, affecting the derivation of χ, since the assumption of suction-independent shear strength parameters can be rendered obsolete.

Despite the above-mentioned limitations, the exponent m = −0.55 has proven appropriate to describe the suction-induced effective stress in many fine-grained soils. From Figure 3.1, however, the value of the exponent follows to range from m = −0.44 for clayey soils up to m = −0.80 for clayey sands. Thus, the results from Khalili and Khabbaz (1998) also hint at a dependency of exponent m on the soil type.

Note also that the state variable χ may have further dependencies (e.g., on mineralogy or microstructure). The finding that χ depends on soil type can thus be regarded only as provisional, since it does not regard any other influences. In their study, Khalili and Khabbaz (1998) used soils having more than 17% fines. Clean sands and sands with smaller fines content were not included. In addition, data for silty soils were rare. The exponent m for such soils is thus explored in the following.

3.2 Data from Donald (1956)

The unsaturated shear strength of the four silty soils already shown in Figure 2.25 (Donald 1956) are re-evaluated in the framework of Khalili's definition of the state variable χ.

Donald (1956) derived the evolution of the suction-induced effective stress with suction from shear test data. However, since the procedure of data processing is not properly detailed in his paper, the derivation of the suction-induced effective stress will be again carried out in the following.

As described in Section 2.4.2, it is known that for suctions less than the air entry value ($s < s_{AE}$), the shear strength linearly increases according to $\Delta\tau = \tan\varphi' \cdot s$. Therefore, the friction angles of the four silty soils can be derived from the linear part of the increase in the shear strength with increasing suction (Figure 2.25). The results are shown in Table 3.1. Note that Donald (1956) conducted the shear tests on loose samples in order to minimize the effect of dilatancy on the shear strength. It is therefore assumed that the friction angles do not change with increasing suction.

Using the friction angles in Table 3.1, the suction-induced effective stress is obtained from the shear strength in Figure 2.25 as follows:

$$\Delta\sigma' = \frac{\tau_{unsat} - \tau_{sat}}{\tan\varphi'}. \tag{3.2}$$

The results are shown in Figure 3.2a as a function of the applied suction. The state variable χ was deduced from

$$\chi = \frac{\Delta\sigma'}{s}, \tag{3.3}$$

where s is the initial suction according to the SWRCs shown in Figure 2.25b.

Figure 3.2b shows the state variable χ for the four soils as a function of the suction ratio s/s_{AE} in a double-logarithmic scale. Note that the air entry values s_{AE} applied to the samples and summarized in Table 3.1 were derived from the SWRCs shown in Figure 2.25b.

Soil name	BS	GF	MF	FF
Friction angle φ'	30.3°	32.6°	39.9°	33.0°
Air entry value s_{AE}	18 kPa	7 kPa	11 kPa	7 kPa

Table 3.1: Friction angles φ' and air entry values s_{AE} of four silty soils, derived from data in Donald (1956)

Figure 3.2b reveals a linear increase in χ with an increasing suction ratio beginning at $s/s_{AE} \approx 1$. This behavior is in good agreement with the findings for various soils observed by Khalili and Khabbaz (1998). The adaption of (2.26) to the experimental results gives an exponent $m = -1.4$. This value is considerably smaller than the smallest value $m = -0.8$ derived from Figure 3.1, but fits the experimental data for the four soils remarkably well.

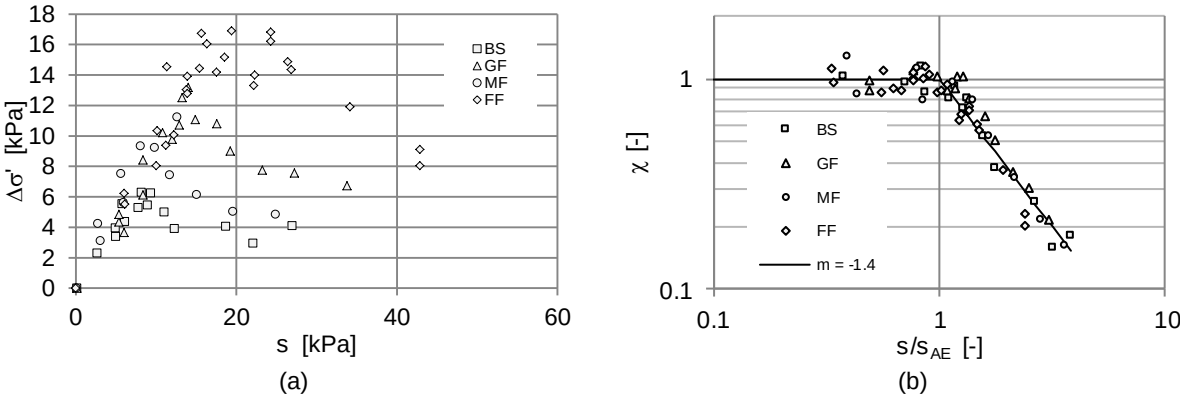

Figure 3.2: (a) Suction-induced effective stress $\Delta\sigma'$ vs. suction s. (b) Measured and predicted state variable χ for m = −1.4 vs. suction ratio s/s_{AE}

Figure 3.3a shows χ—described with (2.26) and m = −1.4—as a function of the degree of saturation corresponding to the SWRCs shown in Figure 2.25b. Figure 3.3b shows the according suction-induced effective stresses $\Delta\sigma' = \chi \cdot s$.

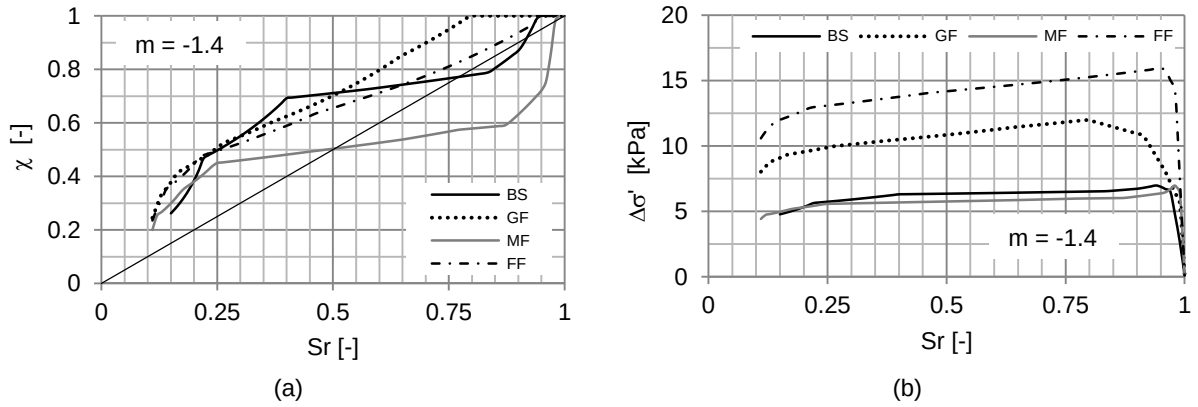

Figure 3.3: (a) State variable χ vs. degree of saturation Sr. (b) Predicted suction-induced effective stress $\Delta\sigma'$ for m = −1.4 vs. degree of saturation Sr

For the four silty soils, at low degrees of saturation, Figure 3.3b indicates that the suction-induced effective stress tends to drop toward zero. This range of low degrees of saturation appears to correspond to the residual zone of the SWRCs, where menisci between adjacent soil particles begin to vanish. For higher degrees of saturation, the suction-induced effective stress is shown to be approximately constant until it reaches the degree of saturation corresponding to the air entry value of the SWRCs. In accordance with the findings from Section 2.4.2, the suction-induced effective stress then approximately equals the suction with $\chi \approx 1$.

3.3 Data from Lu et al. (2009)

Lu et al. (2009) analyzed UTTs on as-compacted samples of a silty sand with about 10% fines. Samples were compacted at target water content to an initial void ratio of $e_0 = 0.82$. The authors interpreted the uniaxial tensile strength as being a shear strength at low effective stress. They derived the suction-induced effective stress from the measured tensile strength σ_t:

$$\Delta\sigma' = \frac{\sigma_t}{2 \cdot \tan\varphi' \cdot \tan(45° - \varphi'/2)} \tag{3.4}$$

For the small expected effective stress levels, Lu et al. (2009) assumed a peak friction angle of $\varphi' = 48°$.

The experimental results shown in Figure 3.4 reveal that the suction-induced effective stress was considerably constant over a wide range of degrees of saturation, ranging from Sr = 20% to Sr = 90%. For degrees of saturation less than Sr ≈ 20%, the suction-induced effective stress decreased, indicating a drop toward zero.

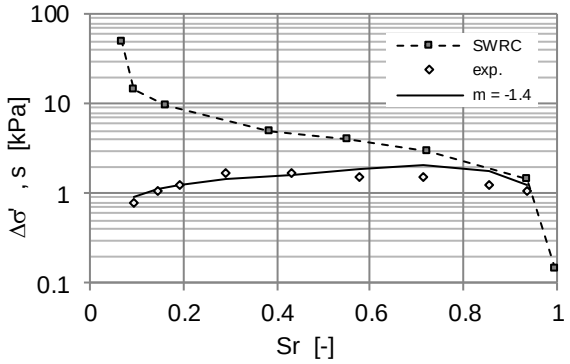

Figure 3.4: Measured and predicted suction-induced effective stress $\Delta\sigma' = \chi \cdot s$ for m = −1.4 vs. degree of saturation Sr of a silty sand and the corresponding SWRC, experimental data from Lu et al. (2009)

From the experimental data presented in Figure 3.4, the state variable χ can be derived with (3.3). Note that UTTs do not represent suction-controlled tests (Section 2.4.1.5). In order to derive χ, a constant suction corresponding to the initial value had to be assumed for all tests. The suction was therefore estimated from the SWRC (Figure 3.4).

In Figure 3.5a, the resulting χ is plotted against the suction ratio s/s_{AE}. The air entry value $s_{AE} = 2.2$ kPa applied to the silty sand was derived from the SWRC in Figure 3.4. Figure 3.5b shows χ as a function of the degree of saturation.

Figure 3.5a shows that in a double-logarithmic scale, χ exhibits an approximately linear trend with increasing suction ratio. Fitting (2.26) to the experimental results leads to an exponent of m = −1.4. This exponent corresponds to the exponent m = −1.4 deduced from the test results presented in Donald (1956). It appears appropriate to reproduce the experimental results for the suction-induced effective stress $\Delta\sigma'$, especially at degrees of saturation Sr < 0.5 (Figure

3.4). At degrees of saturation Sr ≥ 0.5, the predicted χ is higher than that of the experimental results (Figure 3.5). However, due to the small suctions at high degrees of saturation, a variation in χ does not cause a significant variation in $\Delta\sigma$'. Therefore, the suction-induced effective stress is only slightly overestimated (Figure 3.4).

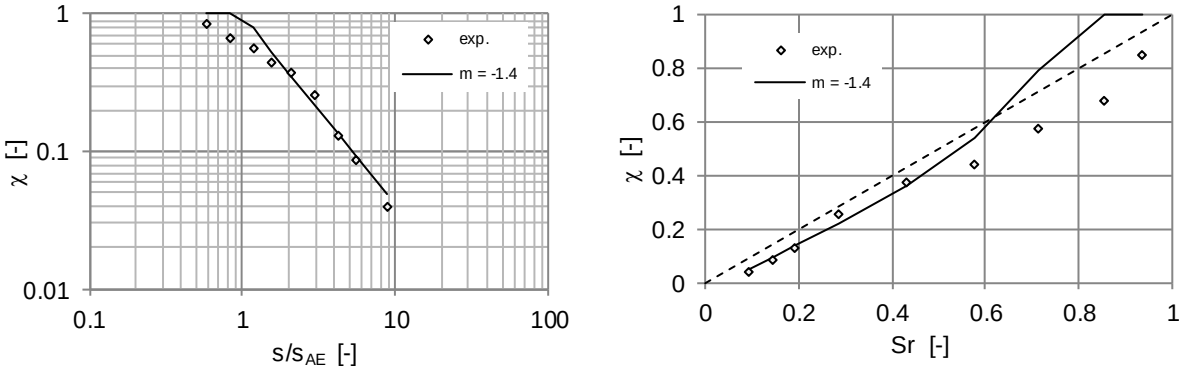

Figure 3.5: (a) Measured and predicted χ vs. suction ratio s/s_{AE}. (b) Measured and predicted χ vs. degree of saturation Sr for silty sand for m = −1.4, experimental data derived from Lu et al. (2009)

In this context, note that the derivation of χ from the experimental results exhibits some uncertainties, listed below:

- At high degrees of saturation, the assumption of constant suction is questionable, as suction tends to change during the test (Section 2.4.1.5). This assumption may therefore influence the above derivation of χ in this range of degrees of saturation.
- The suction is derived from the SWRC shown in Figure 3.4. Due to the different water content at which the samples were compacted for the uniaxial tests, it is possible that the microstructure and thus the corresponding SWRC changed between the tests. Therefore, the suction taken from Figure 3.4 may not be representative for all data, which may affect the test evaluation.
- Lu et al. (2009) used a constant peak friction angle of $\varphi' = 48°$ to derive the suction-induced effective stress shown in Figure 3.4, while neglecting the dependency of the friction angle on suction (Section 2.4.3). The above evaluation of χ may therefore be influenced by the assumption of the constant friction angle.

Despite these shortcomings, the expression derived from the experimental data for the state variable χ was suitable to sufficiently reproduce the measured suction-induced effective stress over the entire range of degrees of saturation. The exponent m = −1.4 may, therefore, be regarded as reference value for the investigated silty sand.

3.4 Data from Schnellmann et al. (2013)

Following (3.2), the friction angle must be known in order to derive the suction-induced effective stress from the shear strength. Notably, with respect to peak states, the friction angle depends on dilatancy, which is influenced by suction. Since both the suction-induced effective stress and the friction angle depend therefore on the suction, they can no longer be regarded as independent of each other (cf. Figure 2.36). In order to demonstrate the consequences of this interrelation, the experimental results of Schnellmann et al. (2013) already presented in Section 2.4.2 are here re-evaluated in the framework of Bishop's effective stress concept.

Figure 3.6a shows the peak shear strength of the unsaturated samples plotted against the net normal stress for all tested suctions. In addition, the failure criterion for saturated conditions is depicted in the figure as a dotted line.

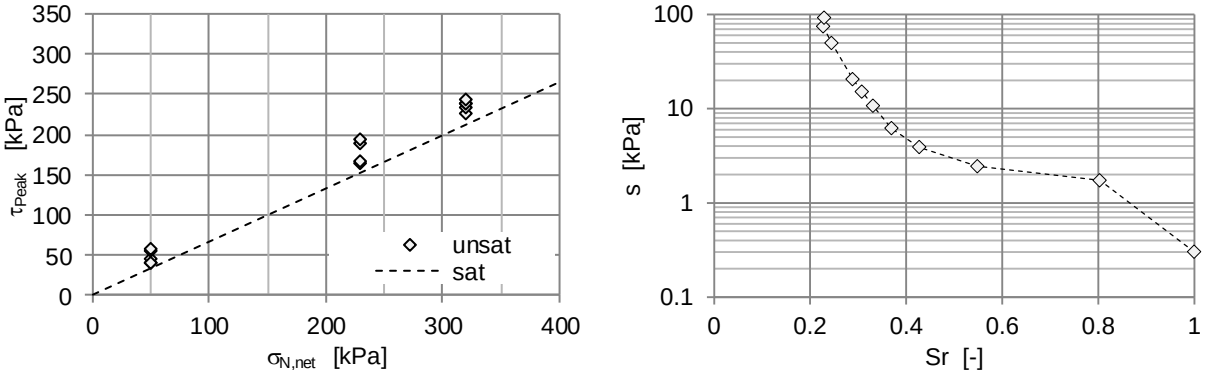

Figure 3.6: (a) Peak shear strength τ_{Peak} in the σ_{net} - τ plane and (b) soil-water retention curve (SWRC) of the silty sand, data from Schnellmann et al. (2013)

Since the peak friction angle and the suction-induced effective stress depend on each other, an assumption had to be made about Bishop's state variable χ, for instance by using (2.26) and defining an appropriate exponent m. For this purpose, three arbitrary values were assigned to the exponent m (−0.35, −0.55, and −1.05). One of the values represents Khalili's approach (m = −0.55), while the other two—according to the provisional findings of m's dependency on soil type, in Sections 3.1 through 3.3—may be regarded as being representative values for fine-grained (m = −0.35) and coarse-grained soils (m = −1.05). The air entry value s_{AE} = 1.5 kPa was derived from the SWRC shown again in Figure 3.6b.

Depending on the exponent m, the peak friction angle was derived from the following:

$$\varphi' = \arctan \frac{\tau_{peak}}{\sigma_{N,net} + \left(\frac{s}{s_{AE}}\right)^{m} \cdot s} \tag{3.5}$$

Figure 3.7a shows the evolution of χ as a function of the degree of saturation for the three examined exponents m (−0.35, −0.55, and −1.05). In Figure 3.7b, the corresponding suction-induced effective stress $\Delta\sigma' = \chi \cdot s$ is depicted.

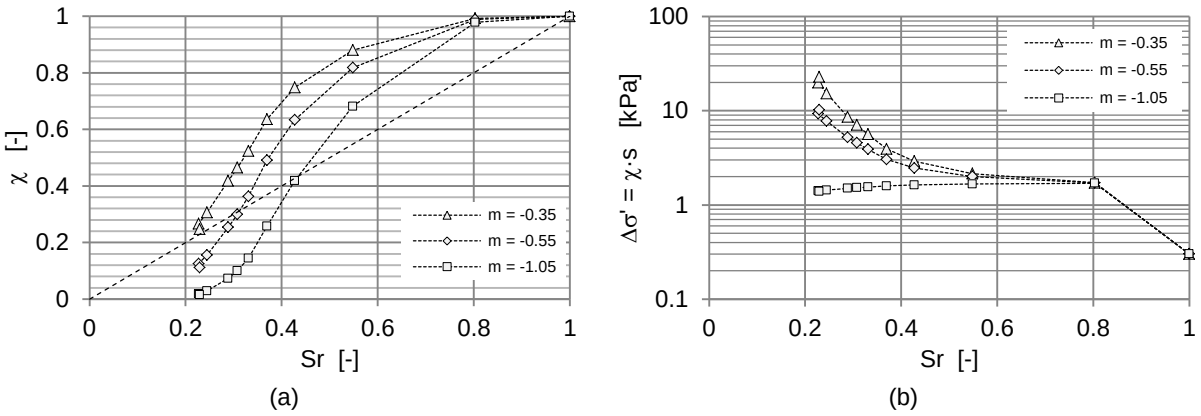

Figure 3.7: (a) Predicted state variable χ vs. degree of saturation Sr, (b) Predicted effective stress $\Delta\sigma$' vs. degree of saturation Sr of a silty sand for different values of m, derived from Schnellmann et al. (2013)

Figure 3.8 shows the peak shear strength in the σ_N' - τ - plane, which results from the respective definitions of χ.

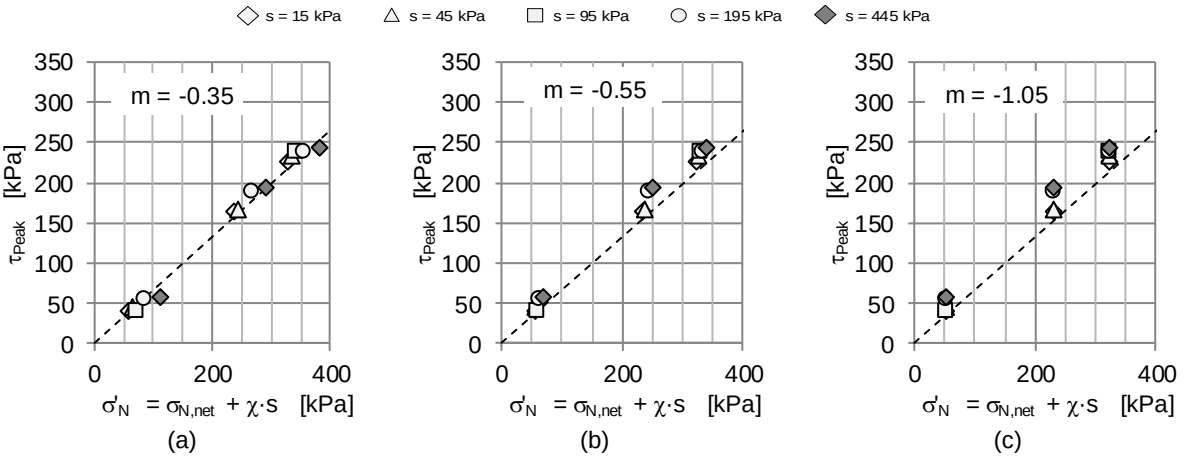

Figure 3.8: Peak shear strength τ_{Peak} of the silty sand in the σ_N' - τ plane for (a) m = −0.35, (b) m = −0.55, and (c) m = −1.05

In Figure 3.9, the peak friction angles derived from (3.5) are shown as a function of suction and effective stress, respectively.

Over the entire range of the degree of saturation, $\Delta\sigma$' is the highest for m = −0.35 (Figure 3.7b). Therefore, this value leads to the largest shift of the peak shear strength toward the saturated failure criterion in the σ_N' - τ plane (Figure 3.8) resuting in no increase in peak friction angle with increasing suction. Accordingly, the peak friction angle is independent of the effective stress (Figure 3.9a right). Note that both figures show a pronounced scattering of the peak friction angle, which results- in friction angles smaller than the saturated friction angle.

Figure 3.7b shows that the suction-induced effective stress $\Delta\sigma$' resulting from m = −0.55 is generally less than $\Delta\sigma$' resulting from m = −0.35. Therefore, in the τ - σ' - plane, the peak

shear strengths are shifted less toward the saturated failure criterion (Figure 3.8b). Thus, the associated peak friction angles are higher than that of m = −0.35 (Figure 3.9b left). The friction angles reach a maximum at s = 198 kPa and tend to decrease at the highest measured suction for each net normal stress (Figure 3.9b left). Figure 3.9b (right) shows that the peak friction angles decrease with increasing effective stress.

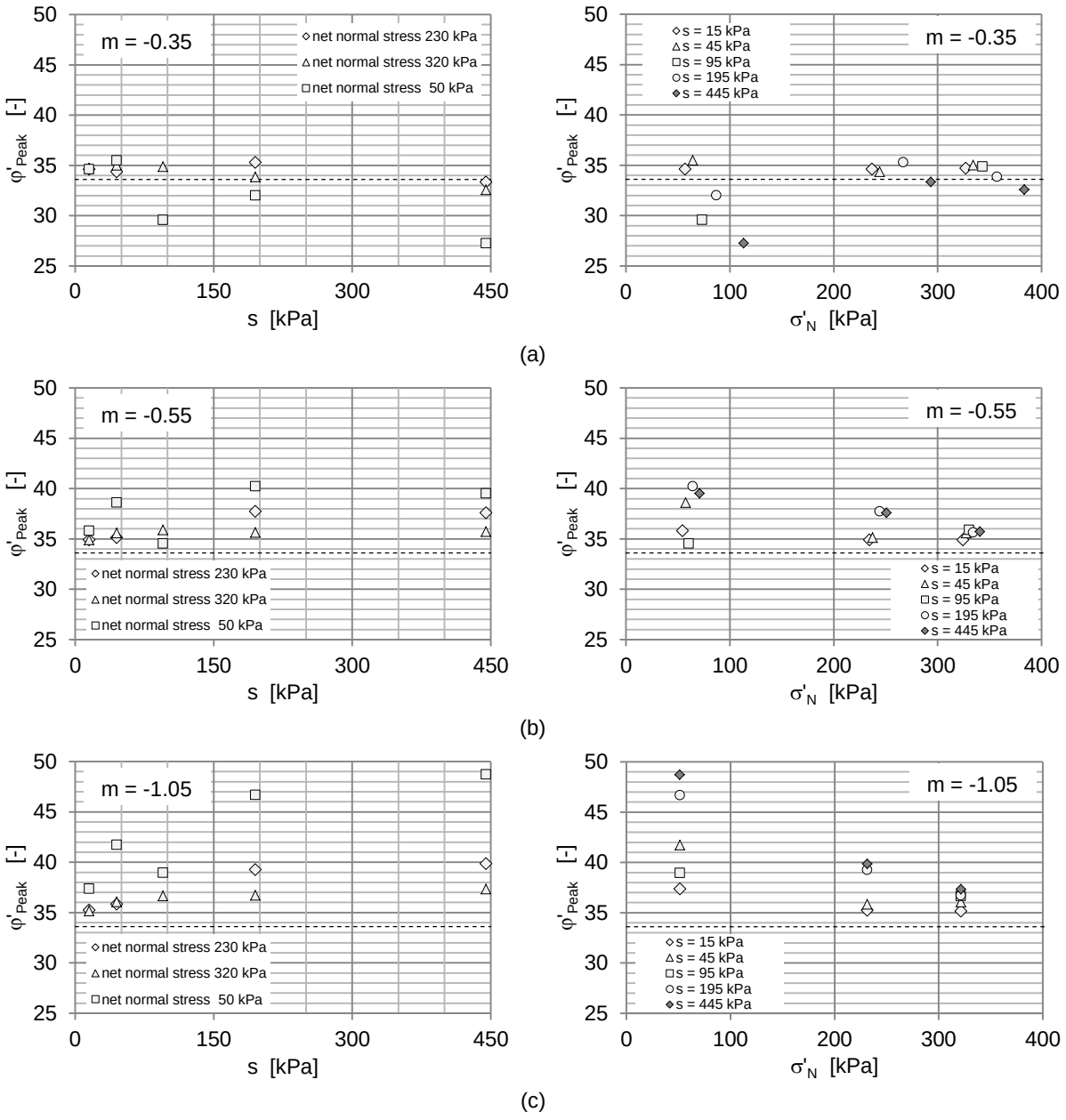

Figure 3.9: Secant peak friction angle φ'_{peak} vs. suction s and vs. effective stress, for (a) m = −0.35, for (b) m = −0.55, and for (c) m = −1.05. The dashed lines represent the effective friction angle $\varphi'_{sat} \approx 34°$ for saturated states (c' = 0)

The suction-induced effective stress is the lowest for m = −1.05 and drops toward zero at low degrees of saturation (Figure 3.7b). Therefore, in the τ - σ' - plane, the peak shear strengths

are shifted least toward the saturated failure criterion (Figure 3.8c). Figure 3.9c shows the corresponding peak friction angles. Compared to those derived with exponents m = −0.35 and m = −0.55, they are the highest. The friction angles gradually increase with increasing suction (Figure 3.9c, left) and decreasing effective stress (Figure 3.9c, right).

According to the well-known behavior of granular soils, the friction angle increases, as the rate of dilatancy increases. For the examined silty sand, the rate of dilatancy gradually increases with increasing suction (Figure 3.10).

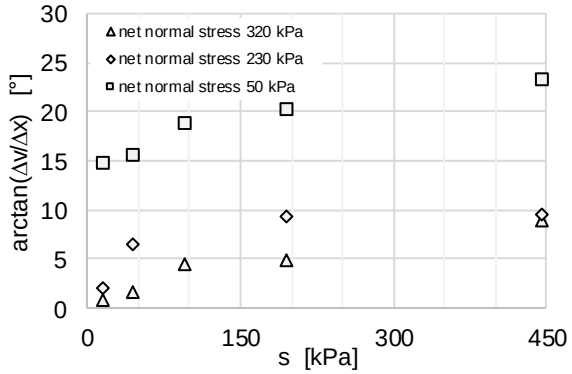

Figure 3.10: Maximum rate of dilatancy, data from Schnellmann et al. (2013)

Accordingly, the peak friction angle of the soil can be expected to increase gradually with increasing suction. From the three exponents examined above, this expectation could only be fulfilled by the application of m = −1.05, which, in accordance to the measured rate of dilatancy, resulted in a gradually increasing peak friction angle with increasing suction. In contrast, the exponent m = −0.35 yielded a suction-independent friction angle with large scatter resulting in unrealistic small friction angles (i.e., smaller than the saturated friction angle), while the exponent m = −0.55 indicated a maximum friction angle at a suction of s = 198 kPa with a subsequent decrease at higher suctions. Neither result agrees with the evolution of the dilatancy with suction in Figure 3.10.

In addition, the decrease in the suction-induced effective stress at low water content for m = −1.05 may be interpreted as a realistic approach for the silty sand, although the value remains arbitrary and may not be exactly accurate. This interpretation applies in particular to soils with aggregates, in which the soil-water can retreat at low water content, causing the suction-induced effective stress to break down. In this context, note that the samples examined in Schnellmann et al. (2013) were prepared by being compacted on the dry side of Proctor optimum. Aggregated structures can therefore be presumed.

Also, note that in order to reproduce the disappearance of the suction-induced effective stress in granular soils at low water content (high suctions), (3.7) requires an exponent of m < −1.0, as shown in the following:

$$\lim_{s\to\infty} \chi \cdot s = \lim_{s\to\infty} \left[\left(\frac{s}{s_{AE}}\right)^{m} \cdot s\right] = \lim_{s\to\infty} \frac{s^{1+m}}{s_{AE}^{m}} = \begin{cases} \infty & \text{for } m > -1.0 \\ s_{AE} & \text{for } m = -1.0. \\ 0 & \text{for } m < -1.0 \end{cases} \tag{3.6}$$

Although the exact value of m cannot be derived from the experiments, it can be concluded that, on the one hand, the peak shear strength of the silty sand with aggregated fines is significantly influenced by the increased dilatancy caused by the initial microstructure and suction. On the other hand, the peak shear strength is influenced to a small extent by the suction-induced effective stress, according to the small values of $\Delta\sigma'$ for m = −1.05, which led to the most realistic results.

3.5 Conclusions

In view of the above, Khalili's definition of Bishop's state variable,

$$\chi = \left(\frac{s}{s_{AE}}\right)^{m}, \tag{3.7}$$

proved to be an appropriate approach to describe the suction-induced effective stress in unsaturated silty sands. The evaluation of experimental results from the literature suggested a dependency of the value of exponent m in (3.7) on the soil type and thus on the shape of the SWRC, confirming the findings from Section 2.4.3. For the soils examined in this chapter, the values ranged from m = −0.8 for glacial till to m = −1.4 for silts and silty sands.

Note that independent of the above investigations, an exponent of m = −1 was reported by Russell (2004) for Krunell sand for suction ratios $s/s_{AE} > 25$. Also, Aitchison (1985) noted that m = −1 may be a reasonable approach to determine the state variable of granular soil.

When compared to the findings of Khalili and Khabbaz (1998), the exponent m for granular soils (with fines) is generally smaller than the exponent m for fine-grained soils. According to Jiang et al. (2017), this may be caused, on the one hand, by the flatter course of the SWRC of granular soils in the transition zone, which results in smaller values of exponent m (Section 2.5.3). The findings of Jiang et al. (2017) also indicate, on the other hand, that in a semi-logarithmic scale, the dependency of χ on the suction ratio s/s_{AE} may be non-linear at small suction ratios. Since—especially in shear tests on cohesive soils—the suction exerted on the samples usually correlates with the transition zone of the SWRC corresponding to relatively small suction ratios, the linear branch of the relationship for χ may not be reached in these tests. The linearization of the non-linear course of χ may therefore result in smaller values for the exponent m.

In the evaluation of shear tests on unsaturated soils, the definition of the state variable χ has a strong influence on the determination of the failure criterion from peak states due to the dual effect of suction. When applying Bishop's effective stress concept, both the suction-induced effective stress and the peak friction angle depend on the suction and the description of χ. Therefore, the influence of the initial microstructure, in particular that of aggregates in compacted granular soils with fines, on dilatancy and thus on the peak shear strength should be considered in the interpretation of the test results. In fact, stronger dilatancy in such soils seems to affect the peak shear strength much more than the suction-induced effective stress, which may generally be expected to be low. Therefore, if χ is not properly defined, the test evaluation may lead to misinterpretation of the shear strength, especially if the failure criterion is to be investigated. In the literature, however, no method has been proposed to distinguish experimentally between the effect of suction on effective stress and dilatancy. This absence is addressed in more detail in Chapter 5.

4 Exploratory drilling on a railway embankment from the early 1900's

4.1 General remarks

The goal of the exploratory drilling was to assess the *in situ* conditions of the material in a typical old traffic embankment. The *in situ* conditions comprise the hydraulic properties (i.e., the distribution of water content and suction), soil types and densities. The study provides a momentary picture, in particular of the hydraulic properties, which may change over the long-term due to climatic influences. According to Section 2.6, however, it is expected that these will only affect the hydraulic properties of the soils in the upper near-surface part of the embankment (less than 1 m below the surface).

4.2 Sampling

In order to find a suitable embankment, different sites were investigated with regard to the height, slope inclination and expected soil types. A further prerequisite was that it had to be possible to block the traffic on the envisaged track during the sampling period, enabling access to the embankment for the drilling rig (Figure 4.1).

Figure 4.1: Drilling rig on the traffic embankment *(*named *Neißedamm),* Eastern Germany

Based on the above pre-conditions, a railway embankment (*Neißedamm*) of height 8 m to 9 m, with an inclination of 1:1.4 near the town Horka at the German-Polish border was selected. The dimensions and location of the embankment represented the desired worst-case conditions with respect to embankment stability.

Exploratory drilling was implemented during the closure of the railway track, as it was expanded to two tracks. For the tests, two cross sections were selected in which percussive core drilling of diameter 146 mm under dry conditions was implemented, a drilling at the crest of the slope and one at the middle of the embankment (boreholes KB 1 to KB 4 in Figure 4.2). The boreholes were uncased apart from the upper 1 m to 2 m, since in the first meter of drilling, mainly railroad ballast was encountered (Figure 4.3).

Two undisturbed samples of approximately 12 cm diameter and 26 cm height were taken every meter through a dynamically driven thick-walled liner. From a depth of six meters to a maximum of about 9 m, only one undisturbed sample was taken each meter. Due to the unsaturated conditions, the soils predominantly exhibited a cohesive-like behavior. Therefore, sampling class A and quality class 2 were achieved, according to DIN EN ISO 22475-1:2006. Between the undisturbed samples, disturbed samples were taken, resulting in 43 undisturbed and 51 disturbed samples from the four boreholes. The liners of the undisturbed samples were closed with a plastic lid, labelled and sealed with adhesive tape (Figure 4.4). The disturbed samples were then labelled and stored in such a way as to prevent the loss of water.

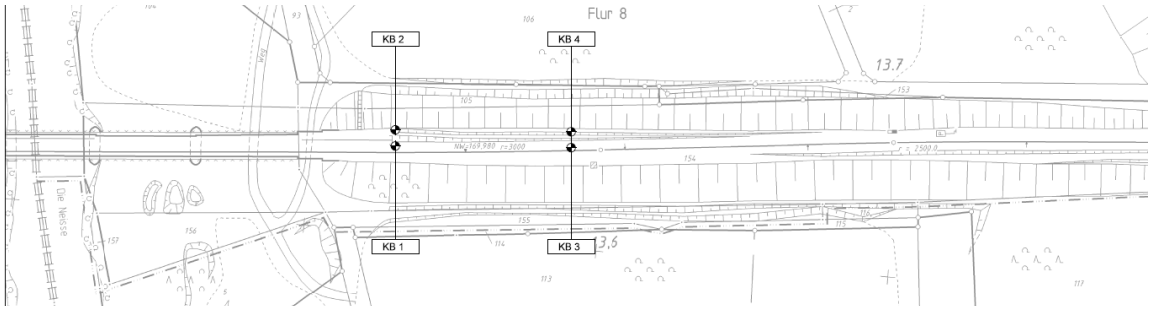

Figure 4.2: Location and labelling of the four percussion core drillings on the *Neißedamm* at coordinates: 51°17'09.9"N 15°01'46.8"E

Figure 4.3: Core samples from the first two meters of the borehole KB 1

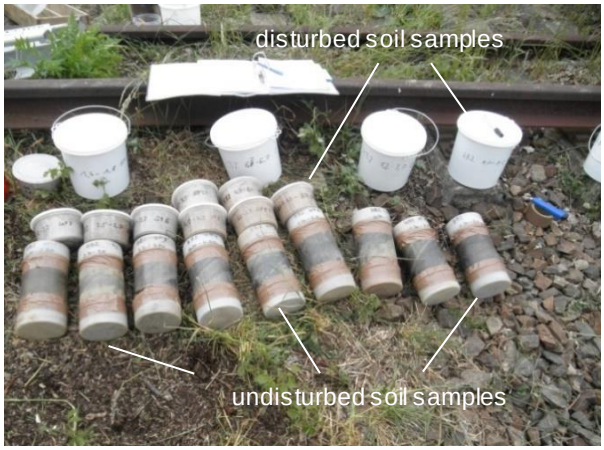

Figure 4.4: Disturbed and undisturbed soil samples, *Neißedamm*

4.3 Experimental investigations

4.3.1 Disturbed samples from boreholes KB 1 to KB 4

The disturbed samples were examined for the grain size distribution and water content, in accordance with DIN EN ISO 17892-4 and DIN EN ISO 17892-1, respectively.

4.3.2 Undisturbed samples

The undisturbed samples were examined for water content, suction, dry density (DIN EN ISO 17892-2) and particle (specific) density (DIN EN ISO 17892-3).

The suction measurements were performed by means of T5 tensiometers (Figure 4.5) from the German company UMS (Umweltanalystische Mess Systeme AG).

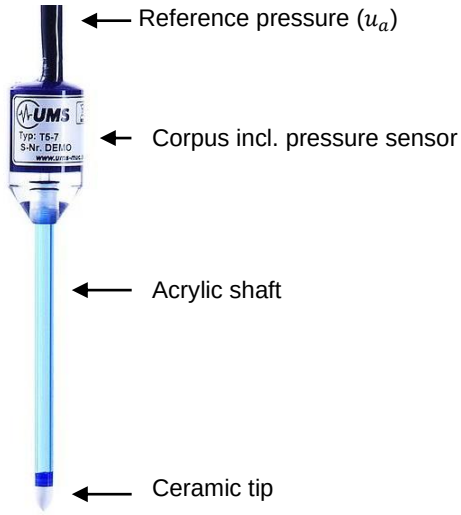

Figure 4.5: Tensiometer T5 (UMS GmbH Munich, 2009)

The tensiometers were calibrated and thoroughly filled with distilled and de-aired water, allowing for measurements of suctions of up to 150 kPa. Note that with this method, osmotic suction cannot be determined (cf. Section 2.1.3.1). According to Fredlund et al. (2012), however, no osmotic suction was expected for the encountered soils. During the suction measurements, the liners were stored in a climate chamber at a constant temperature of 20°C and RH of 60%.

4.3.2.1 Samples of borehole KB 1

For the undisturbed samples of the borehole KB 1, the ends of the liners were sealed with diffusion-tight foil and pre-drilled with a steel pin. Subsequently, the tensiometers were carefully inserted into the sample, and measurements began (Figure 4.6). Note that the liners were horizontally placed to minimize the effect of gravity on the measured suction (Figure

4.6). Up to three undisturbed samples were measured simultaneously over approximately one day.

After the suction measurement was completed, the corresponding water content and density were determined at both ends of the liners. For this purpose, defined soil volumes were pressed out of the liners at both ends. Note that the procedure of pressing-out was prone to errors, the most prominent are listed below.

- Whenever a sample exhibited a small fines content, the ends of the cylinder were unstable. To avoid disturbing the sample structure, the pressing process had to be carried out carefully. This process might have affected the suction measurements.
- Due to the irregular diameter of the liners, the extruded volumes were difficult to determine accurately.
- The extrusion of the soil resulted in a loading of the specimens' ends, which might have influenced the density.

Note that utmost care was taken when the samples were handled. With these precautions, it became obvious that the above effects had only a negligible influence on the results. However, to minimize the occurrence of the above-described uncertainties, an improved measurement method was applied, as described in the next section.

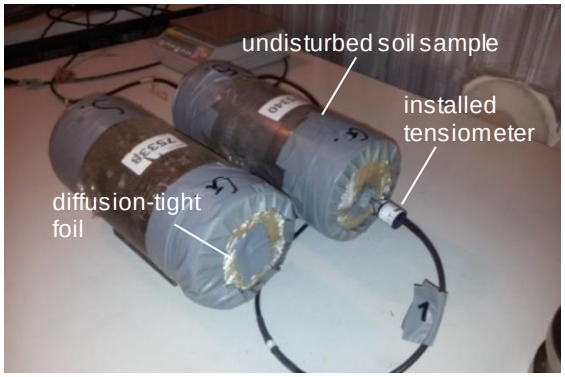

Figure 4.6: Testing setup for the samples from borehole KB 1

4.3.2.2 Samples of boreholes KB 2 to KB 4

The testing setup for the liners from the boreholes KB 2 to KB 4 is schematically shown in Figure 4.7a. For the tests, the cylinders were initially placed vertically. After the plastic lid was removed, 0.5 cm of the soil was carefully cut from the edges of the undisturbed samples before a cutting ring was centrically pressed into the sample (Figure 4.7b). Thereafter, the liner was sealed by a steel lid with a 0.5-cm-deep stamp, ensuring full contact with the specimen surface. The stamp supported the soil, while the liner was turned to the other side and the procedure was repeated. Subsequently, the sample was placed horizontally and carefully pre-drilled before the tensiometers were installed through the cable bushings and suction measurements were carried out (Figure 4.7c). The density and water content corresponding to the measured suctions were determined on the soil in the cutting rings,

which were carefully trimmed out after completion of the suction measurement. This procedure minimized the sample disturbance during testing.

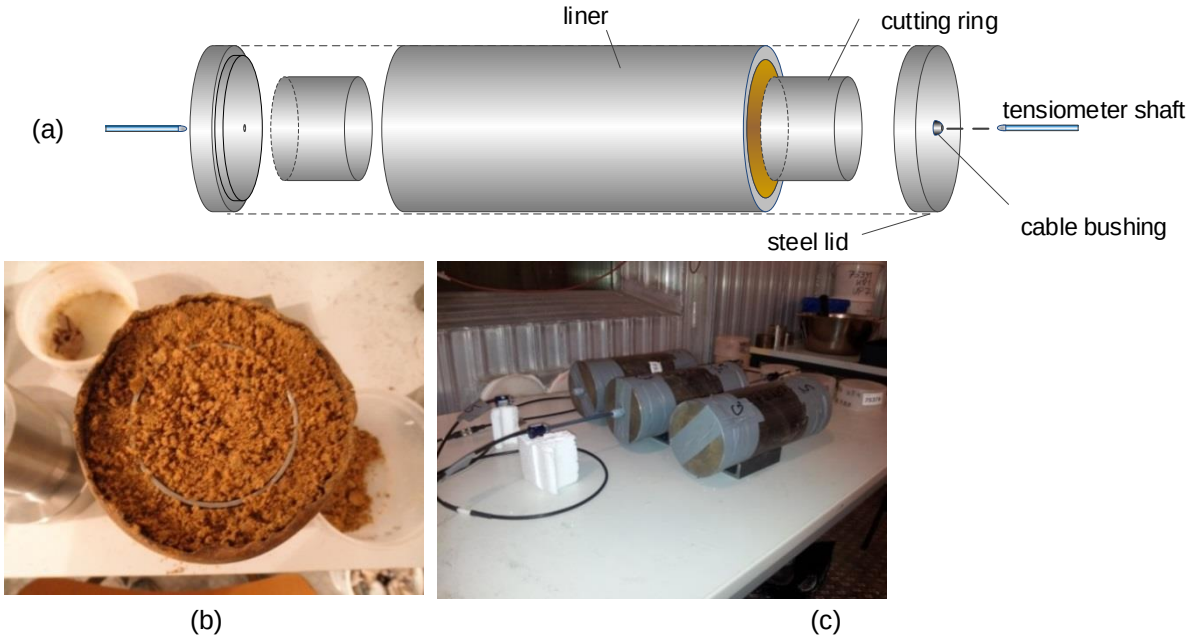

Figure 4.7: Testing setup for the liners from boreholes KB 2 to KB 4: (a) schematic, (b) installed cutting ring, (c) sealed liners with installed tensiometers

4.4 Test results

Figure 4.8 shows the grading curves of the disturbed samples from boreholes KB 1 to KB 4 and the distribution of fines content over the exploration depth.

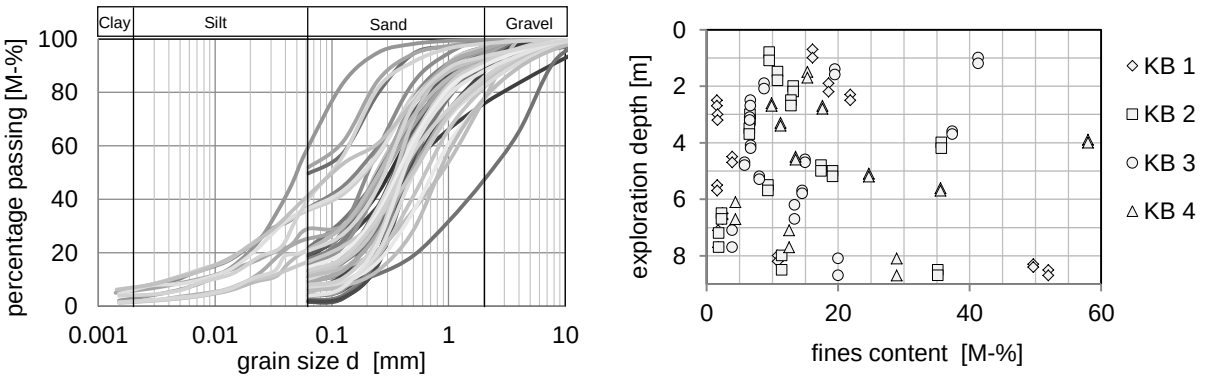

(a) (b)

Figure 4.8: (a) Grading curves, (b) distribution of fines content in borehole KB 1 to KB 4

The majority of the soils were gravelly medium-to-coarse sands with a fines content between 1.6% and 35.7%, some of which were observed to be in aggregated form. The fines fractions consisted mainly of silts with a minor fraction of clay (determined for soils exhibiting more than 15% fines). Occasionally, fine-grained soils with a fines content of about 50% to 60% were discovered. From a depth of approximately 8 m, sandy silts were detected with a fines content between 49.7% and 52.0%. These soils were considered part of the subsoil. Figure 4.9 demonstrates that the majority of the detected soils exhibited a fines content between 5% and 15%, with a mean value of 10.2%.

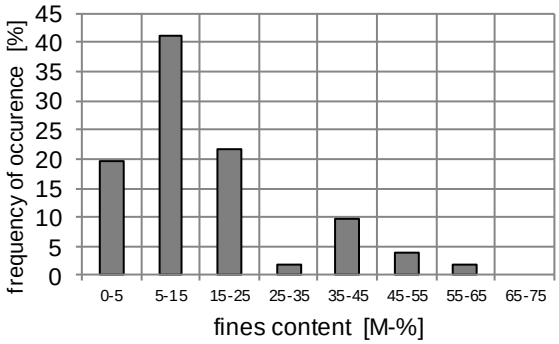

Figure 4.9: Frequency of occurrence of the fines content (borehole KB 1 to KB 4)

According to the frequency of occurrence (Figure 4.10), the void ratios determined at the ends of the liners ranged between approximately e = 0.35 and e = 0.75, while the majority showed values between e = 0.55 and e = 0.65. Given the empirical values and the low stress level in the embankment, these void ratios indicate medium-dense to dense soil states (Cudmani 2001).

Figure 4.11 shows the evolution of suction with the exploration depth and its frequency of occurrence. In general, the suction was observed to be relatively constant in the range

between s = 2.5 kPa and s = 7.5 kPa over the exploration depth, with a mean value of s = 4.5 kPa. Only a few values were relatively high, up to s = 60 kPa. These high suctions could be mainly attributed to soils with high fines content.

Figure 4.12 shows the water content for the exploration depth and that water content's frequency of occurrence. The detected water content was predominantly smaller than w = 10%, with some exceptions of very high water content. These high-water-content samples, however, could be mainly related to soils with high fines content, which were a minor portion of the total sample of soils. The majority of the water content was in the range of w = 2.5% to w = 7.5%, with a mean value of w = 4.5%.

Figure 4.13 shows the corresponding degree of saturation derived from the measured void ratio and gravimetric water content of the samples. The degree of saturation was generally low, with some exceptions for soils with high fines contents. The majority of the derived values ranged between Sr = 5% and Sr = 35%, with a mean value of Sr = 18.4%.

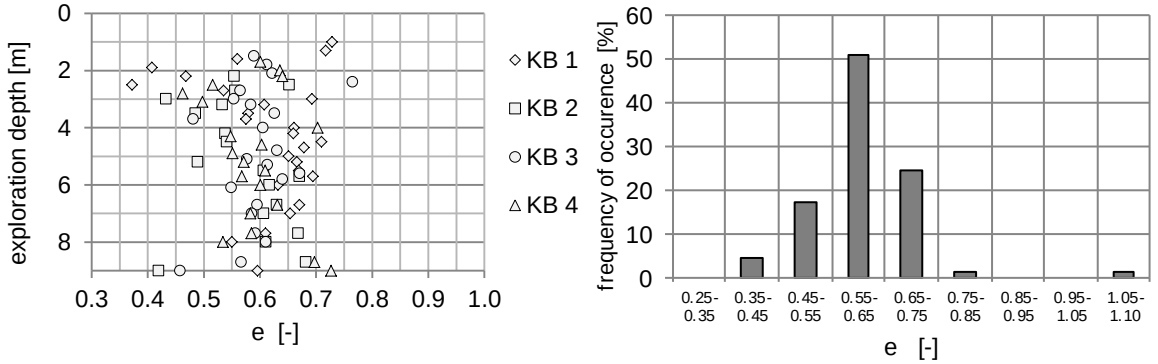

Figure 4.10: Distribution and frequency of occurrence of void ratio (borehole KB 1 to KB 4)

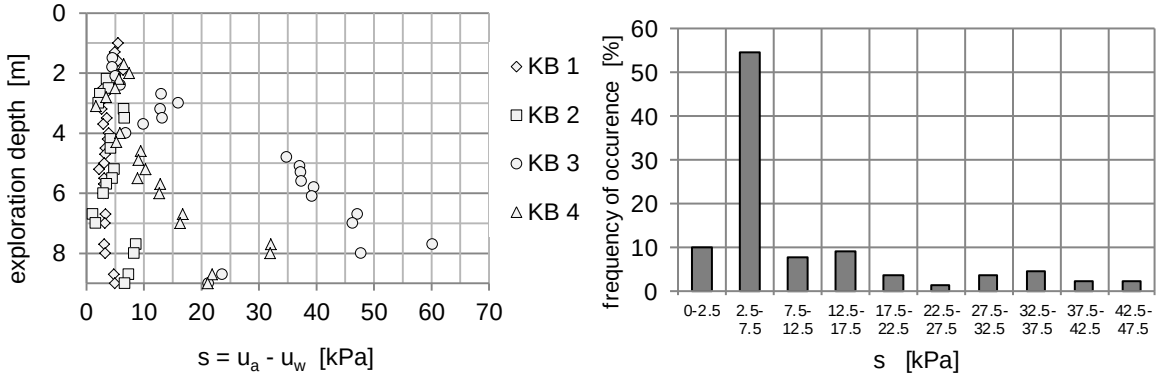

Figure 4.11: Distribution and frequency of occurrence of suction (borehole KB 1 to KB 4)

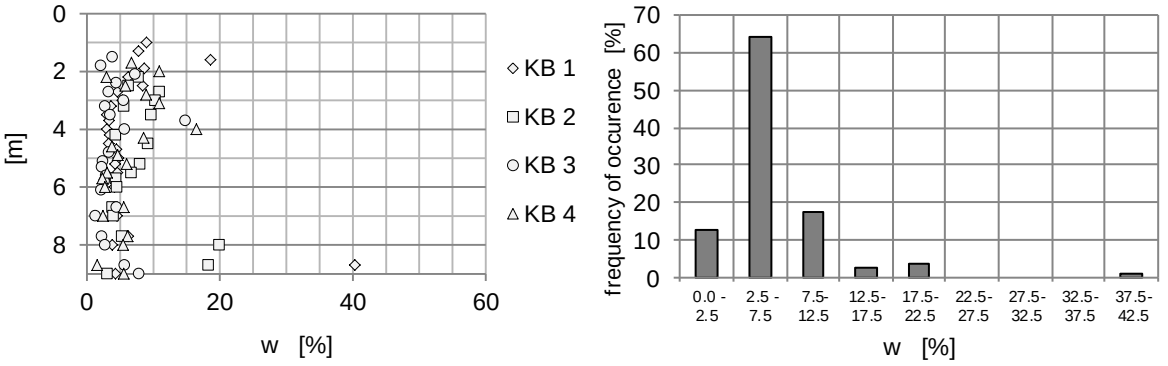

Figure 4.12: Distribution and frequency of occurrence of water content (borehole KB 1 to KB 4)

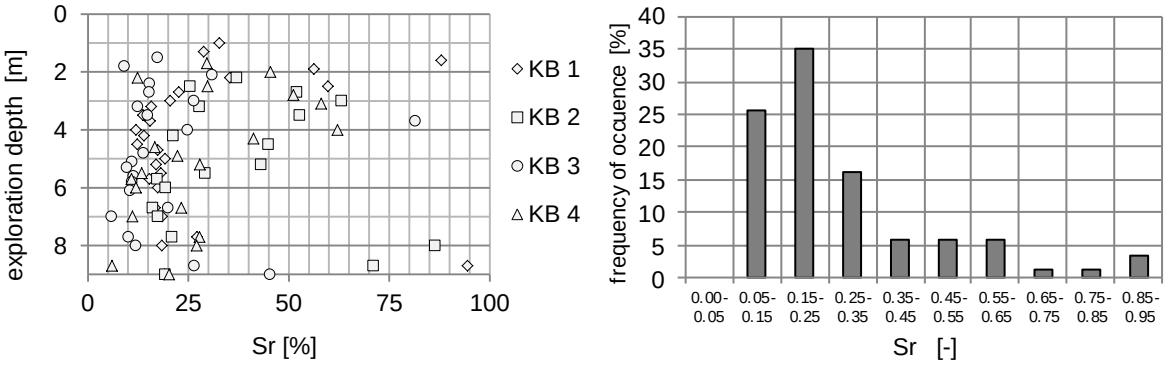

Figure 4.13: Distribution and frequency of occurrence of degree of saturation (borehole KB 1 to KB 4)

4.5 Summary and conclusion

The grading curves in Figure 4.8 depict the largely homogeneous soil conditions in the investigated embankment. The embankment material consisted predominantly of medium-dense to dense silty sands with a mean fines content of approximately 10%.

Figure 4.14 shows the measured suction as a function of the corresponding degree of saturation measured in the undisturbed samples from the boreholes KB 1 to KB 4. Due to the relative constant suction and homogenous densities, high degrees of saturation can be assigned to soils with high fines content, while the predominant low degrees of saturation can be attributed to sands with less fines. Considering typical SWRCs for silty sands (e.g., Angerer & Birle 2016), the average degree of saturation of Sr = 18% is situated between the transitional zone and the residual zone of the SWRC (see also Figure 4.14).

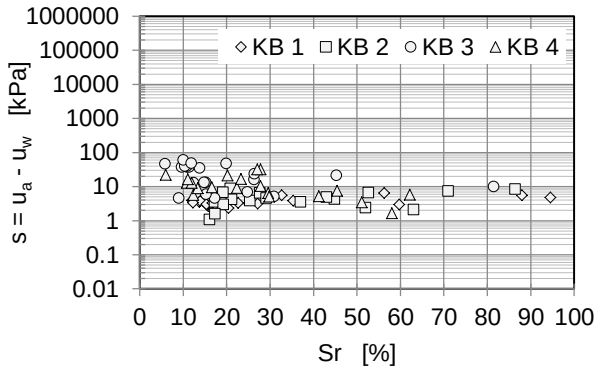

Figure 4.14: Suction s vs. degree of saturation Sr (KB 1 to KB 4)

Since from a depth of about one meter below the embankment surface, the water content can be expected to vary only slightly with time (cf. Section 2.6), the low water content of on average w = 4.5% may be assumed to represent a constant hydraulic state.

Note that since the water content is nearly constant inside of the embankment, it is not possible to determine whether it represents the drying or wetting path of the SWRC or a scanning path in between. However, for the encountered silty sands with (on average) low fines content, a minor influence of the hysteretic behavior on the SWRC can be expected (Angerer and Birle 2016). Therefore, henceforth, the drying branch of the SWRC is used to characterize the hydraulic state of the silty sand.

In general, no information was available about the construction procedure of the traffic embankment examined in this chapter. However, aggregated fine-grained fractions have often been found in the undisturbed and disturbed soil samples. It is assumed that the embankment was backfilled and compacted layer by layer. In addition, it is assumed that the water content of the built-in soil corresponded to the natural water content. It can therefore be assumed that the observed low *in situ* water content corresponds approximately to water content during compaction, leading to bimodal porosity of the soils.

In summary, the encountered silty sands can be expected to represent approximately as-compacted conditions at low water content without considerable changes over the long-term.

In Chapter 3, approximate values were found for the suction-induced effective stress in silty sands from the literature. However, the derivation of these values was subject to several assumptions, which cannot be justified without detailed investigation, in particular when evaluating peak shear strength at low water content.

In order to investigate the effect of suction on the shear strength of silty sand at *in situ* conditions encountered during the exploratory drilling, the experimental boundary conditions listed below must therefore be fulfilled. Experiments shall be carried out

- at low to high stress levels,
- on samples in medium-dense to dense states, and
- on as-compacted samples at low water content.

5 Characterization of a representative silty sand

5.1 Experimental program

The silty sand selected for the experimental investigations was taken from a traffic embankment located in Northern Germany (Angerer, Birle, and Vogt 2013). This embankment consists of soils similar to those encountered during the exploratory drilling at the traffic embankment in Eastern Germany (Chapter 4), as demonstrated throughout this chapter.

From the embankment located in Northern Germany, disturbed and undisturbed soil samples were collected and tested for

- particle size distribution, in accordance with DIN EN ISO 17892-4,
- (specific) grain density, in accordance with DIN EN ISO 17892-3,
- maximum and minimum void ratio, in accordance with the German standard DIN 18126,
- in-situ void ratio, in accordance with DIN EN ISO 17892-2,
- in-situ water content, in accordance with DIN EN ISO 17892-1,
- SWRC, and
- PSD.

The SWRC was experimentally determined on reconstituted samples compacted at increasing water content, w_{comp} = 3%, w_{comp} = 6% and w_{comp} = 10%. For each level of compaction water content, the SWRC was investigated for three relative densities. Section 5.3 details the experimental procedure.

The microstructure was investigated in sense of the PSDs derived from the SWRCs. The results were compared to the PSDs derived from three mercury intrusion porosimetries (MIP tests). The MIP tests were carried out on samples compacted at three different levels of water content (w_{comp} = 3% / 6% / 10%) to the same density. The experimental procedure is described in detail in Section 5.4.

5.2 Classification, index properties and *in situ* conditions

Prior to testing, the soil was passed through a 4 mm sieve, resulting in the particle size distribution shown in Figure 5.1a.

In accordance with DIN EN ISO 14688-2, the silty sand was classified as sigrSa, having a silt content of 8.5%, a clay content of 1% and a gravel content of 8.5%.

The minimum and maximum void ratio, e_{min} = 0.472 and e_{max} = 0.764, were determined on the dry soil using the vibratory table method and funnel pouring. Both methods were considered appropriate for the fines content of 9.5%.

The grain (specific) density, ρ_s = 2.63 g/cm³, was determined with a gas pycnometer device.

The shape of the coarse grains was characterized as subrounded to subangular, exhibiting moderate to high sphericity (Figure 5.1b). The silty sand had a lime content of 6.43% of total weight. For the grain fraction with d < 0.125 mm, a liquid limit of w_L = 22.8% and a plasticity index of I_P = 10.5% were determined in accordance with DIN EN ISO 17892-12.

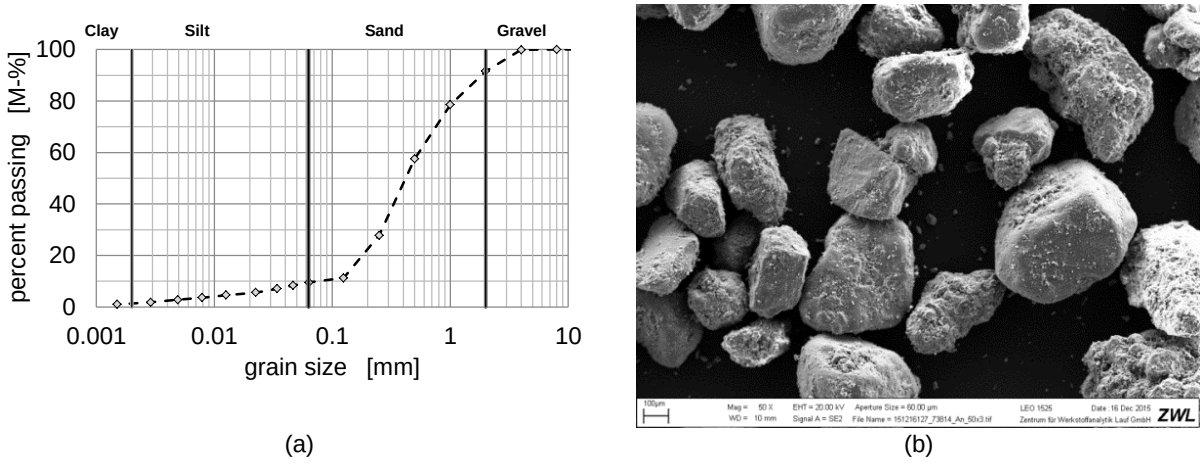

(a) (b)

Figure 5.1: (a) Grain size distribution. (b) Microscopic image of sand particles of the silty sand used in the study (scale in the lower left corner: 100 μm)

The classification, grain size fractions and index properties are summarized in Table 5.1.

DIN EN ISO 14688	Particle size distribution by weight				C_u	C_c	G_s	e_{min}/e_{max}
	Clay (d<0.002mm) **[M-%]**	**Silt** (0.002<d<0.063) **[M-%]**	**Sand** (0.063<d<2mm) **[M-%]**	**Gravel** (d>2 mm) **[M-%]**	**[-]**	**[-]**	**[-]**	**[-]**
si gr Sa	1.0	8.5	82	8.5	7.9	1.8	2.63	0.472/0.764

Table 5.1: Classification, grain size fractions and index properties

The *in situ* dry density of the selected silty sand was ρ_d = 1.683 g/cm³, corresponding to a relative density of I_D = 0.69, indicating dense packing, according to DIN EN ISO 14688-2. The *in situ* water content was w = 4%.

Regarding the in-situ conditions of the traffic embankment (the *Neißedamm*) presented in Chapter 4, the grading curve of the silty sand with 9.5% fines compares well with the average grading curve of the soils encountered in the *Neißedamm* (Figure 5.2). In addition, the *in situ* state of the silty sand can be considered representative of the soils in the Neißedamm, since they showed a low *in situ* water content and were present in a dense state.

The following experimental investigations were therefore undertaken on this soil.

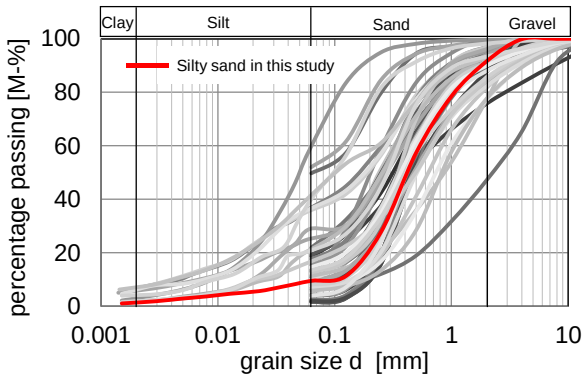

Figure 5.2: Comparison of the grading curve of the silty sand used in this study with the grading curves of the soils detected in the *Neißedamm*

5.3 Soil-water retention curve

5.3.1 Experimental methods

5.3.1.1 Hydraulic property analyzer

For suctions up to approximately s = 120 kPa, the hydraulic property analyzer (HYPROP) from the company UMS GmbH (Figure 5.3) was used to determine the drying branch of the soil-water retention curve (SWRC). The test is based on the simplified evaporation method described in Peters and Durner (2008). In this method, the sample weight and the suction at two height levels are recorded for a soil sample subjected to evaporation from the top (Figure 5.4).

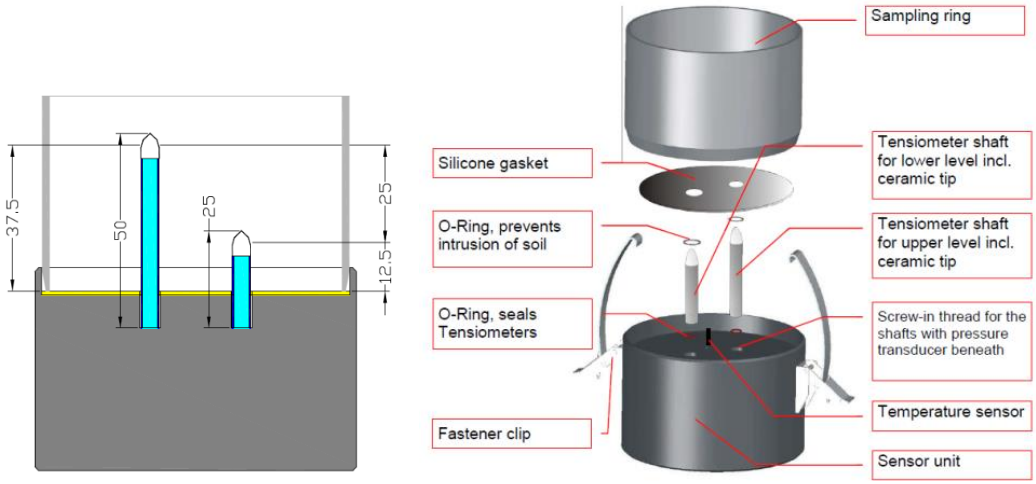

Figure 5.3: Hydraulic property analyzer (HYPROP) sampling ring and sensor unit, from UMS GmbH (2017)

The sample weight was recorded from balance readings, and the loss of weight of the sample was attributed to a loss in total water content. Based on findings related to this topic (Peters and Durner 2008), the distribution of water content was assumed to decrease linearly over the height of the sample. Given such a linear decrease, the total water content corresponded to the water content in the mid-section of the sample (Figure 5.4).

Suctions were measured in the quarter points of the sample height by conventional T5 tensiometers, already described in Section 4.3.2. The suction in the mid-section of the sample was calculated to be the arithmetic mean value of the two measured suctions. This suction was then related to the water content in the mid-section of the sample (Figure 5.4).

Thus, the evaluation of the SWRC relied on linearization assumptions with respect to the distribution of suction and water content within the sample (Peters and Durner 2008). This method is approximately valid for small sample heights as it is implemented in the HYPROP device (Figure 5.3).

Unfortunately, volumetric deformation cannot be recorded when using the HYPROP device. However, for the low-plasticity silty sand at the investigated medium-dense to dense states, it

was assumed that volumetric straining due to hydraulic loading is negligible. With this assumption, the simplified evaporation method was regarded as being a quick and appropriate method to determine the drying branch of the SWRC. Further details can be found in Peters and Durner (2008).

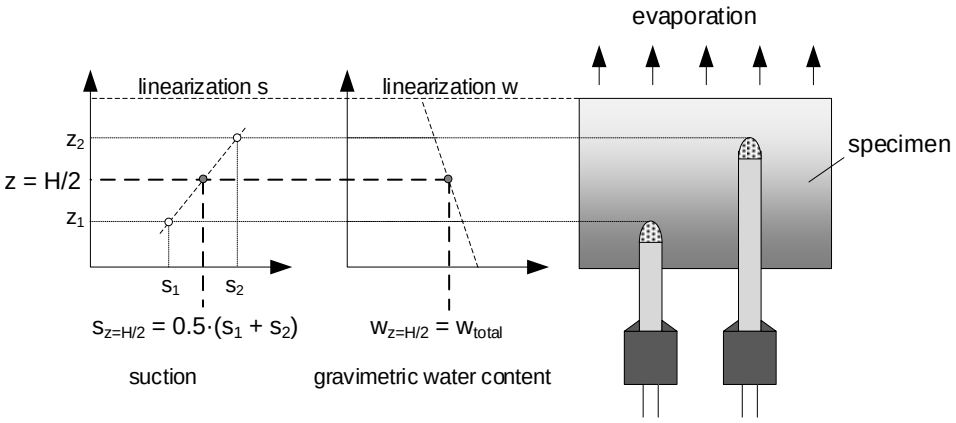

Figure 5.4: Schematic, simplified evaporation method, derived from Peters and Durner (2008)

5.3.1.2 Chilled mirror hygrometer

For determining suctions higher than 1,000 kPa, a chilled mirror hygrometer was used (Decagon device WP4C, Figure 5.5). Measurements with this device are based on the dew point method, as described in Section 2.1.3.2.

Prior to use, the WP4c was calibrated using a 0.5 molar potassium chloride (KCl) solution with defined osmotic potential (for further, see Birle 2011).

According to Fredlund et al. (2012), osmotic suction can be neglected for the examined granular soil with low plasticity fines. Therefore, only matric suction can be expected to be measured by both methods.

Figure 5.5: Dew point PotentiaMeter, WP4C (Decagon Device 2017)

5.3.2 Sample preparation

5.3.2.1 Samples for the hydraulic property analyzer

The samples for the measurements with the hydraulic property analyzer (HYPROP) were statically compacted in five layers directly into a sample ring with a diameter of 8 cm and a height of 5 cm. Before compaction, the soil was oven-dried and thoroughly mixed with distilled water until the target water content was reached. It was then stored for several days in an airtight container for homogenization.

Compaction was achieved by compressing the soil from the top with a hydraulic press. The individual layers were 1 cm high each and compacted to increasing relative densities, while the layer of the mid-section was compacted to the target density. Applying such a procedure allowed for the most homogeneous possible density distribution. In order to avoid inhomogeneous pore structures at the interfaces due to the pressure of the stamp, these interfaces were carefully roughened before inserting the next layer. This sample preparation method is called the *undercompaction method*, first introduced by Ladd (1978) and further developed by Chan (1985). An increase in ΔI_D = 1% per layer was found to be appropriate for the examined silty sand (see Section 5.4.2).

After sample preparation, the sample ring was transferred to a water bath, and the sample was saturated for several days. After saturation, the sample ring was connected to the sensor unit of the HYPROP (Figure 5.3). The sensor unit comprises a pressure transducer and two tensiometers. All components of the sensor unit were thoroughly filled with distilled de-aired water. When the connection of the sensor with the sample was made, the two tensiometers were inserted into the sample. Through pre-drilling, the disturbance of the sample due to the installation process of the tensiometers was minimized. Subsequently, the sensor unit with the sample ring was placed on a balance and subjected to the atmosphere at the top while the measurement was started. Each such measurement took about 7 to 10 days. Details of the installation process are presented in the related UMS GmbH (2017) manual.

5.3.2.2 WP4C

For the measurements with the chilled mirror dew-point hygrometers (WP4C), the soil samples were statically compacted in a single layer of 0.6 cm height into sample cups with a diameter of 4 cm and a height of 1.2 cm. The sample cups were provided by the Decagon Company for the WP4C measurements.

In order to measure suctions corresponding to the drying path, the samples were initially wetted by carefully adding water with a pipette and were thereafter homogenized for several days. Subsequently, the specimens were stepwise dried under a heating lamp to the desired water content while measurements were carried out for every step of drying. Prior to each such measurement, a homogenization time of 7 days to 14 days was allowed, with the interval depending on the actual homogeneity achieved.

5.3.3 Test results and discussion

5.3.3.1 Soil-water retention curves

Nine soil-water retention curves (SWRCs) were measured. The data from these tests are shown in Table 5.2. All nine measured SWRCs are shown in Figure 5.6.

#	Compaction water content [%]	Dry density [g/cm³]	Void ratio [-]	Relative density [-]
1	6	1.636	0.608	0.536
3	6	1.750	0.503	0.894
4	3	1.683	0.563	0.689
8	6	1.690	0.556	0.712
9	3	1.640	0.604	0.549
10	3	1.750	0.503	0.894
11	10	1.683	0.563	0.689
12	10	1.750	0.503	0.894
13	10	1.625	0.619	0.498

Table 5.2: Summary and designations of the measured soil-water retention curves (SWRCs)

For the measurements using the HYPROP device, the saturation process in the water bath was carried out without a preceding flushing with $C0_2$ or without applying a vacuum and a backpressure, respectively. Thus, the samples were not able to saturate fully even though the process took up to three days. The lack of full saturation was related to entrapped air bubbles within the soil's pore structure. In addition, lifting the samples out of the water bath also caused a loss of some water. This loss occurred due to the largest pore openings, in which the generated suction was not sufficient to hold the water against the gravitational potential. This led to draining of initially saturated pores when the sample was lifted from the water bath to the balance. Even through water was carefully added to the sample after placing it on the balance, this procedure did not lead to a considerable increase in the maximum water content. As such, the maximum degree of saturation is less than 100%.

The experimental data of the SWRCs were fitted using the equation proposed by Durner (1994) for the description of multimodal SWRCs. The function consists of two superimposed expressions for the SWRC initially presented by van Genuchten (1980):

$$\mathrm{Sr} = \mathrm{N}_1 \cdot (1 + (\mathrm{a}_1 \cdot \mathrm{s})^{\mathrm{n}_1})^{-\mathrm{m}_1} + \mathrm{N}_2 \cdot (1 + (\mathrm{a}_2 \cdot \mathrm{s})^{\mathrm{n}_2})^{-\mathrm{m}_2} \quad (5.1)$$

with
- $\mathrm{N}_1, \mathrm{N}_2$ Fitting parameters: degrees of saturation indicating the beginning of the SWRCs
- $\mathrm{a}_1, \mathrm{a}_2$ Fitting parameters: approximately the reciprocal values of the air entry values of the macro- or microporosity
- $\mathrm{m}_1, \mathrm{m}_2$ Fitting parameters
- $\mathrm{n}_1, \mathrm{n}_2$ Fitting parameters.

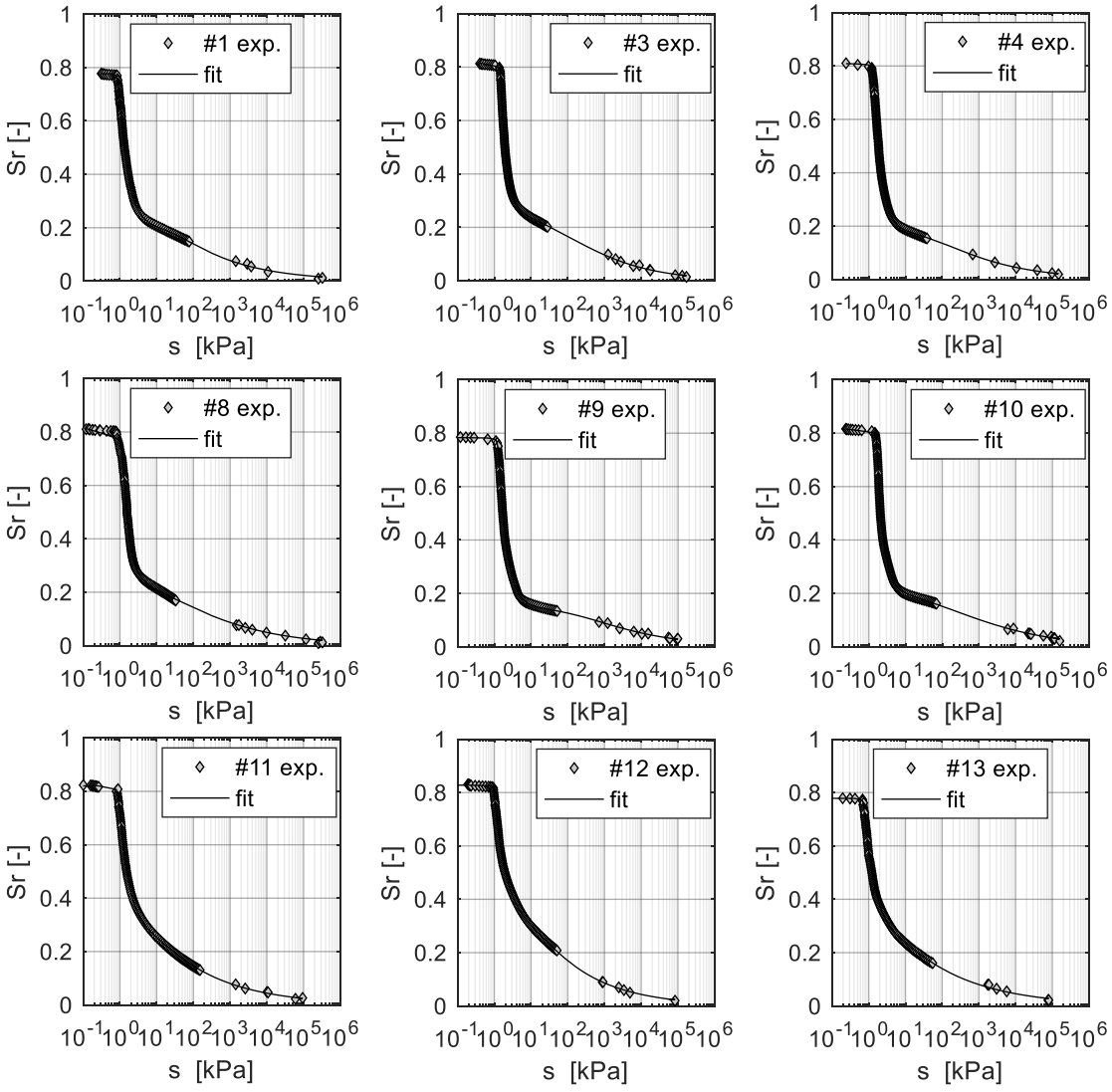

Figure 5.6: Measured soil-water retention curves (SWRCs) and the performance of (5.1)

Equation (5.1) requires the definition of eight parameters. The fitting parameters for each SWRC are summarized in Table 5.3. Note that a maximum degree of saturation $Sr_{max} = N_1 + N_2$ corresponding to the maximum measured degrees of saturation smaller than one was chosen.

The results show that equation (5.1) performs very well for all tested specimens (Figure 5.6).

The eight parameters in (5.1) show a linear trend with respect to the relative density and an approximately quadratic dependency on the compaction water content (Figure 5.7). Thus, each parameter can be expressed as a function of the relative density I_D [-] and the compaction water content w_{comp} [%] using a polynomial fit:

$$\mathrm{par}(I_D, w_{comp}) = p_0 + p_1 \cdot I_D + p_2 \cdot w_{comp} + p_3 \cdot w_{comp} \cdot I_D + p_4 \cdot w_{comp}^2 \quad (5.2)$$

with p_i Polynomial coefficients (i = 0…4)

#	N_1	N_2	a_1	a_2	m_1	m_2	n_1	n_2
1	0.57	0.22	1	0.06	0.15	0.21	14	1.2
3	0.55	0.285	0.85	0.035	0.075	0.51	30	0.58
4	0.613	0.198	0.738	0.0044	0.085	0.7	25	0.51
8	0.56	0.24	0.95	0.045	0.12	0.3	20	0.95
9	0.635	0.155	0.8	0.0047	0.099	0.5	18.4	0.59
10	0.58	0.27	0.617	0.004	0.069	1.046	34.288	0.309
11	0.45	0.37	1.1	0.28	0.145	0.2	18	1.4
12	0.43	0.45	1	0.25	0.08	0.3	28	1
13	0.48	0.29	1.2	0.31	0.2	0.105	9	2

Table 5.3: Fitting parameters for (5.1) for each soil-water retention curve (SWRC)

The polynomial coefficients in (5.2) are summarized in Table 5.4 for each fitting parameter in (5.1).

Coefficient	N_1	N_2	a_1	a_2	n_1	n_2	m_1	m_2
p_0	0.729	0.053	0.769	0.0266	1.791	0.107	0.046	0.077
p_1	−0.14	0.252	−0.55	0.0557	48.91	−0.41	−0.031	1.972
p_2	−0	−0.03	0.127	−0.024	−4.39	0.403	0.0447	−0.18
p_3	0.003	0.013	0.004	−0.021	0.086	−0.23	−0.029	−0.15
p_4	−0	0.003	−0.01	0.006	0.259	−0.01	−0.001	0.017

Table 5.4: Polynomial coefficients for (5.2) for each fitting parameter of (5.1)

Note that the chosen polynomial fit is only valid within the bounds of the measured data. An extrapolation to compaction water content and relative densities outside these bounds may lead to erroneous results. Thus, the polynomial fit should be treated with care, especially with respect to the compaction water content.

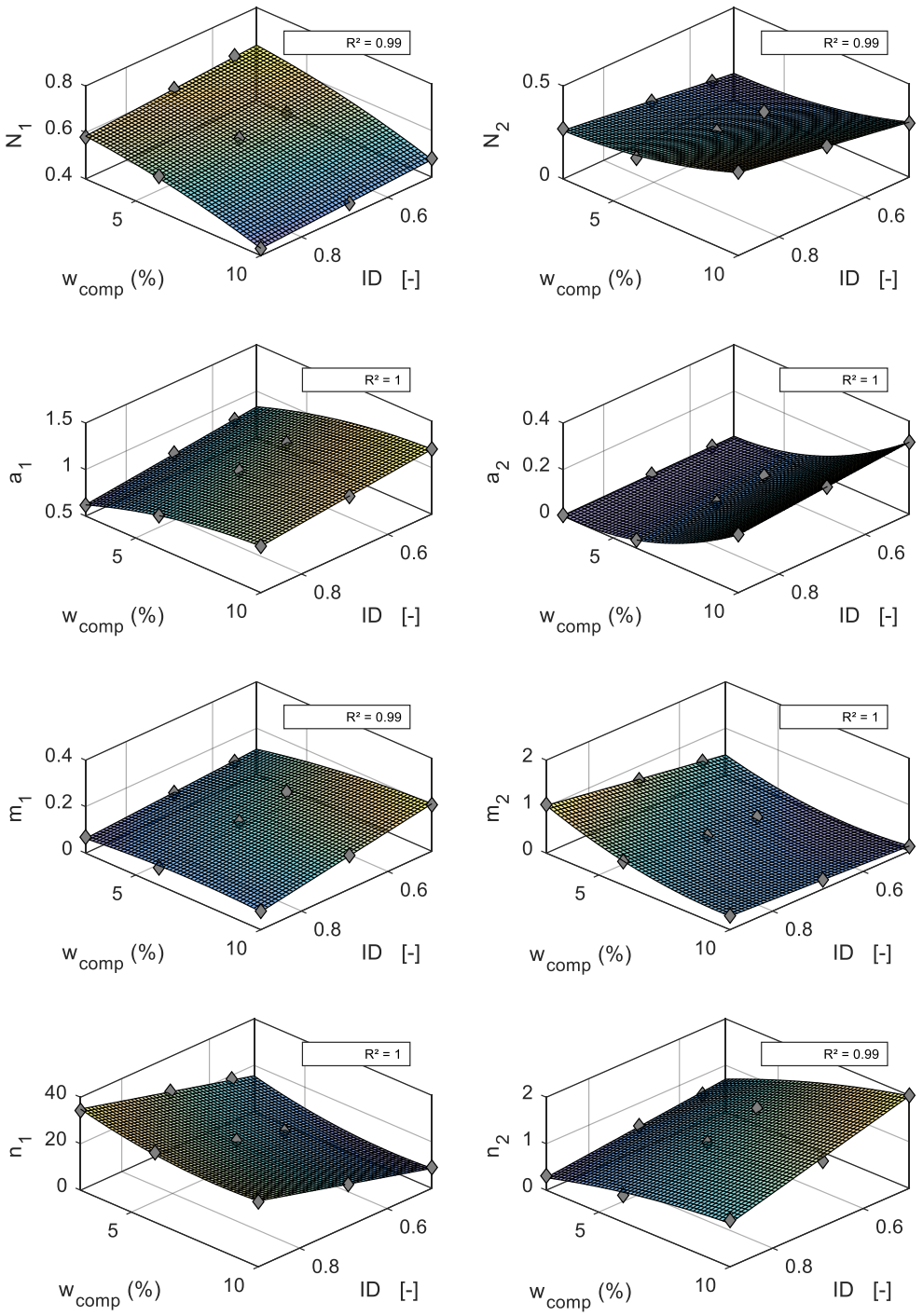

Figure 5.7: Parameter of the bimodal soil-water retention curve (SWRC) equation as a function of I_D and w_{comp}

5.3.3.2 Pore size distributions

The pore size distribution (PSD) was derived from the measured SWRCs by applying the conceptual model of capillary tubes (Section 2.2.2).

For this purpose, the following assumptions were made:

- constant void ratio throughout the drying path,
- constant temperature of T = 20°C,
- a contact angle between water and solid phase of α_w = 0°, and
- a surface tension for the air-water interface at 20°C of T_w = 72.75 mN/m.

These assumptions lead to the expression of the pore-size diameter d in dependency on the measured suction:

$$d = \frac{2 \cdot 72.5}{s} \cdot 2\ [\mu m]. \tag{5.3}$$

The pore-size density function was calculated by choosing the degree of saturation Sr as the volumetric measure of the water content. Applied to equation (2.8), the degree of saturation and the diameter yielded the following pore-size density:

$$\omega = -\frac{Sr^i - Sr^{i-1}}{\log d^i - \log d^{i-1}} \quad i = 2 \ldots m\,. \tag{5.4}$$

The PSD was examined by plotting ω as a function of the mean entrance pore diameter:

$$D^i = \sqrt{d^i \cdot d^{i-1}} \quad i = 2 \ldots m\,. \tag{5.5}$$

The results are shown in Figure 5.8 and Figure 5.9. More specifically, Figure 5.8 shows the SWRCs and PSDs determined on samples compacted at different water content to similar relative densities. Figure 5.9 shows the SWRCs and PSDs determined on samples compacted at the same water content to different relative densities.

Note that in both figures, the PSDs are depicted in a double-logarithmic scale, as only small volumes of intra-aggregate pores were present due to the relatively small proportion of fine grains in the examined soil. However, the effects of intra-aggregate pores can be clearly seen in the course of the measured SWRCs, in particular at low degrees of saturation. Regarding low compaction water content of w_{comp} = 3%, the SWRCs as well as the PSDs exhibit a bimodal course indicating an aggregated structure (Figure 5.8).

Figure 5.8 demonstrates that with increasing compaction water content, the PSDs and the SWRCs become increasingly unimodal. As compared to a bimodal microstructure, a unimodal microstructure results in a smaller air entry value and a slightly steeper course of the SWRC in the transition zone. The more pronounced the double porosity, the later the beginning of the residual zone of macropores at low degrees of saturation. This shape of the

SWRC indicates the formation of a more granular (macroporous) soil-structure, confirming the results of Toll (1988). In such samples, the fines are not evenly distributed and therefore gathered into aggregates. Note that due to the lack of experimental results at high water content (Sr > 80%), the distribution of the largest void diameters could not be adequately depicted.

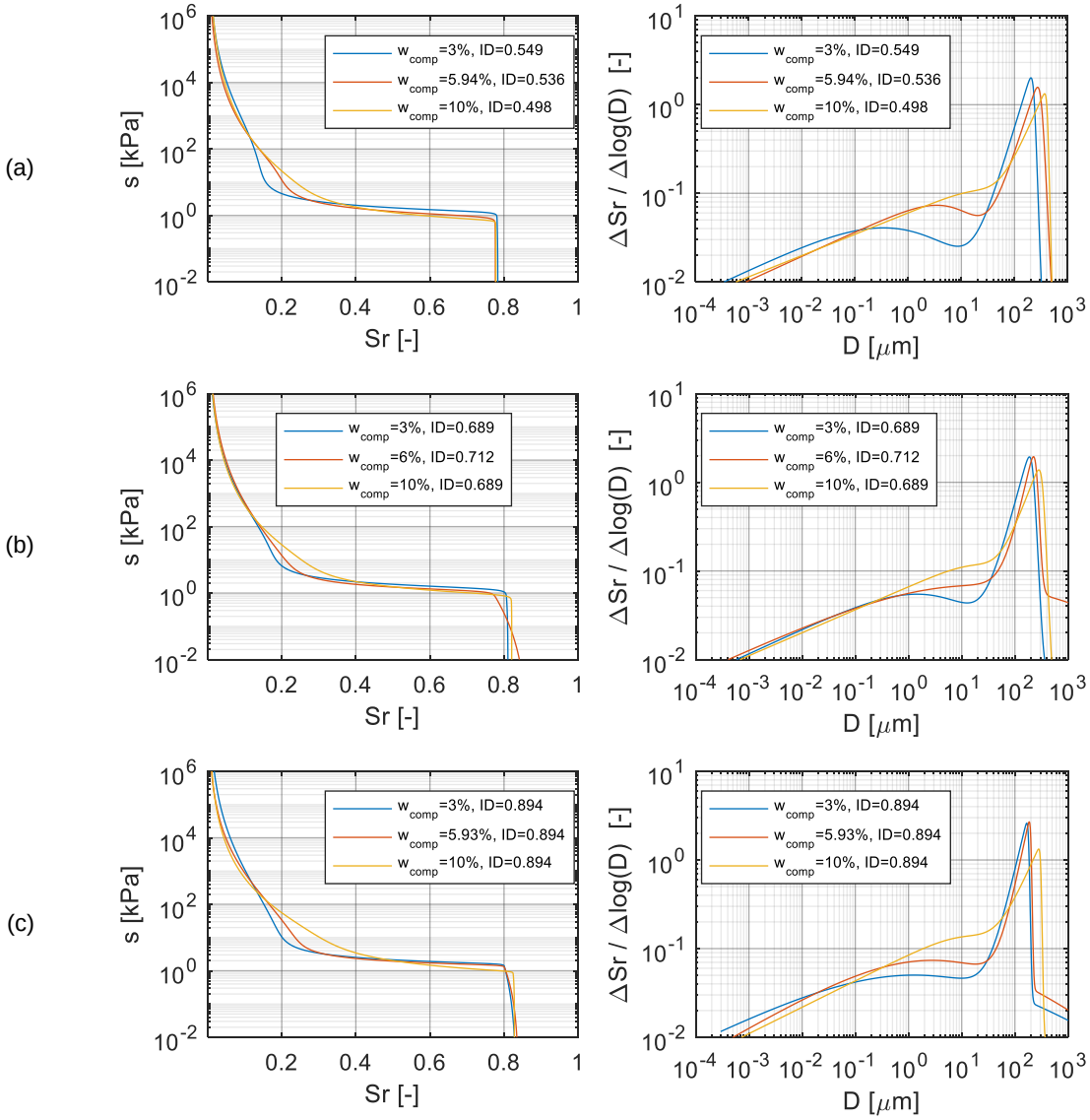

Figure 5.8: Influence of compaction water content on the soil-water retention curve (SWRC) and pore size distribution (PSD) for a relative density of (a) $I_D \approx 0.50 - 0.55$, (b) $I_D \approx 0.69$, (c) $I_D = 0.89$

Figure 5.9 shows that especially the transition zone from macro- to microporosity is affected by relative density. The SWRCs compacted at $w_{comp} = 3\%$ yield the most pronounced bimodality of the PSDs for the lowest density of $I_D = 0.55$ (Figure 5.9a). For higher relative densities, the microstructure appears to be less influenced by aggregates, even at low compaction water content (Figure 5.9a), which may be related to the compaction effort that had to be applied to the samples in order to achieve the target densities. The higher

compaction forces required to achieve the higher densities may have deformed or destroyed some of the aggregates, which initially existed in the non-compacted material. However, for samples compacted at w_{comp} = 3% and w_{comp} = 6% (Figure 5.9a and b), a double-porous fabric could still be observed for the highest tested relative densities of $I_D \approx 0.9$.

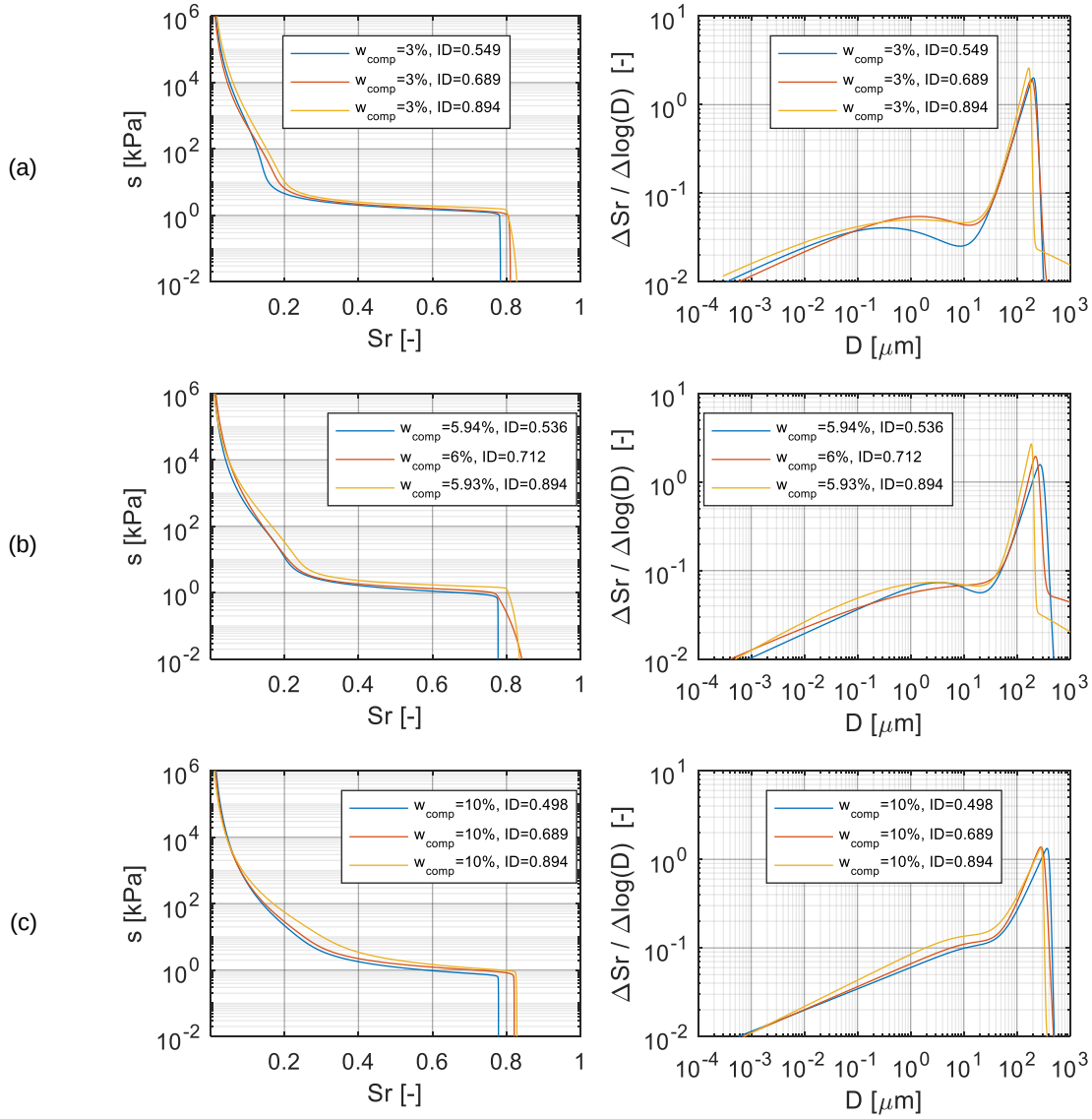

Figure 5.9: Influence of relative density I_D on the soil-water retention curve (SWRC) and pore size distribution (PSD) for a compaction water content of (a) w_{comp} = 3%, (b) w_{comp} = 6%, (c) w_{comp} = 10%

From Figure 5.9, it can also be seen that the air entry value of the SWRC increases with increasing relative density. For the investigated relative densities, however, the increase appears to be generally small. It is interesting to note that all SWRCs apparently exhibit an almost parallel shift upward with increasing relative density. This shift occurs up to degrees of saturation indicating the transition from macro- to microporosity. For low degrees of saturation, at which the aggregates are almost fully de-saturated and only adsorbed water should be left in the soil matrix, the SWRCs merge into a unique course. This high-suction regime was not significantly influenced by changes in density.

5.4 Mercury intrusion porosimetry

5.4.1 Experimental method

The mercury intrusion porosimetry (MIP) tests were carried out at the Centre for Building Materials of the Technical University of Munich. A Micrometrics - AutoPore IV Series 9500 device was available for this purpose. This testing equipment can perform high-pressure measurements over a wide range from 2.2 kPa to 412,946 kPa, allowing the detection of pore entrance diameters from 735 μm down to 0.0039 μm.

5.4.2 Sample preparation

The size of the samples for the MIP tests was limited to approximately 1.5 cm in each direction, related to the dimensions of the sample container of the tests apparatus. The procedure of preparing such small samples with a known homogeneously distributed density is explained in the following.

First, three specimens with a height of 10 cm and a diameter of 5 cm were prepared. The samples were compacted at gravimetric water content of w_{comp} = 3%, w_{comp} = 6% and w_{comp} = 10% to a density of ρ_d = 1.683 g/cm³. For this purpose, oven-dry material was mixed with water until the desired compaction water content was reached. Subsequently, the material was sealed and stored for several days to homogenize. Afterwards, the material was statically compacted in five layers into a split mold of height of 2 cm while the layer interfaces were carefully roughened. Applying the undercompaction method introduced in Section 5.3.2.1, the individual layers were compacted to increasing relative densities, while the layer of the mid-section was compacted to the target density. A layer-wise increase in the compaction density by ΔI_D = 1% proved to be suitable to produce a homogeneous density distribution. After compaction, the split mold was stripped, and the specimen was oven-dried. During the drying process, no volumetric deformation was observed. The samples appeared to be stable, which may be related to the lime content of 6% in the soil that caused a cementation of inter-particle contacts during oven-drying. For the MIP tests, small portions of approximately 1.5 cm height and diameter were carefully broken out of the dry sample. These small portions were expected to have the same dry density as the large oven-dried specimens and a homogeneous density distribution. They were therefore transferred to the container used for the MIP tests and placed into the apparatus.

Note that the above assumption—ΔI_D = 1% is sufficient to produce a homogeneous density distribution with undercompaction method—was checked on a sample of silty sand with 25% fines examined in a previous study (Angerer & Birle 2016, Sand 1). This silty sand was statically compacted into a split mold with a height of 10 cm and a diameter of 5 cm. Subsequently, slices of 1 cm height were pressed out in steps. After each step, the slices were carefully cut from the sample, and the remaining sample weight was determined. From the difference in the sample weight before and after cutting the slices, the weight of each slice was determined. Together with the known extruded volume of each slice, the density

could be calculated. Figure 5.10 indicates that the measured densities of the slices were very close to the target density, given ΔI_D = 1%. Note that it was expected that the first and last slice of the sample would be disturbed by the testing procedure. The deviations of the density from the target density in these slices were therefore neglected. Note that the stability of the slices was considerably increased by the use of soil with high fines content (28%), easing the procedure considerably. It can, however, be expected that the results shown in Figure 5.10 are also applicable to the silty sand with 9.5% fines examined in this study.

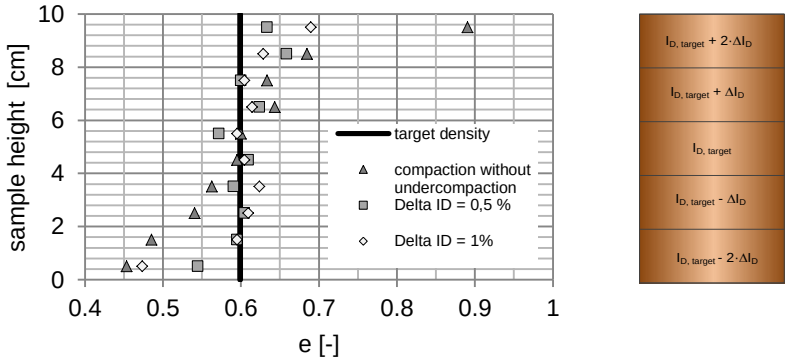

Figure 5.10: Void ratio distribution within a statically compacted silty sand with 25% fines

5.4.3 Data processing

The evaluation of the MIP tests was based on the following assumptions:

- constant void ratio throughout the intrusion process $e_{0,}$
- constant temperature of T = 25°C,
- contact angle between mercury and quartz: α_w = 147°, and
- surface tension of mercury-air interface at 25°C: T_w = 484 mN/m.

The degree of saturation was calculated from the measured intruded mercury volume per gram of soil as follows (Birle 2011):

$$Sr_{MIP} = 1 - \frac{V_{cum}}{V_{total}}\left(1 + \frac{e_0 - e_{MIP}}{e_0}\right) \tag{5.6}$$

with V_{cum} Cumulative volume of intruded mercury per gram of soil [cm³/g]

V_{total} Total volume of intruded mercury at the end of the test per gram of soil [cm³/g]

e_0 Initial void ratio of the specimen

e_{MIP} Measured void ratio: $e_{MIP} = \frac{V_{voids}}{V_{solids}} = \frac{V_{total} \cdot m_d}{m_d/\rho_s} = V_{total} \cdot \rho_s$.

With: m_d dry mass

ρ_s (specific) grain density

Note that the total volume has to be corrected for system-inherent deviations of the intruded volume at low pressures. These deviations were probably caused by the penetration of mercury into very coarse pores that are generated when breaking out the samples. They do therefore not represent the natural PSD. An example is shown in Figure 5.11 of the MIP test on the sample compacted at 3% water content. Note that the measured and corrected intruded mercury volumes for each of the tests are offered in Appendix A.

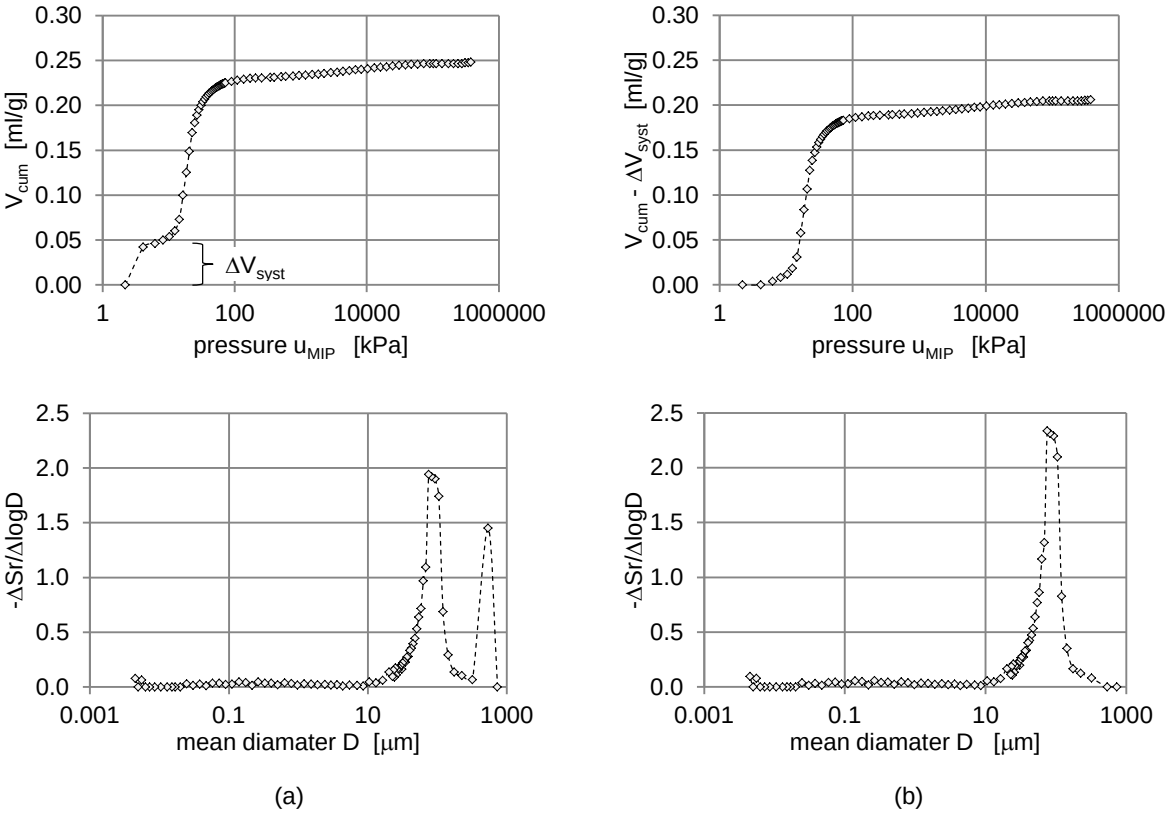

Figure 5.11: Correction of the total intruded volume and its effect on the derivation of the pore size distribution (PSD): (a) measured volume and (b) corrected volume (sample compacted at w_{comp} = 3%)

The PSD was derived from the intruded mercury volume by applying equations (5.4) and (5.5) to the experimental data.

In order to obtain the SWRC from the MIP test data, the suction corresponding to the applied mercury pressure u_{MIP} was calculated with

$$s = -\frac{72.75 \cos 0°}{484 \cos 147°} \cdot u_{MIP} \,. \tag{5.7}$$

5.4.4 Test results and discussion

In Figure 5.12a, the measured PSDs derived from the MIP tests and the SWRCs (calculated from the PSDs) are shown for the same relative density $I_D \approx 0.69$, and the three different levels of compaction water content $w_{comp} = 3\%$, $w_{comp} = 6\%$ and $w_{comp} = 10\%$.

Figure 5.12b shows the measured SWRCs and the PSDs (calculated from the SWRCs) for the same relative density $I_D \approx 0.69$ and for the three levels of compaction water content, $w_{comp} = 3\%$, $w_{comp} = 6\%$ and $w_{comp} = 10\%$.

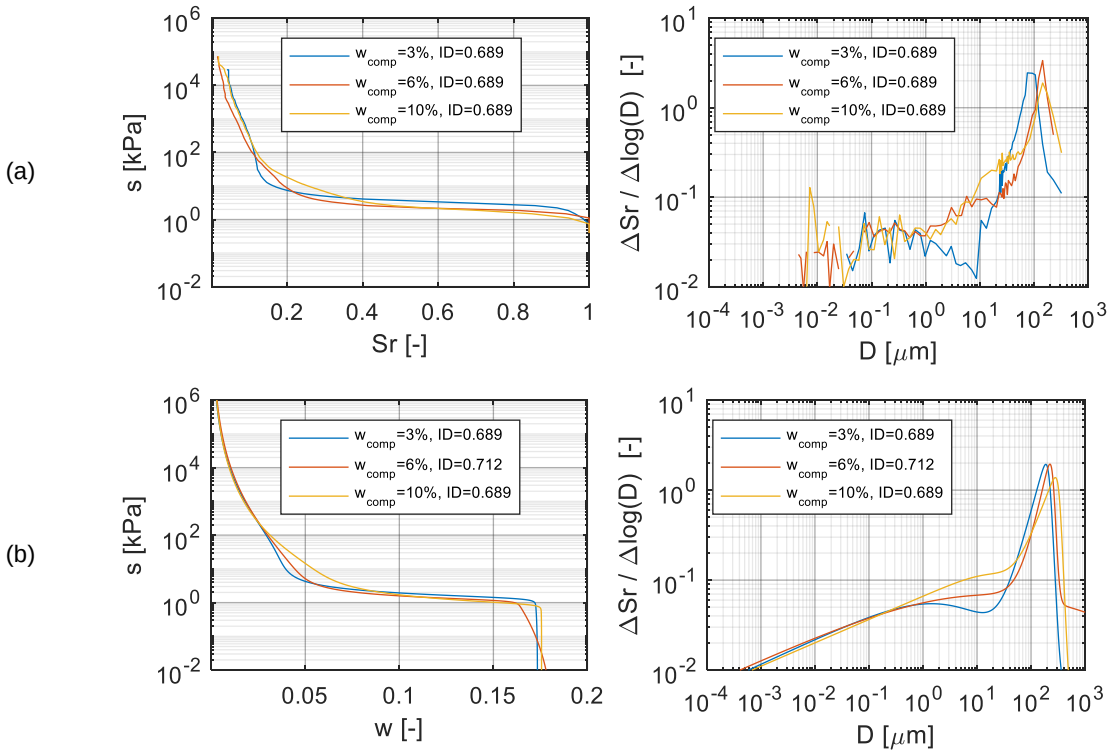

Figure 5.12: Comparison of soil-water retention curve (SWRC) and pore size distribution (PSD), determined with (a) mercury intrusion porosimetry (MIP) and (b) suction measurements

Regarding the SWRCs derived from both methods, the MIP tests produce SWRCs that start from full saturation. This results because the mercury intrusion process could capture the largest entrance diameter of the voids, whereas the samples of the SWRC tests began to drain as soon as they were lifted from the water bath. Thus, the largest pore sizes could not be derived from the SWRC using the saturation procedure described above. Nevertheless, the distribution of the large voids is considered to have minor impact on unsaturated soil behavior at low water content, which is examined in the scope of this work.

Generally, the results indicate that the main features of the PSD and its dependency on the compaction water content can be captured by deriving the PSD from the SWRC. In turn, the SWRCs calculated from the MIP tests and the measured SWRCs show a similar pattern exhibiting a similar dependency on the compaction water content. For $w_{comp} = 3\%$, both the PSDs obtained from the MIP tests and the PSDs derived from the measured SWRCs show a

pronounced bimodal porosity, which becomes more and more unimodal with increasing compaction water content. This behavior is also reflected in both the measured SWRCs and the SWRCs calculated from the MIP tests.

Quantitatively, the suctions calculated from the MIP tests are slightly higher than the measured suctions, while the microporosity tends to begin at lower degrees of saturation. This finding can be attributed to the fact that the assumptions made for the evaluation of the MIP tests may not always be correct (Simms and Yanful 2002). In fact, small and undetectable local shrinkage of the specimens for the MIP tests may have occurred during oven-drying. Furthermore, some swelling may have occurred during the saturation process of the samples envisaged for the SWRC measurements, not be detected by the HYPROP device. However, the dependency of the air entry value and the slope of the SWRC in the transition zone on the compaction water content are reflected in both the MIP test data and the measured SWRCs. Obviously, the results are therefore qualitatively very similar for both methods and show strong agreement between the measured and the calculated PSDs as well as between the measured and the calculated SWRCs. This similarity indicates that the procedure of deriving the PSD from the measured SWRC is a feasible approach to assess the main features of the microstructure of the silty sand examined in this study.

Another conclusion may be drawn when incorporating the hydraulic paths to which the samples for both MIP tests and SWRC measurements were subjected. Each measured SWRC represents the drying branch of the silty sand when compacted at a specific compaction water content. To measure the drying branch, each specimen first had to be saturated starting from the as-compacted state. Hence, for each measured point on the SWRCs, the formerly as-compacted sample was subjected to a hydraulic path initially incorporating full saturation of the sample and subsequent drying to the desired water content at which suction was measured. Starting from the as-compacted state, the samples for the MIP tests, on the other hand, were completely dried without previous saturation. Comparison of the PSDs derived from both methods (Figure 5.12) shows that the resulting microstructure seems to be very similar. Therefore, the initial as-compacted microstructure appears to be preserved irrespective of the hydraulic path to which the samples were subjected before the PSD was measured. The aggregations of fines created by the compaction process can thus be considered a permanent feature of the compacted silty sand.

It can therefore be expected that the measured SWRCs represent the initial microstructure of the as-compacted samples before saturation and subsequent drying. For instance, if hysteresis has a minor influence on the SWRC, the suction in any as-compacted state can thus be derived from the measured SWRC as long as the SWRC was measured on samples with the same initial microstructure as that of the as-compacted sample.

6 Shear strength and suction-induced effective stress from uniaxial tests

6.1 General remarks

According to the findings in Chapter 3, only low suction-induced effective stresses may be expected for the silty sand under investigation. Therefore, the increase in shear strength due to an increase in effective stress is expected to be small.

In view of the dual effect of suction on shear strength, the suction-induced effective stress should be most preferably derived from critical states. In this context, the question arises as to whether the expected small increase in effective stresses due to suction will result in measurable changes in the shear strength at the critical state. It is also questionable whether the critical state reflects “element test”-like conditions (Section 2.3.3). Particularly regarding the use of the axis-translation technique in triaxial testing, water pressure is usually applied via a porous ceramic disk underneath the sample (Section 2.4.1.1). This technique requires as much contact with the specimen as possible, which in turn makes it very difficult to apply lubrication of the end surfaces in these tests in order to minimize end-restraint effects. The control of the suction via mid plane tensiometers is challenging in granular soils due to the associated difficulties during installation, especially with rather unstable samples. The difficulties in installing such tensiometers may also lead to problems in terms of achieving full contact with the specimen (Milatz 2016).

Despite the above, the microstructure evolves during shearing and, at peak, differs from the microstructure at the critical state. It is therefore likely that the suction-induced effective stress derived from critical states does not correspond to the suction-induced effective stress at peak. The determination of the suction-induced effective stress from peak shear strength data, however, depends on the chosen approach for the state variable χ (Section 3.4). Up to now, a clear separation of the effect of the suction-induced effective stress from the dilatancy (and thus the peak friction angle) on the shear strength has *a priori* not been possible, and their mutual influence can only be approximated.

In view of the above-mentioned arguments, specifically the difficulties in evaluation of experimental data at the critical state, it was decided to use the shear strength at the peak state to evaluate both the friction angle and the suction-induced effective stresses of the silty sand.

6.2 Development of a conceptual model

6.2.1 Assessing non-linearity with different stress paths

Regarding saturated states, the non-linearity of the failure envelope can be determined not only by conventional drained triaxial compression tests via changing the confining pressure, but also by non-conventional triaxial tests following different stress paths from the same initial effective mean stress. Figure 6.1 shows three different effective stress paths starting from the same initial effective mean pressure. All three effective stress paths lead to a failure of the specimen at different effective stress states. Thus, in this stress range, they are suitable to describe the failure criterion. Note that also stress paths representing triaxial extension may be applied to the sample.

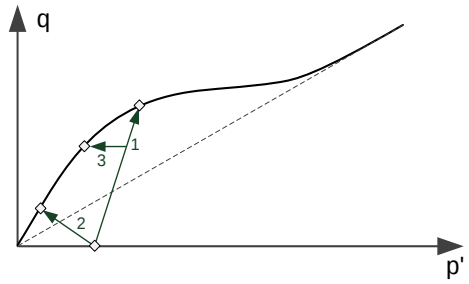

Figure 6.1: Examples of effective stress paths at the same initial effective mean stress to assess non-linearity of failure envelope, modified from Bergholz and Herle (2016)

Regarding triaxial tests on unsaturated samples, it is virtually impossible to observe effective stress paths without making assumptions as to the microstructure-dependent evolution of dilatancy and suction-induced effective stress during shearing. Further, at the beginning of each test, the effective stress state can only be assumed (e.g., by using models to describe the suction-induced effective stress as a function of the degree of saturation or suction). As discussed in Section 2.5.3, these models may lead to significantly different predictions especially in the range of low degrees of saturation to be investigated in this study.

However, the above difficulties can be overcome by performing shear tests at very low stress levels, such as UTTs and UCTs.

6.2.2 Uniaxial tests

Provided that samples are of cylindrical shape, the UCT and the UTT may be regarded as tests under radial symmetric stress conditions. In the framework of continuum mechanics, the total stress path of the UCT corresponds to the effective stress path 1 in Figure 6.2 for drained triaxial compression starting from zero total stress. The total stress path of the UTT, on the other hand, coincides with the effective stress path 2 for drained triaxial extension starting from zero total stress. The loading of unsaturated samples in both UTTs and UCTs leads therefore to a deviatoric stress unequal to zero.

The above interpretation of uniaxial tests being shear tests similar to triaxial tests will be elaborated using the example of UTTs in the following chapter.

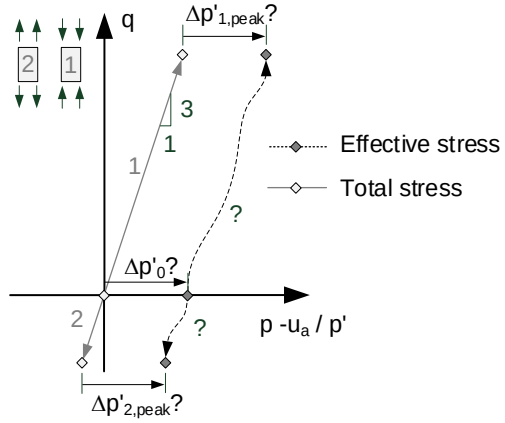

Figure 6.2: Uniaxial testing of unsaturated soils in p'/(p-u_a)-q plane

6.2.3 Interpretation of uniaxial tensile tests

The above problem may be addressed with the help of a force-displacement curve of uniaxial tensile tests (UTTs) (Figure 6.3). The figure schematically represents a commonly measured force-displacement curve when performing displacement controlled UTTs (e.g., Nahlawi et al. 2004). In Figure 6.3, the UTT device consists of two cylinder halves which are pulled apart (Angerer 2016).

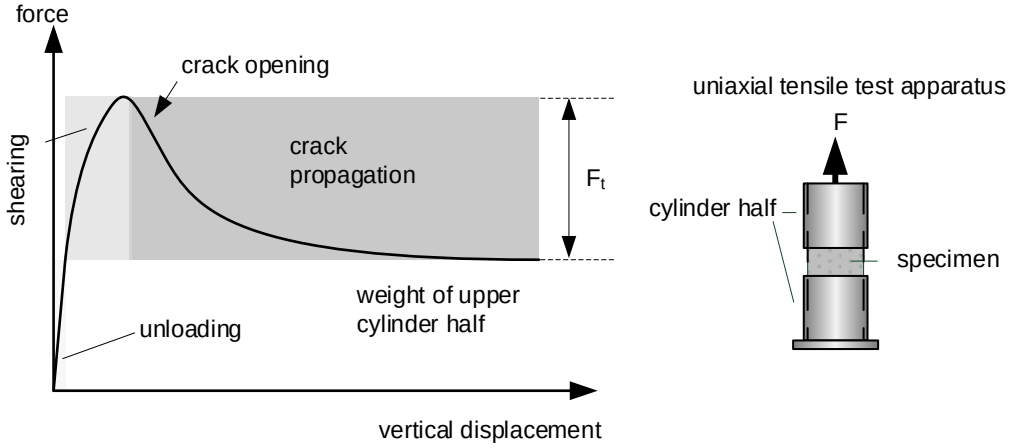

Figure 6.3: Typical test result of the displacement controlled uniaxial tensile tests (UTTs)

The test results can be interpreted as follows:

- The first part of the curve can be traced back to the unloading of the specimen by lifting the upper cylinder together with the soil in it. After unloading, the specimen is solely isotropically confined by the suction-induced effective stress.
- In the further course of the curve, the specimen is increasingly sheared until maximum shear resistance is reached. Shearing may be expected to prevail over tensile loading since the stiffness of the specimen decreased prior to peak. In the post-peak regime,

strain softening linked to strain localization occurs, ultimately leading to a crack opening and crack propagation. The residual force is reached once all menisci are broken and no more shear resistance can be generated. The residual force does not reflect shear strength but is rather a measure of the weight of the upper cylinder, including the weight of the soil within.

– The difference between the peak force and the residual force is the maximal applicable tensile force F_t. This force is used to describe the tensile strength applied to the sample by assuming a constant vertical stress over the transmitting cross-section.

There are three major difficulties regarding the determination of the shear strength from UTTs:

i. Because there is in any case a localization of strain and crack propagation during the execution of the test, it is questionable whether the force at peak corresponds to a homogeneous stress-strain field rendering approximately element test conditions.

ii. The initial value of the effective stress and its evolution during testing is unknown.

iii. In general, while the interpretation of the axial stress measured in UCTs as a deviatoric stress has long been regarded as standard, the question seems to be still relevant whether the tensile strength derived from UTTs is the isotropic (suction-induced) effective stress (e.g., Zeh & Witt 2007) or a deviatoric stress (Lu et al. 2009).

The first and the third issues are discussed with the help of a simple sphere model in the next section. Based on the findings from the sphere model, the second issue is addressed in Section 6.2.3.2.

6.2.3.1 Sphere model

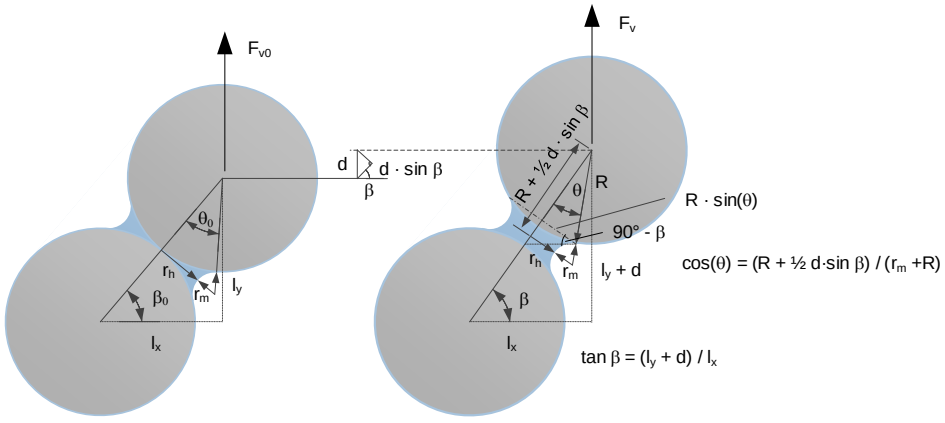

Figure 6.4: Geometry and definition of variables of a model of two spheres of the same diameter R with an interposed capillary bridge

Figure 6.4 shows the geometry and variables of two rigid spheres of the same diameter R with a capillary bridge in between (cf. Section 2.1.2). This model is used to calculate the

vertical force F_v, which is transmitted between the spheres via the capillary bridge as a function of the vertical particle distance d, the filling angle θ and the particle orientation β.

Based on the variables defined in Figure 6.4, the volume of the capillary bridge is described in dependency of the filling angle θ, the initial particle orientation β_0 and the vertical distance d:

$$V = 2\pi\left[\left(R^{*2} + \left(\sqrt{R^{*2}+\overline{R}^2} - R\right)^2\right)\cdot\frac{\left(\sqrt{R^{*2}+\overline{R}^2} - R\right)\overline{R}}{\sqrt{R^{*2}+\overline{R}^2}} - \right. \tag{6.1}$$

$$\left. -R^*\cdot\left(\sqrt{R^{*2}+\overline{R}^2} - R\right)^2\cdot\left(\frac{\overline{R}}{R^{*2}+\overline{R}^2}R^* + \arcsin\left(\frac{\overline{R}}{\sqrt{R^{*2}+\overline{R}^2}}\right)\right) - \frac{\left(\sqrt{R^{*2}+\overline{R}^2} - R\right)^3\overline{R}^3}{3\left(\sqrt{R^{*2}+\overline{R}^2}\right)^3}\right] -$$

$$-\frac{2\pi}{3}\left[R^3\left(1 - \frac{\overline{R}}{\sqrt{R^{*2}+\overline{R}^2}}\right)^2\cdot\left(2 + \frac{\overline{R}}{\sqrt{R^{*2}+\overline{R}^2}}\right)\right]$$

with R Radius of spheres

$$R^* = r_m + r_h$$

$$r_h = \frac{\overline{R}\sin\theta - \overline{R} + R\cos\theta}{\cos\theta} = R^* - \sqrt{R^{*2}+\overline{R}^2} + R$$

$$r_m = R\left(\frac{1}{\cos\theta} - 1\right) = \sqrt{R^{*2}+\overline{R}^2} - R$$

$$\overline{R} = R + \frac{1}{2}d\cdot\sin\beta = \cos\theta\,(R + r_m)$$

$$\tan\theta = \frac{R + \frac{1}{2}d\cdot\sin\beta}{R^*}$$

$$\tan\beta = \frac{2\cdot R\cdot\sin\beta_0 + d}{2\cdot R\cdot\cos\beta_0}$$

The derivation of the above equation and its variables is offered in Appendix B.

The suction results from (2.4) and the variable definitions in (6.1) as

$$s = 0.07275\cdot\left(\frac{1}{r_m} - \frac{1}{r_h}\right) = 0.07275\cdot\left(\frac{1}{\sqrt{R^{*2}+\overline{R}^2} - R} - \frac{1}{R^* - \sqrt{R^{*2}+\overline{R}^2} + R}\right). \tag{6.2}$$

From the previous term, the inter-particle force, which is transmitted through the capillary bridge, is derived as follows:

$$F = s \cdot \pi \cdot \left(R^* - \sqrt{R^{*2} + \overline{R}^2} + R\right)^2 + 2\pi \cdot \left(R^* - \sqrt{R^{*2} + \overline{R}^2} + R\right) \cdot 0.07275. \tag{6.3}$$

The force in vertical (pulling) direction results from (6.3) as

$$F_v = F \cdot \sin\beta\,. \tag{6.4}$$

The initial state, prior to pulling, may be defined by choosing proper initial values for the variables:

$$\theta = \theta_0, \quad d = 0\,, \quad \beta_0, \quad R\,. \tag{6.5}$$

In order to describe the separation of the two spheres, the above expressions must be evaluated for increasing vertical distances d. This evaluation may be done in two ways. The first describes volume constant vertical pulling, representing a rapid lifting rate for the upper particle:

$$g_V = V(\theta_0, d_0, \beta_0, d) - V_0(\theta_0, d_0, \beta_0) = 0\,. \tag{6.6}$$

The second way describes suction constant pulling, representing a rather slow lifting rate for the upper sphere:

$$g_s = s(\theta_0, d_0, \beta_0, d) - s_0(\theta_0, d_0, \beta_0) = 0\,. \tag{6.7}$$

Equations (6.6) and (6.7) may be solved numerically for R^*, depending on the vertical distance d. Subsequently, by using (6.1) and (6.2), the suction and volume change can be derived from the particle distance d. Based on these results, the vertically transmittable forces can be calculated with (6.4).

Figure 6.5a shows the change in suction ratio s/s_0 (where s_0 is the initial suction at d = 0) during volume-constant vertical pulling and the evolution of the vertical force F_v with increasing vertical distance d between the spheres for different initial filling angles θ_0. Figure 6.5b shows the change in water volume ratio V/V_0 (where V_0 is the initial water volume at d = 0) during suction-constant vertical pulling and the evolution of the vertical force F_v with increasing vertical distance d between the spheres for different initial filling angles θ_0.

Figure 6.6 shows the results of (6.6) and (6.7) similarly to those in Figure 6.5, but for different initial particle orientations β_0. A sphere diameter of R = 0.2 mm was chosen to represent approximately the mean diameter D_{50} of the grading curve of the silty sand used in this study (see Figure 5.1).

In general, a vertical force may exist up to a particle separation distance d, at which the water bridges break up because of positive water pressures resulting from the water-bridge geometry, according to (6.2).

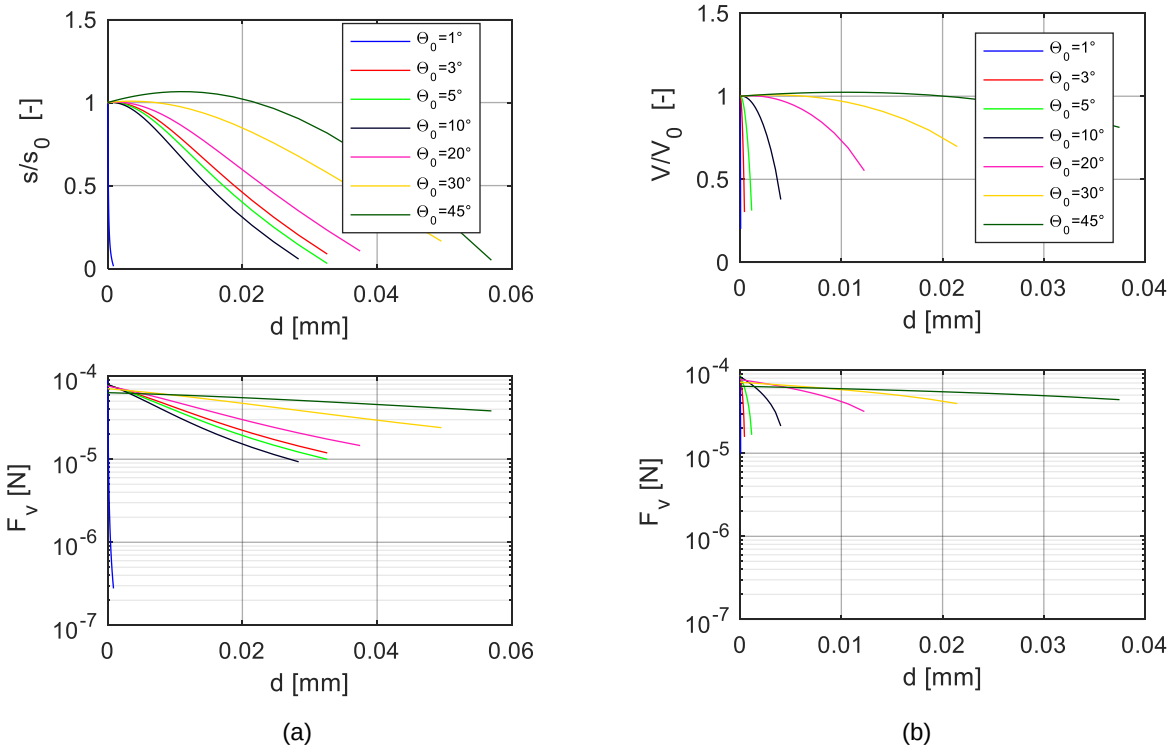

Figure 6.5: Results of the sphere model for (a) volume-constant, (b) suction-constant vertical pulling for different initial filling angles θ, $d_0 = 0$ $\beta_0 = 90°$ and R = 0.2 mm

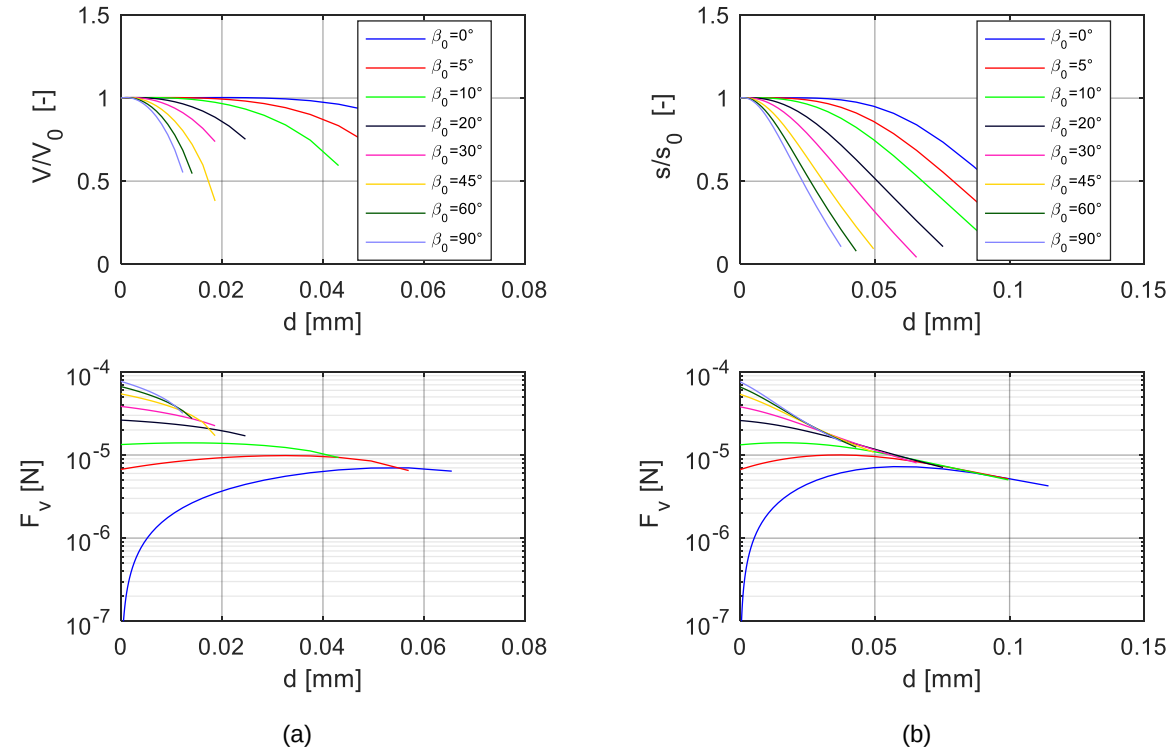

Figure 6.6: Results of the sphere model for (a) volume-constant, (b) suction-constant vertical pulling for different initial angles β, $d_0 = 0$, $\theta_0 = 20°$ and R = 0.2 mm

The results show that independent of the pulling rate (suction constant or volume constant), the initial filling angle and the particle orientation, the vertically transmittable force decreases

as soon as the particles are pulled apart. These results are consistent with the findings of Gabrieli et al. (2013) and Lian et al. (1993), who also note that the maximum transmittable force between two rigid sphere bodies occurs at particle gaps of d = 0 and β = 90°.

An exception to this behavior is observed for initial particle orientations β_0 < 10°, for which the vertical force increases with increasing vertical distance (Figure 6.6). This exception arises because of the erection of the capillary bridge from a horizontal to a more upright position during the pulling. However, regarding the sum of the vertical forces transmitted through an assemblage of spheres, the impact of the slight increase in the vertical force may be neglected when compared to the drop of the vertical force caused by capillary bridges, which are initially oriented in rather upright positions (β_0 = 90°).

This conclusion is supported by the fact that the number of the various possible capillary bridge orientations are approximately equal when averaged over a representative volume. Furthermore, the particle separation required to fully mobilize the vertical tensile resistance for particle alignment β_0 = 0° would previously lead to a collapse of all other capillary bridges (Figure 6.5 and Figure 6.6).

The question whether the measured tensile force corresponds to an isotropic tensile strength and thus directly to the effective stress state or whether it corresponds more to shear strength may be investigated with the above sphere model (problem iii). When transferring the idealized behavior of the sphere model to a force-displacement curve of a tensile test on a sample of idealized spheres without shear resistance, after unloading, the following behavior can be expected (Figure 6.7):

- At the particle level, the applied tensile force is transmitted through the randomly orientated capillary bridges between the spheres. Therefore, the tensile force increases while the sample shows approximately no deformation. Up to peak, the force-displacement curve is thus vertical.
- At peak, the capillary bridges cannot withstand any further tensile loading, and the particles begin to separate. The measured tensile force rapidly decreases according to Figure 6.5 or Figure 6.6.
- A further pulling of the sample immediately leads to pronounced strain localization at the menisci-level (crack opening). Therefore, an abrupt decrease in the force with further vertical displacement occurs (Figure 6.7).

In Figure 6.7, however, a pronounced discrepancy emerges in the comparison of the force-displacement curves resulting from the sphere model with the schematical force-displacement curve as it can be expected from real UTTs (cf. Figure 6.17). This generally divergent behavior may be explained by the contribution of inter-particle friction to the tensile resistance. Inter-particle friction is generated by inter-particle forces created by the capillary bridges and relative particle displacements. The deformation necessary to reach the peak in reality may thus be traced to the mechanism of inter-particle sliding. On average, the particles' tendency to separate during loading is counteracted by the samples' tendency to

dilate when sheared at low stress states. Up to the peak of the force-displacement curve, no pronounced particle separations can be expected, as any would lead to a sudden drop in the tensile resistance, according to the sphere model. This sudden drop of tensile resistance would occur due to the decrease in inter-particle forces with increasing particle distance and the accompanying loss of shear resistance at former particle contacts. A sudden drop of tensile resistance is, however, not observed in displacement-controlled UTTs (Nahlawi et al. 2004 and Figure 6.17). The vertical deformation up to peak is thus associated with the shear deformation necessary to mobilize the shear strength of the sample, rather than with particle separation. Similar to triaxial tests, shearing of the sample decreases its shear stiffness, which is why the force-displacement curve appears to be non-linear in this regime. The interpretation of the UTTs as a test for the direct determination of isotropic tensile strengths can therefore not be justified on the basis of the sphere model and the observed force-displacement curves (problem iii).

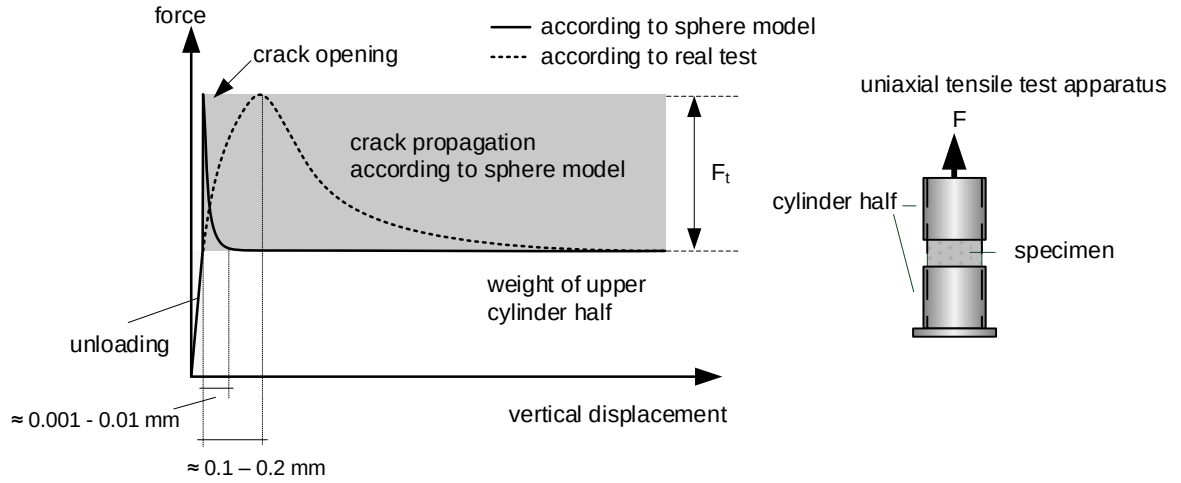

Figure 6.7: Theoretical force-displacement curve according to the sphere model (solid line) and schematical force-displacement curve as it can be expected for real uniaxial tensile tests (UTTs) (dotted line)

From the above considerations, it can be assumed that up to the peak of the force-displacement curve, the stress-strain field is approximately homogeneous (problem i). The decrease in tensile resistance in the post-peak regime may be related both to strain softening due to shearing and to particle separation causing the crack to open. Both mechanisms indicate significant strain localization, which is why the interpretation of tensile tests presented in this thesis does not apply to this regime of the force-displacement curve. However, it is not necessary to consider the post-peak regime when evaluating tensile tests with regard to effective stress and peak shear strength. Notably, the nature of applying the tensile force to the sample via wall friction leads to a disturbed stress-strain field in this region. In order to minimize the influence of force application on the stress-strain field in the sample, care should be taken when applying tensile force to the sample. It appears useful to distribute the application of the force over a large area in order to minimize the disturbance of

the stress-strain field. The influence of the nature of force application on the test results is detailed in Section 6.6.

Within the presented framework, the applied tensile force at peak F_{peak} can be used to derive the maximum total tensile strength applied to the specimen:

$$\sigma_t = \frac{F_{peak} - F_{ult}}{A_t} = \frac{F_t}{A_t} \tag{6.8}$$

with F_{peak} Peak force

F_{ult} Force at end of the test

A_t Specimen cross section.

The above considerations represent a conceptual approximation of the behavior of unsaturated granular soils during unconfined tensile loading. Since it is based on the description of capillary bridges, it is valid only for test interpretation with low water content in the range of the residual zone of the SWRC (i.e., the discontinuous water phase). In view of this limitation, the presented interpretation of tensile tests cannot be applied to tests on samples at high water content as they indicate a continuous water phase. However, since the assumption of constant suction during constant water content tests is also valid only for low water content (Section 2.4.1.5), the above limitation does not introduce any further restriction to the framework for interpreting UTTs.

6.2.3.2 Effective stress

Based on the results of Section 6.2.3.1, the effective stress state can be evaluated at the peak of the force-displacement curve. After unloading, it seems reasonable that an isotropic stress state induced by suction exists in the sample. With the application of tensile force, the effective stress in the axial direction decreases until the deviatoric stress at the resulting effective mean pressure reaches the failure criterion. Uniaxial tensile tests may thus be interpreted as tests under triaxial stress conditions, with the principle stresses acting in the axial and radial direction. However, in order to evaluate the effective stress paths, two assumptions are necessary: First, during deviatoric loading, the suction-induced effective stress remains unchanged; second, the radial effective stress remains unchanged throughout the test, up to the peak of the force-displacement curve.

In general, the product $\chi \cdot s$ may depend on suction, water content, density and microstructure. For this reason, the evolution of these influencing factors during uniaxial constant water content tests are investigated in more detail below.

As discussed before, the suction remains unchanged throughout constant water content tests at low water content. Regarding the silty sand examined in this study, the dependency of the measured suction on the gravimetric water content confirms this assumption (Figure 6.8). When depicted as a function of gravimetric water content, the SWRCs do not show a

pronounced dependency of suction on density even for the highest compaction water content w_{comp} = 10% (Figure 6.8c).

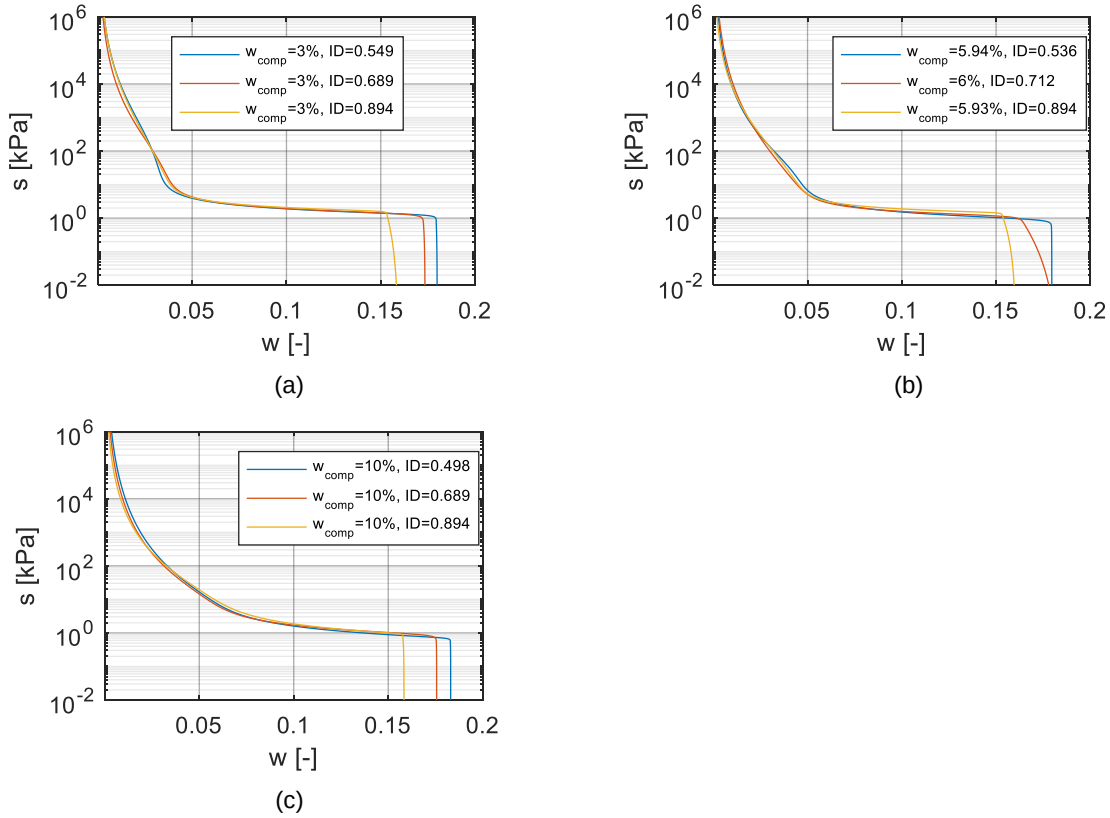

Figure 6.8: Dependency of suction on water content and relative density for (a) w_{comp} = 3%, (b) w_{comp} = 6%, (c) w_{comp} = 10%,

Following the findings from the previous Section 6.2.3.1, the deformations necessary to reach the peak generate a homogeneously distributed field of strains to the sample. As these strains are small (as is the case in uniaxial tensile testing at low water content), they are unlikely to change the microstructure of the sample significantly. For example, consider the air entry value of the macropores of the soil. The air entry value is directly linked to the largest entrance pore sizes, thus it is also linked to the density and microstructure of the soil. Note that (5.1) was used to fit the measured SWRCs. In this equation, the reciprocal value of the van Genuchten parameter a_1 is a measure for the air entry value of the macropores. Using (5.2) to evaluate the dependency of a_1 on density reveals that within the considered density range, the air entry value of the macropores of the silty sand is not considerably affected (Figure 6.9).

In summary, up to force peak, no significant changes in density, microstructure, suction and water content may be expected. Thus, the suction-induced effective stress at the beginning of the UTTs corresponds to the effective stress at peak, confirming the first assumption necessary to determine the effective stress.

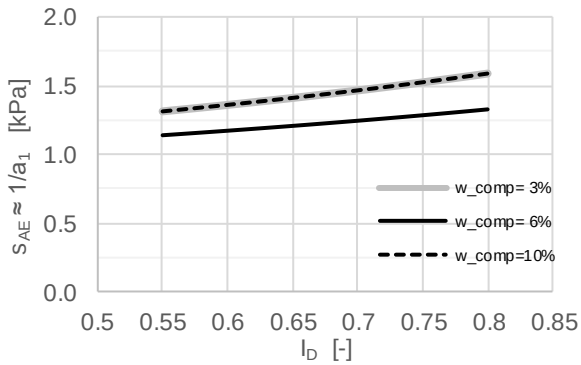

Figure 6.9: Dependency of $1/a_1$ as a measure for the air entry value on relative density

The second assumption of constant radial effective stress up to peak is met by the expectation that the suction-induced effective stress is isotropic in nature. The assumption of constant radial effective stress has therefore already been confirmed by the confirmation of the assumption of a constant suction-induced effective stress. No further investigations on the second assumption are necessary.

6.2.4 Effective stress and Mohr–Coulomb's failure criterion from uniaxial tests

Given the results above, the total stress paths of the UTTs and UCTs can be shifted in parallel to define an effective stress-based failure criterion (Figure 6.10).

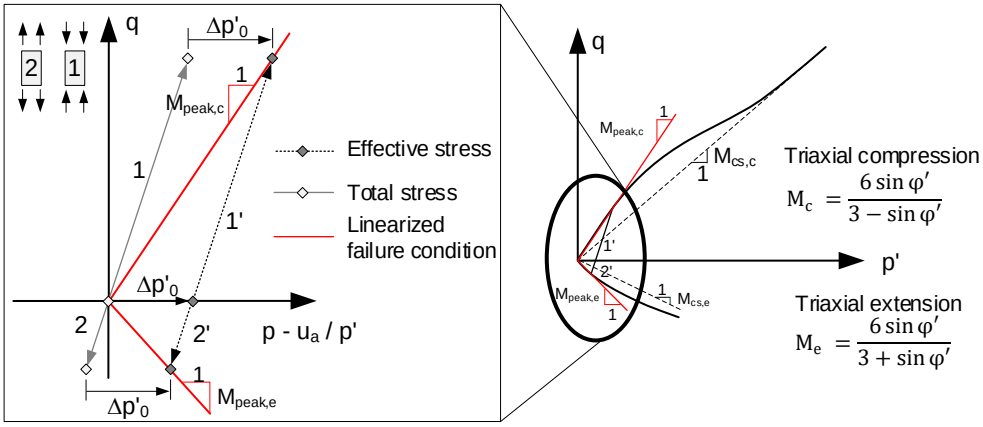

Figure 6.10: Stress paths for uniaxial testing of unsaturated soils in p' - or (p - u_a) - q plane

The failure criterion must be reached by both tests and—at low effective stresses and in a small stress range—may be considered linear and to pass through the origin. The horizontal shift of the total stress paths from the origin toward positive values reflects the isotropic suction-induced effective stress, which, for the same water content and sample preparation method, can be expected to be equal for both test types. Assuming that the Mohr–Coulomb failure criterion is valid in the considered small effective stress range, the shear strength of triaxial extension and triaxial compression can therefore be described by a unique friction angle.

Note that the effective stress path between the start point and the failure point remains unknown, but (by applying the assumptions of the above) may also be approximated as being linear. The inclinations of the linearized failure criteria (M_c and M_e) represent the secant peak friction angle according to equations (2.13) and (2.17), as indicated in the Figure 6.10.

Applying the above procedure to the test interpretation in the τ - σ' - plane, the measured total stress circle of a UTTs is shifted from the negative (tensile) domain into the regime of positive stresses. Thus, the total negative stresses measured are transferred to positive effective stresses, as indicated in Figure 6.11.

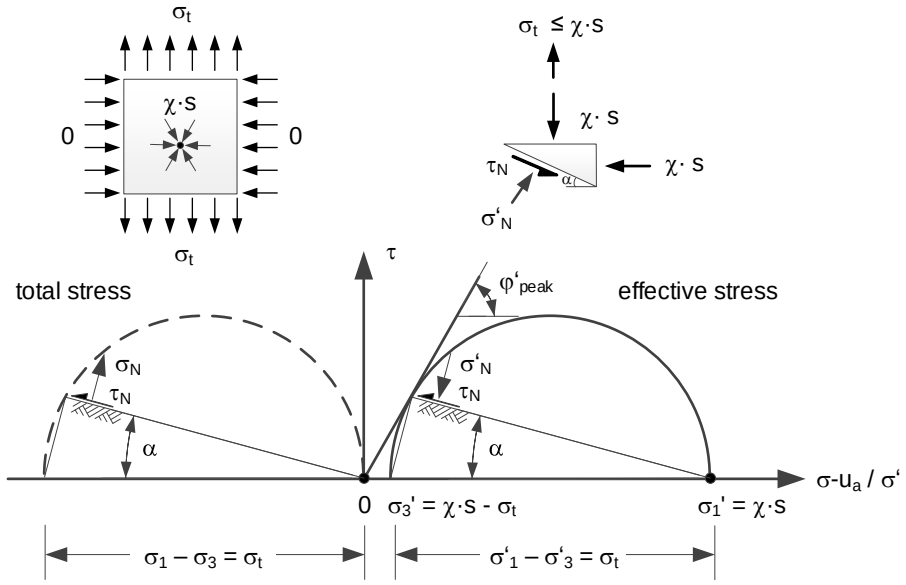

Figure 6.11: Total and effective stress states at failure for uniaxial tensile tests (UTTs)

Figure 6.11 furthermore demonstrates that the measured tensile strength σ_t corresponds directly to the deviatoric stress $\sigma_1 - \sigma_3$ at peak and not to the suction-induced effective stress $\sigma_1' = \chi \cdot s$. The suction-induced effective stress may be evaluated by horizontally shifting the measured Mohr's circle until it touches the Mohr–Coulomb failure criterion. As already mentioned above, at low effective stresses, the linearized failure criterion can be assumed to pass through the origin. The slope of the failure criterion is derived from the tangent to the Mohr's circles measured in both the UCT and in the UTT, starting from the same initial isotropic effective stress state $\chi \cdot s$ (Figure 6.12).

Notably, this procedure is valid only at low effective stresses. At higher effective stresses, the idealization of the non-linear failure criterion through a tangent to the two Mohr's stress circles would require the application of a numerical cohesion c', which cannot be determined. The cohesion would be necessary to avoid the determination of too-large suction-induced effective stresses, which would occur if the linearized failure criterion were forced to pass through the origin (Figure 6.13a). At low effective stress states, however, the errors associated with the idealization of the non-linear failure criterion as a straight line passing through the origin can be considered negligible (Figure 6.13b).

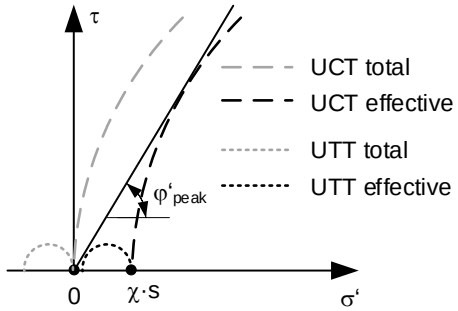

Figure 6.12: Deriving peak friction angle and suction-induced effective stress from unconfined compression test (UCT) and uniaxial tensile test (UTT) in the τ - σ' plane

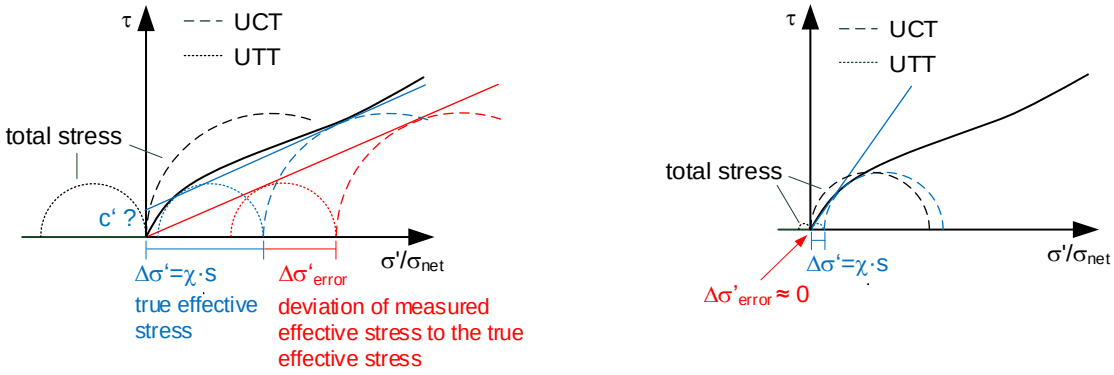

Figure 6.13: Errors associated with the linearization of the failure criterion in the τ - σ' plane at (a) high effective stresses and (b) low effective stresses

6.3 Uniaxial tensile tests

In the framework developed above, uniaxial tensile tests (UTTs) correspond to triaxial extension tests if the stress state in the specimen exhibits rotational symmetry. Tests on samples with rectangular cross-sections or on samples that may additionally not be supported on one side of the specimen (Mikulitsch and Gudehus 1995, Kim and Sture 2008, Nahlawi, Chakrabarti, and Kodikara 2004, Tamrakar, Mitachi, and Toyosawa 2007) cannot be evaluated in this framework. To minimize the influence of gravity on the test results, the specimen should furthermore be loaded vertically rather than horizontally (Nahlawi, Chakrabarti, and Kodikara 2004) or slanted (Lu, Wu, and Tan 2005). As described below, these two aspects were taken into account in the development of a test bench for carrying out displacement-controlled UTTs and UCTs.

6.3.1 Apparatus and test setup

The developed apparatus for uniaxial tensile testing of unsaturated silty sand is shown in Figure 6.14 (Angerer 2016). It consists essentially of a guiding frame into which cylindrical samples (diameter D = 7 cm, height H = 16 cm) can be clamped.

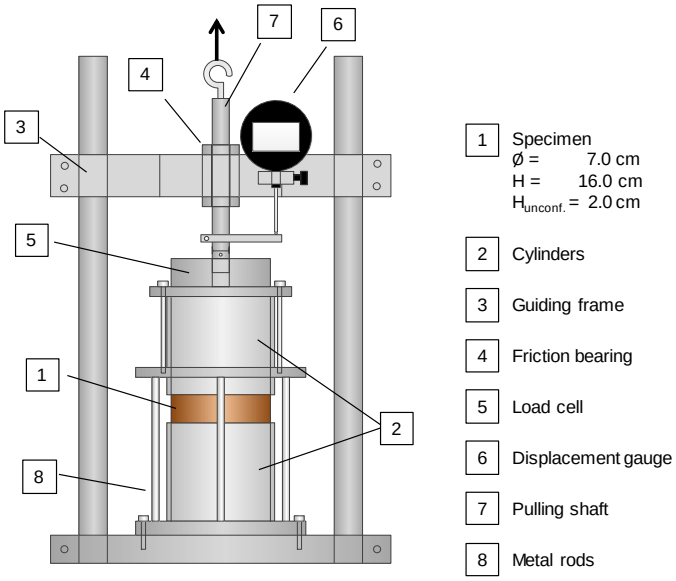

Figure 6.14: Uniaxial tensile test (UTT) apparatus

The sample is axially loaded through a pulling shaft, guided by a friction bearing. This way of applying the load ensures exact centric pulling and avoids the application of a moment or horizontal forces to the sample's top. The force applied through the pulling shaft is transferred to the soil sample via the slightly roughened walls of two cylinders (D = 7 cm, H = 7 cm), which confine the sample in the upper and lower area. The lower cylinder is fixed to the base plate of the guiding frame, while the upper cylinder is directly connected to the pulling shaft. In this way, the load is applied to the specimen over a large area, which is why an approximately homogeneous stress-strain field can be expected. In order to create a

controlled uniaxial total stress state, the mid-section of the sample between the two cylinders is unconfined.

To enable displacement-controlled loading, the guiding frame is situated in an electromechanical load frame. Note that a fine-resolution load cell (measuring range ± 200 N, accuracy 0.1%) was used to measure the expected small forces.

In order to minimize the influence of frictional or compressive forces generated by the testing system on the measured force, the load cell is placed below the frictional bearing and the displacement gauge. Any vertical loading of the unsupported mid-section of the sample prior to tensile force application through the dead weight of the components of the upper testing system is minimized by vertically supporting the upper cylinder with three metal rods, attached to the base plate.

6.3.2 Sample preparation and test procedure

All tests were carried out on as-compacted samples. The silty sand characterized in Chapter 5 was statically compacted by means of a hydraulic press. During compaction, a split mold was attached to the mid-section of the sample between the two cylinders, while the upper cylinder was fixed to the metal rods (Figure 6.15a).

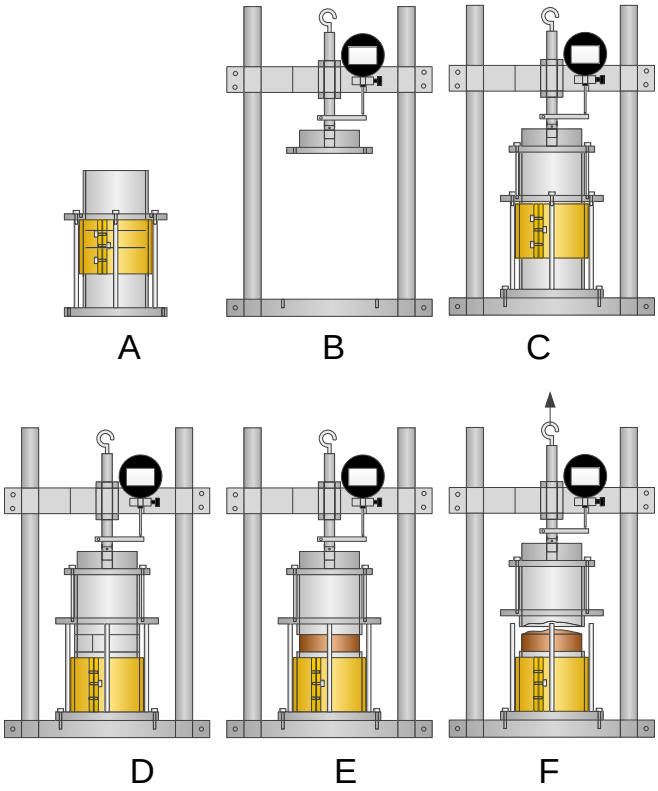

Figure 6.15: Schematic test procedure for uniaxial tensile tests (UTTs)

Static compaction was carried out at target water content to a relative density of I_D = 0.69. The tested levels of compaction water content were chosen to cover the range of low water content detected in the samples taken during the exploratory drilling (Chapter 4). The *in situ*

density of the examined silty sand corresponds to a relative density of I_D = 0.69. This relative density compares well with the medium-dense to dense relative densities explored in the old traffic embankment in Chapter 4, which were seen as representative of the average *in situ* condition. Within the cylinders, compaction was carried out in layers 3-cm thick. The interfaces between the layers were carefully roughened to maximize the composite effect. In order to ensure that the desired force was applied via the lateral edges above and below the unconfined area whilst minimizing the disturbance of the microstructure in that area by an interface, the middle layer was compacted to a height of 4 cm. No undercompaction method could thus be used. However, it was expected that the unconfined mid-section of the sample, which is only 2 cm high, shows a constant density and a homogeneous microstructure corresponding to the target conditions.

After compaction, the specimens were installed into the guiding frame while the split mold and the fixations between the upper and lower cylinders were released (Figure 6.15C to E). Subsequently, the samples were axially loaded with a displacement rate of 0.05 mm/min. For unsaturated soil testing, this deformation rate appears to be fast (Section 2.4.1.3). In this case, however, it ensured that the sample did not dry out significantly during the test. As described in Section 2.4.1.4, a relatively fast shearing rate can be chosen for constant water content tests without suction control. The chosen displacement rate thus proved appropriate for the UTTs.

After full specimen separation, the weight of the upper half of the cylinder was measured and subtracted from the tensile force, together with the soil mass contained therein (Figure 6.15-F). At least two tests were carried out on samples with the same water content in order to check the reproducibility of the test results. The water content of the specimen was checked after each test. Only a minor degree of dehydration was observed during the tests.

A summary of the UTTs performed may be found in Table 6.1.

# - UTT	$w_{comp.}$ [%]	$w_{test\ end}$ [%]	ρ_d [g/cm³]	e [-]	I_D [-]
1	1.8	1.40	1.683	0.563	0.689
2	1.8	1.37	1.683	0.563	0.689
3	2.2	1.61	1.683	0.563	0.689
4	2.2	1.60	1.683	0.563	0.689
5	3.3	2.64	1.683	0.563	0.689
6	3.3	2.64	1.683	0.563	0.689
7	4.3	3.52	1.683	0.563	0.689
8	4.3	3.67	1.683	0.563	0.689
9	6.5	5.81	1.683	0.563	0.689
10	6.5	5.66	1.683	0.563	0.689
11	7.2	6.52	1.683	0.563	0.689
12	7.2	6.52	1.683	0.563	0.689
13	8.9	7.94	1.683	0.563	0.689
14	8.9	7.94	1.683	0.563	0.689

Table 6.1: Summary and designations of uniaxial tensile tests (UTTs)

6.4 Unconfined compression tests

6.4.1 Apparatus and Test Setup

The unconfined compression tests (UCTs) were carried out in the guiding frame already used for the uniaxial tensile tests (UTTs). For this purpose, the cylinders used for uniaxial tensile testing were replaced by polished stainless steel plates arranged both below the specimen and below the load cell (Figure 6.16).

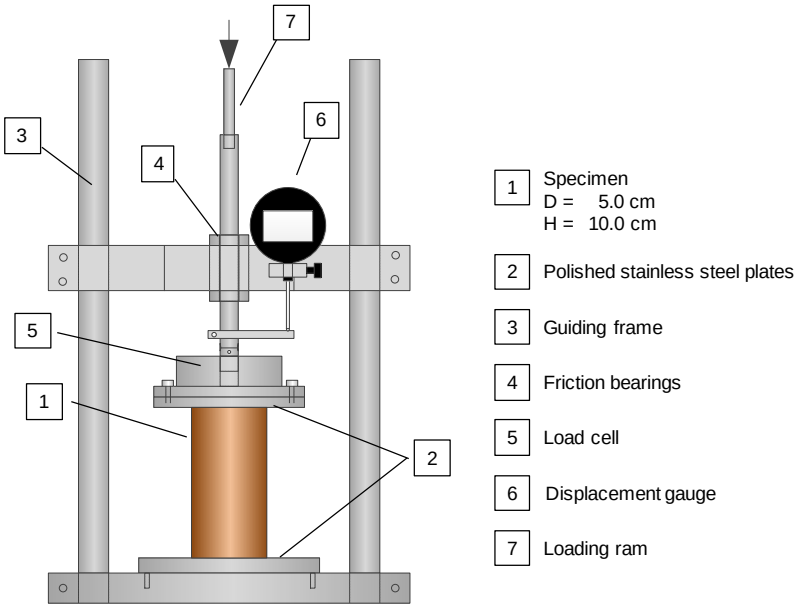

Figure 6.16: Unconfined compression test (UCT) apparatus

6.4.2 Sample preparation and test procedure

As-compacted soil samples with of height H = 10 cm and diameter D = 5 cm were prepared by statically compacting them into a split mold using the undercompaction method already described in Section 5.4.2.

After placing the as-compacted specimens into the guiding frame, the split mold was carefully removed. Subsequently, the loading stamp was lowered until the sample was just prior to contact with the upper stainless steel plate to which the load cell was attached. This procedure allowed the specimen to shear without a preceding uncontrolled loading (e.g., by the dead weight of a top cap). Contact detection between specimen and loading stamp was thus part of the sample loading.

Analogously to the UTTs, the specimens for the UCTs were loaded with a displacement rate of 0.05 mm/min.

At very low compaction water content, the edges of the samples tended to break off after stripping the formwork. For these samples, the edges of the specimen surfaces were stabilized by dripping a little bit of silicone oil before removing the formwork. This was done to allow the application of the compressive force to a controlled sample area. The silicone oil

penetrated the sample only a few millimeters, which is why no effects on shear strength were expected.

At the end of the test, the final water content of each sample was checked. Only slight dehydration was detected during the testing period. To check the reproducibility of the results, at least two tests were carried out for each level of compaction water content. Table 6.2 summarizes the UCTs.

# - UCT	$w_{comp.}$ [%]	$w_{test\ end}$ [%]	ρ_d [g/cm³]	e [-]	I_D [-]
1	2.2	1.6	1.683	0.563	0.689
2	2.2	1.6	1.683	0.563	0.689
3	4.4	3.6	1.683	0.563	0.689
4	4.4	3.7	1.683	0.563	0.689
5	7.2	5.9	1.683	0.563	0.689
6	7.2	5.8	1.683	0.563	0.689
7	8.9	8.1	1.683	0.563	0.689
8	8.9	7.9	1.683	0.563	0.689
9	8.9	8.0	1.683	0.563	0.689

Table 6.2: Summary and designations of unconfined compression tests (UCTs)

6.5 Test results and discussion

6.5.1 Uniaxial tensile tests and unconfined compression tests

Figure 6.17 shows the evolution of the measured tensile forces with vertical displacement for each uniaxial tensile test (UTT). The labeling of the results refers to the water content measured at the end of the tests (Table 6.1). The peaks of the tensile forces are generally reached at small vertical displacements of 0.1 mm for the samples compacted at the lowest water content, 1.8%, up to 0.3 mm for the samples compacted at the highest water content, 8%. Since the deformation field was not directly measured, no strains were calculated for the tensile tests.

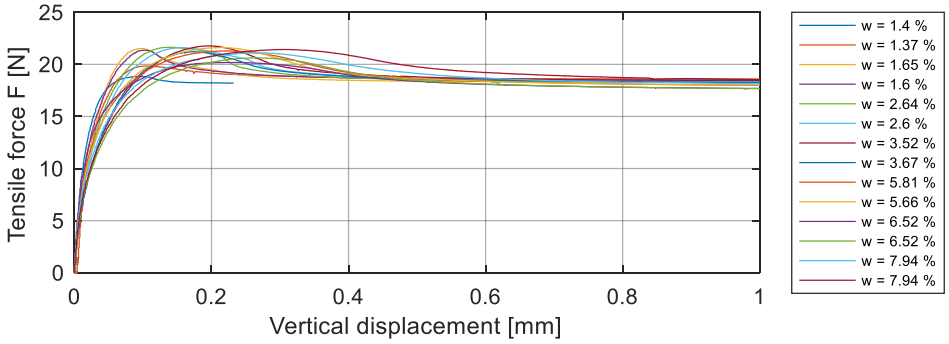

Figure 6.17: Tensile force F vs. vertical displacement for the tested samples

After complete separation of the upper and lower part of the specimen (Figure 6.15F), the force F_{ult} generated by the weight of the upper cylinder including the soil was subtracted from the measured peak tensile force F_{peak} and the tensile strength was derived from

$$\sigma_t = \frac{F_t}{A_t} = q_t, \tag{6.9}$$

where $F_t = F_{peak} - F_{ult}$. The determined tensile strengths are shown in Figure 6.18a. Note that the tensile strength represents the deviatoric stress at peak q_t (Section 6.2.3).

The degree of saturation in Figure 6.18 was calculated from the measured water content at the end of the experiments and from the initial density, neglecting the small changes in density and water content upon peak.

In general, the tensile strength σ_t derived from the experiments showed a high degree of repeatability (Figure 6.18). At degrees of saturation ranging between approximately Sr = 6.5% and Sr = 40%, σ_t varies in a narrow range of σ_t = 0.7 kPa to 1.0 kPa.

At a degree of saturation of approximately Sr = 6.5%, σ_t drops to zero. This behavior indicates that—at this low water content—the soil-water was present only within the aggregates and did not contribute to the inter-particle forces between the sand particles and the aggregates.

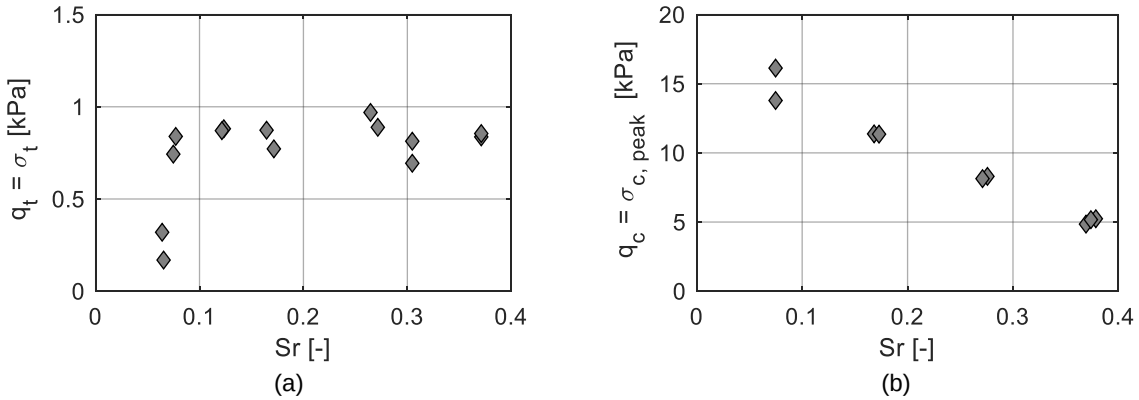

Figure 6.18: (a) Tensile strength q_t and (b) unconfined compressive strength q_c vs. degree of saturation Sr

For each UCT, Figure 6.19 shows the axial compressive stress σ_c as a function of the axial strains ε_a.

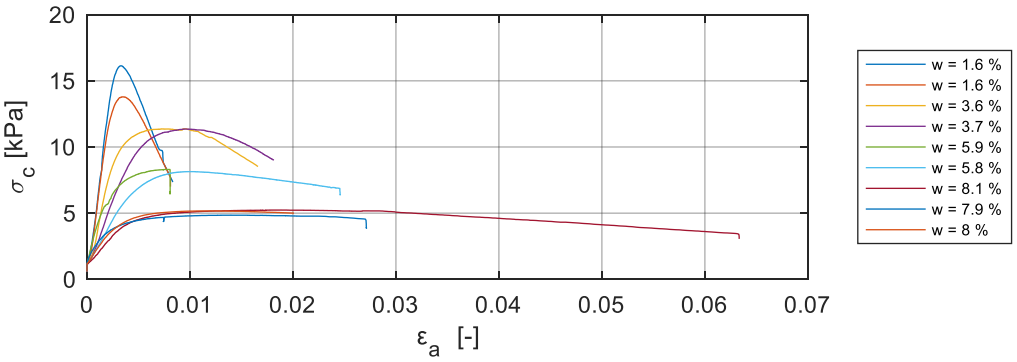

Figure 6.19: Axial compression stress σ_c vs. axial strain ε_a for the tested samples

The data were corrected for the influence of the dead weight of the specimen. In this way, the compressive stress was evaluated in the mid-section of the samples as follows:

$$\sigma_c = \frac{F_c}{A_c} + (1 + w_{test\ end}) \cdot \rho_{d,0} \cdot g \cdot \frac{H_0}{2} \tag{6.10}$$

with

F_c	Compression force
A_c	Initial cross section of the specimen
$w_{test\ end}$	Water content at the end of the test
$\rho_{d,0}$	Initial dry density
H_0	Initial sample height
G	Gravity constant.

Since no volumetric or radial deformations were measured, the stresses were not corrected for the deformed sample geometry. However, due to the quite small axial strains necessary to reach peak, the errors induced by this assumption can be considered negligible.

From Figure 6.19 it can be seen that the behavior of the samples in the UCTs is rather brittle for low compaction water content. This brittleness was also observed from the formation of clear shear bands in the post-peak regime of these samples. At the highest compaction water content, however, the samples' behavior is more ductile. The latter behavior is well reflected in the σ_c - ε_a diagram, as no pronounced peak is detectable there. Correspondingly, no pronounced shear bands were observed.

Figure 6.18b shows the unconfined compressive strength $q_c = \sigma_{c,\ peak}$—obtained from the peak state of the σ_c - ε_a curves—as a function of degree of saturation. The degree of saturation was calculated from the measured water content at the end of the experiments and from the initial density, neglecting the small density changes upon peak. Again, the test results showed a high degree of repeatability while q_c decreased approximately linearly from the highest measured value of $q_c \approx 15$ kPa at Sr = 7.5% to $q_c \approx 5$ kPa at Sr = 37%.

Note that the minimum water content tested in the UCTs (w = 1.6%) was slightly higher than the compaction water content tested in the UTTs (w = 1.4%), since for w = 1.4% (Sr = 6.5%), the UTT specimens collapsed due to their self-weight as soon as the split mold was removed ($F_c = 0$).

This result confirms the assumption that the soil-water withdraws into the aggregates at these degrees of saturation and does not significantly contribute to the effective stress state. Note that although $q_c \approx 0$ kPa might be assumed for Sr = 6.5%, according to (6.10), the unconfined compressive strength for $F_c = 0$ is only known to be $0 \leq q_c < \text{approx.}\, 17 \frac{\text{kN}}{\text{m}^3} \cdot 0.1\ \text{m} = 1.7\ \text{kPa}$, if the self-weight of the sample of height 10 cm is taken into account. Since q_c is not exactly known for Sr = 6.5%, it is not included in Figure 6.18b.

6.5.2 Effective stress and peak friction angle

Due to their rather ductile behavior, it was not clear whether the assumption of a constant suction during the test is fulfilled for the samples of the UTTs and UCTs at the highest water content of w ≈ 8% (Section 2.4.1.5).

However, note that Figure 6.8c shows that even for samples compacted at w_{comp} = 10%, the measured SWRCs showed no pronounced dependency on the density when suction was depicted as a function of gravimetric water content. The UCTs and UTTs at the highest water content were therefore also used to evaluate the suction-induced effective stress and the peak friction angle as follows.

Interpreting q_t as the shear strength in triaxial extension test and q_c as the shear strength in triaxial compression test—both characterized by the same friction angle φ'_{peak} according to

Mohr–Coulomb (see Figure 6.10)—the isotropic suction-induced effective stress $\Delta\sigma' = p_0'$ can be derived from the unconfined compressive strength q_c:

$$\Delta\sigma' = p_0' = \frac{q_c}{M_{c,peak}} - \frac{q_c}{3} = q_c \cdot \left(\frac{1 - \sin\varphi'_{peak}}{2 \cdot \sin\varphi'_{peak}}\right) \tag{6.11}$$

with $$M_{c,peak} = \frac{6 \cdot \sin\varphi'_{peak}}{3 - \sin\varphi'_{peak}},$$

or from the uniaxial tensile strength q_t

$$\Delta\sigma' = p_0' = \frac{q_t}{M_{e,peak}} + \frac{q_t}{3} = q_t \cdot \left(\frac{1 + \sin\varphi'_{peak}}{2 \cdot \sin\varphi'_{peak}}\right) \tag{6.12}$$

with $$M_{e,peak} = \frac{6 \cdot \sin\varphi'_{peak}}{3 + \sin\varphi'_{peak}}.$$

Assuming the same suction-induced effective stress for both test types at the same initial conditions, the peak friction angle is obtained by equating (6.11) and (6.12):

$$\sin\varphi'_{peak} = \frac{q_c - q_t}{q_c + q_t}. \tag{6.13}$$

Since the experiments were carried out on as-compacted samples, the microstructure of the specimens differed for the various compaction water content. Therefore, only UTTs and UCTs with similar compaction water content were used to evaluate the peak friction angle and the suction-induced effective stress. For data processing, an averaged degree of saturation was calculated from the degrees of saturations measured on the samples of the UCT and UTT at the end of the tests (Table 6.3).

The peak friction angles derived from the experimental results with (6.13) are shown in Figure 6.20a. The suction-induced effective stresses are depicted in Figure 6.20b.

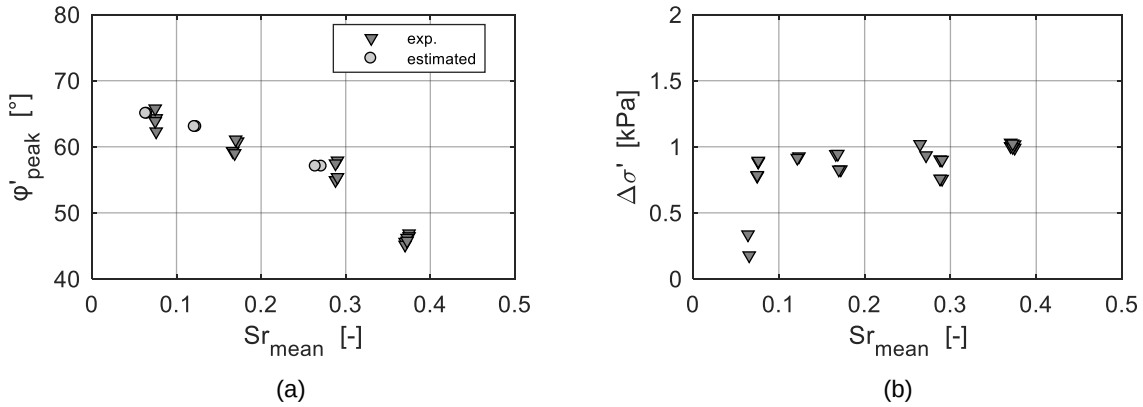

Figure 6.20: (a) Secant peak friction angle φ'_{peak} and (b) suction-induced effective stress $\Delta\sigma'$ vs. mean degree of saturation Sr_{mean}

# UCT	w_0 [%]	$w_{end\ test}$ [%]	Sr [%]	# UTT	w_0 [%]	$w_{end\ test}$ [%]	Sr [%]	Sr_{mean} [%]
1	2.20	1.60	7.48	**3**	2.20	1.65	7.71	7.60
1	2.20	1.60	7.48	**4**	2.20	1.60	7.48	7.48
2	2.20	1.60	7.48	**3**	2.20	1.65	7.71	7.60
2	2.20	1.60	7.48	**4**	2.20	1.60	7.48	7.48
3	4.40	3.60	16.83	**7**	4.30	3.52	16.45	16.64
3	4.40	3.70	17.29	**8**	4.30	3.67	17.15	17.22
4	4.40	3.60	16.83	**8**	4.30	3.67	17.15	16.99
4	4.40	3.70	17.29	**7**	4.30	3.52	16.45	16.87
5	7.20	5.90	27.58	**11**	7.20	6.52	30.47	29.03
6	7.20	5.80	27.11	**12**	7.20	6.52	30.47	28.79
5	7.20	5.90	27.58	**12**	7.20	6.52	30.47	29.03
6	7.20	5.80	27.11	**11**	7.20	6.52	30.47	28.79
7	8.90	8.10	37.86	**13**	8.90	7.94	37.11	37.49
7	8.90	8.10	37.86	**14**	8.90	7.94	37.11	37.49
8	8.90	7.90	36.92	**13**	8.90	7.94	37.11	37.02
8	8.90	7.90	36.92	**14**	8.90	7.94	37.11	37.02
9	8.90	8.00	37.39	**13**	8.90	7.94	37.11	37.25
9	8.90	8.00	37.39	**14**	8.90	7.94	37.11	37.25

Table 6.3: Combination of tests used to evaluate φ'_{peak}

Figure 6.20a shows very high peak friction angles ranging from $\varphi'_{peak} = 55°$ at $Sr_{mean} = 29\%$ to $\varphi'_{peak} = 65°$ at $Sr_{mean} = 7.5\%$. The lowest peak friction angle of $\varphi'_{peak} = 46°$ resulted from the highest tested degree of saturation $Sr_{mean} \approx 37\%$. Note that at degrees of saturation for which only UTTs were performed, the peak friction angles could not be derived from (6.13), since the unconfined compressive strength was unknown. To evaluate the suction-induced effective stress for these UTTs, nonetheless, the missing peak friction angles were estimated from the peak friction angles obtained from the experimental results by assuming a gradual evolution of φ'_{peak} with the degree of saturation (Figure 6.20a and Table 6.4). Also note that the tensile strength at $Sr \approx 6.5\%$ lies between $q_t \approx 0.32$ kPa and $q_t \approx 0.17$ kPa (Figure 2.18a and Table 6.4), while q_c is known only to lie between 0 kPa and approximately 1.7 kPa (Section 6.5.1). For this range of q_c, equation (6.13) suggests unrealistic friction angles between $\varphi'_{peak} = -90°$ for $q_c = 0$ kPa and $\varphi'_{peak} = 55°$ for $q_c = 1.7$ kPa. For this reason, the friction angle at $Sr \approx 6.5\%$ was assumed to correspond to the friction angle of $\varphi'_{peak} = 65°$ at $Sr = 7.5\%$. This assumption was made because it was not expected that the enhancing effect of suction on the dilatancy would have vanished from $Sr = 7.5\%$ to $Sr = 6.5\%$, according to the findings in Section 2.4.2.

Based on the observed and estimated peak friction angles, the suction-induced effective stress shown in Figure 6.20b was determined with (6.12) for each UTT. At degrees of saturation ranging from $Sr_{mean} = 7.5\%$ to 37%, the increase in effective stress due to suction is remarkably constant at $\Delta\sigma' = 0.8$ kPa to 1.0 kPa. However, between $Sr_{mean} = 6.5\%$ and $Sr_{mean} = 7.5\%$, $\Delta\sigma'$ rapidly drops toward zero, indicating the withdrawal of the pore water into the aggregates.

$w_{t\ end}$ [%]	$w_{c\ end}$ [%]	q_t [kPa]	q_c [kPa]	φ'_{peak} [°]	$\Delta\sigma'$ [kPa]	Sr_{mean} [%]	s_{mean} [kPa]
1.65	1.60	0.84	16.14	64.31	0.89	7.60	532.25
1.60	1.60	0.74	16.14	65.78	0.78	7.48	576.46
1.65	1.60	0.84	13.81	62.30	0.89	7.60	532.25
1.60	1.60	0.74	13.81	63.88	0.79	7.48	576.46
3.52	3.60	0.87	11.61	59.33	0.94	16.64	45.77
3.67	3.70	0.77	11.37	60.79	0.83	17.22	26.23
3.67	3.60	0.77	11.61	61.08	0.83	16.99	32.66
3.52	3.70	0.87	11.37	59.02	0.95	16.87	36.28
6.52	5.90	0.69	8.38	57.90	0.76	29.03	3.16
6.52	5.80	0.81	8.15	54.93	0.90	28.79	3.20
6.52	5.90	0.81	8.38	55.40	0.90	29.03	3.16
6.52	5.80	0.69	8.15	57.46	0.76	28.79	3.20
7.94	8.10	0.84	5.36	46.87	0.99	37.49	2.20
7.94	8.10	0.85	5.36	46.44	1.02	37.49	2.20
7.94	7.90	0.84	5.02	45.60	1.00	37.02	2.23
7.94	7.90	0.85	5.02	45.16	1.03	37.02	2.23
7.94	8.00	0.84	5.18	46.20	1.00	37.25	2.21
7.94	8.00	0.85	5.18	45.77	1.02	37.25	2.21
'peak estimated from the above results							
1.40	-	0.17	-	65.00	0.18	6.54	3440.43
1.37	-	0.32	-	65.00	0.34	6.40	6858.80
2.64	-	0.88	-	63.00	0.93	12.34	114.56
2.60	-	0.87	-	63.00	0.92	12.15	116.61
5.81	-	0.89	-	57.00	0.93	27.16	3.53
5.66	-	0.97	-	57.00	1.02	26.45	3.71

Table 6.4: Summary of test results from uniaxial tests

Figure 6.21 shows the peak friction angle (estimated friction angles excluded) as a function of the suction-induced effective stress. Although some tendency of decreasing friction angle with increasing effective stress can be observed, this trend is rather arbitrary, according to comparison of the results derived from tests on as-compacted samples with different microstructures. Obviously, the different microstructures have a stronger influence on the peak friction angle than the effective stress.

From Figure 6.20a, it can be seen that the peak friction angle is the highest for the lowest degree of saturation while it decreases with increasing saturation. This relationship can be traced back to the microstructure of the soil. At low degrees of saturation, the samples were compacted at low water content, which produced an aggregated soil structure (Figure 5.9). The lower the compaction water content, the more aggregated fines. When assuming fully saturated aggregates throughout all tests (even at the lowest tested water content), suction directly corresponds to a kind of intra-aggregate (effective) stress ($\chi_{aggregate} = 1$).

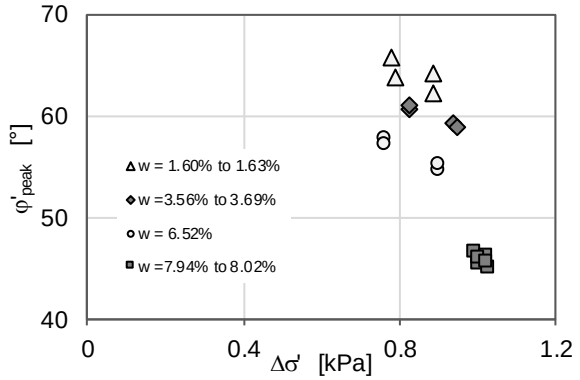

Figure 6.21: Secant peak friction angle φ'_{peak} vs. suction-induced effective stress $\Delta\sigma'$

The intra-aggregate stress therefore increases with increasing suction and increasingly stabilizes the aggregates. Decreasing compaction water content leads therefore to an increasing number of aggregates, which also become more stable due to increasing suction. Both effects enhance the tendency of the soil to dilate when sheared, which in turn increases the secant peak friction angle. Vice versa, with increasing compaction water content, the microstructure tends to show more unimodal porosity. Hence, fewer aggregates are formed, and these are also less stable. The latter two effects reduce the soil's tendency to dilate, which in turn decreases the secant peak friction angle.

In order to estimate the suction of the as-compacted samples during the tests, an equivalent 'as-compacted' SWRC was derived from the measured SWRCs of the silty sand (Section 5.3.3). The evaluation takes advantage of the finding from Section 5.4.4 that the microstructure of the as-compacted silty sand is widely preserved when subjected to hydraulic loading. It is therefore not necessary to measure the suction of an as-compacted sample directly on the sample. The suction can also be obtained from an SWRC measured on samples compacted at the same level of water content. Therefore, the suction of the as-compacted specimens used for UTTs and UCTs was derived from the parameterized SWRC determined in Section 5.3.3. For each compaction water content, the degree of saturation was calculated and the suction was obtained from the corresponding SWRC, as shown in Figure 6.22.

To limit the scope of the experiments, an SWRC was not determined for each tested compaction water content w_{comp}. The thereby missing SWRCs were obtained by using (5.1). The corresponding parameters were estimated with (5.2) applying a constant relative density $I_D = 0.69$. This method resulted in an SWRC for each w_{comp}. In doing so for a wider range of w_{comp}, an 'as-compacted' SWRC was obtained. The general procedure is illustrated in Figure 6.23.

The effective degree of saturation

$$S^e = \frac{Sr - Sr_0}{Sr_{max} - Sr_0} = N_1 \cdot (1 + (a_1 \cdot s)^{n_1})^{-m_1} + N_2 \cdot (1 + (a_2 \cdot s)^{n_2})^{-m_2} \quad (6.14)$$

was used to fit the bimodal 'as-compacted' SWRC (Figure 6.23).

For this purpose, based on the experimental results, the degree of saturation at which the effective stress had to disappear was set to $Sr_0 = 0.063$ (Figure 6.20b). Similarly, the maximum degree of saturation was defined as $Sr_{max} = 0.8$. The resulting parameters are summarized in Table 6.5.

#	N_1	N_2	a_1	a_2	m_1	m_2	n_1	n_2
as-comp	1	0.14	1.1	0.015	0.11	0.2	13	5

Table 6.5: Parameters in (6.14) for the as-compacted SWRC

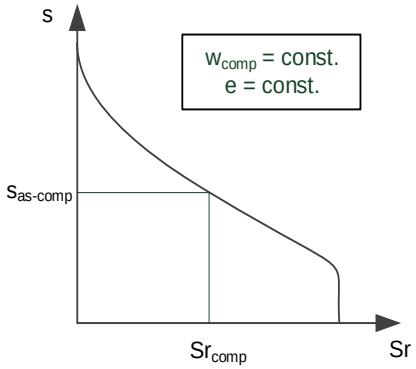

Figure 6.22: Determination of the suction in as-compacted samples

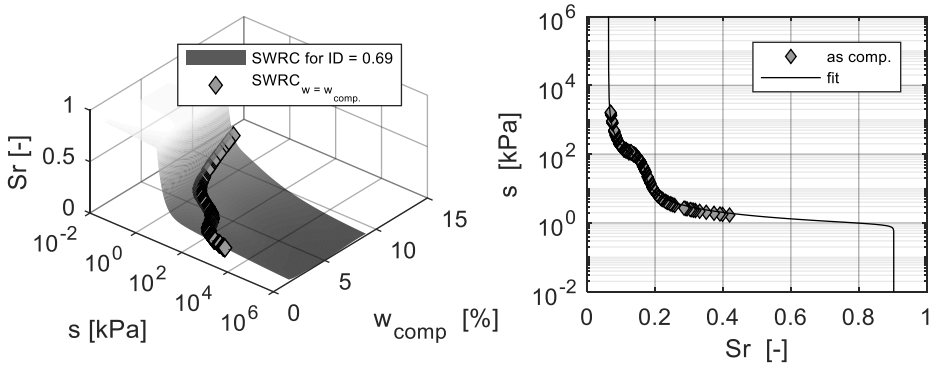

Figure 6.23: Determination of the 'as-compacted' SWRC for $I_D = 0.69$

Note that the above procedure is valid within the range of experimentally examined w_{comp}. An extrapolation to water content other than those used to determine the SWRCs may result in erroneous results. However, in order to account for the smallest compaction water content tested in the uniaxial tests ($w_{comp.} = 1.8\%$), this range was extended in this case. This extension was made because no significant change in the trend of the parameters of (5.1) was expected for low w_{comp}.

To evaluate the data from the UTTs and UCTs, suctions corresponding to the averaged degrees of saturation as already described in the previous chapter were derived from the as-compacted SWRC. The results are summarized in Table 6.4.

In Figure 6.24, the secant peak friction angle and the suction-induced effective stress are depicted as a function of suction.

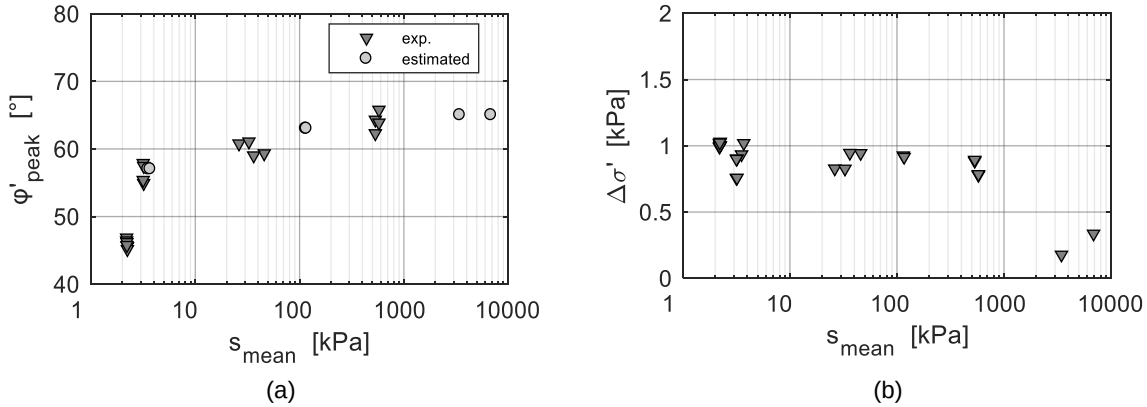

(a) (b)

Figure 6.24: (a) Secant peak friction angle φ'_{peak} and (b) suction-induced effective stress $\Delta\sigma'$ vs. mean suction s_{mean}

Since the degree of saturation and suction depend on one another via the SWRC, the observations made above for the friction angle and the effective stresses as a function of the degree of saturation analogously apply to the results as a function of suction. Obviously, the peak friction angle is strongly influenced by suction, confirming above assumptions that there are fewer and less stable aggregated fines with increasing compaction water content. Compaction at low water content induces high suctions, which stabilize a larger number of aggregates. When assuming fully saturated aggregates ($\chi_{aggregate} \approx 1$), suction induces an intra-aggregate stress ($1 \cdot s$) up to several hundred kilopascals. The tendency of the soil to dilate increases with increasing suction, which in turn increases the secant peak friction angle.

Note that the effective stress was not affected by the intra-aggregate stress, as the soil-water had withdrawn completely into the aggregates. This conclusion can also be drawn because the suction-induced effective stress vanishes at high suctions (Figure 6.24b).

6.5.3 State variable χ

The state variable can be derived from the suction-induced effective stress and from the suction, estimated from the as-compacted SWRC, as follows:

$$\chi_{exp.} = \frac{\Delta\sigma'_{exp.}}{s}. \tag{6.15}$$

Figure 6.25a shows the 'as-compacted' SWRC obtained with (6.14). Figure 6.25b shows the experimentally obtained state variable χ as a function of degree of saturation.

At low degrees of saturation between Sr_{mean} = 7% and 17%, the results show that the state variable χ is well below the curve representing χ = Sr. In this range of low degrees of saturation, χ increases only slightly with decreasing degree of saturation. At degrees of

saturation between Sr_{mean} = 28% and 37.5%, the general trend of χ changes. The values of χ lie on or above the line $\chi = Sr$ and increase considerably with decreasing degree of saturation. When these values are compared with the 'as-compacted' SWRC (Figure 6.25a), it can be seen that the change in $\Delta\chi/\Delta Sr$ occurs in the range of the transition from microporosity to macroporosity.

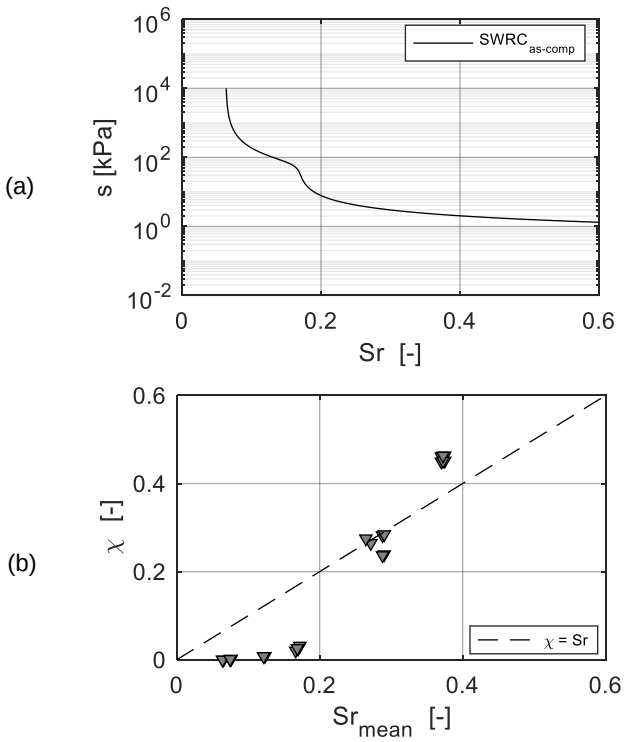

Figure 6.25: (a) As-compacted SWRC and (b) χ as a function of degree of saturation

Figure 6.26 shows that when depicting χ as a function of the suction ratio s/s_{AE} in a double-logarithmic scale, an approximately linear trend is observed. Note that the air entry value s_{AE} = 1.1 kPa of the 'as-compacted' SWRC was chosen to calculate the suction ratio s/s_{AE}. The suction s corresponds to s_{mean} estimated from the 'as-compacted' SWRC, as described above.

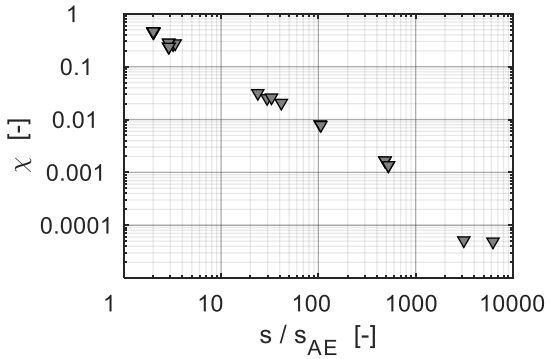

Figure 6.26: State variable χ vs. suction ration s/s_{AE}

In order to fit χ to the experimental data, two approaches were used. The first was the equation proposed by Khalili and Khabbaz (1998),

$$\chi = \begin{cases} 1 & \text{for } s \leq s_{AE} \\ \left(\frac{s}{s_{AE}}\right)^{m} & \text{for } s > s_{AE} \end{cases}, \tag{6.16}$$

which requires two parameters, the exponent m and the air entry value s_{AE} of the SWRC.

The second is based on the description of χ as a function of the effective degree of saturation (see Section 2.5.3):

$$\chi = \begin{cases} 1 & \text{, for } s \leq s_{AE} \\ \left(\langle\frac{Sr - Sr_0}{Sr_{max} - Sr_0}\rangle\right)^{\alpha} & \text{, for } s > s_{AE} \end{cases}. \tag{6.17}$$

The latter approach requires four parameters, the degree of saturation at which the effect of the suction on effective stress disappears (Sr_0), the maximum degree of saturation (Sr_{max}), the exponent α and the air entry value s_{AE} of the SWRC.

The parameters for both expressions were obtained from non-linear least square fitting to χ derived from the experimental data. The results are depicted in Figure 6.27.

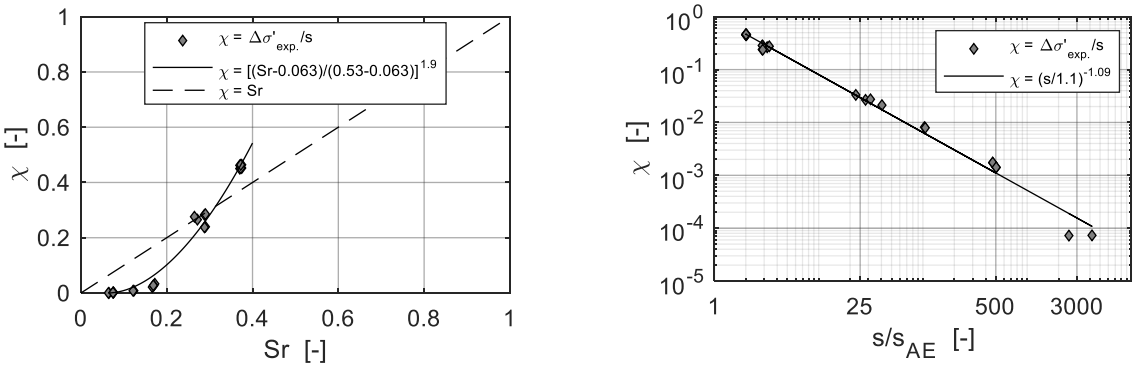

Figure 6.27: (a) State variable χ from (6.17) vs. degree of saturation Sr. (b) State variable χ from (6.16) vs. suction ratio s/s_{AE}

Figure 6.27a shows the experimentally determined χ and the best fit of (6.17). A maximum degree of saturation of Sr_{max} = 0.53 and an exponent α = 1.9 are necessary to reproduce the experimental results. Although a value of Sr_{max} = 0.53 is not a physically meaningful measure, it serves well as a fitting parameter. Note that Sr_0 was not considered a fitting parameter but was set to 0.063 in order to force the breakdown of the suction-induced effective stress at this degree of saturation, according to the experimental results (Table 6.4). At high degrees of saturation, (6.17) seems to fit the test results quite well, although it tends to overestimate χ at low degrees of saturation.

Figure 6.27b shows the performance of (6.16) in a double-logarithmic scale. Using the air entry value of s_{AE} = 1.1 kPa, m = −1.09 is necessary to fit the experimental results. The exponent m = −1.09 is smaller than Khalili's exponent m = −0.55 but compares well to the findings on the exponent for compacted silty sand with similar fines content in Section 3.4 (m = −1.05). The fit with m = −1.09 works well over the entire range of the tested suction ratios, even for s/s_{AE} >> 25. Therefore, the limitation to the applicability of a unique exponent m to suction ratios s/s_{AE} < 25—as mentioned by Khalili and Khabbaz (1998) and applied by Russell (2004) to a clean sand—is not necessary for the examined silty sand.

Figure 6.28 shows the experimental and predicted χ for both approaches over the entire range of degrees of saturation Sr.

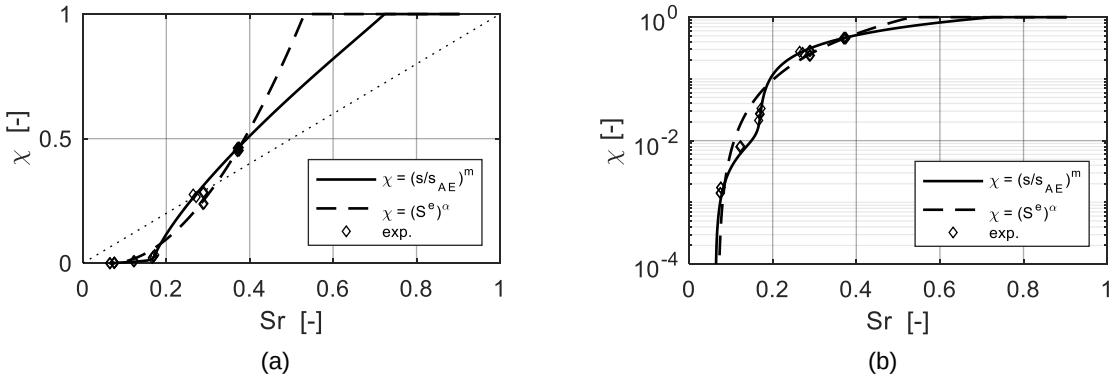

Figure 6.28: Experimental and predicted state variable χ vs. degree of saturation Sr. (a) Linear scale. (b) Semi-logarithmic scale

Presented in a semi-logarithmic scale, it appears that Khalili's expression (6.16) can reproduce the change in the general behavior of χ between Sr ≈ 20% to 30% (Figure 6.28b). Equation (6.17), on the other hand, is not appropriate to capture correctly the behavior in this range of degrees of saturation. In addition, for Sr > Sr_{max} = 53%, the predicted state variable χ was manually set to 1. Otherwise, (6.17) would have predicted values χ > 1, which is considered unrealistic.

The performance of both approaches can be better illustrated by comparing the experimental and predicted effective stress (Figure 6.29).

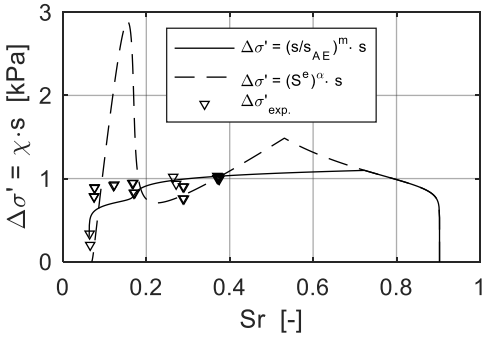

Figure 6.29: Predicted and measured effective stress Δσ' vs. degree of saturation Sr

With regard to the product $\chi \cdot s$, apparently slight deviations in the predicted χ and the measured χ may lead to significant deviations in the predicted effective stress. These deviations are most pronounced at low degrees of saturation corresponding to high suction values. Comparing the prediction of (6.17) with the experimental results confirms this consideration, as the predicted effective stress shows considerable deviation for $Sr < 20\%$. On the other hand, over the entire range of the tested degrees of saturation, the use of (6.16) leads to strong agreement between the predicted and the measured effective stress.

Note that the 'as-compacted' SWRC is described by the van Genuchten type (6.14). Hence, the residual degree of saturation $Sr_0 = 6.3\%$ (which defines the position of the vertical asymptote of the SWRC in the s - Sr - plane) was used to control the degree of saturation at which the predicted effective stress drops to zero.

At $Sr > 40\%$, the predicted effective stress seems to be reasonable only when using (6.16). In this range of degree of saturation, the suction-induced effective stress was not determined experimentally, but according to the findings in Section 3, is likely to stay approximately constant at about $\Delta\sigma' = 1$ kPa until the air entry value of about the same value $s_{AE} = 1$ kPa is reached. This behavior is well captured by (6.16). Equation (6.17), on the other hand, overestimates the effective stress in this region since the maximum degree of saturation was found to be $Sr_{max} = 53\%$. Although this parameter is best suited for fitting the experimental results, it gives too high values at degrees saturations higher than those tested. This is because, in the χ-Sr plane, (6.17) is not able to model a change in the direction of the curvature $\Delta\chi/\Delta Sr$ (Figure 6.28b) indicated by the experimental data and well reproduced by Khalili's expression (6.16). Note that (6.17) would overestimate the effective stress at high degrees of saturation much more if—at degrees of saturation higher than $Sr_{max} = 53\%$—the predicted χ had not been limited to values smaller than or equal to 1 (see above).

In view of the above, the experimental results are best captured by Khalili's equation (6.16) when using $m = -1.09$. Only this expression for χ realistically predicts the suction-induced effective stress for compaction water content outside the range of the experimental investigations.

For these reasons, equation (6.16) and the exponent $m = -1.09$ will be used in the following to describe the suction-induced effective stress in the silty sand under investigation.

6.6 Plausibility control

The findings from the uniaxial tests were checked for plausibility. To achieve this check, the geometry of the failure patterns observed in the UTTs were compared to the theoretical inclinations of the failure surfaces. For this, the experimentally determined effective stress and friction angle were assigned to a soil element vertically loaded by tensile stress (Figure 6.30a).

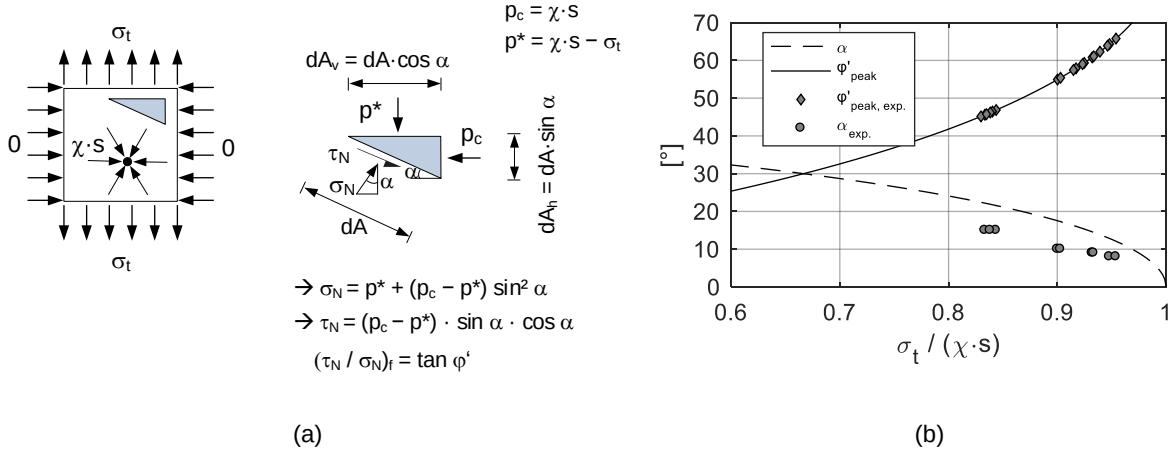

Figure 6.30: (a) Total and effective stress state of a vertically loaded unsaturated soil element. (b) Prediction and experimental results of inclination α of the failure surface and the friction angle φ'_{peak} vs. stress ratio $\sigma_t / (\chi \cdot s)$

This simple model is based on the assumptions made to evaluate the tensile tests (i.e., a suction-induced effective stress that acts isotropically and is not altered during the test). In addition, the tensile stress applied to the element assumed that the stress field was not disturbed by the load applied to the specimen edges. The axial and radial directions therefore represent the principle stress directions.

Meeting these assumptions, the well-known theoretical inclination of the failure surface of the loaded element,

$$\alpha = 45° - \frac{\varphi'_{peak}}{2}, \tag{6.18}$$

was derived. Considering furthermore the interrelations depicted in Figure 6.30a, the representation of both the friction angle and the corresponding expected inclination of the failure surface may be depicted as a function of the ratio $\sigma_t / (\chi \cdot s)$ (Figure 6.30b). The derivation of the expressions for α and φ' as a function of the stress ratio $\sigma_t / (\chi \cdot s)$ can be found in the Appendix D.

Figure 6.31 shows some of the failure patterns observed in the UTTs. In the experiments, the observed failure surfaces were mostly shell-shaped and arched into the upper cylinder. The beginning of the failure surface was observed to start usually at the lower edge of the upper cylinder.

This behavior can be attributed to the influence of the dead weight of the soil, which enhances the tendency of the failure pattern to begin in the upper region of the unconfined mid-section. Only in a few cases was an approximately plane failure surface formed within the unconfined mid-section of the specimen. Although the fracture patterns of the experiments were photographed after each test, the geometry of the failure surfaces was not directly determined. Therefore, the inclination angles α were derived from the photographs of the failure patterns (Figure 6.31). Inclinations between $\alpha = 8°$ and $\alpha = 15°$ were determined from these images. However, the values of α derived from the photographs may be regarded only as approximations of the true values.

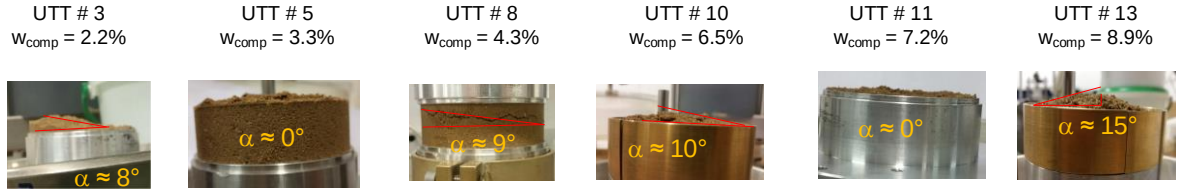

Figure 6.31: Photographs of failure surfaces after uniaxial tensile tests (UTTs #3, #5, #8, #10, #11 and #13)

Note that inclined surfaces did not adjust with every test (UTTs #5 and #11). This lack of adjustment may be intuitively traced back to a marked influence of the load application via the rough walls of the upper cylinder on the stress-strain field. However, when comparing the inclinations of the failure patterns depicted in Figure 6.31 as a function of w_{comp}, it appears evident that the inclination $\alpha = 0°$ observed for UTT #5 and UTT #11 did not reflect a general trend (Figure 6.32).

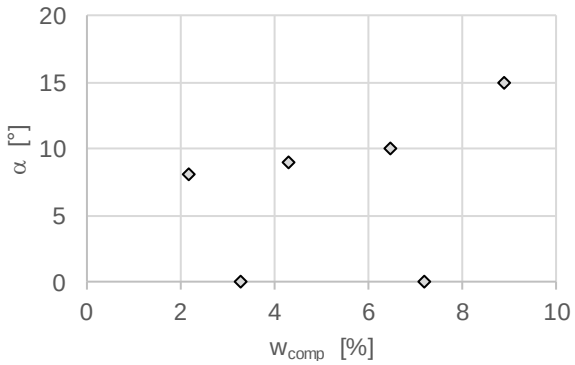

Figure 6.32: Measured inclinations of failure patterns after uniaxial tensile tests (UTTs #3, #5, #8, #10, #11 and #13)

As such, with these samples a significant influence of the load application on the inclination of the slip plane and thus also on the stress field is rather unlikely. It seems more likely that a flattening of the failure surface took place due to weak spots within the samples. When comparing the measured tensile stresses and peak friction angles, the flattening of the failure surface did not cause a significant change in the measured values (Section 6.5.1). Such a change would be the case if the failure surface was formed before reaching the peak of the force-displacement curve. Since the results from the UTTs are insensitive to changes in the failure patterns, they therefore confirm the assumption that at peak there is no pronounced

stress or strain localization. The disturbance of the stress field due to the load application can therefore considered to have no pronounced effect on the measured suction-induced effective stress and on the peak friction angle.

The experimental results for φ'_{peak} and α (α = 0° excluded) are depicted in Figure 6.30b. A satisfactory agreement between the theoretical and the measured inclinations can be observed. Although the measured values of α are approximately 5–10° smaller than the theoretical values, they nevertheless capture the theoretical trend. The deviations of the measured inclinations from the theoretical inclinations may be caused by uncertainties concerning the visual determination of α, by weak spots in the samples, or by the discrepancy between the assumed two-dimensional failure plane in the simple model and the mainly three-dimensional failure pattern of the tested specimens. A small change in the ratio $\sigma_t/(\chi \cdot s)$ would be sufficient to shift the measured values for α to the theoretical line. This shift would lead to only a small decrease in effective stress, on the order of tenths of a kilopascal, which may be considered negligible.

Note that the absolute agreement between the measured friction angles and the theoretical friction angles is implicitly based on the model's conception and can therefore not be used for plausibility control.

In summary, the simple model confirmed the plausibility of the framework for the interpretation of UTTs. The assumptions made for the interpretation of the uniaxial tensile and UCTs were implicitly included in the model. Even though the assumptions made cannot clearly be confirmed with the help of this model, they do, however, result in a model for the appropriate interpretation of UTTs and UCTs within a continuum mechanical framework.

6.7 Summary and conclusion

Based on micro-mechanical considerations, a theoretical framework was developed to experimentally determine both the suction-induced effective stress and the peak friction angle from UTTs and UCTs. Within this framework, the uniaxial tests represent a suitable means of evaluating the shear strength of an as-compacted silty sand at low effective stresses and low water content.

The experiments revealed high peak friction angles ranging from approximately $\varphi'_{Peak} = 45°$ to $\varphi'_{Peak} = 65°$ at low suction-induced effective stresses of about $\Delta\sigma' = 1$ kPa. Changes in microstructure resulting from different compaction water content were directly reflected in the measured peak friction angles. The highest friction angles were determined for samples with the most pronounced double porosity due to aggregated fines and the highest suction. Both decreasing suction and decreasing double porosity had a diminishing effect on the peak friction angle.

The experimentally determined suction-induced effective stresses showed constant values of approximately $\Delta\sigma' = 0.8$ kPa to $\Delta\sigma' = 1$ kPa for all samples except for the samples compacted at $w_{comp} < 2\%$, corresponding to $Sr < 6 - 7\%$. At these low levels of water content, the effect of suction on the effective stress vanished, as the soil water withdrew into the intra-aggregate pores. In the UTTs, this absence of inter-aggregate water was reflected by a sudden decrease in the measured tensile strengths toward zero, while in the UCTs, the samples collapsed due to their self-weight. For test evaluation, an equivalent SWRC capturing the as-compacted states was used to derive the corresponding suctions.

The measured effective stresses were best captured by Khalili's equation (6.16). A unique exponent $m = -1.09$ and a unique air entry value $s_{AE} = 1.1$ kPa derived from an 'as-compacted' SWRC were sufficient to describe the measured effective stresses over a wide range of suction ratios from $s/s_{AE} \approx 3$ to $s/s_{AE} \approx 6000$. For these reasons, equation (6.16) was identified as an appropriate approach to describe Bishop's effective stress variable χ if the exponent $m = -1.09$ is used.

Using (6.16) as an approach for χ, it is possible to determine the suction-induced effective stress in triaxial tests under the provision that the air entry value and its evolution with microstructure and density is known. Regarding the small magnitude of the measured suction-induced effective stresses, however, it may be expected that the influence of suction on the effective stress, and therefore on shear strength, will be negligible. In this context, any observed increase in shear strength due to suction can be expected to mainly correspond to a microstructure-induced increase in dilatancy. In more detail, when assuming fully saturated aggregates ($\chi_{aggregate} \approx 1$), suction induces an intra-aggregate stress ($1 \cdot s$) up to several hundred kilopascals which causes an inherent strength of the aggregates but does not considerably affect the effective stress state as defined in section 6.2. The higher the suction, the stronger the aggregates and the higher the dilatancy.

This expectation will be discussed in more detail in the following chapter.

7 Shear strength from triaxial tests

7.1 Experimental program

To explore the saturated shear strength of the silty sand, drained triaxial compression tests (i.e., CD tests) were carried out on dense saturated samples at confining pressures ranging from 10 kPa to 200 kPa. The influence of the initial microstructure on the shear strength was investigated by additional tests on saturated samples compacted at different levels of water content varying from w_{comp} = 2% to w_{comp} = 10% (Becker 2017).

To determine the shear strength of the unsaturated silty sand, conventional triaxial compression tests at constant water content (CW tests) were carried out on as-compacted medium-dense to dense samples at confining pressures ranging from 25 kPa to 100 kPa. For these tests, a compaction water content of w_{comp} = 3% was chosen throughout.

Since the evaluation of the CW tests presupposes constant suction during the tests, this assumption was checked by conducting suction-controlled triaxial compression tests (CS tests) at a confining pressure of 25 kPa. Suction was controlled with the axis-translation technique (Section 2.4.1.1). Samples compacted at w_{comp} = 3% and w_{comp} = 6% were tested. The corresponding suctions were selected according to the 'as-compacted' SWRC to be s = 46.8 kPa for w_{comp} = 3% and s = 6.8 kPa for w_{comp} = 6%. To investigate the influence of variations of the water content of the embankment material on the shear strength, two other CS tests were specifically chosen, at a suction of s = 11 kPa for samples compacted at w_{comp} = 3% and s = 47.1 kPa for samples compacted at w_{comp} = 6%, which did not represent the as-compacted states.

A summary of all triaxial compression tests on saturated and unsaturated samples can be found in Table 7.2. The designation of the tests are of the form shown in Table 7.1.

Type of test	**Designation of test**
Consolidated, unsaturated drained with suction control: constant suction (CS)	CS - w_{comp}[(1)] - Suction during shearing - $I_{D,0}$[(2)]
Consolidated, saturated drained (CD)	CD - w_{comp} - Confining pressure - $I_{D,0}$
Consolidated, unsaturated undrained without suction control: constant water content (CW)	CW - w_{comp} - Confining pressure - $I_{D,0}$

(1) Compaction water content, (2) Initial relative density before shearing.

Table 7.1: Designation of triaxial compression tests

Designation	w_{comp}[1] [%]	Material inner cell	$I_{D,0}$[2] [-]	u_a[3] [kPa]	u_w[4] [kPa]	σ_{cell}[5] [kPa]	shearing rate [mm/min]
Constant suction (CS) tests:							
CS-3%-s=46.8kPa-0.64	3	Acrylic glass	0.64	300	250	325	0.002
CS-6%-s=6.8kPa-0.67	6	Glass	0.67	300	290	325	0.002
CS-6%-s=47.1kPa-0.69	6	Glass	0.69	300	250	325	0.002
CS-3%-s=11kPa-0.63	3	Glass	0.63	300	285	325	0.002
Constant water content (CW) tests							
CW-3%-25kPa-0.68	3	Acrylic glass	0.68	0	-	25	0.05
CW-3%-25kPa-0.69	3	Acrylic glass	0.69	0	-	25	0.05
CW-3%-50kPa-0.71	3	Acrylic glass	0.71	0	-	50	0.05
CW-3%-50kPa-0.70	3	Acrylic glass	0.70	0	-	50	0.05
CW-3%-100kPa-0.68	3	Acrylic glass	0.68	0	-	100	0.05
CW-3%-100kPa-0.71	3	Acrylic glass	0.71	0	-	100	0.05
CW-3%-200kPa-0.69	3	Acrylic glass	0.69	0	-	200	0.05
CW-3%-200kPa-0.70	3	Acrylic glass	0.70	0	-	200	0.05
CW-3%-25kPa-0.64	3	Acrylic glass	0.64	0	-	25	0.05
CW-3%-25kPa-0.71	3	Acrylic glass	0.71	0	-	25	0.05
Saturated, consolidated drained (CD) tests							
CD-2%-10kPa-0.71	2	Acrylic glass	0.71	-	300	310	0.05
CD-3%-25kPa-0.7	3	Acrylic glass	0.70	-	300	325	0.05
CD-2%-50kPa-0.74	2	Acrylic glass	0.74	-	300	350	0.05
CD-2%-100kPa-0.77	2	Acrylic glass	0.77	-	300	400	0.05
CD-6%-25kPa-0.67	6	Acrylic glass	0.67	-	300	325	0.05
CD-10%-25kPa-0.67	10	Acrylic glass	0.67	-	300	325	0.05

[1] Compaction water content, [2] Initial relative density before shearing, [3] Applied pore-air pressure (gauge pressure), [4] Applied pore-water pressure (gauge pressure), [5] Applied cell pressure (gauge pressure)

Table 7.2: Summary of triaxial compression tests and test conditions

7.2 Triaxial test setups

The setups of the test rigs for the three testing methods described above are shown in Figure 7.1, Figure 7.2 and Figure 7.3. The components numbered in the figures are shown in detail in Table 7.3. Note that all electronic devices were thoroughly calibrated before the tests.

No.	Component	Annotations
1	Double-wall triaxial cell	Inner cell of glass for CS[(1)] tests, acrylic glass for CD[(2)] and CW[(3)] tests
2	3-channel APC[(4)]	Maximal air pressure 500 kPa, 300 kPa, 300 kPa Resolution 0.1 kPa Accuracy 0.2%
3	Pressure converter (air – water)	Rolling diaphragm in acrylic glass cylinder
4	Volume measuring burettes	Maximum water volume $V_{burette}$ = 100 ml Resolution 0.001/100 ml Linearity 0.2%
5	Pore-water pressure transducer	Measuring range 0 – 300 kPa Accuracy < 0.75 kPa
6	External incremental displacement transducer	Accuracy ± 1 μm / 50 mm
7	Internal submersible load cell	Measuring range 0–2 kN With ambient pressure compensation Non-linearity <0.1%
8	Top cap with coarse corundum disk	Acrylic glass
9	Specimen with rubber membrane and O-rings	Height 100 mm, diameter 50 mm
10	Base pedestal with HAE[(5)]-disk	High-Porosity ceramic filter plate: air entry value 100 kPa Flushing channel for removal of the air volume diffused through the ceramic
10'	Base pedestal with coarse corundum disk	For CD and CW tests, the HAE is replaced by a coarse corundum disk
11	Thermostat	Platinum measuring resistor Pt100
12	Analogue pressure regulator	-
13	Reference burette	$V_{burette}$ = 100 ml Resolution 0.001/100 ml Linearity 0.2%
14	Moisturizing cells	-

(1) Constant suction, (2) saturated consolidated drained, (3) constant water content, (4) air pressure controller, (5) high air entry

Table 7.3: Summary of components of the triaxial testing setup

For all three triaxial testing methods, the test rig essentially consists of a double-wall triaxial cell (Fredlund, Rahardjo, and Fredlund 2012) placed in an electromechanical static load frame, which is able to run speed-controlled tests via a spindle drive.

The individual components of the various testing setups are listed below:

- The double-wall cell ([1] in Figure 7.1 to Figure 7.3.) was chosen to measure the volume change in the specimens during the tests for both saturated and unsaturated tests. This method was selected to eliminate the influence of the cell expansion due to pressure changes on the measured volume changes, since applying the same cell pressure to the

inner and outer cell causes a net pressure of zero on the inner cell wall. Therefore, changes in cell-water volume directly reflect changes in the specimen volume.

- Since acrylic glass absorbs water over time (Delage 2002), an inner cell made of glass was used for most of the long-term CS tests. For the short-term CD and CW tests, an inner cell of acrylic glass was used, as it is less prone to damage.
- The water volume change of both the inner cell and the pore water were measured with electronic volume measuring devices [4], called *burettes*.
- A microprocessor-controlled, three-channel, fully automatic, pneumatic pressure generator (air pressure controller [APC]) was used to control the cell pressure, pore-air pressure and pore-water pressure [2]. With this unit, a maximum cell pressures up to 500 kPa can be applied. The maximum pore-air pressure and pore-water pressure are limited to 300 kPa. The air pressures generated by the APC are converted into pore water and cell-water pressure by the burettes [4, 13] or by a pressure converter [3], as shown in Figure 7.1, Figure 7.2 and Figure 7.3.
- The axial load was captured using an internal submersible load cell [7] with ambient pressure compensation.
- A sensor to measure the water temperature of the system [11] was installed to the outer cell in order to avoid any influence of potential leakage on the water volume change measurements of the inner cell.
- An external incremental displacement transducer was used to record the axial deformation [6].
- In the CD and CS tests, the pore-water pressure was measured by a pore water transducer connected to the water compartment at the bottom of the samples ([5] in Figure 7.1 and Figure 7.2).
- In order to control suction during CS tests, an HAE ceramic disk was placed below the specimen [10]. Taking into account a potential diffusion of pore air through the ceramic disk during the long-term tests, a helical flushing channel for the removal of the diffused air volume was cut into the base pedestal under the HAE disk. Flushing was done by opening the flushing valve of the pore-water pressure transducer [5] and by decreasing and subsequently increasing the pressure of the reference burette [13] via an analogue pressure regulator [12]. For the saturated CD and unsaturated CW tests, the HAE disk was replaced by a coarse corundum disk ([10'] in Figure 7.2 and Figure 7.3).
- For the long-term CS tests (Figure 7.1), a reference burette [13] was used to correct the measured water volumes for temperature fluctuations and leakage (Section 7.4.1).
- For the long-term CS tests (Figure 7.1), the pore-air pressure directly connected to the sample was passed through moisturizing cells [14] in order to minimize the water loss in the sample. Details on the construction and the principle of function of the cells can be found in Birle (2011).

– Software was used to control the test procedure, the load frame and the APC and to log the data.

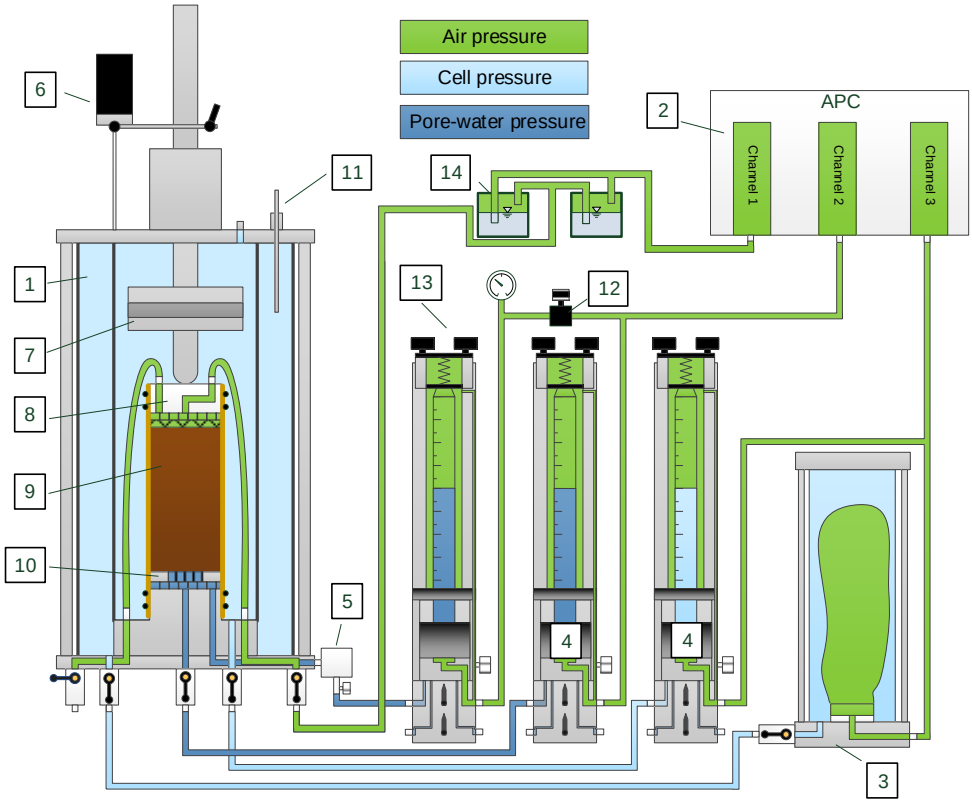

Figure 7.1: Triaxial test rig for constant suction (CS) testing

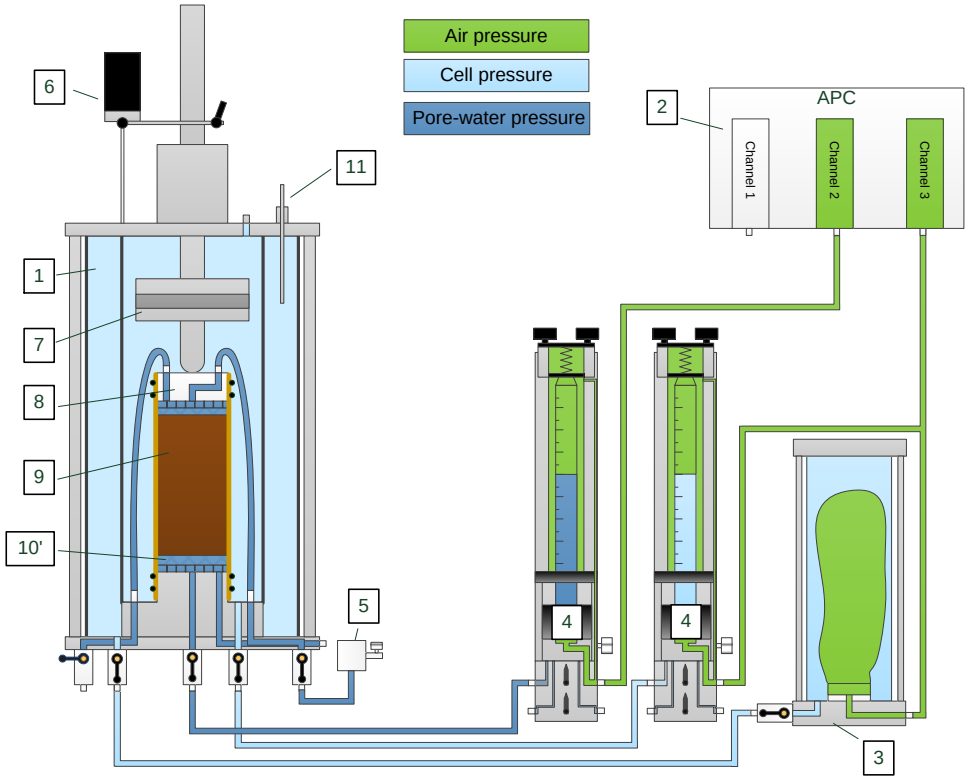

Figure 7.2: Triaxial test rig for consolidated drained (CD) testing

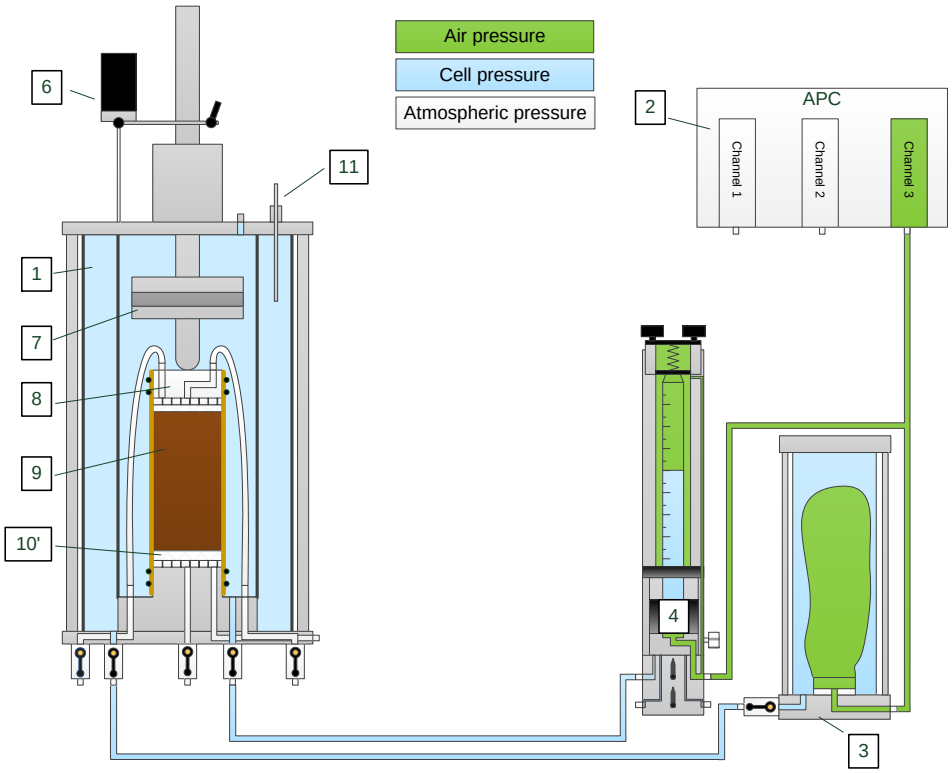

Figure 7.3: Triaxial test rig for constant water content (CW) testing

7.3 Test procedures

7.3.1 Sample preparation

All triaxial tests were performed on statically compacted samples of 100 mm height and 50 mm diameter. The samples were prepared using the undercompaction method already described in Section 5.4.2.

7.3.1.1 Constant water content tests

The specimens for the constant water content (CW) tests were stripped after compaction into the split mold and carefully placed on the base pedestal with a coarse corundum disk on it. The top cap and the upper coarse corundum disk were then carefully arranged on top of the sample. The membrane was installed via a membrane stretcher, and the O-rings were attached to the membrane. Subsequently, a slight vacuum of −10 kPa to −25 kPa was applied, and the sample dimensions were measured.

For low compaction water content, the samples were unstable, which in some cases led to a collapse when the top cap or the membrane was installed. This instability could be avoided only with utmost caution during the installation of either. Analogous to the samples of the UCTs, in some cases the edges of the samples had to be additionally stabilized by dripping silicone oil on the edges.

7.3.1.2 CD and CS tests

The samples for the consolidated drain (CD) and constant suction (CS) tests were compacted directly into the split mold, which was attached to the base pedestal. For this purpose, the membrane was stretched over the base pedestal and sucked to the split mold via a slight vacuum, as illustrated in Figure 7.4.

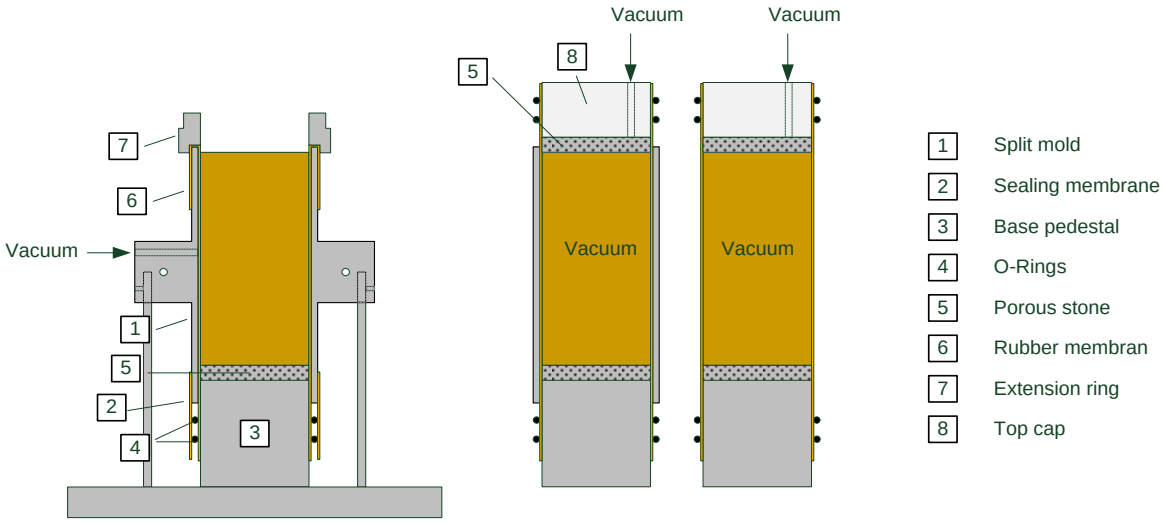

Figure 7.4: Specimen preparation for the saturated and unsaturated suction-controlled tests

After compaction, the top cap was carefully placed on the specimen and a slight vacuum of −10 kPa to −25 kPa was applied to the sample. Subsequently, the specimens were stripped and the sample dimensions checked.

Note that for the CS tests, the samples had to be compacted directly onto the HAE-disk. Therefore, prior to the sample preparation, the pore water compartment and the ceramic disk were thoroughly saturated, and a small amount of water was added to the surface of the ceramic disk to prevent cavitation. The added water was recorded, and the test results were corrected for it.

Note that with this procedure the microstructure of the bottom layer of the specimen might have been slightly changed compared to the subsequent layers. However, it is expected that the test results are not significantly influenced by the water content of the bottom layer during compaction.

7.3.2 Filling of the inner cell

After the samples were installed into the base pedestal and connected to the vacuum to stabilize it, the double-walled triaxial cell was assembled, and both outer and inner cell were filled with distilled, de-aired water. In order to minimize the influence of air bubbles on the water volume measurement, special attention was paid to achieve a fully saturated state for the inner cell and all fittings and hoses connected to it. For this purpose, the external filling system shown in Figure 7.5 was connected to the inner cell. The system comprises a water supply compartment of thoroughly de-aired water connected to the base plate of the inner cell and a burette connected to the top of the inner cell.

Both the water supply compartment and the burette were subjected to a vacuum. Before the valve at the base plate of the inner cell was opened, the vacuum applied to the sample and the vacuum applied to the filling system were simultaneously increased, while an effective confining pressure of at least 10 kPa was maintained. After a vacuum of approximately −90 kPa in the sample and −65 kPa to −80 kPa in the filling system was sustained, the valve was opened. Driven by the initial pressure head, the inner cell was filled with de-aired water until both the pressure head in the water compartment and in the burette connected to the top of the inner cell were balanced (Figure 7.5).

Subsequently, the valve at the base plate of the inner cell was closed, and the vacuum in the specimen and in the filling system was simultaneously decreased while an effective confining pressure of at least 10 kPa was maintained. This pressure was maintained until the filling system again reached atmospheric pressure conditions, while the specimen was subjected to its initial vacuum of −10 kPa to −25 kPa.

This filling procedure was performed for all triaxial tests. It ensured a thorough filling of the inner cell with de-aired water.

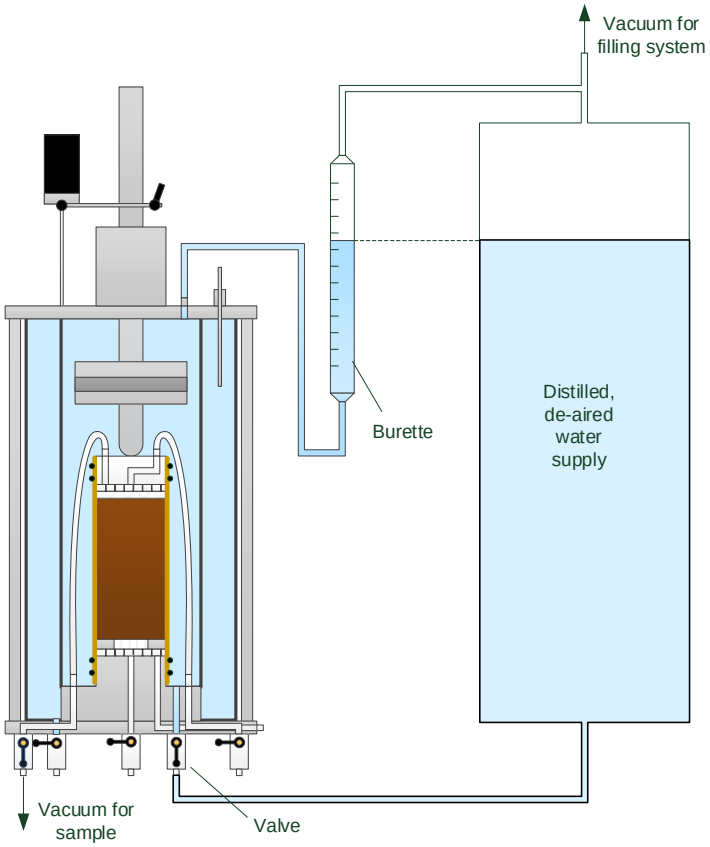

Figure 7.5: External filling system for the inner cell, status after filling has been completed

7.3.3 CD tests

In order to carry out the consolidated drained (CD) tests, the samples had to be saturated. Saturation was completed after installation of the samples in the triaxial cell and filling of the inner and outer cells.

The saturation process was performed by the use of the dry setting method (Ampadu and Tatsuoka 1993, Santucci de Magistris and Tatsuoka 2004). For this procedure, the external filling system already used to fill the inner cell was connected to the specimen lines (Figure 7.6). An additional burette was connected to the top of the inner cell in order to apply a vacuum to it.

Starting from atmospheric conditions in the inner cell, the vacuum in both the inner cell and specimen was simultaneously increased by keeping a constant effective confining pressure of 10 kPa to 25 kPa. The pressure difference of 10 kPa was used for samples subsequently tested at a confining pressure of 10 kPa in order to avoid any influence due to over-consolidation of the sample during the saturation process on the test results. The pressure difference of 25 kPa was used for the other tests.

At the end of the above procedure, the sample was subjected to a vacuum of −90 kPa, and the inner cell to a vacuum of 10–25 kPa less. In this state, the valve of the supply line was

opened, and the sample was flushed from the bottom to the top. The saturation process was driven by the pressure head of the filling system. This method ensured a slow saturation of the samples within 15 to 45 minutes, while no erosion of fines content was observed. The volume change in the samples during the saturation process was captured by the change in the height of water column of the burette connected to the inner cell.

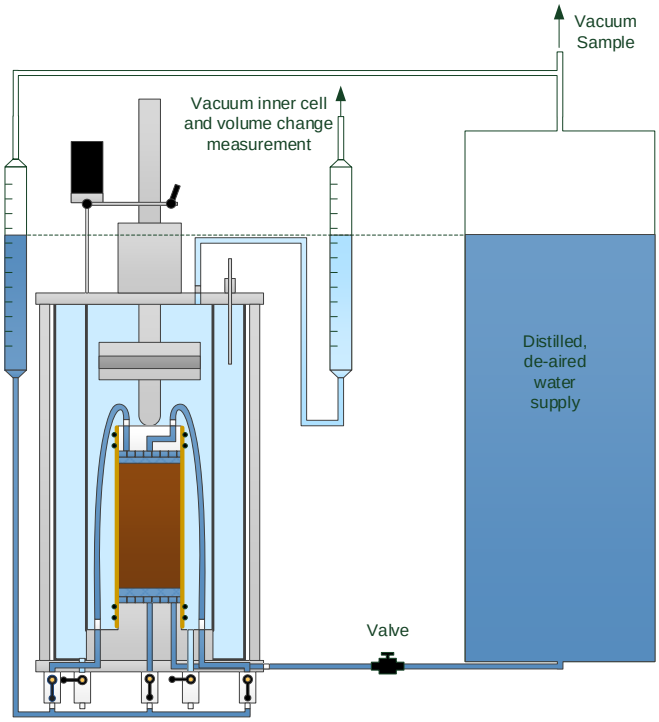

Figure 7.6: Saturation set-up, status after saturation has been completed

After saturation, the valve connected to the filling system was closed and the vacuum in the specimen and in the inner cell was simultaneously decreased while keeping a constant pressure difference of 10 kPa to 25 kPa. This pressure difference was maintained until the inner cell reached again atmospheric pressure conditions and the specimen was subjected to its initial vacuum of −10 kPa to −25 kPa.

Subsequently, the burette at the top of the inner cell was disconnected. The burette used to measure the water volume changes of the inner cell was thoroughly filled with de-aired, distilled water and connected to the base plate. The cell pressure was stepwise increased to 10 kPa to 25 kPa via the APC. Simultaneously, the vacuum in the sample was stepwise decreased to 0 kPa by keeping a constant confining pressure of 10 kPa to 25 kPa. Then the thoroughly saturated pore water burette and the pore-water pressure transducer were connected to the base plate (Figure 7.2). Care was taken to flush out all air bubbles in the system, ensuring a full saturation of the burettes, the fittings and the tubing.

The specimens were consolidated to the target confining pressures with a backpressure of 300 kPa, and B-tests were carried out. B-values of 0.85 to 0.95 were observed.

Eventually, the specimens were sheared with a shearing rate of 0.05 mm/min. This shearing rate proved to be sufficiently low to generate no excess pore-water pressures during drained testing.

7.3.4 CW tests

For the constant water content (CW) tests, the thoroughly saturated inner cell burette was connected to the base plate after the filling of the inner and outer cell was completed (Figure 7.3). Subsequently, the samples were consolidated to the target confining pressures, while the pore-air pressure line was exposed to the atmosphere. Each specimen was sheared with a shearing rate of 0.05 mm/min. In order to avoid pore-air pressure changes during shearing, the pore-air pressure line was exposed to atmospheric pressure. No significant changes in the water content of the samples were observed after the end of these tests.

7.3.5 CS tests

For the constant suction (CS) tests, after filling the inner and outer cell, the pore water burette and the inner cell burette were thoroughly filled with de-aired distilled water and connected to the base plate. The cell pressure was increased to 25 kPa while the vacuum in the sample was simultaneously decreased to 0 kPa. Subsequently, the thoroughly saturated reference burette and the pore-water pressure transducer were connected to the base plate (Figure 7.1). Care was taken that the burettes, the pressure transducer, the pore water compartment, the fittings and the tubing achieved full saturation. Finally, the air-pressure line was connected to the sample.

7.3.5.1 Saturation stage

The samples were brought to the target suction by simultaneously increasing the pore-air pressure, the pore-water pressure and the cell pressure by keeping a constant effective confining pressure of 25 kPa (saturation stage). The changes in pore-water volume and specimen volume were recorded via the measuring burettes. The saturation stage was maintained until changes in pore-water volume of less than 0.1 ml were observed over one day. In this state, the samples were considered to be in equilibrium with the applied suction. The pore water compartment was flushed approximately once per day. Note that due to the small difference between pore-water pressure and pore-air pressure (~5 kPa to 50 kPa) no diffused air volume was detected.

7.3.5.2 Shearing stage

After the saturation stage, the specimens were sheared by controlling both the pore-air and pore-water pressure. To enable a fast shearing rate, an HAE ceramic disk was used with an air entry value of 100 kPa and with the associated high hydraulic conductivity. Based on the findings from the literature review (Section 2.4.1.3), a shearing rate of 0.002 mm/min was considered sufficient to ensure a homogeneous, equilibrated pore water and pressure

distribution in the sample throughout the test. Note that this strain rate is less than the strain rates found for silts and silty sands in Table 2.4. At this slow strain rate, the pore-water pressure was assumed to be in equilibrium throughout the tests, as no experiments were carried out on the influence of the strain rate on the shear behavior of the silty sand examined in this study. To check this assumption, however, a plausibility control of the test results was carried out for each CS test, based on the density-dependent water-retention behavior of the samples (Section 5.3).

7.4 Data processing

In signal processing, the following influences are considered:

- Temperature fluctuations of the measuring system result in changes in the measured water volumes.
- Leakage, evaporation on air-water interfaces and water absorption into acrylic glass result in a time-dependent loss of water volumes, especially in the inner cell.
- Barrel shaped deformation patterns appear in the specimens.
- With ongoing shearing, the radial expansion of the rubber membrane generates an increasing radial stress.
- The load stamp penetrates the inner cell and therefore displaces the cell-water.

7.4.1 Corrections to the measured water volume changes

Especially during the long-term CS tests, the volume change measurement is affected by temperature fluctuations. Additionally, a time-dependent loss of water can be expected due to leakage, water absorption at the water-acrylic glass interfaces and evaporation at the air-water interfaces. For the sake of simplicity, the time-dependent loss of water volume is summarized hereinafter under the term *leakage*. In order to quantify the influence of temperature and leakage on the measurement results, a calibration process was performed, the details of which are described below.

Note that the influence of membrane penetration on the volume changes is expected to be negligible. The absence of this influence was reasonable to assume, as only tests with constant cell pressures were carried out. In these tests, membrane penetration had only a minor influence on the volume change reading because the related surface area was only slightly changed (Russell 2004).

7.4.1.1 Temperature fluctuations

According to Leong et al. (2004), the changes in the water volume due to temperature fluctuation can be calculated with the following:

$$\Delta V_T = V_0 \cdot \alpha \cdot \Delta T \cdot \left(1 + \frac{\alpha}{3} \cdot \Delta T + \frac{\alpha^2}{27} \cdot \Delta T^2\right) \tag{7.1}$$

with $\Delta T = T - T_{ref}$

V_0 Initial water volume at the initial (reference) temperature T_{ref}

α Coefficient of volume expansion of the system [1/C°].

In (7.1), the coefficient α accounts not only for the density fluctuation of the water but also for the temperature-dependent volume changes of, for instance, the triaxial cell, O-rings, fittings,

tubing or volume measuring devices. Thus, (7.1) describes the expansion or contraction of the entire measuring system due to temperature changes.

Regarding all three test setups (Figure 7.1, Figure 7.2 and Figure 7.3), changes in the measured water volume of the inner cell also comprise the changes in the water volume of the burette connected to it (Figure 7.7, left). However, the burette that measures the volume changes of the inner cell is expected to show a different temperature-dependent volume change behavior than the inner cell. To account for this difference, the water volume changes of the inner cell and the burette, both described with (7.1), may be superimposed. Therefore, two coefficients of volume expansion have to be determined (α_{Bu} and α_{IC}). In addition, according to (7.1), two initial water volumes have to be defined (i.e., $V_{IC,0}$ and $V_{Bu,IC,0}$).

The pore water system consists of the burette and the water compartment underneath the sample (Figure 7.7, middle). Due to its small volume, however, the influence of changes in the water volume in the water compartment on the measured pore-water volume were considered negligible ($\alpha_{PW} = 0$). For this reason, the expansion coefficient for the pore water system has only to be determined for the burette connected to the pore water system.

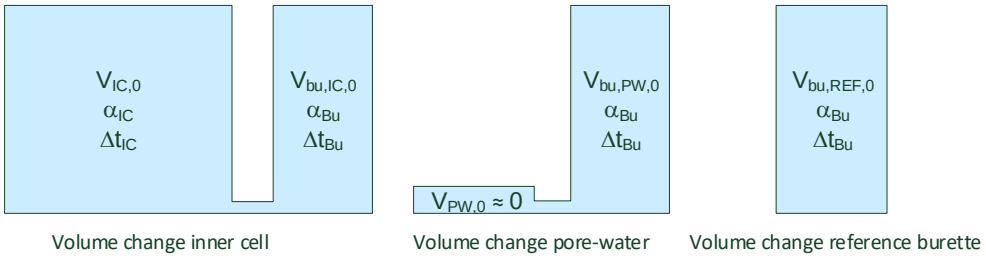

Figure 7.7: Parameters for temperature correction

It is expected that the burettes used to measure the pore-water volume and the reference water volume (Figure 7.7, right) exhibit a similar temperature-dependent behavior as does the burette of the inner cell. Therefore, the same expansion coefficient (α_{Bu}) can be applied the three burettes.

Note that since the water temperature was measured in the outer cell, the temperature fluctuations in the burettes and in the inner cell were both expected to exhibit a phase shift Δt relative to the measured temperature signal (Figure 7.7). Analogously to the expansion coefficient α_{Bu}, a unique phase shift Δt_{Bu} was therefore assigned to the burettes. The temperature-dependent volume change behavior of the inner cell is expected to show a different phase shift (Δt_{IC}).

Taking into account the designations of the parameters shown in Figure 7.7, the temperature-dependent change of the pore-water volume can be determined from the following:

$$\Delta V_{T,PW} = V_{bu,PW,0} \cdot \alpha_{Bu} \cdot \Delta T_{t+\Delta t_{Bu}} \left(1 + \frac{\alpha_{Bu}}{3} \cdot \Delta T_{t+\Delta t_{Bu}} + \frac{{\alpha_{Bu}}^2}{27} \cdot \Delta T^2_{t+\Delta t_{Bu}}\right) \quad (7.2)$$

with $V_{bu,PW,0}$ Initial water volume of the burette connected to the pore water system including tubing, fittings and pore water compartment

$\Delta T_{t+\Delta t_{Bu}}$ Temperature fluctuation as a function of time t and time shift Δt_{Bu}.

The temperature-dependent change in the water volume change of the inner cell (including the burette connected to it) can be estimated as follows:

$$\Delta V_{T,IC} = V_{IC,0} \cdot \alpha_{IC} \cdot \Delta T_{t+\Delta t_{IC}} \left(1 + \frac{\alpha_{IC}}{3} \cdot \Delta T_{t+\Delta t_{IC}} + \frac{{\alpha_{IC}}^2}{27} \cdot \Delta T^2_{t+\Delta t_{IC}}\right) + \\ + V_{bu,IC,0} \cdot \alpha_{Bu} \cdot \Delta T_{t+\Delta t_{Bu}} \left(1 + \frac{\alpha_{Bu}}{3} \cdot \Delta T_{t+\Delta t_{Bu}} + \frac{{\alpha_{Bu}}^2}{27} \cdot \Delta T^2_{t+\Delta t_{Bu}}\right) \quad (7.3)$$

with $V_{IC,0}$ Initial water volume of the inner cell

$V_{bu,IC,0}$ Initial water volume of the burette connected to the inner cell including tubing and fittings.

The temperature-dependent water volume change of the reference burette can be determined from

$$\Delta V_{T,REF} = V_{bu,REF,0} \cdot \alpha_{Bu} \cdot \Delta T_{t+\Delta t_{Bu}} \left(1 + \frac{\alpha_{Bu}}{3} \cdot \Delta T_{t+\Delta t_{Bu}} + \frac{{\alpha_{Bu}}^2}{27} \cdot \Delta T^2_{t+\Delta t_{Bu}}\right) \quad (7.4)$$

with $V_{bu,REF,0}$ Initial water volume of the reference burette including tubing and fittings.

Note that since both the time- and temperature-dependent volume change behavior of all burettes can be expected to be similar and the initial water volumes of the burettes are also approximately equal ($V_{bu,REF,0} \approx V_{bu,PW,0} \approx V_{bu;IC,0}$), the tared signal of the reference burette,

$$\Delta V_{REF} = V_{REF} - V_{bu,REF,0}\ , \quad (7.5)$$

can be used to correct the measured volume signals of the inner cell and of the pore-water. Therefore, equations (7.2) and (7.3) can be replaced by

$$\Delta V_{T,PW} = \Delta V_{REF} \quad (7.6)$$

and

$$\Delta V_{T,IC} = V_{IC,0} \cdot \alpha_{IC} \cdot \Delta T_{t+\Delta t_{IC}} \left(1 + \frac{\alpha_{IC}}{3} \cdot \Delta T_{t+\Delta t_{IC}} + \frac{{\alpha_{IC}}^2}{27} \cdot \Delta T^2_{t+\Delta t_{IC}}\right) + \Delta V_{REF}\ . \quad (7.7)$$

7.4.1.2 Leakage

Leakage is considered by adding a time-dependent increase in water volume ΔV_{laek} to the measured water volume signals. For simplicity, this correction can be assumed to be linear with time:

$$\Delta V_{laek} = t \cdot c_{laek} \tag{7.8}$$

with c_{laek} Coefficient accounting for leakage, absorption and evaporation [ml/day].

It is expected that all burettes loose approximately the same water volume with time and have therefore the same coefficient, $c_{laek,bu}$.

Note that the time-dependent loss in water volume $\Delta V_{laek,Bu}$ is already included in (7.5). Therefore, if the signal of the reference burette is used to correct the water volume signals for temperature fluctuations, described with equations (7.6) and (7.7), the time-dependent loss must not be considered separately a second time.

7.4.1.3 Calibration tests

In order to find suitable parameters for the above corrections, a calibration process was performed. The triaxial cell was assembled using a stainless steel dummy and filled with de-aired water. Subsequently, the cell was pressurized to the pressure levels also used for the CS test. To avoid the influence of water volume changes caused by air bubbles dissolving into water, special care was taken to ensure a properly saturated and de-aired system (Section 7.3.2). Two tests were carried out. One was performed using an inner cell of acrylic glass; the other used an inner cell of glass. For each test, the signals were recorded over several days. The results of the calibration tests are shown in Figure 7.8 through Figure 7.11.

The corrections were done with and without a reference burette. For the corrections with the reference burette, the signal of the pore-water volume corrected for temperature and leakage was determined from

$$V_{PW,corr.} = V_{PW,meas.} - \Delta V_{T,PW} + \Delta V_{laek,bu} \tag{7.9}$$

with $V_{PW,meas.}$ Measured signal

$\Delta V_{T,PW}$ Equation (7.2)

$\Delta V_{laek,bu}$ Equation (7.8).

Correspondingly, the signal of the inner cell volume corrected for temperature and leakage was calculated with

$$V_{IC,corr} = V_{IC,meas.} - \Delta V_{T,IC} + \Delta V_{laek,IC} + \Delta V_{laek,bu} \tag{7.10}$$

with $\Delta V_{T,IC}$ Equation (7.3)

$\Delta V_{laek,bu}$ Equation (7.8)

$\Delta V_{laek,IC}$ Equation (7.8).

For the corrections with the reference burette, the pore-water volume was calculated with

$$V_{PW,corr.} = V_{PW,meas.} - \Delta V_{REF} \quad (7.11)$$

with ΔV_{REF} Equation (7.5).

Accordingly, the inner cell water volume was determined from

$$V_{IC,corr} = V_{IC,meas.} - \Delta V_{T,IC} + \Delta V_{laek,IC} \quad (7.12)$$

with $\Delta V_{T,IC}$ Equation (7.7)

$\Delta V_{laek,IC}$ Equation (7.8).

Figure 7.8a shows the measured water volume change of the inner cell (in the figure referred to as IC) of acrylic glass, the measured water volume change in the reference burette (REF), the measured water temperature changes (T) and the corrected water volume signal of the inner cell (IC_corr). The correction was done using equations (7.11) and (7.12). The parameters applied to the equations are shown in Table 7.4. Figure 7.8b shows the same procedure for the corrected pore-water volume.

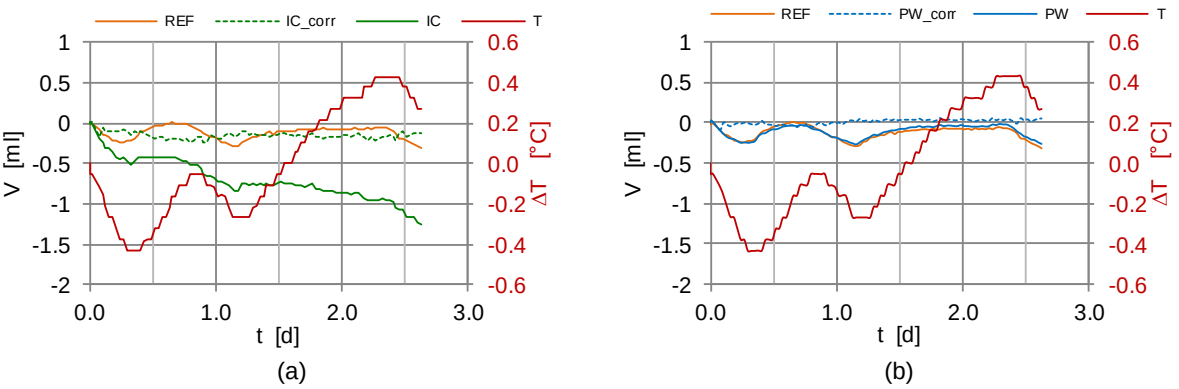

Figure 7.8: Correction of water volume data (acrylic glass cylinder): (a) inner cell water volume; (b) pore-water volume when using the reference burette

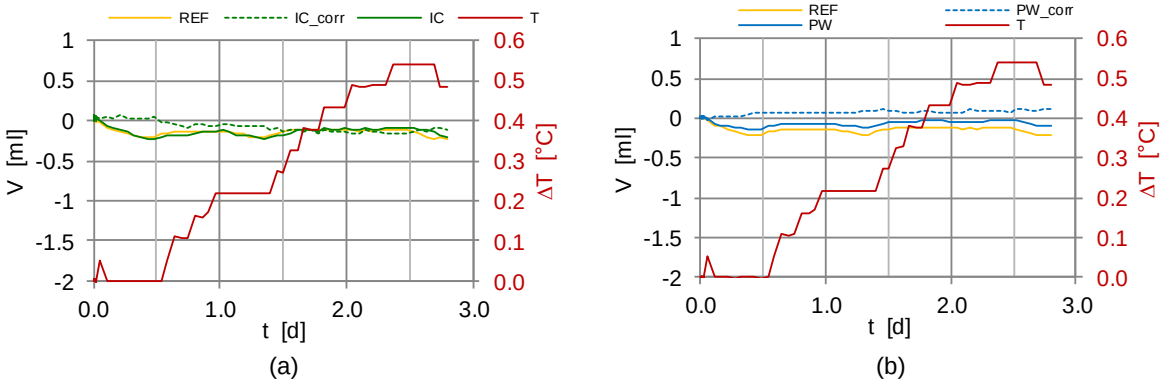

Figure 7.9: Correction of water volume data (glass cylinder): (a) inner cell water volume; (b) pore water when using the reference burette

Figure 7.9a and Figure 7.9b show the measured and the corrected water volume change of the inner cell made of glass and the pore-water volume. The corrections were done using (7.11) and (7.12). The parameters applied to the equations are shown in Table 7.4.

Material of the inner cell	Coefficient of leakage		Water volume at initial (reference) temperature		Coefficient of volume expansion	
	$c_{laek,IC}$ [ml/day]	$c_{laek,bu}$ [ml/day]	$V_{IC,0}$ [ml]	$V_{PW,0}$ [ml]	α_{IC} [1/°C]	α_{Bu} [1/°C]
Acrylic glass	0.32	0	1500	0	0.000350	0
Glass	0.03	0	1500	0	0.000350	0

Table 7.4: Summary of parameters when using the reference burette, equations (7.11) and (7.12)

Figure 7.10 shows the measured and corrected signals for both the water volume of the inner cell made of acrylic glass and the pore-water volume. Since the signal of the reference burette was not considered, the measured volumes were corrected using equations (7.9) and (7.10). The corresponding parameters are summarized in Table 7.5.

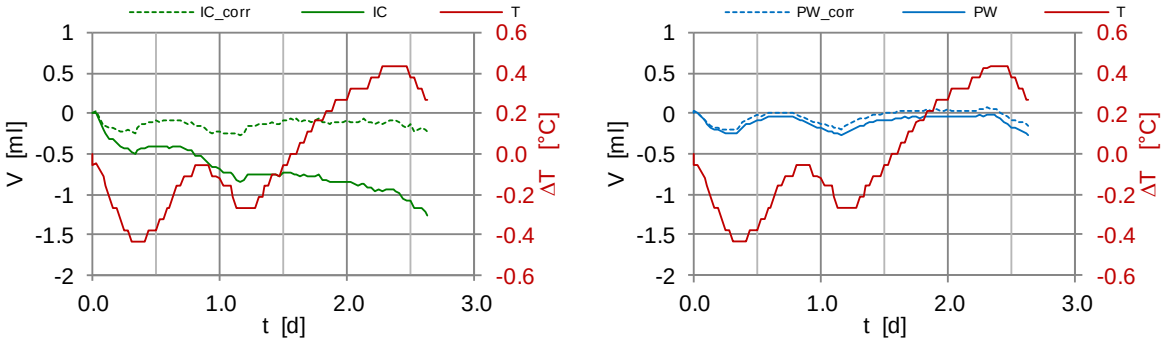

Figure 7.10: Correction of water volume data (acrylic glass cylinder): (a) inner cell water volume; (b) pore-water volume without the use of a reference burette

Material of the inner cell	Coefficient of leakage		Water volume at initial (reference) temperature		Coefficient of volume expansion	
	$c_{laek,IC}$ [ml/day]	$c_{laek,bu}$ [ml/day]	$V_{IC,0}$ / $V_{IC,bu,0}$ [ml]	$V_{PW,0}$ [ml]	α_{IC} [1/°C]	α_{Bu} [1/°C]
Acrylic glass	0.42	0.05	1500 / 70⁺ + $V_{bu,0}$*	70⁺ + $V_{bu,0}$*	0.000150	0.0010
Glass	0.10	0.05	1500 / 70⁺ + $V_{bu,0}$*	70⁺ + $V_{bu,0}$*	0.000350	0.0010

** initial water volume of the respective burettes* ⁺ water volume in tubing and fittings

Table 7.5: Summary of parameters without the use of a reference burette, equations (7.9) and (7.10)

Figure 7.11 shows the measured and corrected signals for both, the water volume of the inner cell made of glass and the pore-water volume. Again, the measurements were corrected by the means of (7.9) and (7.10), using the parameters summarized in Table 7.5.

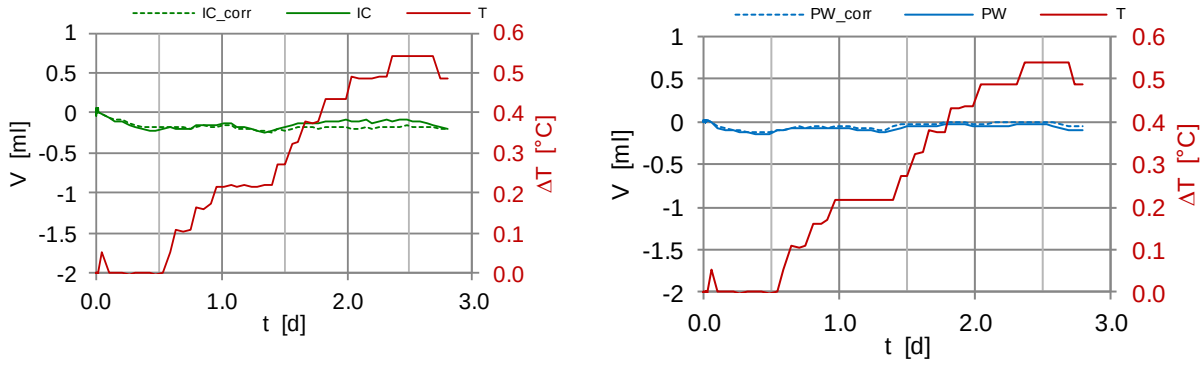

(a) (b)

Figure 7.11: Correction of water volume data (glass cylinder): (a) inner cell water volume; (b) pore-water volume without the use of a reference burette

The results show that the measured water volume signals are strongly influenced by the temperature, even though only small water temperature variations were measured. However, both examined correction methods are appropriate to subtract the influence of both the temperature and leakage on the water volume of the inner cell and the pore-water volume, when the parameters summarized in Table 7.4 and Table 7.5 are used. Regarding leakage, the inner cell cylinder made of acrylic glass lost more water than the inner cell cylinder made of glass, which can be attributed to the absorption of water from the inner cell into the acrylic glass cylinder (Delage 2002).

The parameters summarized in Table 7.4 and Table 7.5 can account for all conditions during the triaxial tests carried out in this study. Together with the corresponding equations, these parameters are therefore used in the following to correct the measured water volume signals. Note that for the tests, a proper phase shift has to be found for each signal, since it was not found to be a constant in the calibration tests. Thus, no values for Δt are shown in Table 7.4 and Table 7.5.

7.4.2 Evaluation of strain

Global natural strains are used to represent the test results. Therefore, the axial strain was derived from

$$\varepsilon_a = \varepsilon_1 = -\ln\left(1 - \frac{\Delta v}{H_0}\right) \tag{7.13}$$

with H_0 Initial sample height

Δv Vertical penetration of the loading ram into the inner cell.

The volumetric strains were calculated from the measured volume change in the inner cell corrected for temperature fluctuations, leakage and water absorption. Additionally, water volume replacement caused by the penetration of the loading ram into the inner cell was accounted for.

Hence,

$$\varepsilon_V = -\ln\left(1 - \left(-\frac{\Delta V_{IC} - \Delta v \cdot A_{ram}}{V_0}\right)\right) \tag{7.14}$$

with V_0 Initial sample volume

ΔV_{IC} Volume change in the inner cell

A_{ram} Cross sectional area of the loading ram.

The radial strains were calculated from

$$\varepsilon_r = \varepsilon_3 = \frac{1}{2}(\varepsilon_V - \varepsilon_1). \tag{7.15}$$

The void ratio was derived from the volumetric strains:

$$e = \exp(-\varepsilon_V) \cdot (1 + e_0) - 1 \tag{7.16}$$

with e_0 Initial void ratio.

7.4.3 Evaluation of stress

7.4.3.1 Sample deformation

Throughout all triaxial tests, barrel-shaped specimen deformations were observed that rose to a significant magnitude in the post-peak regime. For the non-uniform deformation pattern, stresses were corrected for the effects of a change in sample geometry.

To account for the increase in the cross-section area due to barreling, the procedure described in Zhang and Garga (1997) was applied. This approach assumes a parabolic distribution of the radial sample diameter with the height of the sample. Following this concept, the actual diameter in the middle of the sample (H/2) was calculated with

$$D_{H/2} = \frac{D_0}{4}\left(\sqrt{\left[30\frac{(1-\varepsilon_V)}{(1-\varepsilon_a)} - 5\right]} - 1\right) \tag{7.17}$$

with D_0 Initial sample diameter for non-lubricated end-platens

ε_V Volumetric strain

ε_a Axial strain.

For stress calculations, the sample diameter averaged over the middle third portion of the sample (1/3) was used (Zhang and Garga 1997):

$$D_{1/3} = D_{H/2} - \frac{1}{12}\left(D_{\frac{H}{2}} - D_0\right). \tag{7.18}$$

7.4.3.2 Density changes

The axial stresses were calculated in the mid-section of the sample, accounting for the density of the moist specimen:

$$\rho = \frac{\rho_s}{\left(1 + e_0 + \varepsilon_V \cdot (1 + e_0)\right)} \cdot \left(1 + w_0 + \frac{\Delta V_{PW} \cdot \rho_W}{m_d}\right) \tag{7.19}$$

with
- e_0 Initial void ratio
- ρ_s Specific density
- w_0 Initial water content
- m_d Dry mass of the specimen
- ρ_W Water density.

Hence,

$$\sigma_a = \frac{F + \sigma_{cell} \cdot (A_0 - A_{ram})}{A_{1/3}} + \frac{1}{2}(H_0 - \Delta v) \cdot \rho \cdot g \tag{7.20}$$

with
- F Measured axial force
- σ_{cell} Applied cell pressure
- A_0 Initial cross-sectional area of the specimen
- $A_{1/3}$ Cross-sectional area of the sample $\left(= \pi \cdot {D_{1/3}}^2/4\right)$
- g Gravitational constant.

7.4.3.3 Membrane effect

Due to the radial expansion of the specimen, the stretching of the rubber membrane is expected to impose additional radial stress to the sample, which is not considered negligible, in particular at low confining pressures. Radial stresses were therefore corrected for membrane stretching using the expression described in Lade (2016):

$$\Delta\sigma_{r,m} = -\frac{4}{3} \cdot \frac{E_m \cdot t_m \cdot \varepsilon_V}{D_0} \tag{7.21}$$

with
- E_m Elastic modulus of the rubber membrane (= 1350 kPa)
- t_m Thickness of the rubber membrane.

From the above, the corrected radial stress is derived:

$$\sigma_r = \sigma_{cell} + \Delta\sigma_{r,m}. \tag{7.22}$$

7.4.3.4 Effective stress

CS-tests

The findings from Chapter 6 indicate that a minor increase in the suction-induced effective stress state can be expected ($\chi \cdot s < 1$ kPa). Therefore, in triaxial tests, the net stress state approximately represents the effective stress state. However, for the sake of completeness, the suction-induced effective stress ($\Delta\sigma' = \chi \cdot s$) is included in the test evaluation. In view of the findings from Chapter 6, expression (6.16) was used together with the exponent $m = -1.09$ to calculate the evolution of χ during the triaxial tests.

In the CS tests, the principal axial and radial effective stress follows to be:

$$\begin{aligned} \sigma_1' &= \sigma_a - u_a + \left(\frac{s}{s_{AE}}\right)^{-1.09} \cdot s \approx \sigma_a - u_a \\ \sigma_3' &= \sigma_r - u_a + \left(\frac{s}{s_{AE}}\right)^{-1.09} \cdot s \approx \sigma_r - u_a \end{aligned} \tag{7.23}$$

Since the density of the sample changes during shearing, changes in the air entry value of the SWRC have to be taken into account in the above equation. This was done by applying the reciprocal value of the density-dependent parameter a_1 in equation (5.1) as a measure of the air entry value. The parameter a_1 was calculated with the help of equation (5.2) and the parameters summarized in Table 5.4 at the respective compaction water content and the change in relative density during the triaxial tests.

For the constant suction (CS) tests, it should be noted that the suction may vary slightly during the tests, as the height of the water column in the pore water burette changes. This variation was accommodated by calculating suction as the difference between the applied pore-air pressure u_a and the pore-water pressure $u_{w,meas}$, measured with the pore-water pressure transducer at the base plate of the triaxial cell, since it is loaded by the water column of the pore water burette:

$$s = u_a - u_{w,meas.} + 1\ \text{kPa}. \tag{7.24}$$

The influence of the sample height on the pore-water pressure was accounted for by increasing the suction by 1 kPa. This value corresponds to the vertical distance between the pore-water pressure transducer and the mid-height of the sample (≈ 10 cm).

CW-tests

In the constant water content (CW) tests, the principal effective stress is related to the axial and radial total stress and the increase in effective stress:

$$\sigma_1' = \sigma_a + \left(\frac{s}{s_{AE}}\right)^{-1.09} \cdot s \approx \sigma_a$$
$$\sigma_3' = \sigma_r + \left(\frac{s}{s_{AE}}\right)^{-1.09} \cdot s \approx \sigma_r \ . \quad (7.25)$$

Note that for the test evaluation, the atmospheric pore-air pressure was defined as u_a = 0 kPa. The suction during the CW tests was estimated from the 'as-compacted' SWRC using (6.14) and was assumed constant throughout the tests (Section 2.4.1.4). The evolution of the air entry value during the tests was derived from the SWRCs for the compaction water content and the initial density. For this purpose, (5.1) was used with the corresponding parameters derived from (5.2) and Table 5.4.

CD-tests

For the saturated consolidated drained (CD) tests, the principal effective stresses were calculated by taking into account the measured pore-water pressure $u_{w\ meas}$:

$$\sigma_1' = \sigma_a - (u_{w,meas.} - 1\ \text{kPa})$$
$$\sigma_3' = \sigma_r - (u_{w,meas.} - 1\ \text{kPa}). \quad (7.26)$$

The influence of the sample height on the pore-water pressure was considered by decreasing the measured pore-water pressure by 1 kPa. This value corresponds to the vertical distance between the pore-water pressure transducer and the mid-height of the sample (≈ 10 cm).

7.4.3.5 Stress variables

For each test type, the effective mean stress and the deviatoric stress was calculated:

$$p' = \frac{1}{3}(\sigma_1' + 2\sigma_3')$$
$$q = \sigma_1' - \sigma_3'. \quad (7.27)$$

The mobilized friction angle was derived from

$$\varphi'_{mob} = \arcsin\left(\frac{\sigma_1' - \sigma_3'}{\sigma_1' + \sigma_3'}\right)_{mob} . \quad (7.28)$$

In the following, the results of the triaxial tests are presented as a function of the variables described above.

7.5 Test results and discussion

7.5.1 Results of the CD tests

7.5.1.1 Influence of microstructure

In order to investigate the influence of the initial microstructure on the saturated peak shear strength, samples compacted at water content of w_{comp} = 3%, w_{comp} = 6% and w_{comp} = 10% were tested at a cell pressure of 25 kPa. Before shearing, the samples had relative densities ranging from I_D = 0.67 to I_D = 0.70. The test results are shown in Figure 7.12.

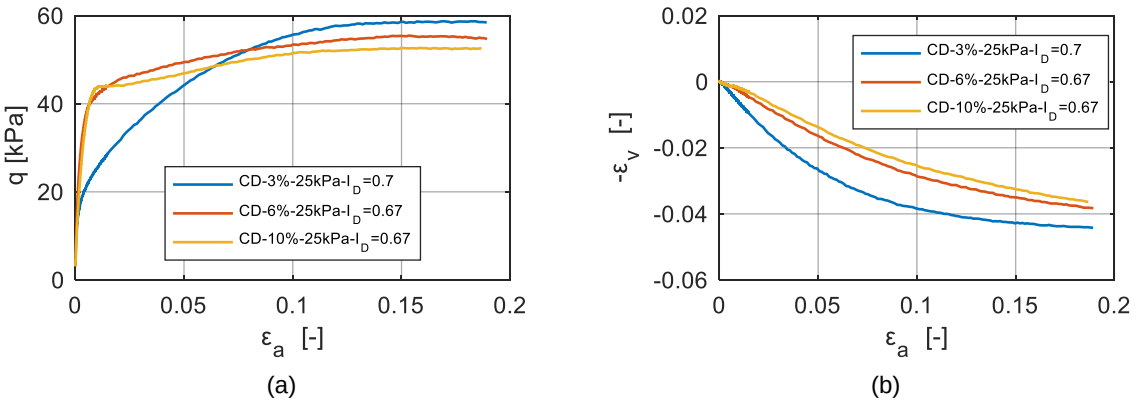

Figure 7.12: Influence of the compaction water content on the saturated shear strength at a cell pressure of 25 kPa and I_D = 0.67 to I_D = 0.7: (a) q vs. ε_a; (b) ε_V vs. ε_a

Figure 7.12b shows that all three samples exhibit contractive volumetric behavior, even at the low tested stress level of 25 kPa and their dense states. This behavior, however, compares well to the findings from other investigations on the volumetric behavior of drained, saturated compacted sands, silts and silty sands when sheared (Vaid and Thomas 1995, Hoeg, Dyvik, and Sandbaekken 2000, Casini, Minder, and Springman 2010, Patil 2014).

Comparing the three tested samples, the initial microstructure varied from an bimodal porosity in the sample compacted at w_{comp} = 3% to an unimodal porosity for the sample compacted at w_{comp} = 10%. At peak states, however, the initial microstructure appears to influence considerably neither the volumetric behavior of the samples nor the shear strength (Figure 7.12). These results confirm the findings from Santucci de Magistris and Tatsuoka (2004) on the influence of compaction water content of the peak shear strength of a silty sand. The authors posit that, at peak, the influence of microstructure on the shear strength of saturated samples compacted at different water content is negligible. Notably, when compared to the samples compacted at w_{comp} = 6% and w_{comp} = 10%, the sample compacted at w_{comp} = 3% exhibited lower shear stiffness.

Under saturated conditions, it may be concluded that, at peak, aggregated fines do not have significant influence on strength. Thus, they do not contribute significantly to the dilatancy and thus shear strength.

7.5.1.2 Influence of confining pressure

Since the microstructure was observed to have no significant influence on shear strength, the failure criterion for the saturated samples was derived from triaxial tests on samples compacted at w_{comp} = 2% to w_{comp} = 3%, at stress levels ranging from 10 kPa to 100 kPa. The initial relative densities ranged from I_D = 0.70 to I_D = 0.77.

Figure 7.13a reveals that for all tested specimens, no pronounced peak behavior of the stress-strain curve can be observed. Correspondingly, all specimens show a contractive behavior (Figure 7.13b).

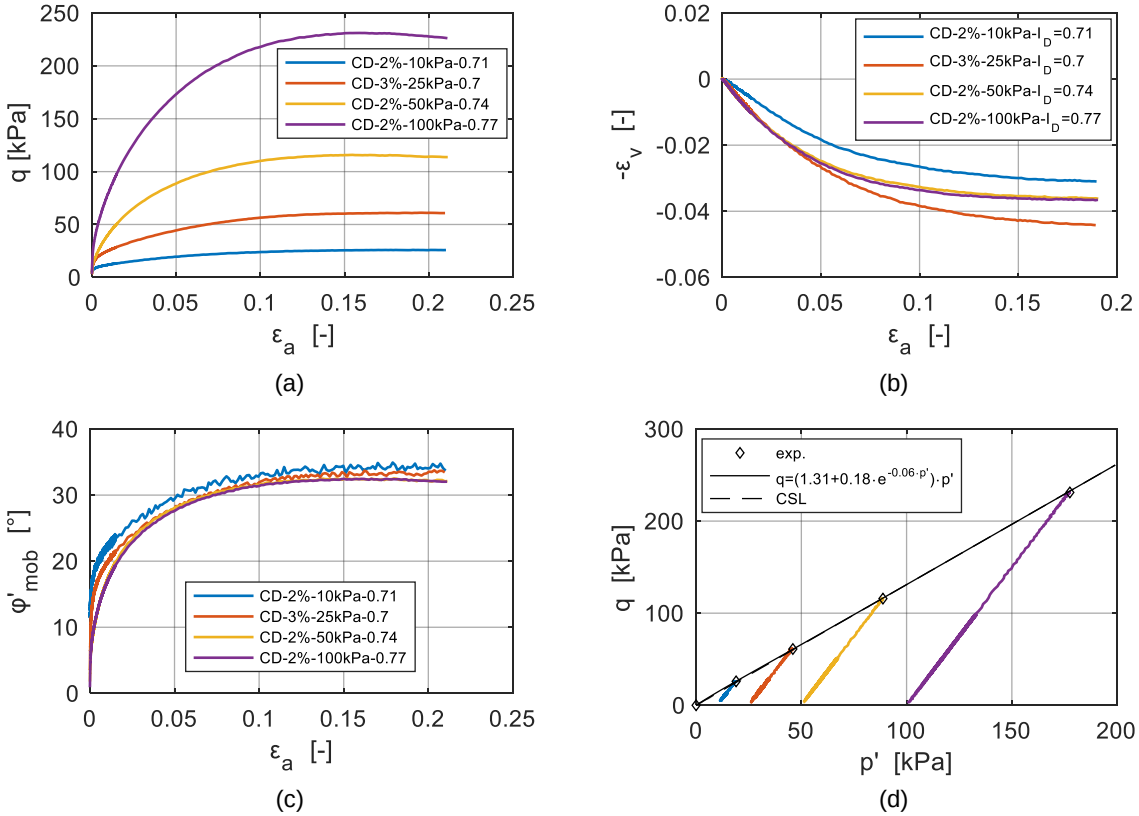

Figure 7.13: Influence of confining pressure on the saturated shear strength for w_{comp} = 2% to w_{comp} = 3% and I_D = 0.7 to I_D = 0.77: (a) q vs. ε_a; (b) ε_V vs. ε_a (c) φ'_{mob} vs. ε_a, (d) q vs. p'

All samples exhibit a mobilized maximum friction angle of approximately φ'_{max} = 32.5° (Figure 7.13c). Since it can be expected that the critical state was approximately reached in all tests, in particular at high confining pressures, this mobilized maximum friction angle corresponds to the critical state friction angle φ'_{CS} = 32.5°.

Although being apparently linear in the tested stress range, the following expression, which is able to account for a potential non-linear course of the failure criterion, was used to fit the maximum shear strength depicted in Figure 7.13d:

$$q = (M_{cs} + a \cdot \exp(-b \cdot p')) \cdot p' \tag{7.29}$$

with M_{cs} Stress obliquity at critical state

a, b Fitting parameters.

The resulting failure criterion is shown in Figure 7.13d and represents the CSL, with M_{cs} = 1.31 corresponding to φ'_{CS} = 32.5°. Note that since no pronounced non-linearity has to be reproduced by (7.29), the fitting parameters a = 0.18 and b = 0.06 are close to zero.

7.5.2 Results of the CW tests

7.5.2.1 Reproducibility

Before the results of the constant water content (CW) tests are assessed with regard to the evolution of shear strength with the effective stress in the next section, they are checked for reproducibility in the following.

Figure 7.14 shows the shear behavior of samples with I_D = 0.68 to I_D = 0.71 compacted at w_{comp} = 3%. For each confining pressure, two samples with the same initial density were tested.

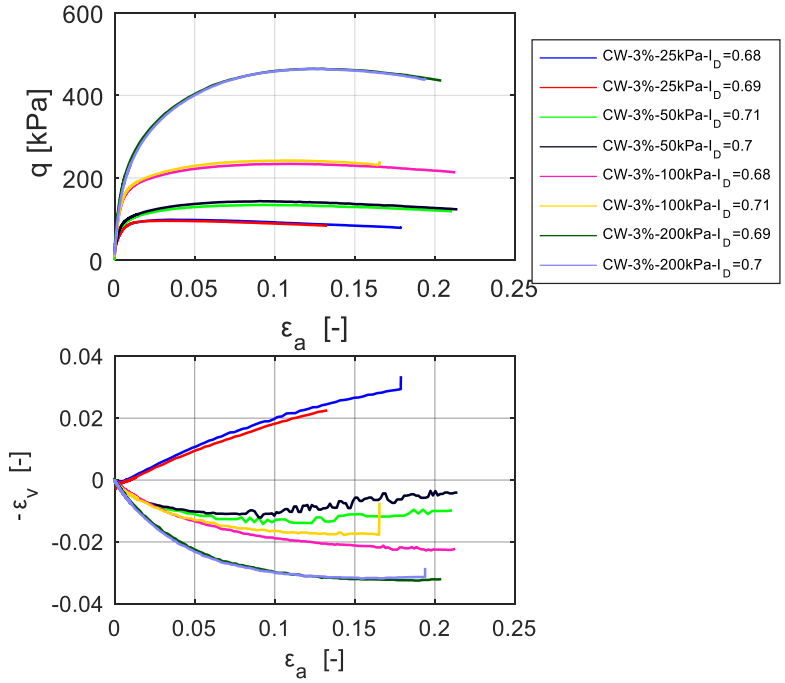

Figure 7.14: Reproducibility of the shear behavior at different confining pressures for w_{comp} = 3% and I_D = 0.68 to I_D = 0.71

From the figure, a good match between the shear behavior of the samples tested at the same confining pressures can be observed, regarding both the shear strength and volumetric behavior. The preparation method presented in Section 7.3.1.1 leads therefore to samples with reproducible shear strength behavior. The sample-preparation method can thus be considered appropriate for the silty sand under investigation.

7.5.2.2 Influence of confining pressure

The influence of the confining pressure on the shear strength of the as-compacted silty sand was examined by conducting CW tests on samples with an initial relative density between I_D = 0.68 and I_D = 0.70 at confining pressures of 25 kPa, 50 kPa, 100 kPa and 200 kPa. The results are shown in Figure 7.15.

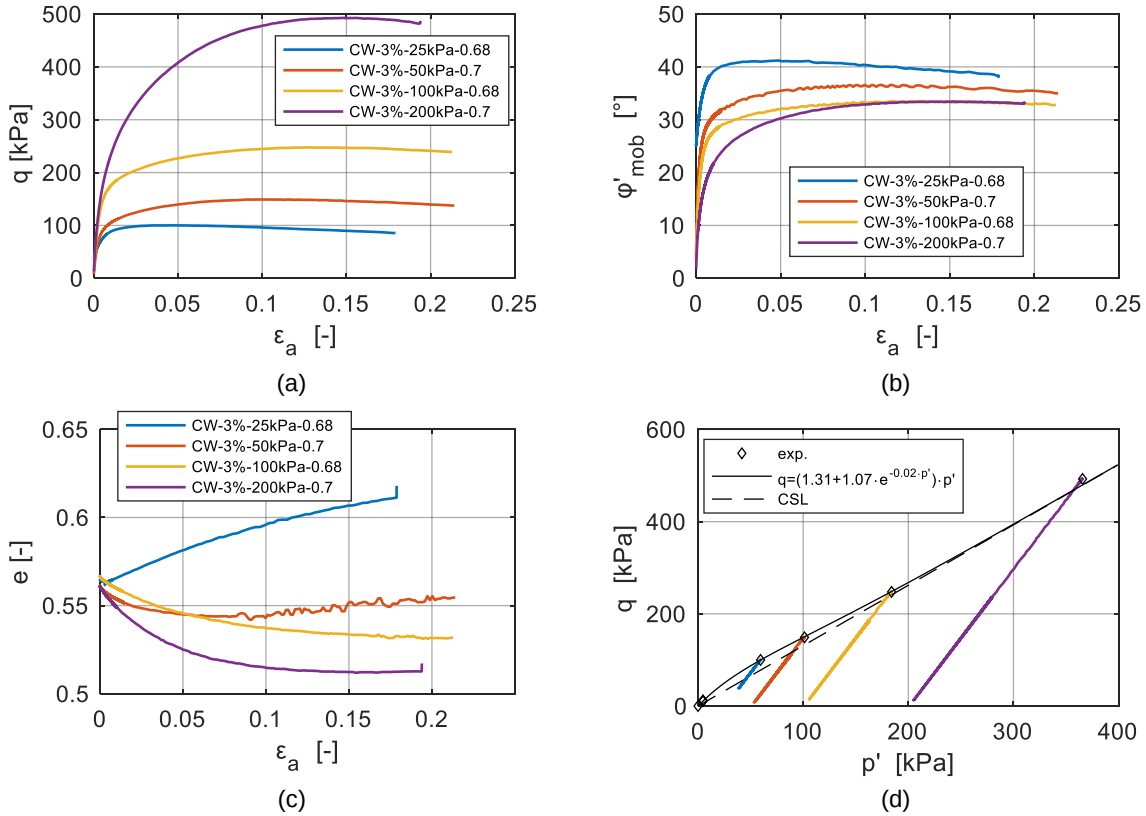

Figure 7.15: Influence of confining pressure on the shear behavior for w ≈ 3% and I_D ≈ 0.68 to I_D ≈ 0.70: (a) q vs. ε_a, (b) φ'_{mob} vs. ε_a (c) e vs. ε_a, (d) q vs. p'

Figure 7.15a reveals slight peak behavior in the stress-strain curves. The volumetric behavior of the tested samples shown in Figure 7.15c clearly indicate a change from dilative toward contractive behavior in the range of confining pressures of 50 kPa to 100 kPa. This result is in good agreement with the derived peak friction angles, which are the highest at the lowest confining pressure of 25 kPa (φ'_{peak} = 41°). For a confining pressure of 50 kPa, the peak friction angle is about φ'_{peak} = 36.5°. At confining pressures of 100 kPa and 200 kPa, the mobilized peak friction angle approaches a critical state friction angle of approximately φ'_{CS} = 32.8°, comparable to the critical state friction angle observed for the saturated samples (φ'_{CS} = 32.5°).

Note that the peak friction angles were calculated using the evolution of the suction-induced effective stress calculated with (7.23) as a function of the measured density changes for a constant suction corresponding to the initial state and. The resulting evolution of the suction-induced effective stress is plotted in Figure 7.16.

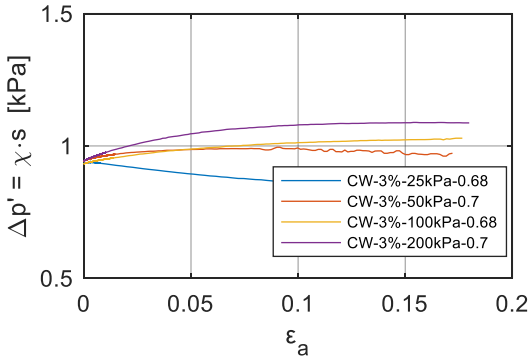

Figure 7.16: Evolution of the estimated suction-induced effective stress $\Delta p' = \Delta\sigma' = \chi \cdot s$ in the constant water content (CW) tests vs. axial strain ε_a for $w \approx 3\%$ and $I_D \approx 0.68$ to $I_D \approx 0.70$

The results confirm the expectations that the suction-induced effective stress of about 1 kPa can be assumed constant during CW tests at low water content (Chapter 6). They have therefore a negligible influence on the test evaluation when compared to the cell pressures applied to the specimens varying between 25 kPa and 200 kPa.

Figure 7.15d shows the corresponding effective stress paths and the failure criterion, which was fitted to the test data with (7.29). To better account for the non-linearity of the failure criterion at low effective stress, the unconfined compressive strength of $q_c \approx 11.5$ kPa of the as-compacted samples having $w \approx 3.6\%$, $I_D = 0.69$ and $\Delta\sigma' = 0.9$ kPa was added to the chart at $p'_{peak} = 11.5/3 + 0.9 = 4.7$ kPa (see Table 6.4).

The resulting failure criterion included in Figure 7.15d is capable of guiding the reproduction of the experimental data for $w \approx 3\%$ and $I_D \approx 0.69$, using the fitting parameter $a = 1.07$ and $b = 0.02$. Note that the parameter $M_{CS} = 1.31$ was fixed according to the CSL for saturated and unsaturated states, also depicted in the figure. The failure criterion shows strong non-linearity between 0 kPa and 100 kPa. The rapid decrease in dilatancy with increasing confining pressures can be explained by the strength of the aggregates, which are more easily destroyed during shearing at high stress levels. At low stress levels, the aggregates can withstand the loading caused by inter-particle forces.

Figure 7.17 shows the peak friction angles for the as-compacted samples at $w_{comp} = 3\%$, with $I_D = 0.68$ to $I_D = 0.70$ as a function of the effective mean stress at peak. In addition, the peak friction angles derived in Section 6.5.2 from the uniaxial tests on as-compacted samples with $w \approx 3.5\%$ and $I_D = 0.69$ are included in the figure.

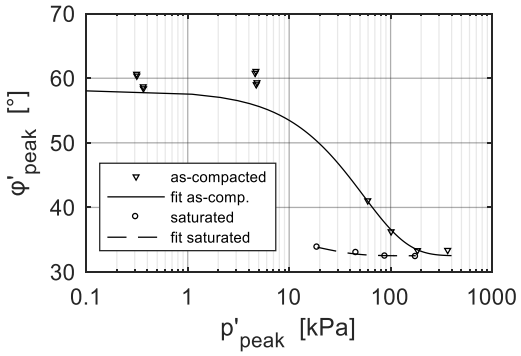

Figure 7.17: Peak friction angles predicted by (7.30) for saturated and unsaturated conditions and experimental results for constant water content (CW) tests, unconfined compression tests (UCTs) and uniaxial tensile tests (UTTs) for $w_{comp} \approx 3\%$ and $I_D = 0.68$ to 0.70 as well as for consolidated drained (CD) tests for $w_{comp} = 2\%$ to $w_{comp} = 3\%$ and $I_D = 0.7$ to $I_D = 0.77$

From (7.29), a closed-form expression for the peak friction angle can be derived:

$$\varphi'_{peak} = \arcsin\left(\frac{3 \cdot [M_{cs} + a \cdot \exp(-b \cdot p')]}{6 + [M_{cs} + a \cdot \exp(-b \cdot p')]}\right). \tag{7.30}$$

Figure 7.17 also includes the evolution of the peak friction angle obtained from this expression with the parameters $M_{cs} = 1.31$, $a = 1.07$ and $b = 0.02$ (valid for as-compacted samples with $w \approx 3\%$ and $I_D \approx 0.68$ to $I_D \approx 0.70$). The results reveal that the dependency of the peak friction angle on the effective stress is well captured by (7.30). In accordance with the experimental results, the peak friction angle approaches a constant value of low effective stress. At the highest tested confining pressure of 200 kPa, the peak friction angle approaches the critical state friction angle $\varphi'_{CS} = 32.5°$, observed for the saturated samples. Note that the peak friction angles derived from (7.30) for the saturated CD tests are also included in the figure (M_{cs} =1.31, a = 0.18 and b = 0.06).

7.5.3 CS tests

7.5.3.1 Corrections to measured water volume changes

In order to evaluate the suction-controlled triaxial tests, special attention was paid to the corrections of the measured volume changes to temperature fluctuation and leakage. While these have only a minor influence on the short-term CD tests and CW tests, their consideration in the long-term constant suction (CS) tests is of great importance.

Note that an acrylic glass cylinder and no reference burette was used to during the test CS-3%-s=46.8kPa-0.64.

A glass cylinder and a reference burette was used for the experiments CS-6%-s=6.8kPa-0.67, CS-6%-s=47.1kPa-0.69 and CS-3%-s=11kPa-0.63. For the test CS-6%-s=6.8kPa-0.67,

however, no proper reference signal could be used for corrections, due to a defect of the reference burette, which appeared during the test.

The measured water volume changes were corrected for temperature fluctuation and leakage as described in Section 7.4.1. The corresponding parameters were chosen from the calibration tests presented in Section 7.4.1, as summarized in Table 7.6.

Test	Inner cell	Reference burette	$c_{laek,IC}$ [ml/day]	$c_{laek,PW}$ [ml/day]	α_{IC} [1/C°]	α_{Bu} [1/C°]	Δt_{IC} [day]	Δt_{Bu} [day]
CS-6%-s=47.1kPa-0.69	Glass	Yes	0.03	0	0.00035	0	0	0.02
CS-3%-s=46.8kPa-0.64	Acrylic glass	No	0.42	0.05	0.00015	0.001	−0.05	0.1
CS-6%-s=6.8kPa-0.67	Glass	Broken during test	0.1	0.05	0.00035	0.001	0	0
CS-3%-s=11kPa-0.63	Glass	Yes	0.03	0	0.00035	0	0	0

Table 7.6: Parameters used to correct the volume change signals measured in the suction-controlled tests

An example of the influence of the corrections applied to the measured water volume signals is given in Figure 7.18 for the test CS-3%-s=11kPa-0.63. The measured and the corrected volume signals are shown together with the measured temperature fluctuations of the water temperature in the outer cell. A clear correlation between the temperature signal and the volume change signals is observed for both the pore-water volume and inner cell volume.

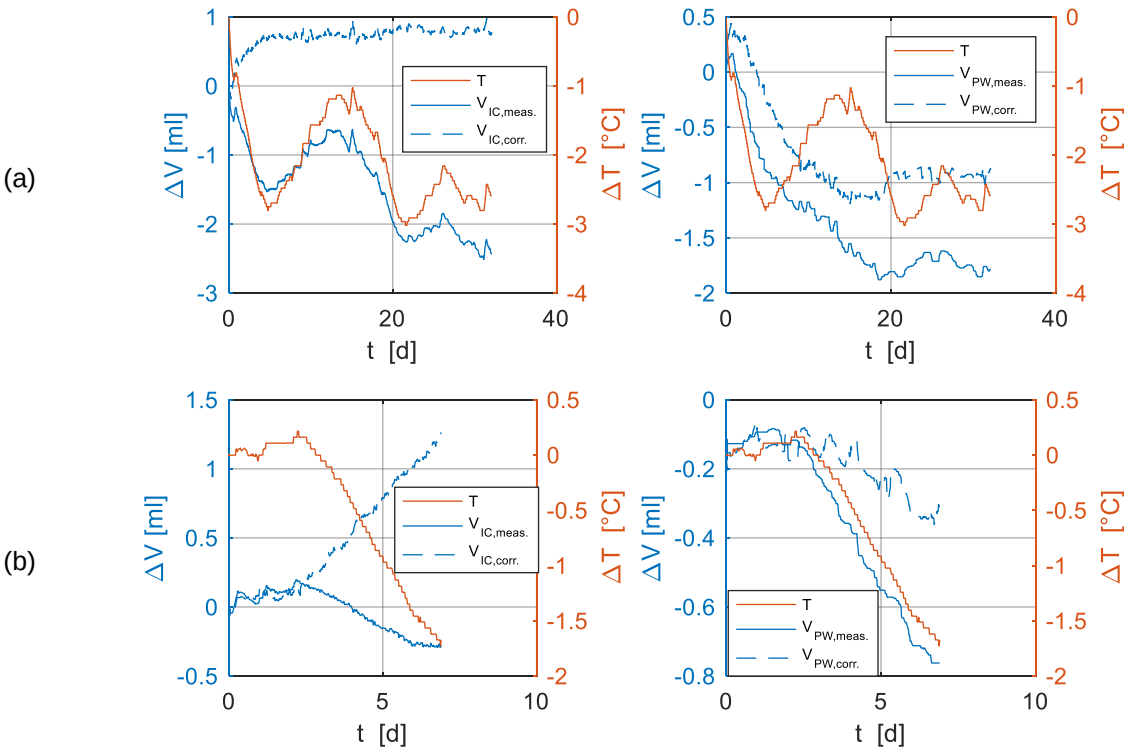

Figure 7.18: Influence of corrections to water volume measurement; (a) saturation stage, (b) shearing stage, CS-3%-s=11kPa-0.63

For the saturation stage, from Figure 7.18a it can be seen that by applying the corrections to the measured data, the fluctuations of the measured water volumes are almost fully eliminated. Therefore, the parameters selected from Table 7.6 can be considered appropriate for the test CS-3%-s=11kPa-0.63. It is also evident that without correcting the signals, no stages of constant water volume could be detected during the saturation stage. Therefore, no reliable statement be made about the completion of the saturation phase, which is assumed to happen at constant water volumes if no corrections are applied. By incorporating the corrections, however, a constant state of pore-water volume and inner cell volume can be detected at the end of the saturation stage.

The temperature fluctuations as well as the measured and the corrected water volumes are shown during the shearing stage in Figure 7.18b. Within five days, the temperature of the water in the outer cell decreased almost linearly by $\Delta T = 1.8°C$. As a result of the continuous temperature decrease and leakage, the measured water volumes of the pore water and the inner cell also continuously decreased over time. Especially with regard to the volumetric deformation of the sample, measured by changes in the water volume in the inner cell, the corrected values show a reversal of the tendency to move from contractive behavior (volume loss) to dilative behavior (volume gain), when compared to the original signal. This example underlines the necessity of water volume correction: The pore-water volume corrected for temperature fluctuation and leakage appeared to show even more fluctuations than the originally measured signal (Figure 7.18b). This finding arises because the reference burette was used to correct the test results, while apparently showing a slightly higher dependency on short-term temperature changes (within hours) than did the pore-water volume. However, the long-term trend of temperature fluctuations (within days) is well captured with the chosen correction approach. Also, note that the remaining variations in pore-water volume are very small (in the range of 1/10 of a ml). Therefore, the corrections applied to the signal are considered appropriate.

The evolution of the gravimetric water content and the degree of saturation resulting from the corrected water volume signals are shown in Figure 7.19 with respect to time. The initial water content was slightly higher than the compaction water content of $w_{comp} = 3\%$, since the HAE ceramic disk was covered with a water film prior to compaction in order to prevent cavitation (Section 7.3). This amount of water was recorded and added to the initial water content for the evaluation of the test.

It should be noted that at the beginning of the test CS-3%-s=11kPa-0.63, the suction was applied in stages in order to determine the influence of short-term changes in the suction on the changes in water content and to learn more about the soil behavior. A very sluggish response of the sample to changes in suction was observed at the beginning of the tests. The sluggish response may be explained by the low initial water content, which led to a low permeability of the soil. However, at the end of the saturation stage—during which a suction of 11 kPa was applied over a period of 10 days—the preceding stages of applied suctions had no influence on the water content. With such an application of suction, a constant water

content was achieved after only a few days. During shearing, the water content slightly increased, while the degree of saturation stayed approximately constant.

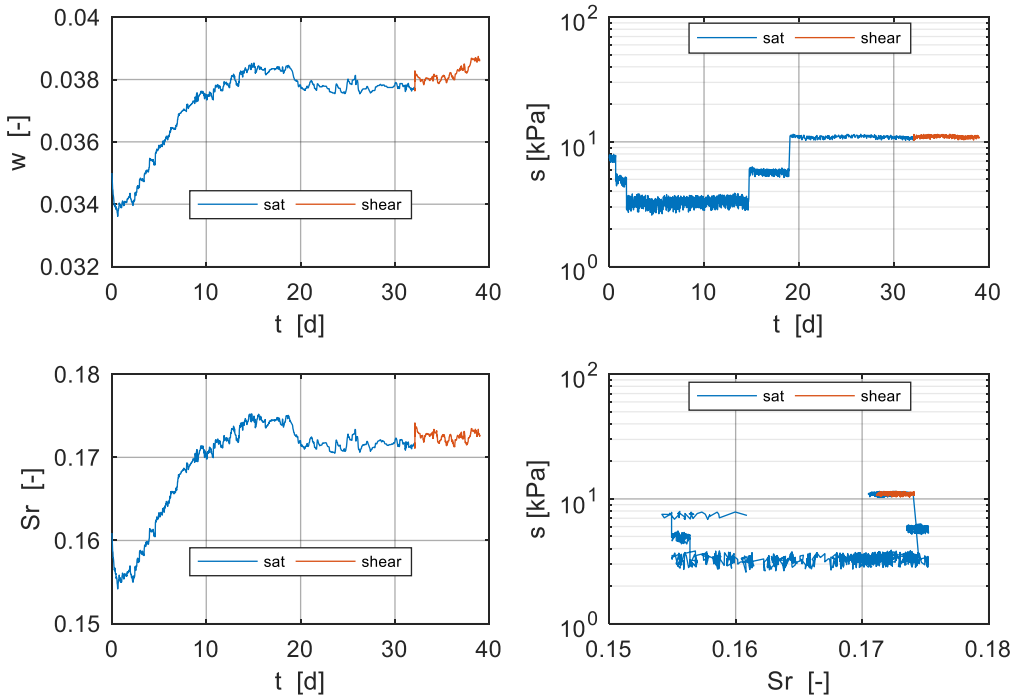

Figure 7.19: Evolution of water content and degree of saturation with respect to time, CS-3%-s=11kPa-0.63

The plausibility of the above results was checked by comparing the measured degrees of saturation during the test with the expected degrees of saturation. For the controlled, constant suction during the test, the expected degrees of saturation were derived from equation (5.1). Corresponding to the respective current relative density of the sample during the test, the parameters of (5.1) were determined by means of (5.2) for a constant compaction water content of w_{comp} = 3%.

Note that according to the water content changes during the saturation process, a wetting branch of the SWRC may be expected to describe the water-retention behavior better than the applied drying branch. However, for the examined silty sand with low fines content, the hysteresis of the SWRC may be expected to be rather small (Angerer and Birle 2016).

For both the saturation and shearing stage, Figure 7.20 shows the measured density changes as a function of the measured degree of saturation. Additionally, the I_D-Sr-paths expected from the density-dependent SWRC for w_{comp} = 3% are depicted in the figure. For an overview, the starting points and the end points of the measured and expected I_D-Sr-paths are also shown. Finally, the suction changes applied to the sample in the beginning of the test are depicted (Δs_1 to Δs_4). Obviously, the first two short-term changes of suction did not cause any measurable response of the pore water. Thus, the expected and the measured I_D-Sr-path do not approach each other considerably (Figure 7.20). Only after a minimum suction value of s_3 = 3 kPa was applied did the pore water begin to change significantly, indicated by

the course of the measured degree of saturation, which begins to approach the expected value at around 3 kPa. With the application of the nominal suction of s_5 = 11 kPa, the measured and expected degrees of saturation more closely match. Finally, at the end of the saturation, phase the two values match well. It can therefore be assumed that at the point of matching, an equilibrium between the externally applied suction and the suction acting in the sample is achieved. In view of the above results, the corrections applied to the measured volume change signals apparently provide reasonable results.

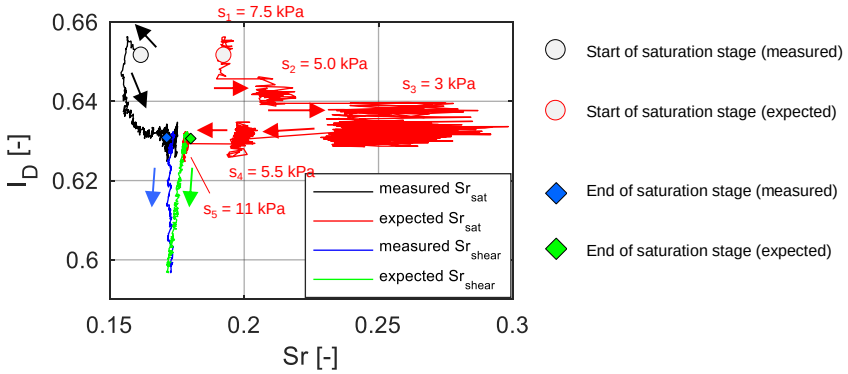

Figure 7.20: Measured and expected I_D-Sr-paths for CS-3%-s=11kPa-0.63

The I_D-Sr-path during the shearing stage—starting from the end points of the saturation stage—indicates that the sample tends to de-saturate slightly during shearing. The measured I_D-Sr-path compares well to the expected path. This agreement indicates that it is reasonable to apply the drying branch of the SWRC for the assessment of the test results.

The procedure carried out for CS-3%-s=11kPa-0.63 with the application of different suction levels was an exception from the procedures carried out for the other three CS tests, in which the saturation stage was conducted at constant suction. To ensure the validity of the experimentally achieved results, however, a plausibility check was also carried out for these tests by comparing the measured and the expected I_D-Sr-paths.

The results presented in Appendix C show a good agreement between the expected and the measured degrees of saturation at the end of the saturation phase, with a maximum deviation of about ΔSr = 1%. The hydraulic paths during shearing always show the same tendency of de-saturation while, the expected and measured course matches quite well. Only for the CS-6%-s=6.8kPa-0.67 was there a marked deviation of the measured degree of saturation from the expected degree of saturation after the end of the saturation phase of approximately ΔSr = 5%. This difference can presumably be attributed to an incorrect measurement of the amount of water, which was required to cover the HAE ceramic prior to compaction and is indicated in the results as an approximately parallel shift in the hydraulic path during shearing. Apart from this parallel shift, however, the hydraulic path during shearing is well aligned with the expected path.

7.5.3.2 Results

The results of the four CS tests are shown in Figure 7.21.

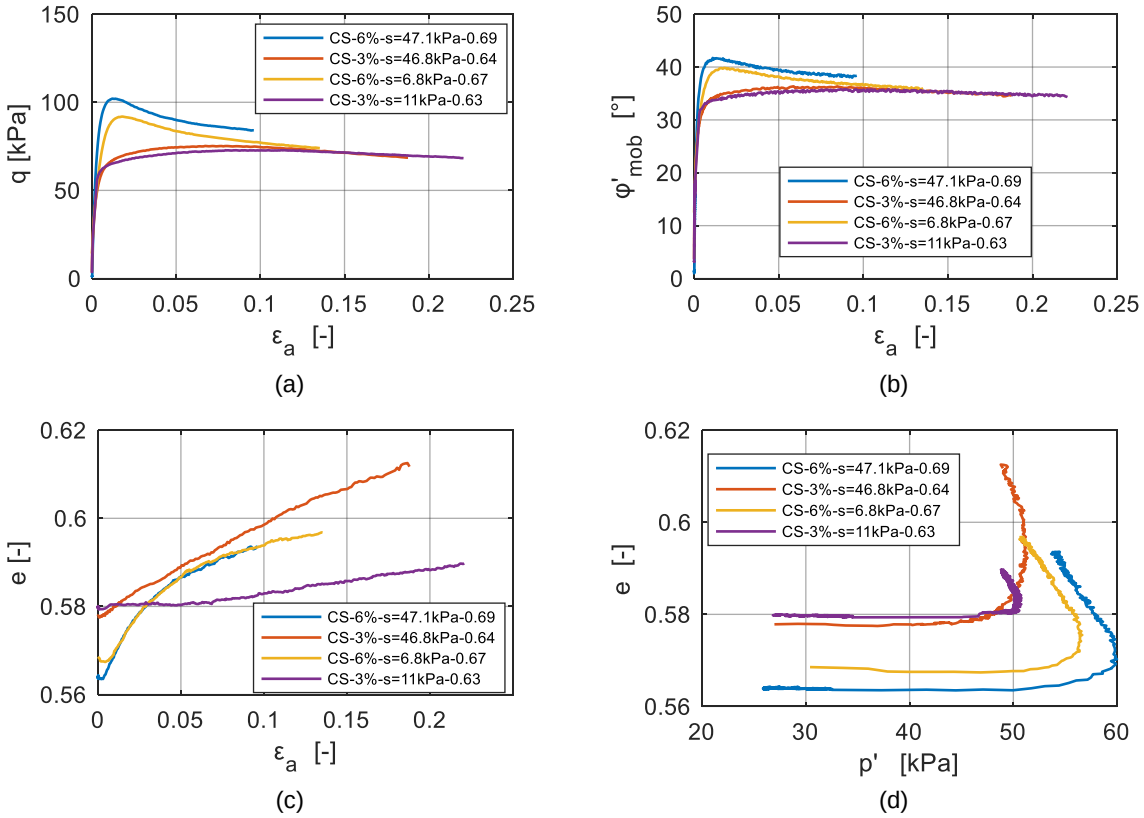

Figure 7.21: Influence of confining pressure on the shear behavior in the constant suction (CS) tests: (a) q vs. ε_a; (b) φ'_{mob} vs. ε_a; (c) e vs. ε_a; (d) e vs. p' at a confining pressure of 25 kPa

The evolution of the suction-induced effective stress determined with (7.23) for the respective constant suction and the measured density changes is shown in Figure 7.22. The results confirm the expectations that the suction-induced effective stress of about 1 kPa is rather negligible when compared to the cell pressure of 25 kPa applied to the specimens.

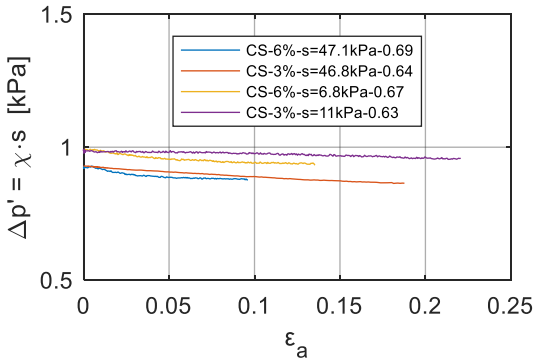

Figure 7.22: Evolution of the estimated suction-induced effective stress $\Delta p' = \Delta\sigma' = \chi \cdot s$ in the constant suction (CS) tests vs. axial strain ε_a

Regarding the samples compacted at w_{comp} = 6%, a pronounced peak is observed in both tests (Figure 7.21a). This peak behavior is well in line with the observed highly dilative behavior (Figure 7.21b). The samples compacted at w_{comp} = 6% reveal only a slight dependency of the peak shear strength on the applied suction, confirming the results of triaxial tests on similar soils (Russell 2004, Milatz 2016, Fern, Robert, and Soga 2016). Accordingly, the change in suction apparently does not change the volumetric behavior of the samples compacted at w_{comp} = 6% in both tests.

The sample in the test CS-3%-s=46.8kPa-0.64 exhibits strong dilative behavior. The volumetric behavior of the sample of CS-3%-s=11kPa-0.63, on the other hand, apparently changed its general trend during the test at small strains. At the beginning, the sample reacts in a rather dilative manner. However, after an axial strain of approximately ε_a = 0.5% to ε_a = 1%, the trend in the rate of dilatancy decreases toward much less dilative behavior (Figure 7.23).

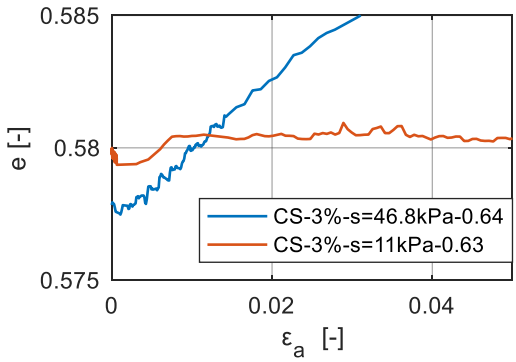

Figure 7.23: Void ratio e vs. axial strain ε_a in the constant suction (CS) tests on samples with w_{comp} = 3% and I_D = 0.63 to I_D = 0.64

This volumetric characteristic can be related to the associated aggregate stability, which is expected to be higher for the test at a suction of s = 46.8 kPa than for the test at a suction of s = 11 kPa. It is very likely that the initially existing aggregates within the sample may have been deformed or destroyed during the course of the test, for small axial strains. Note that the same behavior can be observed in the e-p' plane (Figure 7.21d). While a common critical void ratio is targeted for virtually all experiments, the sample in the test CS-3%-s=46.8kPa-0.64 deviates from this behavior considerably due to the above-mentioned mechanism. However, for the samples compacted at w_{comp} = 3%, the peak shear strengths apparently were not influenced by a change in suction (Figure 7.21a), again confirming the results of triaxial tests on similar soils (Russell 2004, Milatz 2016, Fern, Robert, and Soga 2016).

Note that when compared to the samples compacted at w_{comp} = 6%, the samples compacted at w_{comp} = 3% generally mobilized less shear strength, while the peak was less pronounced, which can be attributed to the smaller initial densities of the samples prepared at w_{comp} = 3%. To check this assumption, an additional CW test was carried out at a confining pressure of 25 kPa on a sample, compacted at w_{comp} = 3% to a relative density of I_D = 0.64, which corresponds to the relative densities achieved for the samples for the CS tests at the same compaction water content. The result of this CW test is shown in Figure 7.24 together with

the CW test on a sample with I_D = 0.68, already shown in Figure 7.15, and the two CS tests on samples compacted at w_{comp} = 3% with I_D = 0.64 and I_D = 0.64, respectively.

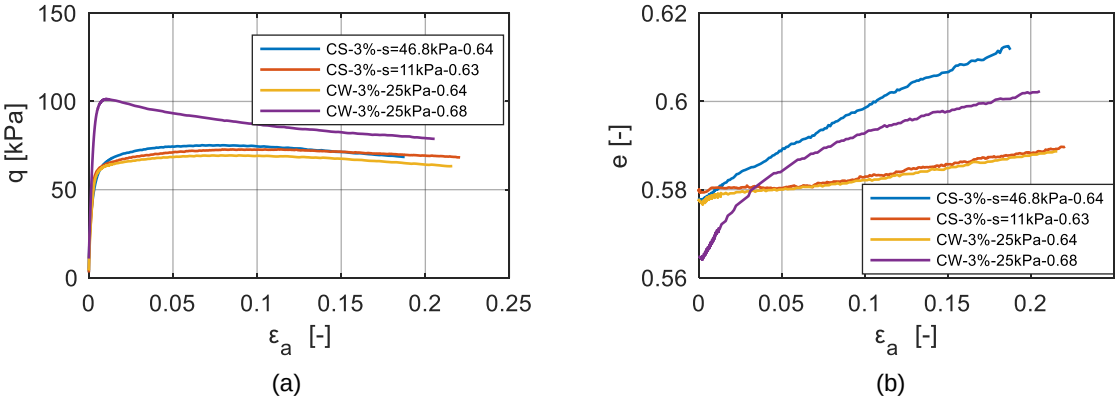

Figure 7.24: Influence of initial density on the shear behavior in constant suction (CS) and constant water content (CW) tests for w_{comp} = 3%: (a) q vs. ε_a, (b) e vs. ε_a at a confining pressure of 25 kPa

As can be seen from Figure 7.24a, the shear strength of the samples in the CW test seems to depend strongly on the initial density, since the sample compacted to I_D = 0.68 has a considerably higher shear strength than the samples compacted to I_D = 0.64. Figure 7.24b demonstrates that both the test CW-3-25kPa-0.64 and CS-3%-s=11kPa-0.63 show the same volumetric behavior, indicating a breakage of aggregates at small axial strains, according to Figure 7.23. The test on the denser sample CW-3-25kPa-0.68, on the other hand, shows a continuously dilative behavior, which does not indicate any particle breakage at small strains.

However, this behavior is probably caused not only by the different densities, but also by a fundamental change in the arrangement of the aggregated fines in the sand matrix (i.e., by a change in the microstructure) and its associated contribution to dilatancy.

At the lowest density tested for (I_D = 0.63), it can be assumed that the aggregated fines are mainly located between the sand-to-sand particle-contacts, whereas this aggregate arrangement in the sand matrix may have changed fundamentally at I_D = 0.68, as the aggregates are more likely to be located between the macrovoids of the sand skeleton. While for both samples, the density is still high enough to initiate dilative behavior, the aggregates of the looser samples do not exhibit enough strength to resist the stresses associated with the interlocking mechanisms on the micro-level from the beginning of the test. In the denser sample, on the other hand, the aggregates may be less stressed from the beginning of the test, since the sand particles are expected to be closer together and to contribute more to dilatancy.

From an energetic point of view, the fracture of the aggregates at small strains can be more favorable for the looser sample than a rotation of the aggregates over the solid sand particles. This fracture can cause the interlocking mechanisms to break down at small strains, resulting in lower shear strength than would be expected from density. High suction may stabilize the aggregates in the ‘loose’ samples with low strains but does not prevent the

shear strength from decreasing considerably. This conclusion can be drawn from the comparison of the shear behavior observed in tests CS-3%-s=11kPa-0.63 and CS-3%-s=46.8kPa-0.64 (Figure 7.24).

Note that the above considerations represent a first approach to describe the significant change in the shear behavior due to small density changes. Further research is required to gain a more comprehensive picture of this issue and to review the assumptions made.

Apart from the above, the results in Figure 7.24 show that the shear strength examined in the CS and CW tests on samples compacted at w = 3% to the same initial density is essentially the same. Since the results of the CW and CS test furthermore exhibit a similar volumetric behavior, this finding confirms the assumption that the suction during CW tests is approximately constant. It also evidences that CW tests can be used to assess the shear behavior of the silty sand at low water content appropriately. Similar results were found in Fern et al. (2014) for the shear strength of Chiba sand in CS and CW tests. The difference in the shear strength examined in the CS tests on samples prepared at w_{comp} = 6% and w_{comp} = 3% shown in Figure 7.21 may be therefore traced to the differences in density and not to a pronounced influence of the different microstructures due to different compaction water content. This assumption is supported by comparing the shear behavior of the samples in the CW test and CS test at the same density, as shown in Figure 7.25 and Figure 7.26.

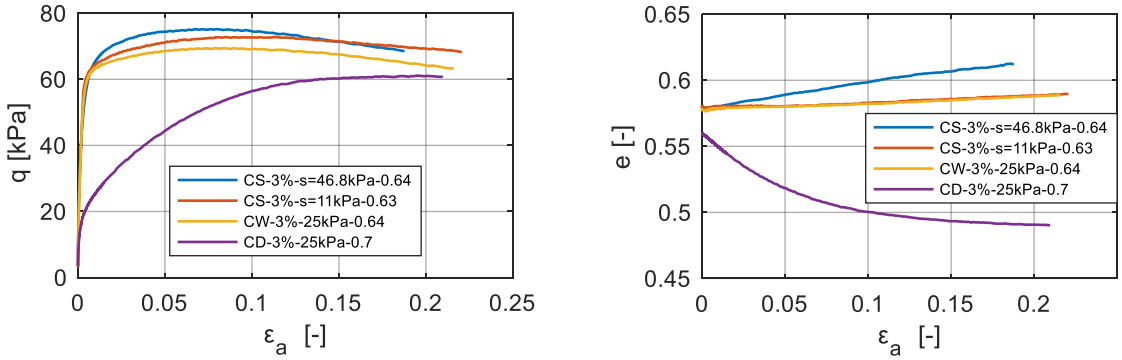

Figure 7.25: Shear behavior in constant water content (CW) and constant suction (CS) tests at 0.63 < I_D < 0.64: (a) q vs. ε_a, (b) e vs. ε_a at a confining pressure of 25 kPa

Both figures make obvious that the initial relative density has a very strong effect on the peak shear strength. They also indicate that both CS and CW tests yield similar shear strength, provided the initial density is the same. Therefore, Figure 7.25 and Figure 7.26 indicate that the initial microstructure achieved by compacting the samples at different water content does not lead to a pronounced difference in the secant peak friction angle. This finding contrasts those from the uniaxial tests on as-compacted samples, for which a strong dependency of the peak friction angles on the microstructure was found. However, the higher stress state is likely to suppress this influence (as also noted by, e.g., Lade 2016).

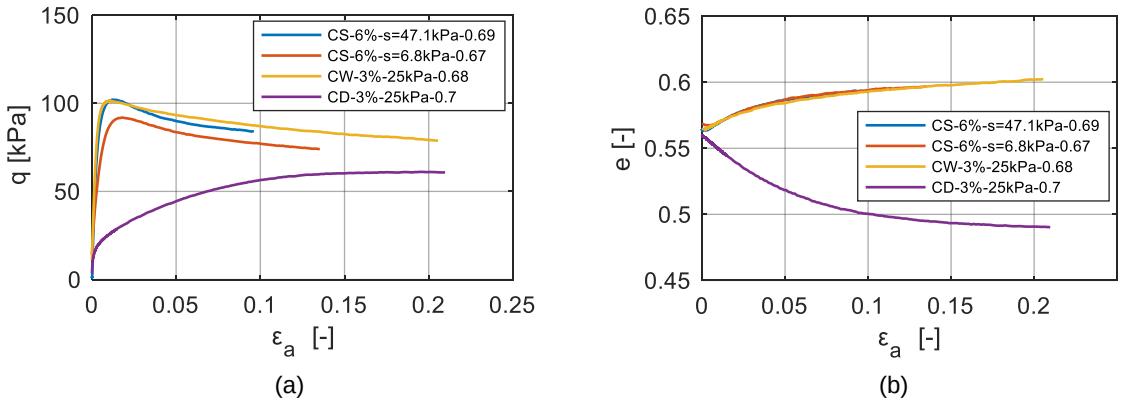

Figure 7.26: Shear behavior in constant water content (CW) and constant suction (CS) tests at $0.69 > I_D > 0.67$: (a) q vs. ε_a, (b) e vs. ε_a at a confining pressure of 25 kPa

In summary, the results show that the conventional CW test can be used to determine the shear strength of the silty sand at the tested low degrees of saturation. The long-term and calibration-intensive CS tests led to very similar measured peak shear strengths. The examined small variations in suctions did not lead to significantly different shear behavior. Because of the expected minor changes in the water content of the embankment material, the encountered small variations in suction may therefore be neglected.

7.6 Summary and conclusion

From CD tests on saturated samples, the critical state friction angle φ'_{cs} = 32.5° was found to describe the saturated shear strength of the silty sand in the tested stress range from 10 kPa to 200 kPa. Any influence of the compaction water content (and thus of microstructure) on the test results could be excluded.

From the CS tests conducted at a confining pressure of 25 kPa, no clear dependency of the peak shear strength of samples with the same initial microstruc and density on the suction could be detected. In the tested narrow range of suction, the influence on the shear strength was therefore considered negligible. For samples with apparently small deviations in initial density, on the other hand, an unexpectedly large change in the measured shear strength was observed. This change in shear strength cannot be related only to the initial density but is also believed to depend on the initial microstructure, in particular the location of the aggregates either in the voids formed by sand particles or between the sand particles as such. According to the test results, the latter is expected to occur in less dense samples, leading to more stress and eventually fracture of the aggregates during shearing, accompanied by a sudden change of volumetric behavior at small strains to less dilatancy than would be expected from the density. Although this consideration is only a first approach to the underlying mechanisms, it emphasizes the importance of considering microstructure in describing the initial state of compacted silty sands when examining shear behavior.

Since the CW tests and the CS tests yielded similar results for the same densities, however, it could be concluded that CW testing is appropriate to determine the shear strength of the as-compacted silty sand. Within the examined boundary conditions, time-consuming suction-controlled triaxial tests are therefore not necessary to assess the shear strength of the silty sand. From CW tests on as-compacted samples, a failure criterion could be derived, strongly non-linear at confining pressures of 10 kPa to 100 kPa. In this stress range, the shear strength of the as-compacted samples was significantly higher than that of the saturated ones. In view of the findings in Chapter 6, the shear strength of the as-compacted samples at low effective stresses of about 1 kPa (examined with the uniaxial tests) depends on the degree of aggregation produced by the different compaction water content and the strength of the aggregates caused by the corresponding suction, the latter generating intra-aggregate stresses. In the triaxial tests at effective stresses higher than approximately 25 kPa, this effect of suction on volumetric behavior still exerts a strong influence on the shear strength since, while the suction-induced effective stress of about χ = 1 kPa remained negligible throughout all tests, the dilatancy was significantly increased. However, at the stress level tested in the CS tests, dilatancy was much less affected by varying compaction water content compared to the very low stress levels tested in uniaxial tests.

Note that in general, one can expect a gradual change in the volumetric behavior from the contractancy of samples tested at high water content and low suctions to a strong dilatancy of samples tested at low water content and high suctions (Section 2.4.2). In accordance with

the scope of the work, however, the suctions tested in this study are too high to examine this change in volumetric behavior and thus in shear strength.

8 Practical aspects of assessing slope stability

8.1 Conventional stability analysis

8.1.1 General remarks

Extending the findings in Chapter 6 and Chapter 7 to the more general case of as-compacted granular soils containing non-plastic fines, the failure criterion may be expressed as follows:

$$q = [M_{cs} + a \cdot \exp(-b \cdot p')] \cdot p' \tag{8.1}$$

with M_{cs} Stress obliquity at critical state

a, b Fitting parameters

p' Effective mean stress.

The above equation is capable of capturing both a linear and a non-linear dependency of the shear strength on the effective stress in saturated and unsaturated states, if its parameters are properly chosen:

- In the saturated state, the parameters a and b in (8.1) depend on the density and microstructure.
- In the unsaturated state, the parameters a and b in (8.1) depend on the density, microstructure and suction. Note that all three influencing variables are reflected in the SWRC. Therefore, it can be concluded that the parameters a and b depend on the SWRC.
- The parameter M_{CS} represents the stress obliquity at the critical state, which is the same for saturated and unsaturated conditions.

For unsaturated conditions, in (8.1), the effective stress is described by

$$p' = \begin{cases} p_{net} + s & \text{for } s \leq s_{AE} \\ p_{net} + s \cdot \left(\frac{s}{s_{AE}}\right)^m & \text{for } s > s_{AE} \end{cases}, \tag{8.2}$$

where $p_{net} = p - u_a$ is the mean net stress, p is the total mean stress and u_a is the pore-air pressure. The parameters in (8.2) can be expected to be affected by the following:

- The parameter m may depend on the soil type and on the microstructure.
- The air entry value s_{AE} depends on the density and microstructure.

Note that for the silty sand under investigation, the exponent m = −1.09 can be assumed to be constant for different microstructures if s is related to an equivalent as-compaced SWRC (Section 6.5.3).

If the shear strength expressed in the τ - σ' plane is used,

$$\tau = \sigma' \cdot \tan \varphi'_{peak} \,, \tag{8.3}$$

a non-linear failure criterion can be described by a secant peak friction angle φ'_{peak}, which depends on the effective stress.

The evolution of the secant peak friction angle with effective stress can be derived from (8.1):

$$\varphi'_{peak} = \arcsin\left(\frac{3 \cdot [M_{cs} + a \cdot \exp(-b \cdot p')]}{6 + [M_{cs} + a \cdot \exp(-b \cdot p')]}\right). \tag{8.4}$$

8.1.2 Shear strength parameters according to Mohr–Coulomb

To calculate slope stability, most conventional computer programs based on the limit equilibrium technique (LET) require a linear failure criterion according to Mohr–Coulomb with shear strength parameters (effective tangent friction angle $\varphi'_{M\text{-}C}$ and effective cohesion $c'_{M\text{-}C}$). To use the conventional software, while taking into account the non-linear failure criterion and suction-induced effective stress, the cross section of the slope can be discretized into areas to which linear Mohr–Coulomb failure criterions can be assigned, according to the respective stress levels.

For example, the cross section of an embankment may be divided into two zones in which different formulations of shear strength can be applied, depending on the hydraulic properties and the stress level:

- Zone 1: From the surface down to approximately 1.0 m, the embankment material is strongly influenced by climate. This influence can lead to almost complete saturation or complete drying of the soil. Consequently, no increase in the shear strength due to unsaturated conditions can be applied for the long-term. This includes neither an increase in effective stress nor an increase in peak friction angle with suction.
- Zone 2: From approximately 1.0 m below the surface of the embankment, climatically unaffected unsaturated conditions may be assumed. Therefore, an increase in both the effective stress and peak friction angle can be taken into account.

Figure 8.1 shows the simplified case of an embankment consisting of one type of soil with a constant void ratio and homogeneous microstructure. The allocation of the cross section into different zones is illustrated in Figure 8.1.

- Zone 1 represents saturated conditions and low effective stresses. Based on the experimentally determined shear strength of the saturated silty sand in this study, a linear failure criterion is assumed for zone 1. Note that in general, the failure criterion can also be non-linear for saturated conditions.
- Zone 2 denotes unsaturated conditions with a constant degree of saturation less than 1 and low to high effective stresses. Corresponding with the findings of the experimental

program in this study, the failure criterion can be assumed to be non-linear for granular soils with non-plastic fines. Note that zone 2 may be subdivided into further zones to better adjust the pressure-dependent shear strength of the soil.

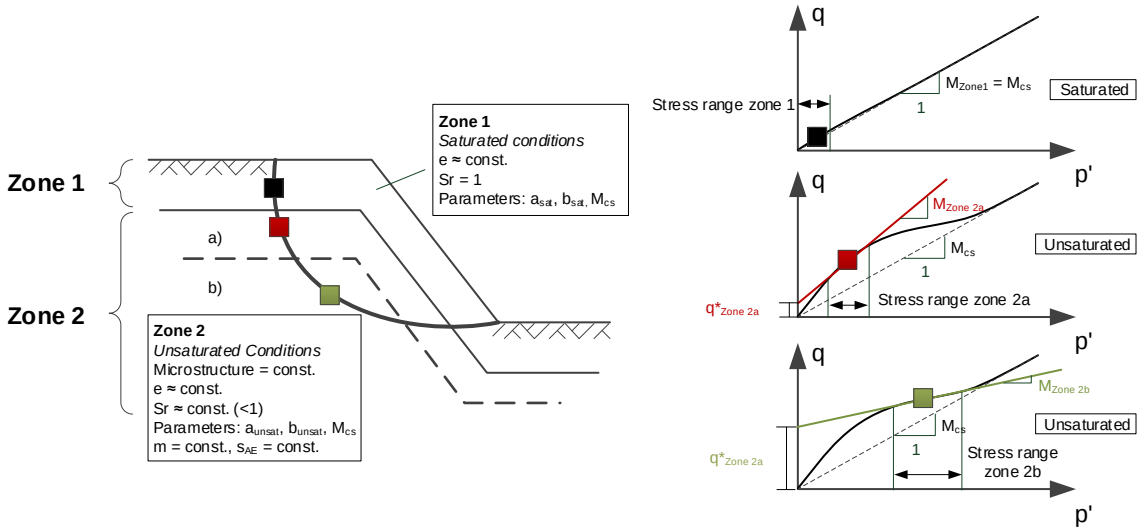

Figure 8.1: Simplified approach to account for a non-linear failure criterion when using the Mohr–Coulomb failure criterion in commercial slope stability software

The shear strength parameters $\varphi'_{M\text{-}C}$ and $c'_{M\text{-}C}$ assigned to each zone can be derived from the non-linear failure criterion by linearizing it within the stress ranges present in the respective zones (Figure 8.1, right).

Note that if Roscoe's invariants are used to describe the failure criterion in the p' – q plane, for each zone i, the inclination $M_{Zone,i}$ of the tangent to the non-linear failure criterion and the intersection of the tangent with the q-axes $q^*_{Zone,i}$ at p' = 0 kPa must be known.

With $M_{Zone,i}$, the Mohr–Coulomb friction angle can be determined:

$$\varphi'_{M-C,i} = \arcsin\frac{3 \cdot M_{Zone,i}}{6 + M_{Zone,i}}. \tag{8.5}$$

The associated (numerical) cohesion can be derived from $q^*_{Zone,i}$:

$$c'_{M-C,i} = q^*_{Zone,i} \cdot \frac{\left(3 - \sin\varphi'_{Zone,i,tangent}\right)}{6 \cdot \cos\varphi'_{Zone,i,tangent}}. \tag{8.6}$$

8.1.3 Suction-induced effective stress and apparent cohesion

Even though the conventional software may not be capable of incorporating a suction-induced effective stress, it is possible to take $\Delta\sigma' = \chi \cdot s$ into account indirectly. Therefore, the failure criterion of the unsaturated soil is shifted to the left by the expected value of $\Delta\sigma'$, as shown in Figure 8.2. From the figure, it can be seen that the horizontal shift of the failure criterion results in an equivalent non-linear failure criterion in the τ - σ_{net} - plane, which does

not pass through the origin but exhibits a well-known apparent cohesion c_{app}. The apparent cohesion is therefore a measure of the additional shear strength due to the suction-induced increase in both the effective stress and dilatancy.

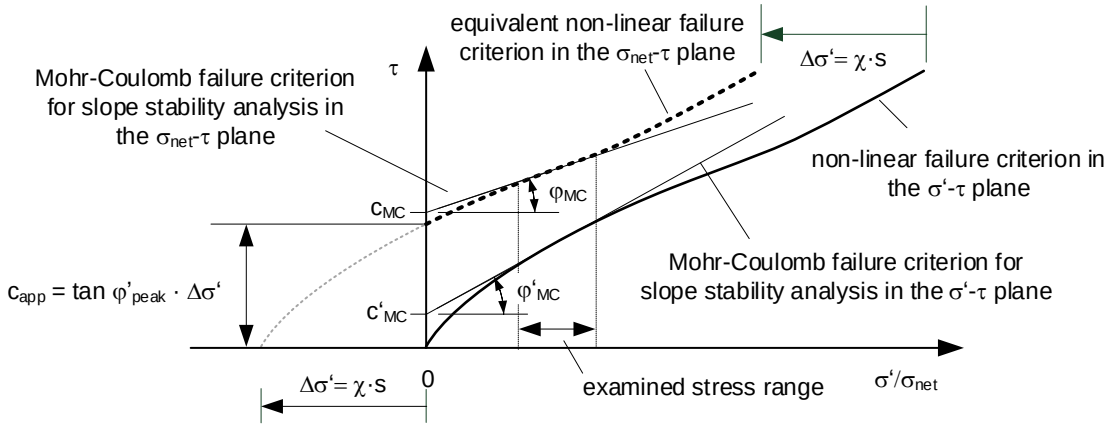

Figure 8.2: Simplified approach to account for unsaturated conditions in conventional slope stability software

In this context, note that the horizontal shift of the non-linear failure criterion to the left does not correspond with a shift upwards. This difference does not appear if the failure criterion is approximately linear, as it is often assumed in the literature. For the non-linear failure criterion of the silty sand, however, the Mohr–Coulomb shear strength parameters derived in the τ - σ' plane differ from those derived in the τ - σ_{net} plane not only in the cohesion, which would be the case for a linear failure criterion, but also in the friction angle (Figure 8.2).

If the suction-induced effective stress cannot be directly accounted for in slope stability analysis, it is therefore important to derive the Mohr–Coulomb shear strength parameters φ_{MC} and c_{MC} from the shifted failure criterion. In this case, the stress range, in which the Mohr Coulomb shear strength parameters are examined, must be expressed in terms of net stress and not effective stress. Note that the assignment of the shear strength parameters φ_{MC} and c_{MC} to the τ - σ_{net} plane is marked by the missing inverted commas.

From Figure 8.2, it can also be seen that due to the non-linearity of the shifted failure criterion, the difference between c_{MC} (τ - σ_{net} plane) and c'_{MC} (τ - σ' plane) can be less than the apparent cohesion c_{app}. For this purpose, the apparent cohesion c_{app} is prone to misinterpretation, since it does not represent a Mohr–Coulomb type of shear strength parameter but takes into account the non-linearity of the failure criterion.

8.2 Case-study

8.2.1 Traffic embankment

Since the goal of this research was to find a procedure to assess the slope stability of existing traffic embankments in Eastern Germany realistically, the effect of the application of the above procedure to slope stability analysis will be demonstrated in the following on an example embankment consisting granular soil with non-plastic fines, which can be considered representative for such traffic embankments.

An embankment of 7.5 m height and slope inclination of $\beta = 35°$ is assumed (Figure 8.3), consisting of the homogeneously distributed silty sand examined above. The embankment is loaded as shown in Figure 8.3 and located above the groundwater level.

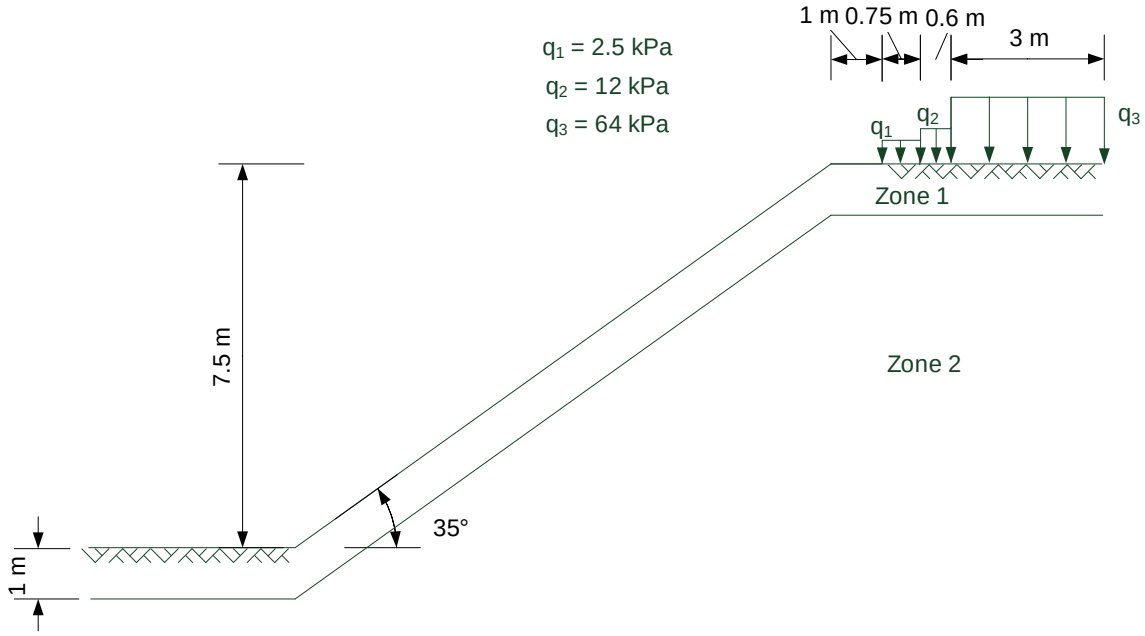

Figure 8.3: Geometry and loading of an example traffic embankment of silty sand

8.2.2 Software

For slope stability analysis, the software LimitStateGEO (from Limit State Ltd) was used. LimitStateGEO applies so-called discontinuity layout optimization (DLO) to identify a critical layout of slip lines, which form the boundaries between the moving rigid blocks of soil, of which the failure mechanism is composed (Limit State Ltd 2016). Associated with this mechanism is a collapse load factor, which is an upper bound on the exact load factor (Limit State Ltd 2016).

For slope stability analysis, also a factor of strength F can be derived, where F corresponds to the factor of safety (FOS) in conventional calculations. It indicates the factor by which the shear strength parameters must be reduced in order to cause the slope to fail:

$$\tan\varphi'_{fail} = \tan\varphi'/F$$
$$c'_{fail} = c'/F. \quad (8.7)$$

Note that the software can account for materials with a bi-linear failure criterion.

Long-term analyses were performed. Partial safety factors were applied according the design approach A2 and M2 for the ultimate limit state GEO defined in the European Standard EN1997-1 (EC7). These partial factors correspond to the design approach for traffic embankments used in Germany (Table 8.1). For simplicity, only permanent loads were applied to the embankment.

Loads and resistance	**Partial factors**
Permanent loads, favorable and unfavorable	1.0
Variable loads, *unfavorable*	1.3
c’	1.25
tan φ’	1.25

Table 8.1: Partial factors used for drained stability analysis, according to GEO A2/M2 (EC7)

8.2.3 Linearization of failure criterion

The non-linear failure criterion of the as-compacted silty sand at w_{comp} = 3% and $I_D \approx 0.69$ (Chapter 7),

$$q = [1.31 + 1.06 \cdot \exp(-0.02 \cdot p')] \cdot p', \quad (8.8)$$

was taken to characterize the shear strength of the embankment material (Figure 8.4).

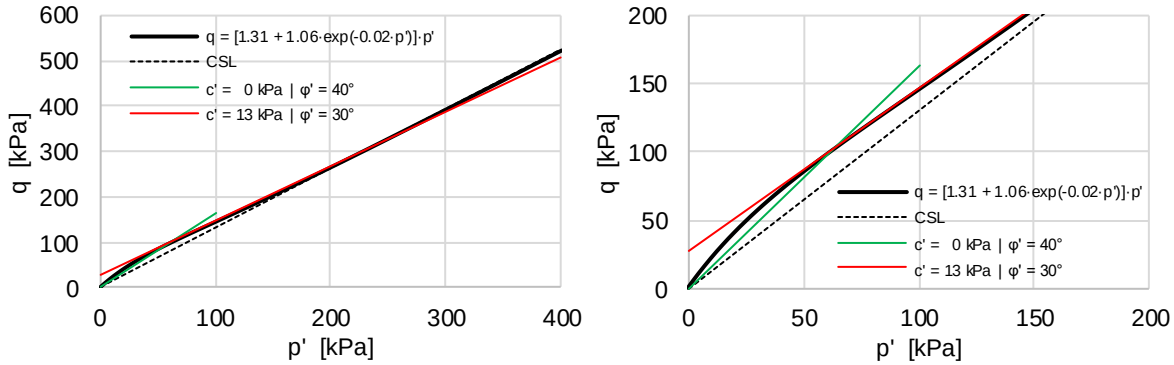

Figure 8.4: Linearized failure criterion for the slope stability analysis

In Figure 8.4, the CSL approximately represents the shear strength of the saturated silty sand (Section 7.5.1.2).

According to the findings from Chapters 6 and 7, the suction-induced effective stress can be expected to be negligible ($\Delta\sigma' \approx 1$ kPa). Note that if no suction-induced effective stress is

applied, the failure criterion should be shifted to the left by the expected $\Delta\sigma$' (Figure 8.2) and the Mohr–Coulomb shear strength parameters should be derived from it. In the present case, however, no significant influence of the slight shift of $\Delta\sigma' \approx 1$ kPa to the left on the determination of the shear strength parameters $c_{M\text{-}C}$ ($\approx c'_{M\text{-}C}$) and $\varphi_{M\text{-}C}$ ($\approx \varphi'_{M\text{-}C}$) is expected. Therefore, the failure condition was not shifted.

The slope stability of the example embankment was calculated for two cases.

- In case 1, zone 2 was expected to be completely saturated. Therefore, according to the CSL representing the shear strength at saturated conditions, the Mohr–Coulomb parameters $\varphi' = 32.5°$ and c' = 0 kPa were assigned to zone 2.
- In case 2, the soil in zone 2 was assumed to be in an homogeneous unsaturated state with w = 3%. In LimitStateGEO, a bi-linear shear strength was applied to zone 2 by linearizing the non-linear failure criterion, as shown in Figure 8.5. Therefore, two Mohr–Coulomb failure criteria were defined, the minimum of which defines the shear strength at any stress state. At low effective stress less than 50 kPa, the bi-linear failure criterion underestimates the non-linear failure criterion, shear strength. At an effective stress between 50 kPa and 200 kPa, the bi-linear failure criterion approximately corresponds to the non-linear failure criterion. At effective stresses higher than approximately 200 kPa, the non-linear failure criterion is again underestimated. Notably, at stresses above about 300 kPa, the linearized failure criterion would even predict a lower shear strength than would be expected for saturated conditions (i.e., CSL). Therefore, the bi-linear failure criterion was on the safe side over the entire range of effective stress. Note that the definition of sub-zones may be useful if slope stability cannot be demonstrated with a single bi-linear failure criterion in zone 2. This demand may arise at high effective stresses in very large embankments, where the bi-linear approach may underestimate the shear strength in a large area of the embankment cross-section.

In both cases, the critical state friction angle $\varphi'_{cs} = 32.5°$ and a cohesion of c' = 5 kPa were assigned to zone 1. The cohesion was applied to stabilize the calculations numerically.

8.2.4 Results and discussion

Figure 8.5 shows the failure mechanisms derived from LimitStateGEO for case 1 and case 2. In addition, the Mohr–Coulomb shear strength parameters assigned to the respective zones are included.

- Case 1 corresponds to a conventional procedure to derive the slope stability of a traffic embankment. It uses saturated shear tests and applies the corresponding shear strength parameters to the slope stability calculation. With this procedure, FOS = 0.95. Since FOS ≥ 1 is required to demonstrate standard-compliant slope stability, the slope is not stable, according to the standard.
- In case 2, the bi-linear failure criterion was applied to zone 2. Although an increase in the effective stress state was neglected, FOS = 1.176. Therefore, the standard-compliant

slope stability can be demonstrated if the Mohr–Coulomb shear strength parameters according the non-linear failure criterion of the unsaturated silty sand are applied.

Note that the failure mechanism has changed slightly from case 1 to case 2. Since in the latter case the shear strength is significantly higher, the failure mechanism appears flatter, which was automatically detected by the calculation routine implemented in LimitStateGEO. Care should be taken, however, when the effect of suction on a failure mechanism predefined by saturated calculations is investigated. It is possible that the determined FOS is not the critical one, as a different geometry of the failure mechanism would be required to detect it.

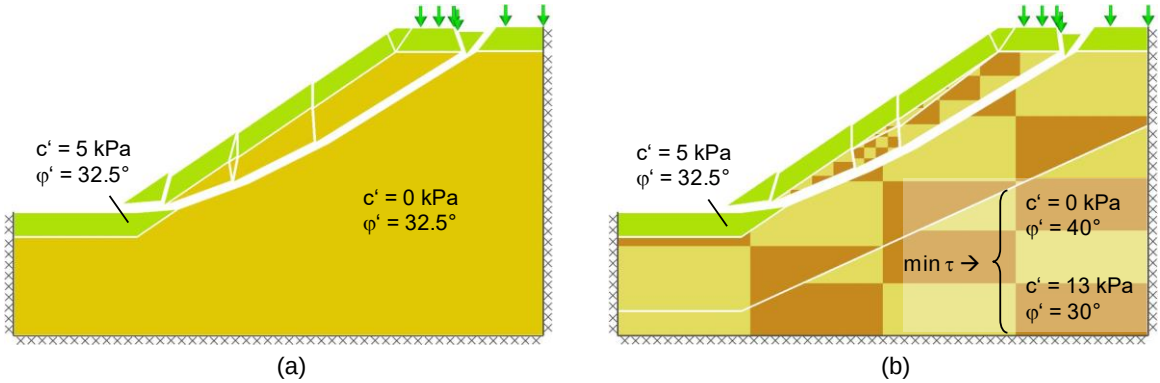

Figure 8.5: Shear strength parameters and failure mechanisms for (a) case 1 (saturated) and (b) case 2 (unsaturated)

Being very simple, the calculations demonstrate the applicability of the above procedure to analyze the stability of slopes of unsaturated silty sand. The results show that by taking into account the dual effect of suction on shear strength, the standard-compliant slope stability of apparently too-steep slopes can be demonstrated. This could not be demonstrated if the conventional procedure for assigning saturated Mohr–Coulomb shear strength parameters to the embankment material was carried out. The subdivision of the slope into different zones and the assignment of Mohr–Coulomb shear strength parameters to these zones, according to the non-linear failure criterion for the examined unsaturated state, is simple and can be performed by practicing engineers. Therefore, for practical purposes, to take into account the dual effect of suction in slope stability analysis, no sophisticated software or constitutive models are required.

9 Summary

The present investigations were motivated by the issue of whether the embankment stability of existing traffic embankments can be verified by considering unsaturated conditions. In this context, the focus of the study was on the experimental determination of the dual effect of suction on both the dilatancy and the effective stress of silty sands, which are predominantly encountered in such embankments.

In order to account for the *in situ* conditions of the embankment material, exploratory drilling was implemented on an old traffic embankment. The embankment material was found to be silty sand at medium-dense to dense states prevailing at low water content in approximately as-compacted conditions. Based on the findings for the hydraulic performance of embankments of similar soils, the detected hydraulic properties (i.e., water content and suction) are expected to be constant over the long-term.

Using shear tests on silty soils similar to those encountered in the exploratory drilling and published in the literature, Bishop's effective stress variable χ was re-evaluated. The results showed that the suction-induced effective stress can be described by Khalili's approach for χ, if the exponent m is set to values smaller than m = −1. Furthermore, the investigation of the shear behavior of such soils showed that the definition of χ and the failure criterion are interrelated due to the dual effect of suction on the effective stress and dilatancy, if experimental results from the peak state are evaluated. It was found that the enhancing effect of suction on dilatancy affects the shear behavior to a greater extent than the effective stress caused by suction, which is generally low.

For the experimental investigations, a representative silty sand was selected, which reflects the average index-properties of the embankment material encountered during the exploratory drilling. On this soil, the soil-water retention curves (SWRCs) and the pore size distributions (PSDs) were determined. The results reveal that the lower the compaction water content and the lower the density, the more pronounced the aggregated structure of the silty sand. Based on the comparison of PSDs derived from both mercury intrusion porosimetries (i.e., MIP tests) and suction measurements (i.e., SWRCs), the different microstructures produced by compacting the samples at various levels of water content to different densities were found to be well reflected in the SWRC. Incorporating the *in situ* conditions encountered during the exploratory drilling, the experimental studies on the shear strength of the silty sand were conducted.

Based on micro-mechanical considerations, a theoretical framework was developed to experimentally determine both the suction-induced effective stress and the suction-induced shear strength by performing uniaxial tensile tests (UTTS) and uniaxial compression tests (UCTs). Both methods allowed shear testing at a very low effective stress level not accessible with triaxial testing. Experiments on as-compacted samples with varying compaction water content but same density revealed high peak friction angles ranging from approximately $\varphi'_{Peak} = 45°$ to $\varphi'_{Peak} = 65°$ at low suction-induced effective stresses of about $\Delta\sigma' = 1$ kPa. Changes in microstructure resulting from varying compaction water content

were directly reflected in the measured peak friction angles while the suction-induced effective stress was approximately constant. The highest friction angles were determined for samples with the most pronounced double porosity and the highest suction. Both decreasing suction and decreasing double porosity had a decreasing effect on the peak friction angle. From this, it could be concluded that suction induces an intra-aggregate stress (e.g. up to several hundred kilopascals when assuming fully saturated aggregates with $\chi_{aggregate} \approx 1$), which on the one hand causes an inherent strength of the aggregates, but on the other hand does not significantly influence the effective stress state. The higher the suction, the stronger the aggregates and the higher the dilatancy. The measured suction-induced effective stress could be best modelled by Khalili's approach for χ by applying a unique exponent $m = -1.09$ and considering an 'as-compacted' SWRC. This approach was used to account for the suction-induced effective stress during triaxial testing.

Triaxial compression tests were performed on both saturated and unsaturated samples to determine the shear strength of the silty sand at higher stress levels than those assessable in the uniaxial tests. From CD tests on saturated samples, the critical state friction angle $\varphi'_{cs} = 32.5°$ was found to describe the saturated shear strength of the silty sand in the tested stress range from 10 kPa to 200 kPa. Any influence of the compaction water content (and thus of microstructure) on the test results could be excluded, confirming the findings from the literature.

For the CS tests conducted at a confining pressure of 25 kPa, an extensive calibration process was carried out to correct the measured water volume signals for temperature fluctuations and leakage. In order to check the equilibrium of the pore-water pressure during the CS tests, a procedure was developed to compare the measured and the expected degree of saturation in dependency of the applied suction and the measured density changes. For constant density, suction changes between $s = 6,8$ kPa to $s = 47,1$ kPa were not found to influence the measured shear strength considerably. In contrast, for a small decrease in density from $I_D = 0.68$ to $I_D = 0.64$, the shear strength appeared to decrease considerably. This change in shear strength cannot be related only to the initial density but is also believed to depend on the initial microstructure, in particular the location of the aggregates either in the voids formed by sand particles or between the sand particles as such. According to the test results, the latter is expected to occur in less dense samples, leading to more stress and eventually fracture of the aggregates during shearing, accompanied by a sudden change of volumetric behavior at small strains to less dilatancy. Although this consideration is only a first approach to the underlying mechanisms, it emphasizes the importance of considering microstructure in describing the initial state of compacted silty sands when examining shear behavior.

Since, for the same densities, the CW tests and the CS tests yielded similar results, it could be concluded that the CW test is an appropriate method to determine the shear behavior of the as-compacted silty sand. Time-consuming and costly suction-controlled shear tests are therefore not necessary.

In view of the above, from CW tests on as-compacted samples with $w_{comp} \approx 3\%$ and $I_D \approx 0.69$, a failure criterion was derived that is strongly non-linear at confining pressures of 10 kPa to 100 kPa. In this stress range, the shear strength of the as-compacted samples is significantly higher than that of the saturated ones, which could be attributed to the increase in the dilatancy due to the suction-induced increase of the intra-aggregate stress. The influence of the suction-induced effective stress on the shear strength, on the other hand, was found to be negligible ($\Delta\sigma' \approx 1$ kPa). The results confirmed the findings from the uniaxial tests, although the variation in shear strength was less pronounced with varying initial microstructure, which may be related to the suppressing effect of increasing confining pressure.

Eventually, the findings from the experimental investigations were transferred to a procedure to calculate standard-compliant slope stability with conventional software based on LET. By determining the slope stability of an example embankment, the applicability of the procedure was demonstrated. The results reveal that the factor of safety can be significantly increased by accounting for the non-linearity of the shear strength of as-compacted granular soils with non-plastic fines.

10 Outlook

In order to improve the understanding of the underlying basic soil mechanics of as-compacted unsaturated granular soils with non-plastic fines, the following issues appeared to be of interest:

- Further experimental investigation on the effect of intra-aggregate stress on the soil behavior during loading may be revealing. In particular, investigations on the intra-aggregate stress variable $\chi_{aggregate}$ causing the suction-induced strength of the aggregates and therefore the dilatant behavior seem interesting. To assess this, the mechanical behavior of the aggregated fines may be experimentally examined in more detail, e.g. by separation from the granular particles.
- Based on the experimental results, numerical models may be useful for describing the mechanical behavior of the mixture of aggregated fines and coarse particles. In this context, with respect to constitutive modeling of such soils, it is evident to consider the (evolving) double porous microstructure, which seems to be more informative than density per se in describing shear behavior of such soils.

Regarding the proposed experimental procedure, the following issues are of particular interest:

- The experimental investigations in this study were carried out on a silty sand, which was considered representative for the average *in situ* conditions encountered during the exploratory drilling on an old traffic embankment. Therefore, the question may arise as to how granular soils with non-plastic fines behave at the limits of these *in situ* conditions and whether they can be subjected to the same experimental methods. Therefore, the experimental procedure to test the suction-induced effective stress and the shear strength developed in this work should be applied to a wider range of as-compacted granular soils with non-plastic fines in order to create a comprehensive database and simplify the transfer of these findings to practical issues.
- In this context, the interpretation of tensile tests is based on a series of assumptions that could be complied with, given the limits defined within the scope of the work. It is a valuable device to test shear behavior of unsaturated granular material at zero confining pressure. However, suction-controlled uniaxial tensile and compression tests would provide information on whether the proposed framework for the interpretation of tensile tests can be extended beyond the limits defined in this work.
- In this context, the test apparatus can be improved to also capture volumetric behavior.

With respect to the boundary value problem of verifying the stability of slopes of existing traffic embankments made of silty sands, the following questions remain unsolved:

- The influence of small changes in water content, which may occur in the embankment core, was investigated with CS tests at a constant confining pressure of 25 kPa. The results did not reveal a considerable effect of changing suction on the shear strength.

However, only a small range of suction changes was examined. It would be advisable to expand the test series to cover a wider range of both suctions and confining pressures.

- In this context, the issue of the hydraulic performance of the traffic embankments was just briefly examined in the literature review, although the results are expected to be representative for the examined embankment in this study. However, long-term measurements of water content and suction changes would be revealing. With simultaneous acquisition of the climate data and water balance, numerical simulations can be carried out to assess the hydraulic performance over the long-term.
- From the comparison of the results of the CS tests on samples compacted at w_{comp} = 6% and w_{comp} = 3% it was concluded that the influence of microstructure could be neglected in the tested stress range. For this reason, no CW tests were done on samples compacted at different levels of water content than w_{comp} = 3%. To gain better insight into the influence of the microstructure on the shear strength, this assumption should be checked through CW tests on samples compacted at higher or lower levels of water content.

References

Abbeche, K., Hammoud, F., and Ayadat, T. (2007) 'Influence of Relative Density and Clay Fraction on Soil Collapse'. in *Experimental Unsaturated Soil Mechanics*. ed. by Schanz, T. Springer-Verlag Berlin Heidelberg, 3–9

Aitchison, G.D. (1985) 'Relationship of Moisture Stress and Effective Stress Functions in Unsaturated Soils'. in *Golden Jubilee of the International Society for Soil Mechanics and Foundation Engineering: Commemorative Volume*. held 1985 at Barton, Australia. 20–25

Aitchison, G.D. and Donald, I.B. (1956) 'Effective Stresses in Unsaturated Soils'. in *Proceedings of the 2nd Australia-New Zealand Conference on Soil Mechanics and Foundation Engineering*. held 1956 at Christchurch, New Zealand. 192–199

Alonso, E.E., Gens, A., and Josa, A. (1990) 'A Constitutive Model for Partially Saturated Soils'. *Géotechnique* 40 (3), 405–430

Alonso, E.E., Pereira, J.-M., Vaunat, J., and Olivella, S. (2010) 'A Microstructurally Based Effective Stress for Unsaturated Soils'. *Géotechnique* 60 (12), 913–925

Alonso, E.E., Pinyol, N.M., and Gens, A. (2013) 'Compacted Soil Behaviour: Initial State, Structure and Constitutive Modelling'. *Géotechnique* 63 (6), 463–478

Ampadu, S.K. and Tatsuoka, F. (1993) 'Effect of Setting Method on the Behaviour of Clays in Triaxial Compression from Saturation to Undrained Shear'. *Soils and Foundations* 33 (2), 14–34

Angerer, L. (2016) 'Zugfestigkeit von Schluffigen Sanden Im Ungesättigten Zustand'. in *Proceedings of the Baugrundtagung, German Society for Geotechnical Engineering (DGGT)*. held 2016 at Bielefeld, Germany

Angerer, L. and Birle, E. (2016) 'Experimental Determination of the Hysteretic Behaviour of Soil-Water Retention Curve of Silty Sands'. in Delage, P., Cui, Y.-J., Ghabezloo, S., Pereira, J.-M., and Tang, A.-M. (eds.) *Proceedings of the 3rd European Conference on Unsaturated Soils (E-UNSAT 2016)*. held 2016 at Paris, France

Angerer, L., Birle, E., and Cudmani, R. (2016) 'Schlussbericht Zur Untersuchungsphase 2 Ermittlung Der Standsicherheit von Bestehenden Eisenbahndämmen (Unpublished Report)'. *Technical University of Munich*

Angerer, L., Birle, E., and Vogt, N. (2013) 'Bericht Zur Vorstudie: Ermittlung Der Standsicherheit von Bestehenden Eisenbahndämmen (Unpublished Report)'. *Technical University of Munich*

Baker, R. and Frydman, S. (2009) 'Unsaturated Soil Mechanics. Critical Review of Physical Foundations'. *Engineering Geology* 106, 26–39

Bao, C., Gong, B., and Zhan, L. (1998) 'Properties of Unsaturated Soils and Slope Stability of Expansive Soils'. in *Proceedings of the 2nd International Conference on Unsaturated Soils (UNSAT 98)*. held 1998 at Bejing, China. 71–98

Bauer, E. (1995) 'Constitutive Modelling of Critical States in Hypoplasticity'. *Proceedings of the 5th International Symposium on Numerical Models in Geomechanics* 15–20

Becker, A. (2017) 'Untersuchungen Zum Einfluss Der Herstellungsmethode Auf Das Scherverhalten von Schluffigen Sanden Bei Triaxialer Kompression'. *Master Thesis, Technical University of Munich*

Been, K., Jefferies, M.G., and Hachey, J. (1991) 'The Critical State of Sand'. *Géotechnique* 41 (3), 365–381

Bergholz, K. and Herle, I. (2016) 'Experimentelle Bestimmung Der Nichtlinearität von Spannungsgrenzbedingungen Im Bereich Geringer Spannungen'. *Geotechnik* 1–13

Bhandari, A.R. and Powrie, W. (2013) 'Strength and Deformation Characteristics of a Locked Sand at Low Effective Stresses'. *Granular Matter* 15 (5), 543–556

Bilz, P. and Vieweg, J. (1993) 'Zur Größe Der Kapillarkohäsion von Sanden'. *Geotechnik* 16, 65–71

Birle, E. (2011) 'Geohydraulische Eigenschaften Verdichteter Tone Unter Besonderer Berücksichtigung Des Ungesättigten Zustandes'. *PhD Thesis, Technical University Munich*

Blatz, J.A., Cui, Y.-J., and Oldecop, L. (2009) 'Vapour Equilibrium and Osmotic Technique for Suction Control'. in *Laboratory and Field Testing of Unsaturated Soils*. ed. by Tarantino, A., Romero, E., and Cui, Y.-J. Springer Science+Business Media,B.V., 49–61

Bolton, M.D. (1986) 'The Strength and Dilatancy of Sands'. *Géotechnique* 36 (1), 65–78

Burger, C.A. and Shackelford, C.D. (2001) 'Soil-Water Characteristic Curves and Dual Porosity of Sand–Diatomaceous Earth Mixtures'. *Journal of Geotechnical and Geoenvironmental Engineering* 127 (9), 790–800

Burland, J.B. and Jennings, J.E.B. (1962) 'Limitations to the Use of Effective Stresses in Partly Saturated Soils'. *Géotechnique* 12 (2), 125–144

Casini, F., Minder, P., and Springman, S.M. (2010) 'Shear Strength of an Unsaturated Silty Sand'. in Alonso, E.E. and Gens, A. (eds.) *Unsaturated Soils - Proceedings of the 5th International Conference on Unsaturated Soil*. held 2010 at Barcelona, Spain. 211–216

Castro, G., Poulos, S.J., France, J.W., and Enos, J.L. (1982) 'Liquefaction Induced by Cyclic Loading'. in *Report to National Science Foundation*.

Chakraborty, T. and Salgado, R. (2010) 'Dilatancy and Shear Strength of Sand at Low Confining Pressures'. *Journal of Geotechnical and Geoenvironmental Engineering* 136 (3), 527–532

Chan, C.K. (1985) *Instruction Manual, CKC E/P Cyclic Loading Triaxial System User's Manual, Soil Engineering Equipment Company, San Francisco*.

Che, R.J., Cai, G.., and Zhao, C.G. (2015) 'Experimental Analysis on Tensile Strength of Unsaturaetd Sandy Clay under Different Initial Densities and Water Contents'. in *Proceedings of the 6th Asia Pacific Conference on Unsaturated Soils*. held 2015 at Guilin, China. 267–274

Ciervo, F., Papa, M.N., Casini, F., and Rigon, R. (2015) 'Bimodal Behavior of a Silty Sand and Its Effects on Slope Stability'. in *Proceedings of the 8th International Conference on Environmental and Geological Science and Engineering*. held 2015 at Salerno, Italy. 320–325

Colmenares, J.E. and Ridley, A.M. (2002) 'Stress-Strain and Strength Relationships for a Reconstituted Clayey Silt'. in *Proceedings of the 3rd International Conference on Unsaturated Soils Unsat 2002*. held 2002. 481–484

Cudmani, R. (2001) 'Statische, Alternierende Und Dynamische Penetration in Nichtbindigen Böden'. *PhD Thesis, University Fridericiana of Karlsruhe*

Cui, Y.-J. and Delage, P. (2009) 'Water Balance and Evapotranspiration Monitoring in Geotechnical and Geoenvironmental Engineering'. in *Laboratory and Field Testing of Unsaturated Soils*. ed. by Tarantino, A., Romero, E., and Cui, Y.-J. Springer Science+Business Media,B.V., 171–186

Cui, Y.-J. and Delage, P. (1996) 'Yielding and Plastic Behaviour of an Unsaturated Compacted Silt'. *Géotechnique,* 46 (2), 291–311

Cunningham, M.R., Ridley, A.M., Dineen, K., and Burland, J.B. (2003) 'The Mechanical Behaviour of a Reconstituted Unsaturated Silty Clay'. *Géotechnique* 53 (2), 183–194

Decagon Device, I. (2017) *WP4C Dew Point PotentiaMeter, Operator's Manual*.

Delage, P. (2007) 'Microstructural Features in the Behaviour of Engineered Barriers for Nuclear Waste Disposal'. in *Experimental Unsaturated Soil Mechanics*. ed. by Schanz, T. Springer-Verlag Berlin Heidelberg, 11–32

Delage, P. (2002) 'Experimental Unsaturated Soil Mechanics'. in Jucá, J.F.., de Campos, T.M.., and Marinho, F.A.. (eds.) *Unsaturated Soils - Proceedings of the 3rd International Conference on Unsaturated Soils, UNSAT 2002*. held 2002 at Recife, Brazil. 973–996

Delage, P., Audiguier, M., Cui, Y.-J., and Howat, M.D. (1996) 'Microstructure of a Compacted Silt'. *Canadian Geotechnical Journal* 33 (1), 150–158

Delage, P., Romero, E., and Tarantino, A. (2008) 'Recent Developments in the Techniques of Controlling and Measuring Suction in Unsaturated Soils'. in Toll, D.G., Augarde, C.E., Gallipoli, D., and Wheeler, S.J. (eds.) *Unsaturated Soils. Advances in Geo-Engineering (E-Unsat 2008)*. held 2008 at Durham, United Kingdom. 33–52

Desrues, J., Chambon, R., Mokni, M., and Mazerolle, F. (1996) 'Void Ratio Evolution inside Shear Bands in Triaxial Sand Specimens Studied by Computed Tomography'. *Géotechnique* 46 (3), 529–546

Desrues, J., Mevoli, F., Andò, E., Bésuelle, P., Viggiani, C., Debove, L., Charrier, P., and Toni, J.B. (2018) 'Localisation Precursors in Geomaterials?' in *Springer Series in Geomechanics and Geoengineering*.

Donald, I.B. (1956) 'Shear Strength Measurements in Unsaturated Non-Cohesive Soils with Negative Pore Pressures'. in *Proceedings of the 2nd Australia-New Zealand Conference on Soil Mechanics and Foundation Engineering*. held 1956 at Christchurch, New Zealand. 200–205

Durner, W. (1994) 'Hydraulic Conductivity Estimation for Soils with Heterogeneus Pore Structure.' *Water Resources Research* 30 (2), 211–223

Fern, E.J., Robert, D.J., and Soga, K. (2016) 'Modeling the Stress-Dilatancy Relationship of Unsaturated Silica Sand in Triaxial Compression Tests'. *Journal of Geotechnical and Geoenvironmental Engineering* 142 (11)

Fern, J., Soga, K., Robert, D., and Sakanoue, T. (2014) 'Shear Strength and Dilatancy of Unsaturated Silica Sand in Triaxial Compression Tests'. *Computer Methods and Recent Advances in Geomechanics* (July), 535–540

Fredlund, D.G. and Morgenstern, N.R. (1977) 'Stress State Variables for Saturated and Unsaturated Soils'. in *Journal of Geotechnical Division*. vol. 103 (GT5). 447–466

Fredlund, D.G., Rahardjo, H., and Fredlund, M.D. (2012) *Unsaturated Soil Mechanics in Engineering Practice*. John Wiley & Sons

Fredlund, D.G. and Vanapalli, S.K. (2002) 'Shear Strength of Unsaturated Soils'. in *Agronomy Soil Testing Manual*. 329–361

Fredlund, D.G. and Xing, A. (1994) 'Equations for the Soil-Water Characteristic Curve'. *Canadian Geotechnical Journal* 31 (6), 1026–1026

Fukushima, S. and Tatsuoka, F. (1984) 'Strength and Deformation Characteristics of Saturated Sand at Extremely Low Pressures'. *Soils and Foundations* 24 (4), 30–48

Gabrieli, F., Artoni, R., Santomaso, A., and Cola, S. (2013) 'Discrete Particle Simulations and Experiments on the Collapse of Wet Granular Columns'. *Physics of Fluids* 25 (10)

Gallipoli, D. (2012) 'A Hysteretic Soil-Water Retention Model Accounting for Cyclic Variations of Suction and Void Ratio'. *Géotechnique* 62 (7), 605–616

Gallipoli, D., Wheeler, S.J., and Karstunen, M. (2003) 'Modelling the Variation of Degree of Saturation in a Deformable Unsaturated Soil'. *Géotechnique* 53 (1), 105–112

Gens, A. (2014) ‘The Development of Unsaturated Soil Mechanics’. *Commemorative*

van Genuchten, M.T. (1980) ‘A Closed-Form Equation for Predicting the Hydraulic Conductivity of Unsaturated Soils1’. *Soil Science Society of America Journal* 44 (5), 892–898

Goulding, R.B. (2006) ‘Tensile Strength, Shear Strength, and Effective Stress for Unsaturated Sand’. *PhD Thesis, University of Missouri - Columbia*

Hall, S.A., Desrues, J., Viggiani, G., Bésuelle, P., and Andò, E. (2012) ‘Experimental Characterisation of (Localised) Deformation Phenomena in Granular Geomaterials from Sample down to Inter-and Intra-Grain Scales’. *Procedia IUTAM* 4, 54–65

Hartge, K.H. and Horn, R. (1991) *Einführung in Die Bodenphysik*. Stuttgart: Ferdinand Enke Verlag

Heibrock, G., Zeh, R.M., and Witt, K.J. (2005) ‘Tensile Strength of Compacted Clays’. in *Unsaturated Soils: Experimental Studies*. ed. by Schanz, T. Weimar: Springer Berlin Heidelberg, 395–412

Heitor, A., Indraratna, B., Rujikiatkamjorn, C., and Mcintosh, G.W. (2017) ‘Influence of Compaction History on the Shear Strength Behaviour of Compacted Soil’. in Lee, W., Lee, J.-S., Kim, H.-K., and Kim, D.-S. (eds.) *Proceedings of the 19th International Conference on Soil Mechanics and Geotechnical Engineering*. held 2017 at Seoul, South Korea. 1361–1364

Heitor, A., Rujikiatkamjorn, C., and Indraratna, B. (2013) ‘Behaviour of a Compacted Silty Sand under Constant Water Content Shearing’. in Delage, P. and Desrues, J.J.M. (eds.) *Proceedings of the 18th International Conference on Soil Mechanics and Geotechnical Engineering*. held 2013 at Paris, France. 1007–1011

Higo, Y., Oka, F., Sato, T., Matsushima, Y., and Kimoto, S. (2013) ‘Investigation of Localized Deformation in Partially Saturated Sand under Triaxial Compression Using Microfocus X-Ray CT with Digital Image Correlation’. *Soils and Foundations* 53 (2), 181–198

Ho, D.Y.F. and Fredlund, D.G. (1982) ‘Strain Rates for Unsaturated Soil Shear Strength Testing’. in McFeat-Smith, I. and Lumb, P. (eds.) *Proceedings of the 7th Southeast Asian Geotechnical Conference*. held 1982 at Hong Kong. 787–803

Hoeg, K., Dyvik, R., and Sandbaekken, G. (2000) ‘Strength of Undisturbed versus Reconstituted Silt and Silty Sand Specimens’. *Journal of Geotechnical and Geoenvironmental Engineering* 126 (7), 606–617

Houston, S.L., Perez-Garcia, N., and Houston, W.N. (2008) ‘Shear Strength and Shear-Induced Volume Change Behavior of Unsaturated Soils from a Triaxial Test Program’. *Journal of Geotechnical and Geoenvironmental Engineering* 134, 1619–1632

Hoyos, L.R., Laloui, L., and Vassallo, R. (2009) ‘Mechanical Testing in Unsaturaetd Soils’. in *Laboratory and Field Testing of Unsaturated Soils*. ed. by Tarantino, A., Romero, E., and Cui, Y.-J. Springer Science+Business Media,B.V., 63–77

Jiang, Y., Einav, I., and Liu, M. (2017) ‘A Thermodynamic Treatment of Partially Saturated Soils Revealing the Structure of Effective Stress’. *Journal of the Mechanics and Physics of Solids* 100, 131–146

Jommi, C. (2000) ‘Remarks on the Constitutive Modelling of Unsaturated Soils’. *… Approaches in Unsaturated Soils* (1968), 139–153

Juang, C.-H. (1981) *Pore Size Distribution of Sandy Soils and the Prediction of Permeability*.

Junge, T., Gräsle, W., Bensel, G., and Horn, R. (2000) ‘Einfluss Des Porenwasserdruckes Auf Die Zugfestigkeit von Bodenproben’. *Journal of Plant Nutrition and Soil Science* 163, 21–26

Khaddour, G. (2015) ‘Multi-Scale Characterisation of the Hydro-Mechanical Behaviour of

Unsaturated Sand : Water Retention and Triaxial Response'. *PhD Thesis, Université*

Khalili, N., Geiser, F., and Blight, G. (2004) 'Effective Stress in Unsaturated Soils: Review with New Evidence'. *International Journal of Geomechanics* 4 (2), 115–126

Khalili, N. and Khabbaz, H. (1999) 'Application of Effective Stress Concept to Unsaturated Soils'. in Vitharana, N.D. and Colman, R. (eds.) *Proceedings of the 8th Australia New Zealand Conference on Geomechanics*. held 1999. 849–854

Khalili, N. and Khabbaz, H. (1998) 'A Unique Relationship of Chi for the Determination of the Shear Strength of Unsaturated Soils'. *Géotechnique* 52 (5), 76–77

Khalili, N. and Khabbaz, M. (1996) *The Effective Stress Concept in Unsaturated Soils*.

Khalili, N., Witt, R., Laloui, L., Vulliet, L., and Koliji, A. (2005) 'Effective Stress in Double Porous Media with Two Immiscible Fluids'. *Geophysical Research Letters* 32 (15), 2–6

Kim, T.-H. and Sture, S. (2008) 'Capillary-Induced Tensile Strength in Unsaturated Sands'. *Canadian Geotechnical Journal* 45 (5), 726–737

Klotz, E.U. and Coop, M.R. (2002) 'On the Identification of Critical State Lines for Sands'. *Geotechnical Testing Journal* 25 (3), 289–302

Konrad, J.-M. and Lebeau, M. (2015) 'A Capillary-Based Effective Stress Formulation for Predicting the Shear Strength of Unsaturated Soils'. *Canadian Geotechnical Journal* 52, 2026–2076

Kuerbis, R. and Vaid, Y.P. (1988) 'Sand Sample Preparation - The Slurry Deposition Method'. *Soils and Foundations* 28 (4), 107–118

Kuerbis, R.H., Negussey, D., and Vaid, Y.P. (1988) 'Effect of Gradation and Fines Content on the Undrained Response of Sand'. in *Geotechnical Special Publication*. 330–345

Ladd, R.S. (1978) 'Preparing Test Specimens Using under Compaction'. *Geotechnical Testing Journal* 1 (1), 16–23

Lade, P. V., Liggio, C.D., and Yamamuro, J.A. (1998) 'Effects of Non-Plastic Fines on Minimum and Maximum Void Ratios of Sand'. *Geotechnical Testing Journal* 21 (4), 336–347

Lade, P.V. (2016) *Triaxial Testing of Soils*. John Wiley & Sons, Ltd.

Lambe, T.W. and Whitman, R.V. (1969) *Soil Mechanics*. John Wiley & Sons

Lancelot, L., Shahrour, I., and Al Mahmoud, M. (2006) 'Failure and Dilatancy Properties of Sand at Relatively Low Stresses'. *Journal of Engineering Mechanics* 132 (12), 1396–1399

Lauer, C. and Engel, J. (2005) 'Investigation on the Unsaturated Stress-Strain Behaviour and on the SWCC of Hostun Sand in a Double-Walled Triaxial Cell'. in *Advanced Experimental Unsaturated Soil Mechanics*. ed. by Tarantino, A., Romero, E., and Cui, Y.-J. London: Taylor & Francis Group, 185–191

Lawton, C.E., Fragaszy, J.R., and Hardcastle, H.J. (1989) 'Collapse of Compacted Clayey Sand'. *Journal of Geotechnical Engineering* 115 (9), 281–289

Lee, J., Salgado, R., and Carraro, J.A.H. (2004) 'Stiffness Degradation and Shear Strength of Silty Sands'. *Canadian Geotechnical Journal* 41 (5), 831–843

Leong, E.C., Agus, S.S., and Rahardjo, H. (2004) 'Volume Change Measurement of Soil Specimen in Triaxial Test'. *Geotechnical Testing Journal* 27 (1), 47–56

Li, X. and Zhang, L. (2007) 'Prediction of SWCC for Coarse Soils Considering Pore Size Changes'. in *Experimental Unsaturated Soil Mechanics*. ed. by Schanz, T. Springer, Berlin, Heidelberg, 401–412

Li, Y. (2017) *Shear Behavior of Composite Soils*. CRC Press/Balkema

Lian, G., Thornton, C., and Adams, M.J. (1993) 'A Theoretical Study of the Liquid Bridge Forces between Two Rigid Spherical Bodies'. *Journal of Colloid and Interface Science* 161 (1), 138–147

Likos, W.J., Wayllace, A., Godt, J., and Lu, N. (2010) 'Modified Direct Shear Apparatus for Unsaturated Sands at Low Suction and Stress'. *Geotechnical Testing Journal* 33 (4)

Limit State Ltd (2016) *LimitState:GEO Manual, Version 3.4.A*.

Lu, N., Godt, J.W., and Wu, D.T. (2010) 'A Closed-Form Equation for Effective Stress in Unsaturated Soil'. *Water Resources Research* 46 (5), 1–14

Lu, N., Kim, T.-H., Sture, S., and Likos, W.J. (2009) 'Tensile Strength of Unsaturated Sand'. *Journal of Engineering Mechanics* 135 (12), 1410–1419

Lu, N. and Likos, W.J. (2006) 'Suction Stress Characteristic Curve for Unsaturated Soil'. *Journal of Geotechnical and Geoenvironmental Engineering* 132 (2), 131–142

Lu, N. and Likos, W.J. (2004) *Unsaturated Soil Mechanics*. John Wiley & Sons

Lu, N., Wu, B., and Tan, C.P. (2005) 'A Tensile Strength Apparatus for Cohesionless Soils'. in *Advanced Experimental Unsaturated Soil Mechanics*. ed. by Tarantino, Romero, E., and Cui. London: Taylor & Francis Group, 105–110

Maleki, M. and Bayat, M. (2012) 'Experimental Evaluation of Mechanical Behavior of Unsaturated Silty Sand under Constant Water Content Condition'. *Engineering Geology* 141–142, 45–56

Marinho, F.A.M., Take, W.A., and Tarantino, A. (2009) 'Measurement of Matric Suction Using Tensiometric and Axis Translation Techniques'. in *Laboratory and Field Testing of Unsaturated Soils*. ed. by Tarantino, A., Romero, E., and Cui, Y.-J. Springer Science+Business Media,B.V., 3–19

Mikulitsch, W.A. and Gudehus, G. (1995) 'Uniaxial Tension, Biaxial Loading and Wetting Tests on Loess'. in Alonso, E.E. and Delage, P. (eds.) *Proceedings of the 1st International Conference on Unsaturated Soils, UNSAT'95*. held 1995 at Paris, France. 145–150

Milatz, M. (2016) 'Untersuchungen Zum Einfluss Der Kapillarität Auf Das Hydraulisch-Mechanische Verhalten von Granularen Tragschichten Für Verkehrswege'. *PhD Thesis, Hamburg University of Technology*

Mooney, M.A., Finno, R.J., and Viggiani, M.G. (1998) 'A Unique Critical State for Sand?' *Journal of Geotechnical and Geoenvironmental Engineering* 124 (11), 1100–1108

Munkholm, L.J. and Kay, B.D. (2002) 'Effect of Water Regime on Aggregate-Tensile Strength, Rupture Energy, and Friability'. *Soil Science Society of America Journal* 66 (3), 702

Murray, E.J. and Sivakumar, V. (2010) *Unsaturated Soils*. John Wiley & Sons, Ltd

Nahlawi, H., Chakrabarti, S., and Kodikara, J. (2004) 'A Direct Tensile Strength Testing Method for Unsaturated Geomaterials'. *Geotechnical Testing Journal* 27 (4), 356–361

Nishimura, T., Toyota, H., Vanapalli, S.K., and Oh, W.T. (2008) 'The Shear Strength Behavior of a Silty Soil in the Residual Zone of Unsaturation'. in Jadhav, M.N. (ed.) *Proceedings of the 12th International Conference of International Association for Computer Methods and Advances in Geomechanics*. held 2008 at Goa, India. 2213–2221

Nitao, J.J. and Bear, J. (1996) 'Potentials and Their Role in Transport in Porous Media'. *Water Resources Research* 32 (2), 225–250

Nuth, M. and Laloui, L. (2008) 'Effective Stress Concept in Unsaturated Soils: Clarification

and Validation of a Unified Framework'. *International Journal for Numerical and Analytical Methods in Geomechanics* 32, 771–801

Nuth, M. and Laloui, L. (2007) 'Implications of a Generalized Effective Stress on the Constitutive Modelling of Unsaturated Soils'. *Theoretical and Numerical Unsaturated Soil Mechanics*

Öberg, A.-L. and Sällfors, G. (1997) 'Determination of Shear Strength Parameters of Unsaturated Silts and Sands Based on the Water Retention Curve'. *Geotechnical Testing Journal* 20 (1), 40–48

Oda, M. (1972) 'Deformation Mechanism of Sand in Triaxial Compression Tests'. *Soils and Foundation* 12 (4), 45–63

Oda, M. and Kazama, H. (1998) 'Microstructure of Shear Bands and Its Relation to the Mechanisms of Dilatancy and Failure of Dense Granular Soils'. *Géotechnique* 48 (4), 465–481

Oh, S., Lu, N., Kim, T., and Lee, Y.H. (2013) 'Experimental Validation of Suction Stress Characteristic Curve from Nonfailure Triaxial K0 Consolidation Tests'. *Journal of Geotechnical and Geoenvironmental Engineering* 139 (9), 1490–1503

Oloo, S.Y. and Fredlund, D.G. (1996) 'A Method for the Determination of Spatial Jb for Statically Compacted Soils'. *Canadian Geotechnical Journal* 33, 272–280

Pagano, A., Tarantino, A., Bagheri, M., Rezania, M., and Sentenac, P. (2016) 'An Experimental Investigation of the Independent Effect of Suction and Degree of Saturation on Very Small-Strain Stiffness of Unsaturated Sand'. in Delage, P., Cui, Y.-J., Ghabezloo, S., Pereira, J.-M., and Tang, A.-M. (eds.) *Proceedings of the 3rd European Conference on Unsaturated Soils (E-UNSAT 2016)*. held 2016 at Paris, France

Patil, U.D. (2014) 'Response of Unsaturated Silty Sand Over A Wider Range of Suction States Using A Novel Double-Walled Triaxial Testing System'. *PhD Thesis, University of Texas at Arlington* (August)

Patil, U.D., Puppala, A.J., and Hoyos, L.R. (2014) 'Assessment of Suitable Loading Rate for Suction-Controlled Triaxial Testing on Compacted Silty Sand via Axis-Translation Technique'. in Abu-Farsakh, M., Yu, X., and Hoyos, L.R. (eds.) *Geo-Congress 2014 Technical Papers: Geo-Characterization and Modeling for Sustainability*. held 2014 at Atlanta, Georgia, USA. 1307–1316

Peters, A. and Durner, W. (2008) 'Simplified Evaporation Method for Determining Soil Hydraulic Properties'. *Journal of Hydrology* 356, 147–162

Pham, H.Q., Fredlund, D.G., and Barbour, S.L. (2005) 'A Study of Hysteresis Models for Soil-Water Characteristic Curves'. *Canadian Geotechnical Journal* 42 (6), 1548–1568

Polito, C.P. and Martin, J.R. (2003) 'A Reconciliation of the Effects of Non-Plastic Fines on the Liquefaction Resistance of Sands Reported in the Literature'. *Earthquake Spectra* 19 (3), 635–651

Ponce, V.M. and Bell, J.M. (1971) 'Shear Strength of Sand at Extremely Low Pressures'. *Journal of the Soil Mechanics and Foundations Division* 97 (4), 625–638

Rabbi, A.T.M.Z., Cameron, D.A., and Rahman, M.M. (2014) 'Role of Matric Suction on Wetting-Induced Collapse Settlement of Silty Sand'. in *Unsaturated Soils: Research & Applications*. ed. by Khalili, N., Russell, A., and Khoshghalb. 129–135

Rampino, C., Mancuso, C., and Vinale, F. (1999) 'Mechanical Behaviour of an Unsaturated Dynamically Compacted Silty Sand'. *Rivista Italiana Di Geotecnica* 2, 26–39

Ridley, A.M. and Burland, J.B. (1993) 'A New Instrument for the Measurement of Soil Moisture Suction'. *Geotechnique* 43 (2), 321–324

Romero, E. (2015) ‘Exploring Microstructural Issues on Compacted Soils along HW Paths.Pdf’. *7th ALERT OZ Summerschool, UPS*

Romero, E., Musso, G., and Jommi, C. (2012) ‘Experimental Techniques for Multi-Scale Description of Soil Fabric and Its Dual Pore Network’. in *Advanced Experimental Techniques in Geomechanics*. 125–156

Romero, E. and Simms, P.H. (2009) ‘Microstructure Investigation in Unsaturated Soils: A Review with Special Attention to Contribution of Mercury Intrusion Porosimetry and Environmental Scanning Electron Microscopy’. in *Laboratory and Field Testing of Unsaturated Soils*. ed. by Tarantino, A., Romero, E., and Cui, Y.-J. Springer Science+Business Media,B.V., 93–115

Russell, A.R. (2004) ‘Cavity Expansion in Unsaturated Soils’. *PhD Thesis, University of New South Wales, Sydney, Australia*

Sadrekarimi, A. and Olson, S.M. (2012) ‘Effect of Sample-Preparation Method on Critical-State Behavior of Sands’. *Geotechnical Testing Journal* 35 (4), 1–15

Salager, S., El Youssoufi, M.S., and Saix, C. (2010) ‘Definition and Experimental Determination of a Soil-Water Retention Surface’. *Canadian Geotechnical Journal* 47 (6), 609–622

Salager, S., El Youssoufi, M.S., and Saix, C. (2007) ‘Influence of Temperature on the Water Retention Curve of Soils. Modelling and Experiments’. in *Experimental Unsaturated Soil Mechanics* [online] ed. by Schanz, T. Springer, Berlin, Heidelberg, 251–258. available from <http://dx.doi.org/10.1007/3-540-69873-6_24>

Salgado, R., Bandini, P., and Karim, A. (2000) ‘Shear Strength and Stiffness of Silty Sand’. *Journal of Geotechnical and Geoenvironmental Engineering* 126 (5), 451–462

Santamarina, J.C. and Cho, G.C. (2004) ‘Soil Behaviour: The Role of Particle Shape’. *Advances in Geotechnical Engineering. Proceedings of the Skempton Conference* (September), 1–14

Santamarina, J.C. and Cho, G.C. (2001) ‘Determination of Critical State Parameters in Sandy Soils—Simple Procedure’. *Geotechnical Testing Journal* 24 (2), 185–192

Santucci de Magistris, F. and Tatsuoka, F. (2004) ‘Effects of Moulding Water Content on the Stress-Strain Behaviour of a Compacted Silty Sand’. *Soils and Foundation* 44 (2), 85–101

Scanlon, B.R., Andraski, B.J., and Bilskie, J. (2002) ‘Miscellaneous Methods for Measuring Matric or Water Potential’. in *Methods of Soil Analysis*. 643–670

Scheuermann, A. (2005) ‘Instationäre Durchfeuchtung Quasi-Homogener Erddeiche’. *PhD Thesis, University Fredericiana of Karlsruhe*

Schnellmann, R., Rahardjo, H., and Schneider, H.R. (2013) ‘Unsaturated Shear Strength of a Silty Sand’. *Engineering Geology* 162, 88–96

Schofield, A. and Wroth, P. (1968) *Critical State Soil Mechanics*. McGraw-Hill

Schubert, H. (1982) *Kapillarität in Porösen Feststoffsystemen*. Springer-Verlag Berlin Heidelberg New York

Sheng, D., Zhou, A., and Fredlund, D.G. (2011) ‘Shear Strength Criteria for Unsaturated Soils’. *Geotechnical and Geological Engineering* 29 (2), 145–159

Simms, P.H. and Yanful, E.K. (2002) ‘Predicting Soil—water Characteristic Curves of Compacted Plastic Soils from Measured Pore-Size Distributions’. *Géotechnique* 52 (4), 269–278

Sivathayalan, S. (2000) ‘Fabric, Initial State and Stress Path Effects in Liquefaction Susceptibility of Sands’. *PhD Thesis, University of British Columbia*

Sture, S., Costes, N., Batiste, S., Lankton, M., AlShibli, K., Jeremic, B., Swanson, R., and Frank, M. (1998) 'Mechanics of Granular Materials at Low Effective Stresses'. *Journal of Aerospace Engineering* 11 (3), 67–72

Tamrakar, S.B., Mitachi, T., and Toyosawa, Y. (2007) 'Factors Affecting Tensile Strength Measurement and Modified Tensile Strength Measuring Apparatus for Soil'. in *Experimental Unsaturated Soil Mechanics*. ed. by Schanz, T. Springer Berlin Heidelberg, 207–218

Tarantino, A. and El Mountassir, G. (2013) 'Making Unsaturated Soil Mechanics Accessible for Engineers: Preliminary Hydraulic-Mechanical Characterisation & Stability Assessment'. *Engineering Geology* 165, 89–104

Tarantino, A., Romero, E., and Cui, Y.-J. (2009) *Laboratory and Field Testing of Unsaturated Soils*. ed. by Tarantino, A., Romero, E., and Cui, Y.-J.

Tarantino, A. and Tombolato, S. (2005) 'Coupling of Hydraulic and Mechanical Behaviour in Unsaturated Compacted Clay'. *Géotechnique* 55 (4), 307–317

Taylor, D.W. (1948) *Fundamentals of Soil Mechanics*. New York: John Wiley and Sons

Taylor, O.S., Winters, K.E., Berry, W.W., Walshire, L.A., and Kinnebrew, P.G. (2018) 'Near-Surface Soils : Self-Supported Unconfined Drained Sand Specimens'. *Canadian Geotechnical Journal* 13 (In Press), 1–13

Thevanayagam, S., Shenthan, T., Mohan, S., and Liang, J. (2002) 'Undrained Fragility of Clean Sands, Silty Sands, and Sandy Silts'. *Journal of Geotechnical and Geoenvironmental Engineering* 128 (10), 849–859

Thu, T.M., Rahardjo, H., and Leong, E.-C. (2006) 'Effects of Hysteresis on Shear Strength Envelopes from Constant Water Content and Consolidated Drained Triaxial Tests'. in Miller, G.A., Zapata, C.E., Houston, S.L., and Fredlund, D.G. (eds.) *Unsaturated Soils 2006 - Proceedings of the 4th International Conference on Unsaturated Soils*. held 2006 at Carefree, Arizona, USA. 1212–1222

Toker, N.K. (2007) 'Modeling the Relation between Suction, Effective Stress and Shear Strength in Partially Saturated Granular Media'. *PhD Thesis, Massachusetts Institute of Technology*

Toll, D.G. (2000) 'The Influence of Fabric on the Shear Behaviour of Unsaturated Compacted Soils'. in Shackelford, C.D., Houston, S.L., and Chang, N.-Y. (eds.) *Advances in Unsaturated Geotechnics, GEODenver 2000*. held 2000 at Denver, Colorado, USA. 222–234

Toll, D.G. (1988) 'The Behaviour of Unsaturated Compacted Naturally Occuring Gravel'. *PhD Thesis, Imperial College of Science and Technology*

Toll, D.G. and Ong, B.H. (2003) 'Critical-State Parameters for an Unsaturated Residual Sandy Clay'. *Geotechnique* 53 (1), 93–103

UMS GmbH, M. (2017) *Operation Manual - HYPROP*.

Vaid, Y.P. and Thomas, J. (1995) 'Liquefaction and Postliquefaction Behavior of Sand'. *Journal of Geotechnical Engineering* 121 (2), 163–173

Vanapalli, S.K., Fredlund, D.G., Pufahl, D.E., and Clifton, A.W. (1996) 'Model for the Prediction of Shear Strength with Respect to Soil Suction'. *Canadian Geotechnical Journal* 33 (3), 2

Vanapalli, S.K., Nicotera, M. V, and Sharma, R.S. (2009) 'Axis Translation and Negative Water Column Techniques for Suction Control'. in *Laboratory and Field Testing of Unsaturated Soils*. ed. by Tarantino, A., Romero, E., and Cui, Y.-J. Springer Science+Business Media,B.V., 33–48

Vanapalli, S.K., Sillers, W.S., and Fredlund, M.D. (1998) 'The Meaning and Relevance of Residual State to Unsaturated Soils'. in *51st Canadian Geotechnical Conference*. held 1998 at Edmonton, Alberta, USA

Verdugo, R.L. (1992) 'Characterization of Sandy Soil Behaviour under Large Deformation'. in *PhD Thesis, University of Tokyo*.

Watabe, Y., Leroueil, S., and Le Bihan, J.-P. (2000) 'Influence of Compaction Conditions on Pore-Size Distribution and Saturated Hydraulic Conductivity of a Glacial Till'. *Canadian Geotechnical Journal* 37 (6), 1184–1194

Watanabe, Y., Lenoir, N., Otani, J., and Nakai, T. (2012) 'Displacement in Sand under Triaxial Compression by Tracking Soil Particles on X-Ray CT Data'. *Soils and Foundations* 52 (2), 312–320

Willson, C.S., Lu, N., and Likos, W.J. (2012) 'Quantification of Grain, Pore, and Fluid Microstructure of Unsaturated Sand from X-Ray Computed Tomography Images'. *Geotechnical Testing Journal* 35 (6)

Wulfsohn, D., Adams, B. a, and Fredlund, D.G. (1998) 'Triaxial Testing of Unsaturated Agricultural Soils'. *Journal of Agricultural Engineering Research* 69 (4), 317–330

Xiao, Y., Liu, H., Chen, Y., and Chu, J. (2014) 'Strength and Dilatancy of Silty Sand'. *Journal of Geotechnical and Geoenvironmental Engineering* 140 (7), 06014007

Yamamuro, J.A. and Wood, F.M. (2004) 'Effect of Depositional Method on the Undrained Behavior and Microstructure of Sand with Silt'. *Soil Dynamics and Earthquake Engineering* 24, 751–760

Yamamuro, J.A., Wood, F.M., and Lade, P. V. (2008) 'Effect of Depositional Method on the Microstructure of Silty Sand'. *Canadian Geotechnical Journal* 45, 1538–1555

Yao, Y.-S., Zheng, J.-L., Chen, Z.-S., Zhang, J.-H., and Li, Y. (2016) 'Field Measurements and Numerical Simulations of Temperature and Moisture in Highway Engineering Using a Frequency Domain Reflectometry Sensor'. *Sensors* 16 (6), 857

Yu, F.W. (2017) 'Particle Breakage and the Critical State of Sand'. *Géotechnique* 67 (8), 713–719

Zeh, R.M. and Witt, K.J. (2007) 'The Tensile Strength of Compacted Clays as Affected by Suction and Soil Structure'. in *Experimental Unsaturated Soil Mechanics*. ed. by Schanz, T. Springer Berlin Heidelberg, 219–226

Zhang, H. and Garga, V.K. (1997) 'Quasi-Steady State: A Real Behaviour?' *Canadian Geotechnical Journal* 34 (5), 749–761

Zhao, H.F., Zhang, L.M., and Fredlund, D.G. (2013) 'Bimodal Shear-Strength Behavior of Unsaturated Coarse-Grained Soils'. *Journal of Geotechnical and Geoenvironmental Engineering* 139 (12), 2070–2081

Zhou, W.., Xu, X., and Garg, A. (2016) 'Measurement of Unsaturated Shear Strength Parameters of Silty Sand and Its Correlation with Unconfined Compressive Strength'. *Measurement: Journal of the International Measurement Confederation* 93, 351–358

Appendix

A Results of the mercury intrusion porosimetries

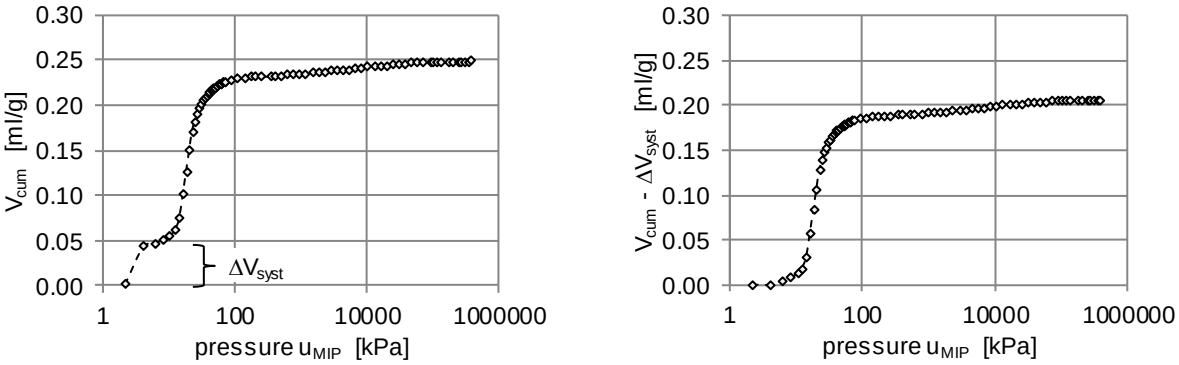

(a) (b)

Figure A.1: Intruded mercury volume for w_{comp} = 3% and I_D = 0.69, (a) measured, (b) corrected

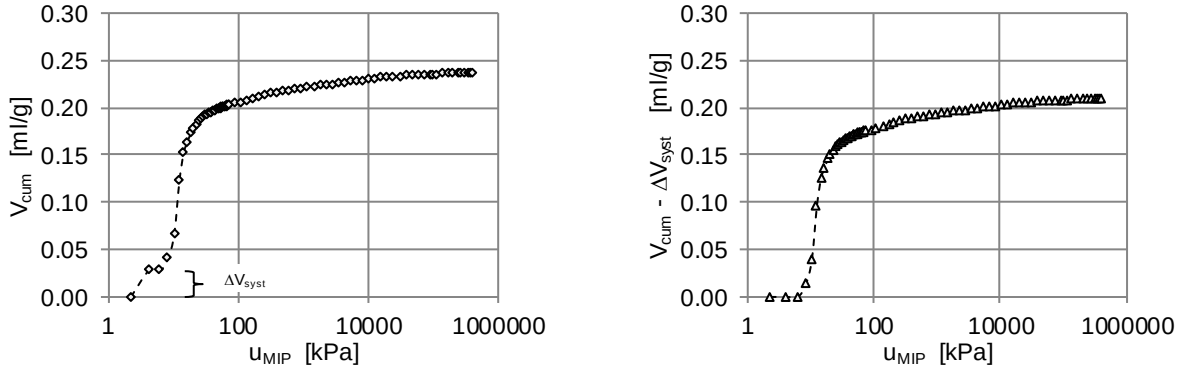

(a) (b)

Figure A.2: Intruded mercury volume for w_{comp} = 6% and I_D = 0.69, (a) measured, (b) corrected

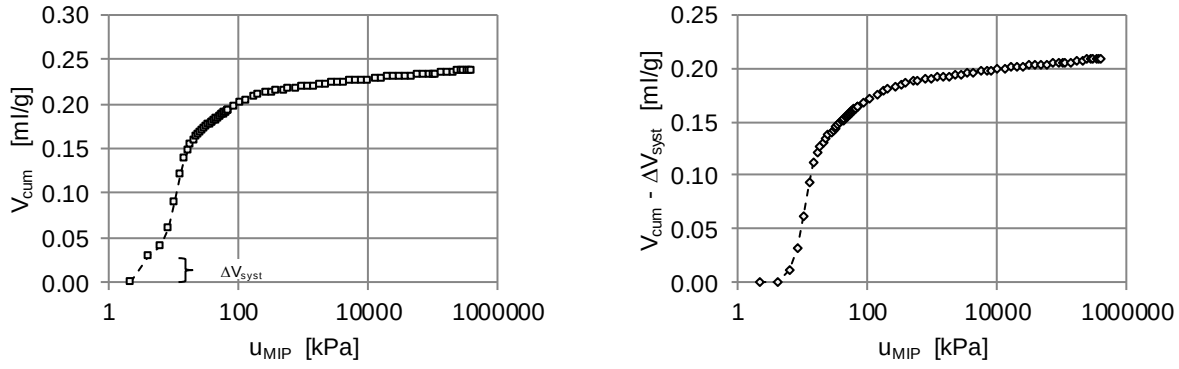

(a) (b)

Figure A.3: Intruded mercury volume for w_{comp} = 10% and I_D = 0.69, (a) measured, (b) corrected

B Derivation of the equations for the sphere model

The geometry and definition of variables of the sphere model are depicted in Figure B.1.

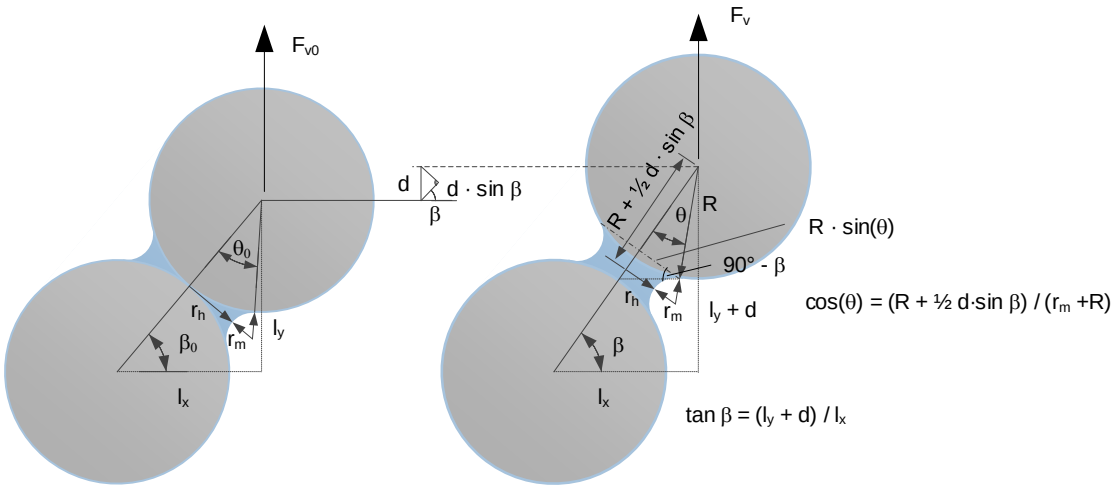

Figure B.1: Geometry and definition of variables of a model of two spheres of the same diameter R with an interposed capillary bridge

The volume of the water lens between the two spheres V_1 is derived from:

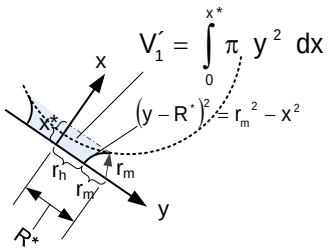

$$V_1 = 2 \cdot V_1' = 2 \cdot \int_0^{x^*} \pi \cdot y^2 dx$$

with

$$y = R^* - \sqrt{(r_m{}^2 - x^2)} \quad \text{for } y < R^* = r_m + r_h$$

From Figure B.1:

$$x^* = R - R\cos\theta + \frac{d \sin\beta}{2}$$

Hence,

$$y^2 = \left(R^* - \sqrt{(r_m{}^2 - x^2)}\right)^2 = \underbrace{R^{*2} + r_m{}^2}_{(I)} - \underbrace{2 \cdot R^*}_{(II)} \cdot \sqrt{(r_m{}^2 - x^2)} - x^2.$$

From the above follows:

$$V_1 = 2\pi \cdot (I) \cdot \int_0^{x^*} dx - 2\pi \cdot (II) \cdot \int_0^{x^*} \sqrt{(r_m{}^2 - x^2)}\, dx - 2\pi \cdot \int_0^{x^*} x^2\, dx$$

$$= 2\pi \cdot (I) \cdot [x]_0^{x^*} - 2\pi \cdot (II) \cdot \left[\frac{1}{2} x \sqrt{(r_m{}^2 - x^2)} + \frac{r_m{}^2}{2} \cdot \arcsin\left(\frac{x}{r_m}\right)\right]_0^{x^*} - 2\pi \cdot \left[\frac{x^3}{3}\right]_0^{x^*}$$

x

$$= 2\pi \cdot \left(R^{*2} + {r_m}^2\right) \cdot x^* - 2\pi \cdot R^* \cdot \left(x^* \sqrt{\left({r_m}^2 - x^{*2}\right)} + {r_m}^2 \cdot \arcsin\left(\frac{x^*}{r_m}\right)\right) - 2\pi \cdot \frac{x^{*3}}{3}$$

With

$$\cos\theta = \frac{R + \frac{1}{2} d \cdot \sin\beta}{r_m + R} = \frac{\overline{R}}{r_m + R}.$$

follows for x*:

$$x^* = R\left(1 - \frac{R + \frac{1}{2} d \cdot \sin\beta}{r_m + R}\right) + \frac{1}{2} d \sin\beta = \frac{r_m \left(R + \frac{1}{2} d \sin\beta\right)}{r_m + R} = \frac{r_m \overline{R}}{r_m + R}.$$

Hence,

$$\frac{V_1}{2\pi} = \left(R^{*2} + {r_m}^2\right) \cdot x^* - R^* \cdot \left[x^* \sqrt{\left({r_m}^2 - x^{*2}\right)} + {r_m}^2 \cdot \arcsin\left(\frac{x^*}{r_m}\right)\right] - \frac{x^{*3}}{3} =$$

$$= \left(R^{*2} + {r_m}^2\right) \cdot \left(\frac{r_m \overline{R}}{r_m + R}\right) - R^* \cdot \left(\frac{{r_m}^2 \overline{R}}{(r_m + R)^2} R^* + {r_m}^2 \cdot \arcsin\left(\frac{\overline{R}}{r_m + R}\right)\right) - \frac{\left(\frac{r_m \overline{R}}{r_m + R}\right)^3}{3} =$$

$$= \left(R^{*2} + {r_m}^2\right) \cdot \left(\frac{r_m \overline{R}}{r_m + R}\right) - R^* \cdot {r_m}^2 \cdot \left(\frac{\overline{R}}{(r_m + R)^2} R^* + \arcsin\left(\frac{\overline{R}}{r_m + R}\right)\right) - \frac{\left(\frac{r_m \overline{R}}{r_m + R}\right)^3}{3}.$$

From Figure B.1 follows

$$R^* = \sqrt{(R + r_m)^2 - \overline{R}^2} \quad \rightarrow \quad r_m = +\left(\sqrt{R^{*2} + \overline{R}^2} - R\right).$$

Thus,

$$\frac{V_1}{2\pi} = \left(R^{*2} + \left(\sqrt{R^{*2} + \overline{R}^2} - R\right)^2\right) \cdot \frac{\left(\sqrt{R^{*2} + \overline{R}^2} - R\right) \overline{R}}{\sqrt{R^{*2} + \overline{R}^2}} -$$

$$-R^* \cdot \left(\sqrt{R^{*2} + \overline{R}^2} - R\right)^2 \cdot \left(\frac{\overline{R}}{R^{*2} + \overline{R}^2} R^* + \arcsin\left(\frac{\overline{R}}{\sqrt{R^{*2} + \overline{R}^2}}\right)\right) - \frac{\left(\sqrt{R^{*2} + \overline{R}^2} - R\right)^3 \overline{R}^3}{3\left(\sqrt{R^{*2} + \overline{R}^2}\right)^3}$$

The volume of the water-covered cap of the two spheres is calculated with

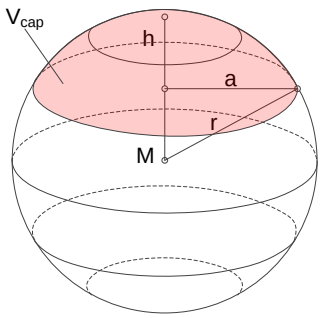

$$V_{cap} = \frac{\pi}{3} \cdot r^2 \cdot (3r - h)$$

With $r = R$, $h = R(1 - \cos\theta)$

follows

$$V_{cap} = \frac{\pi}{3} \cdot R^2(1 - \cos\theta)^2 \cdot \left(3R - R(1 - \cos\theta)\right)$$

$$= \frac{\pi}{3} \cdot R^3(1 - \cos\theta)^2 \cdot (2 + \cos\theta)$$

$$\rightarrow V_{cap} = \frac{\pi}{3} \cdot R^3 \left(1 - \frac{\overline{R}}{\sqrt{R^{*2} + \overline{R}^2}}\right)^2 \cdot \left(2 + \frac{\overline{R}}{\sqrt{R^{*2} + \overline{R}^2}}\right)$$

Eventually, the water volume of the capillary bridge between the two spheres can be described with:

$$V = V_1 - 2 \cdot V_{cap}$$

$$= 2\pi \left[\left(R^{*2} + \left(\sqrt{R^{*2} + \overline{R}^2} - R \right)^2 \right) \cdot \frac{\left(\sqrt{R^{*2} + \overline{R}^2} - R \right) \overline{R}}{\sqrt{R^{*2} + \overline{R}^2}} - \right.$$

$$- R^* \cdot \left(\sqrt{R^{*2} + \overline{R}^2} - R \right)^2 \cdot \left(\frac{\overline{R}}{R^{*2} + \overline{R}^2} R^* + \arcsin\left(\frac{\overline{R}}{\sqrt{R^{*2} + \overline{R}^2}} \right) \right) - \frac{\left(\sqrt{R^{*2} + \overline{R}^2} - R \right)^3 \overline{R}^3}{3\left(\sqrt{R^{*2} + \overline{R}^2} \right)^3} \Bigg] -$$

$$\left. - \frac{2\pi}{3} \left[R^3 \left(1 - \frac{\overline{R}}{\sqrt{R^{*2} + \overline{R}^2}} \right)^2 \cdot \left(2 + \frac{\overline{R}}{\sqrt{R^{*2} + \overline{R}^2}} \right) \right] \right.$$

Note that from Figure B.1, the following relationships can be derived for the variables in the above equation:

(i) $R^* = r_m + r_h = \sin\theta\,(R + r_m)$

(ii) $\overline{R} = \cos\theta\,(R + r_m)$

(i) + (ii)

$$r_h = \frac{\overline{R}\sin\theta - \overline{R} + R\cos\theta}{\cos\theta} = R^* - \sqrt{R^{*2} + \overline{R}^2} + R$$

$$r_m = R\left(\frac{1}{\cos\theta} - 1\right) = \sqrt{R^{*2} + \overline{R}^2} - R$$

with

$$\overline{R} = R + \frac{1}{2} d \cdot \sin\beta$$

$$\tan\theta = \frac{\overline{R}}{R^*} = \frac{R + \frac{1}{2}d \cdot \sin\beta}{R^*}$$

$$\tan\beta = \frac{2 \cdot R \cdot \sin\beta_0 + d}{2 \cdot R \cdot \cos\beta_0}$$

C Water volume correction for CS tests: Plausibility control

CS-6%-s=47.1kPa-0.69

(a)

(b)

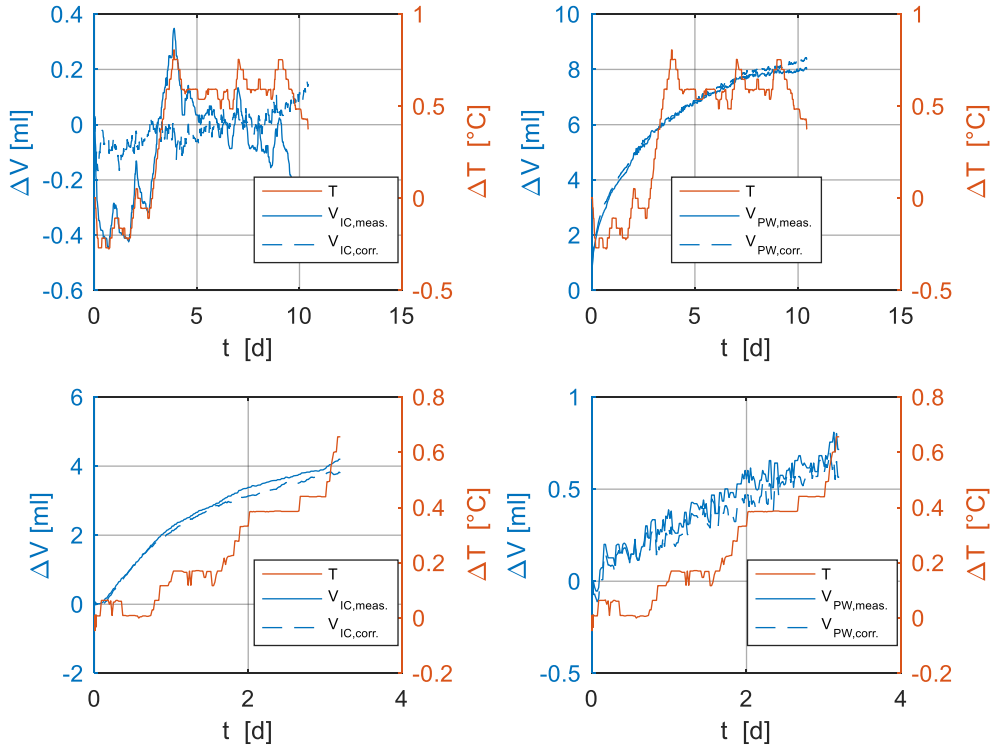

Figure C.1: Influence of corrections to water volume measurement; (a) saturation stage, (b) shearing stage, CS-6%-s=47.1kPa-0.69

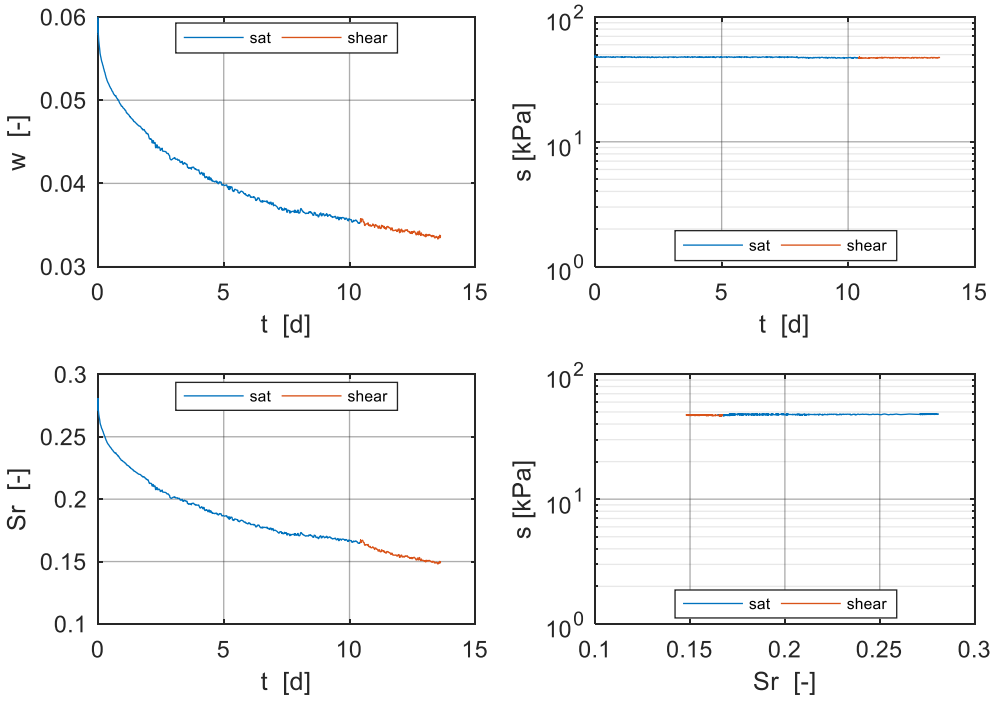

Figure C.2: Evolution of water content and degree of saturation with respect to time, CS-6%-s=47.1kPa-0.69

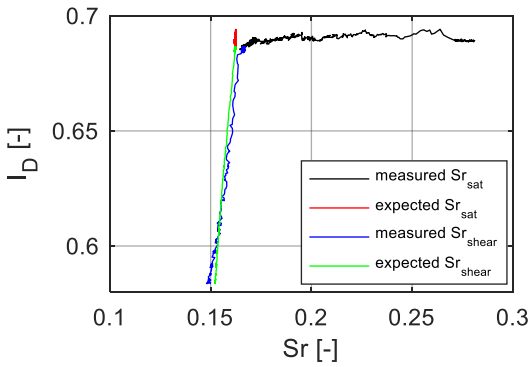

Figure C.3: Plausibility control: CS-6%-s=47.1kPa-0.69

CS-3%-s=46.8kPa-0.64

(a)

(b)

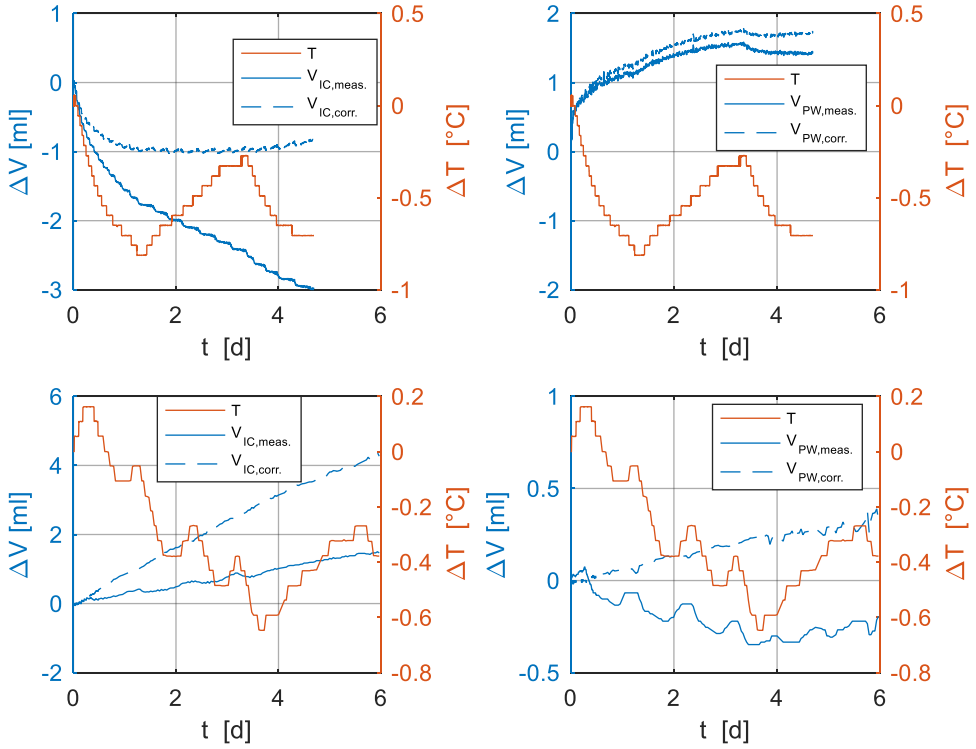

Figure C.4: Influence of corrections to water volume measurement; (a) saturation stage, (b) shearing stage, CS-3%-s=46.8kPa-0.64

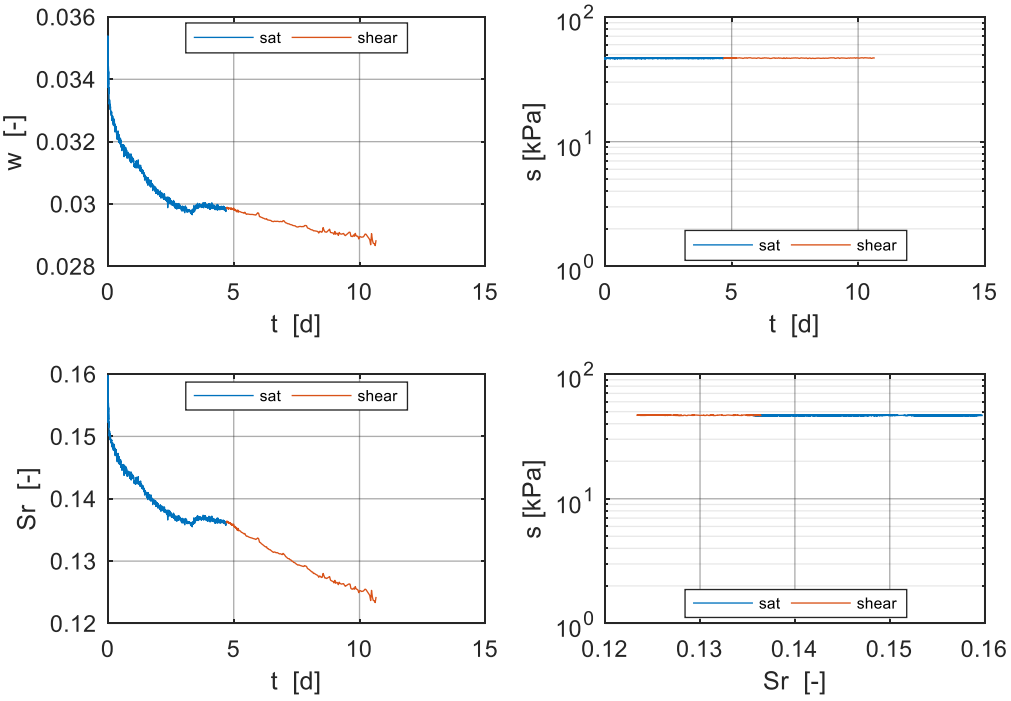

Figure C.5: Evolution of water content and degree of saturation with respect to time, CS-3%-s=46.8kPa-0.64

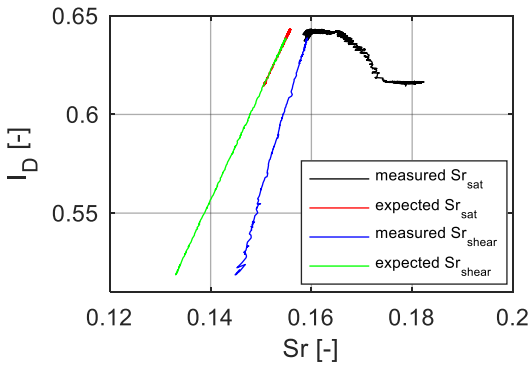

Figure C.6: Plausibility control: CS-3%-s=46.8kPa-0.64

CS-6%-s=6.8kPa-0.67

(a)

(b)

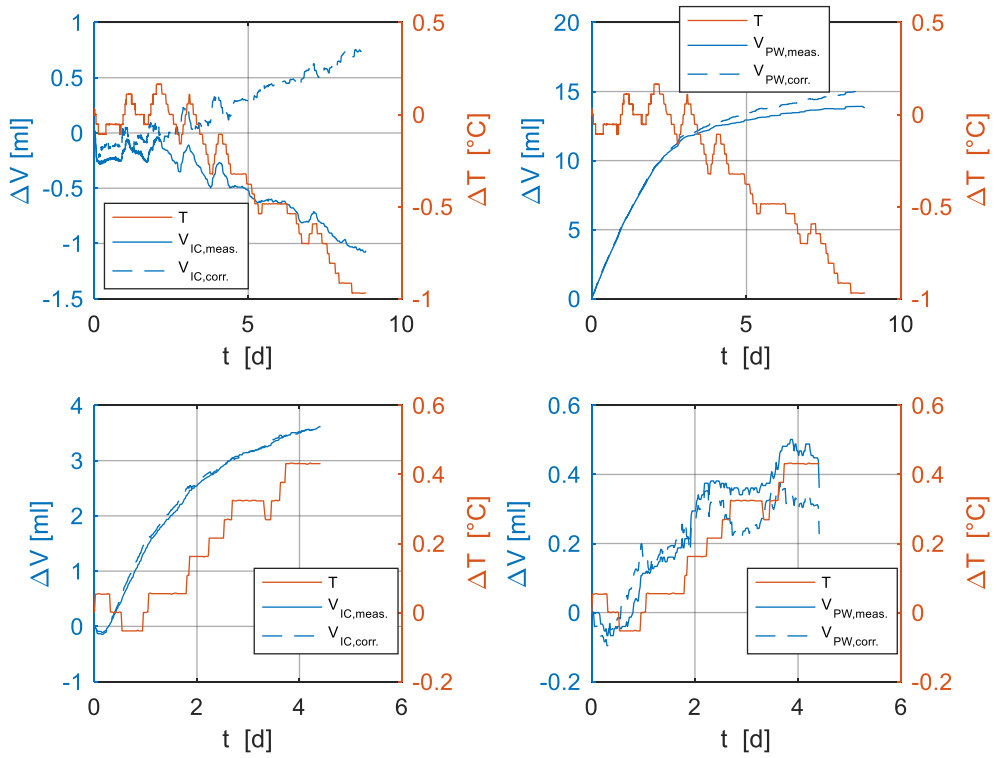

Figure C.7: Influence of corrections to water volume measurement; (a) saturation stage, (b) shearing stage, CS-6%-s=6.8kPa-0.67

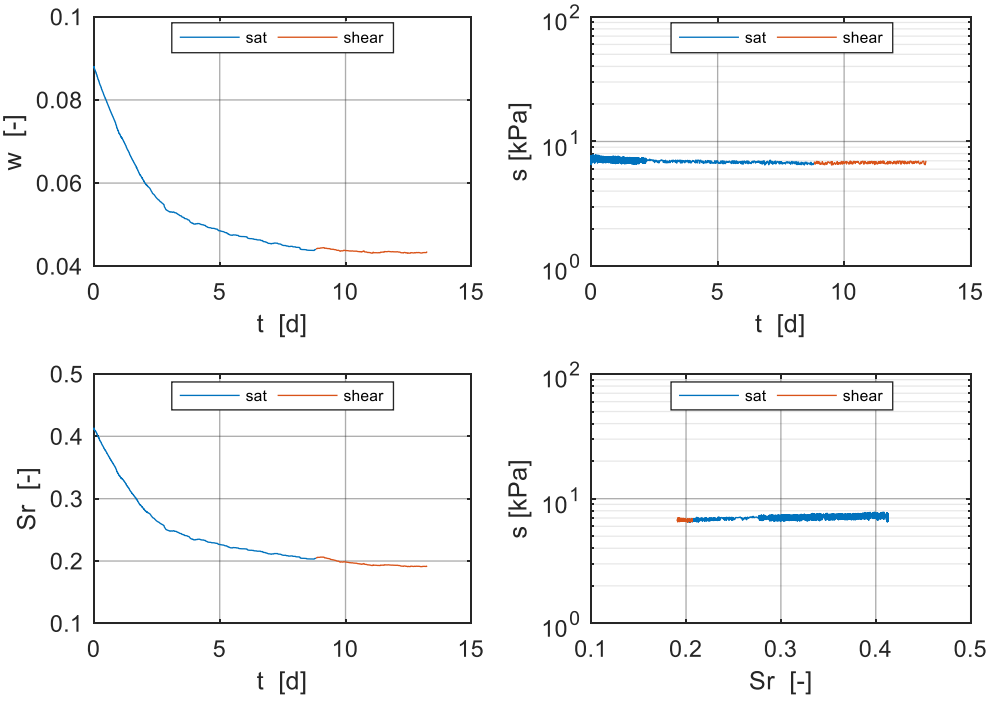

Figure C.8: Evolution of water content and degree of saturation with respect to time, CS-6%-s=6.8kPa-0.67

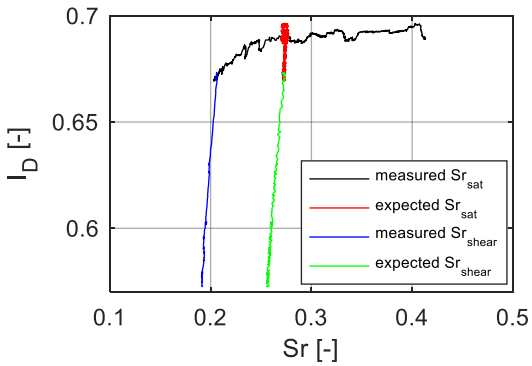

Figure C.9: Plausibility control: CS-6%-s=6.8kPa-0.67

D Derivation of the equations for plausibility control of the results from uniaxial tests

From Figure 6.30, it follows:

$$\frac{\tau_N}{\sigma_N} = \frac{(p_c - p^*) \cdot \sin\alpha \cdot \cos\alpha}{p^* + (p_c - p^*) \cdot \sin^2\alpha} = \frac{\frac{\sigma_t}{\chi \cdot s} \cdot \sin\alpha \cdot \cos\alpha}{1 - \frac{\sigma_t}{\chi \cdot s} + \frac{\sigma_t}{\chi \cdot s} \cdot \sin^2\alpha}$$

with $X = \frac{\sigma_t}{\chi \cdot s}$

The derivation of $\frac{\tau_N}{\sigma_N}$ after X yields:

$$\frac{\partial\left(\frac{\tau_N}{\sigma_N}\right)}{\partial X} = \frac{X \cdot [(X-2)\cos^2\alpha + 1]}{(X\cos^2\alpha - 1)^2}$$

The maximum value of $\frac{\tau_N}{\sigma_N}$ is obtained for:

$$\frac{\partial \frac{\tau_N}{\sigma_N}}{\partial X} = 0 \rightarrow \alpha = \arccos\left(\frac{i}{\sqrt{X-2}}\right)$$

When considering $0 \leq X = \frac{\sigma_t}{\chi \cdot s} \leq 1$, α becomes:

$$\alpha = \arccos\left(\frac{1}{\sqrt{X-2}}\right) = \arccos\left(\frac{1}{\sqrt{\frac{\sigma_t}{\chi \cdot s} - 2}}\right).$$

Inserting the above equation for α into the first expression for $\frac{\tau_N}{\sigma_N}$ yields the expression of the friction angle:

$$\tan\varphi' = \left(\frac{\tau_N}{\sigma_N}\right)_{max} = \frac{\sin\left[\arccos\left(\frac{1}{\sqrt{\frac{\sigma_t}{\chi \cdot s} - 2}}\right)\right] \cdot \frac{\frac{\sigma_t}{\chi \cdot s}}{\sqrt{\frac{\sigma_t}{\chi \cdot s} - 2}}}{1 - \frac{\sigma_t}{\chi \cdot s} + \frac{\sigma_t}{\chi \cdot s} \cdot \sin^2\left[\frac{1}{\sqrt{\frac{\sigma_t}{\chi \cdot s} - 2}}\right]}$$

List of Figures

List of Tables

List of Symbols

Roman Symbols

Symbol	Unit	Remarks
a	-	Parameter to describe the non-linear shear strength
A	kPa	Parameter to describe the SWRC
A	kPa	Area
A_0	cm²	Initial cross-sectional area of specimens in triaxial tests
a_1	1/kPa	Parameter to describe the bimodal SWRC
$A_{1/3}$	cm²	Cross-sectional area of the sample due to barreling
a_2	1/kPa	Parameter to describe the bimodal SWRC
A_c	cm²	Initial cross section of specimens for unconfined compression tests
A_{ram}	cm²	Cross sectional area of the loading ram
A_t	cm²	Initial cross section of specimens for uniaxial tensile testing
b	-	Parameter to describe the non-linear shear strength
c	kPa	Cohesion in τ-σ_{net} plane
c'	kPa	Cohesion in τ-σ' plane
c_{app}	kPa	Apparent cohesion due to the dual effect of suction on shear strength
C_c	-	Curvature coefficient
c_{leak}	ml/day	Coefficient accounting for leakage, absorption and evaporation
$c_{leak.bu}$	ml/day	Coefficient for the burettes accounting for leakage, absorption and evaporation
$c_{leak.IC}$	ml/day	Coefficient for the inner cell accounting for leakage, absorption and evaporation
C_u	-	Uniformity coefficient

xxx

$c'_{M-C,i}$	kPa	Intersection of the tangent to the non-linear failure criterion with the τ-axes in the τ-σ' plane for zone i
$c_{M-C,i}$	kPa	Intersection of the tangent to the non-linear failure criterion with the τ-axes in the τ-σ_{net} plane for zone i
D	cm	Diameter of samples
D	μm	Mean entrance pore diameter
d	μm	Pore diameter
d	mm	Particle distance in the sphere model
$D_{1/3}$	cm	Sample diameter averaged over the middle third portion of the sample
$D_{H/2}$	cm	Sample diameter in the mid-section of the sample due to barreling
e	-	Void ratio
e	-	Euler's number
e_0	-	Initial void ratio
e_{cs}	-	Void ratio at critical state
e_{max}	-	Maximum void ration
e_{min}	-	Minimum void ratio
e_{MIP}	-	Void ratio derived from MIP
e_{wm}	-	Microstructural water ratio separating intra-aggregate pores from inter-aggregate pores
F	N	Axial force measured in triaxial tests
F	-	Strength factor
F_c	N	Peak force measured in unconfined compression tests
FOS	-	Factor of safety
F_{peak}	N	Peak force measured in uniaxial tensile tests
F_t	N	Effective force measured in uniaxial tensile tests
F_{ult}	N	Ultimate force measured in uniaxial tensile tests at end of test

F_v	N	Vertical force in the sphere model
g	m/s²	Gravitional constant ($9.81\ \frac{m}{s^2} \approx 10 \frac{m}{s^2}$)
G_s	-	Specific gravity of the solid
h	m	Height of slope
H	cm	Height of samples
h	m	Capillary rise
H_0	cm	Initial sample height of samples
I_D	-	Relative density
I_P	-	Plasticity index
M	-	Stress obliquity
m	-	Khalili's exponent
m_1	-	Parameter to describe the bimodal SWRC
m_2	-	Parameter to describe the bimodal SWRC
M_{cs}	-	Stress obliquity at critical state
m_d	g	Dry mass of the soil
M_{peak}	-	Stress obliquity at peak
$M_{Zone,i}$	-	Inclination of the tangent to the non-linear failure criterion in the q - p' plane for zone i
n	-	Porosity
N_1	-	Parameter to describe the bimodal SWRC
n_1	-	Parameter to describe the bimodal SWRC
N_2	-	Parameter to describe the bimodal SWRC
n_2	-	Parameter to describe the bimodal SWRC
n_{Hg}	-	Volumetric portion of mercury-filled pores

n_w	-	Volumetric portion of water-filled pores
p	kPa	Total mean stress
p'	kPa	Effective mean stress
p*	kPa	Suction-induced effective mean stress minus tensile stress
p'_0	kPa	Initial effective mean stress
$p_{0,Tmirror}$	kPa	Saturated partial vapor pressure in the sample chamber at temperature T
$p_{0,Tsoil}$	kPa	Saturated partial vapor pressure in the soil at temperature T
p_c	kPa	Suction-induced effective mean stress
p'_{cs}	kPa	Effective mean stress at critical state
p_i	-	Polynomial coefficients (i = 1..5) to describe the parameters which describe the bimodal SWRC
p_{net}	kPa	Net mean stress
p'_{peak}	kPa	Effective mean stress at peak
p_{Tsoil}	kPa	Partial vapor pressure in the soil at temperature T
q	kPa	Deviatoric stress
$q^*_{Zone,i}$	kPa	Intersection of the tangent to the non-linear failure criterion with the q-axes in the q-p' plane for zone i
q_c	kPa	Deviatoric stress at peak at unconfined compression tests
q_{cs}	kPa	Deviatoric stress at critical state
q_{peak}	kPa	Deviatoric stress at peak
q_t	kPa	Deviatoric stress at peak at uniaxial tensile tests
r	m	Radius
R	mm	Radius
R_{gas}	j/mol/K	Universal gas constant
RH	-	Relative humidity

r_h	m	Internal radius to describe a capillary bridge
r_m	m	External radius to describe a capillary bridge
s	kPa	Suction
s_{mean}	kPa	Mean suction
s_{AE}	kPa	Air entry value
$s_{AE,macro}$	kPa	Air entry value of macropores
$s_{AE,micro}$	kPa	Air entry value of micropores
$s_{as\text{-}comp}$	kPa	Suction in as-compacted samples
S^e	-	Effective degree of saturation
Sr	-	Degree of saturation
Sr_r	-	Residual degree of saturation
s_r	kPa	Suction at residual degree of saturation
Sr_0	-	Degree of saturation at which the contribution of suction to effective stress vanishes
Sr_a	-	Degree of saturation mostly ascribed to adsorptive forces
Sr_{comp}	-	Degree of saturation at which samples are compacted
Sr_m	-	Degree of saturation separating intra-aggregate pores from inter-aggregate pores
Sr_{max}	-	Maximum degree of saturation (for describing the SWRC)
Sr_{mean}	-	Mean degree of saturation
Sr_{MIP}	-	Degree of saturation calculated from the measured intruded mercury volume
Sr_r	-	Residual degree of saturation
T	°C	(Water) Temperature
T_{Hg}	N/m	Surface tension of air-mercury interface
T_{mirror}	°C	Temperature of the mirror

T_{soil}	°C	Temperature of the soil
T_w	N/m	Surface tension of air-water interface
u	kPa	Fluid pressure
u_a	kPa	Pore-air pressure
u_{atm}	kPa	Atmospheric pressure
u_{MIP}	kPa	Pressure applied to mercury
u_w	kPa	Pore-water pressure
$u_{w,meas.}$	kPa	Measured pore-water pressure
V	cm³	Volume
V_0	cm³	Initial volume
$V_{bu,IC,0}$	cm³	Initial water volume of the inner cell burette including tubing and fittings
$V_{bu.PW,0}$	cm³	Initial water volume of the pore water burette including tubing and fittings
$V_{bu.REF,0}$	cm³	Initial water volume of the reference burette including tubing and fittings
V_{cum}	cm³/g	Cumulative volume of intruded mercury per gram of soil
V_{Hg}	cm³	Intruded mercury volume
$V_{Hg,total}$	cm³	Intruded mercury volume at end of test
$V_{IC,0}$	cm³	Initial water volume of the inner cell
$V_{IC,corr}$	cm³	Water volume of the inner cell corrected for leakage and temperature
$V_{IC,meas.}$	cm³	Measured water volume of the inner cell
$V_{PW,corr}$	cm³	Water volume of the pore water corrected for leakage and temperature
$V_{PW,meas.}$	cm³	Measured water volume of the pore-water
V_{REF}	cm³	Measured water volume of the reference burette
V_s	cm³	Volume of solids

V_{total}	cm^3/g	Total volume of intruded mercury at end of test per gram of soil
V_v	cm^3	Volume of voids
w	-	Gravimetric water content
w_0	-	Initial gravimetric water content
w_{comp}	-	Gravimetric compaction water content
w_L	-	Liquid limit
$w_{test\ end}$	-	Gravimetric water content at end of test

Greek Symbols

Symbol	Unit	Remarks
α	-	Parameter to describe the state variable χ
α	-	Parameter to describe the SWRC
α	°	Inclination of failure plane
α	1/°C	Coefficient of volume expansion of the measuring system
α_{bu}	1/°C	Coefficient of volume expansion of the burettes
α_d	°	Contact angle of water solid interface for drying
$\alpha_{exp.}$	°	Inclination of failure plane derived from experiments
α_{Hg}	°	Contact angle of mercury solid interface
α_{IC}	1/°C	Coefficient of volume expansion of the inner cell
α_w	°	Contact angle of water solid interface
α_w	°	Contact angle of water solid interface for wetting
β	°	Angle of slope inclination

β	-	Fitting parameter for SWRC
β	°	Particle orientation (sphere model)
χ	-	Bishop's state variable
δ_{ij}	-	Kronecker-Delta
$\Delta\sigma'$	kPa	Suction-induced increase in effective stress
$\Delta\sigma'_{exp}$	kPa	Suction-induced increase in effective stress derived from experiments
$\Delta\sigma_{r,m}$	kPa	Additional radial stress imposed by membrane stretching
Δt	day	Time shift of the water volume signal fluctuation compared to the temperature fluctuation
ΔT	°C	Temperature fluctuation of cell-water
Δt_{bu}	day	Time shift of the water volume fluctuation of the burettes compared to the temperature fluctuation
Δt_{IC}	day	Time shift of the water volume fluctuation of the inner cell compared to the temperature fluctuation
$\Delta T_{t+\Delta t.bu}$	°C	Temperature fluctuation as a function of time t and time shift Δt_{Bu}
$\Delta T_{t+\Delta t.IC}$	°C	Temperature fluctuation as a function of time t and time shift Δt_{IC}
Δv	mm	Vertical penetration of the loading ram into the inner cell
ΔV_{IC}	ml	Water volume change in the inner cell corrected for temperature and leakage
ΔV_{leak}	ml	Changes in water volume due to leakage, evaporation an absorption
$\Delta V_{leak,bu}$	ml	Changes in water volume of the burettes due to leakage, evaporation an absorption
$\Delta V_{leak,IC}$	ml	Changes in water volume of the inner cell due to leakage, evaporation an absorption
ΔV_{PW}	ml	Water volume change in the pore water corrected for temperature and leakage
ΔV_{REF}	ml	Changes in the measured water volume of the reference burette
ΔV_T	ml	Changes in water volume due to temperature fluctuation
$\Delta V_{T,IC}$	ml	Changes in inner cell water volume due to temperature fluctuation
$\Delta V_{T,PW}$	ml	changes in pore-water volume due to temperature fluctuation

$\Delta V_{T,REF}$	ml	Changes in water volume of the reference burette due to temperature fluctuation
ε_1	-	Principle strain
ε_2	-	Principle strain
ε_3	-	Principle strain
ε_a	-	Axial strain
ε_q	-	Deviatoric strain
ε_r	-	Radial strain
ε_V	-	Volumetric strain
φ	°	Friction angle in τ-σ_{net} plane
φ'	°	Effective friction angle in τ-σ' plane
φ'_{mob}	°	Mobilized effective friction angle
φ'_{peak}	°	Effective secant peak friction angle
$\varphi'_{peak,exp.}$	°	Effective secant peak friction angle derived from experiments
$\varphi'_{M\text{-}C,i}$	°	Angle of inclination of the tangent to the non-linear failure criterion in the $\tau-\sigma'$ plane for zone i
$\varphi_{M\text{-}C,i}$	°	Angle of inclination of the tangent to the non-linear failure criterion in the $\tau-\sigma_{net}$ plane for zone i
κ	-	Parameter to describe the state variable χ
Λ	-	Parameter to describe the state variable χ
θ	-	Volumetric water content
θ	°	Filling angle to describe the water bridge between two spheres
ρ	g/cm³	Density of moist soil
ρ_d	g/cm³	Density of dry soil
$\rho_{d.0}$	g/cm³	Initial dry density
ρ_s	g/cm³	Specific density

ρ_w	g/cm³	Water density
$\rho_{w,Tsoil}$	g/cm³	Temperature-dependent density of soil water
σ	kPa	Total stress
σ'	kPa	Effective stress
σ'_1	kPa	Effective principle stress
σ'_3	kPa	Effective principle stress
σ_a	kPa	Total axial stress
σ_c	kPa	Axial stress in unconfined compression tests
σ_{cell}	kPa	Cell pressure
σ_{ij}	kPa	Total stress tensor
σ'_{ij}	kPa	Effective stress tensor
$\sigma_{ij,net}$	kPa	Net stress tensor
σ'_N	kPa	Effective stress acting normal to the failure plane
σ_{net}	kPa	Net stress
σ_r	kPa	Total radial stress
σ_t	kPa	Tensile strength/ tensile stress
τ	kPa	Shear stress
τ	kPa	Shear strength
τ_N	kPa	Shear stress acting on failure plane
τ_{peak}	kPa	Peak shear strength
τ_{sat}	kPa	Saturated shear strength
τ_{unsat}	kPa	Unsaturated shear strength
ω	-	Pore-size density

ω_v	kg/mol	Molar mass of water vapor